Multidisciplinary Optimisation of Radial and Mixed-inflow Turbines for Turbochargers

Jiangnan Zhang

Department of Mechanical Engineering
University College London

This dissertation is submitted for the degree of
Doctor of Philosophy

December 2017

I would like to dedicate this thesis to my loving parents, my wife, my nieces, my nephew and all the people I love ...

DECLARATION

I, Jiangnan Zhang, confirm that the work presented in this thesis is my own. Where information has been derived from other sources, I confirm that this has been indicated in the thesis.

Jiangnan Zhang
December 2017

ACKNOWLEDGEMENTS

I would like to acknowledge, first and foremost, Prof Mehrdad Zangeneh, my principle supervisor, who brought me into the world of turbomachinery and Computational Fluid Dynamics (CFD) when I was studying MSc in the Department of Mechanical Engineering, University College London in 2009 and 2010, for his invaluable guidance and advice throughout my postgraduate work. I am very appreciative of him for supervising me and offering me the opportunity to learn from and work with him.

I would like to acknowledge Cummins Turbo Technologies (CTT) and Engineering and Physical Sciences Research Council (EPSRC) for their financial support (Dorothy Hodgkin Postgraduate Awards) to sponsor this project.

I would like to acknowledge Dr Paul Eynon, who is my industrial supervisor, Michael D Dolton, Dr Keith Nickson and Dr Edward Palmer from CTT for their patience, help and swift response to all my request and questions during the project.

I would like to acknowledge Matthieu de Maillard and Fabio Pengue, who worked at Advanced Design Technology (ADT), for their generous help when I started to use the inverse design code and the CFD software.

I would like to acknowledge Dr Edward Michael John Naylor, who is my manager and working at ADT now, for carefully proofreading this thesis.

I would like to acknowledge my sister, my brother and all my friends for their full support.

I would like to acknowledge my parents, Gui'e Lu and Zonglu Zhang, who raised me and educated me to be a useful man, for their love and trust in me.

Finally, I would like to acknowledge and appreciate my wife, Jing Wang, who has been always there to support and comfort me. Nothing makes me happier than just to be with her.

ABSTRACT

The radial and mixed-inflow turbines have been widely used for the turbocharger application. The design of a turbocharger turbine with good performance still presents a lot of challenges. Apart from the traditional requirements such as high efficiency and low stress, the turbine blade is also required to achieve certain performance targets at multiple operating points, high unsteady efficiency under pulsating flow condition, reduced moment of inertia (MOI) and high vibration characteristic.

To meet these challenges it is important to optimise the radial and mixed-inflow turbines for the aerodynamic performance at multiple operating points and the structural performance subject to MOI, stress and vibration constraints. In this thesis we propose an approach based on 3D inverse design method that makes such a design optimisation strategy possible under industrial timescales.

Using the inverse design method, the turbine blade geometry is computed iteratively based on the prescribed blade loading distribution. The turbine's aerodynamic and mechanical performance is evaluated using CFD and Finite Element Analysis (FEA). A linear regression is performed based on the results of a linear DOE study. The number of design parameters is reduced based on a sensitivity analysis of the linear polynomial coefficients. A more detailed DOE with around 60 designs is generated and Kriging is used to construct a response surface model (RSM). Multi-objective genetic algorithm (MOGA) is then used to search the optimal designs which meet multiple constraints and objectives on the Kriging response surface.

The radial filament blading is always applied by the conventional design method to reduce the stress, while the inverse designed blade is three-dimensional (3D). Two radial filament modification (RFM) methods are proposed to control the

stress level of 3D blades. Radial turbines with a backswept leading edge (LE) designed using the inverse design method show improved cycle-averaged efficiency.

An optimal design is obtained through the second optimisation. Its performance is evaluated in both the aerodynamic and mechanical aspects based on CFD and FEA simulations. The CFD model is validated against the experimental results of the baseline design. The numerical results show that the optimal design leads to better performance in almost all aspects including improved efficiency in the low U/C_{is} (velocity ratio), reduced maximum stress, reduced MOI, and increased vibration frequencies.

TABLE OF CONTENTS

LIST OF FIGURES

LIST OF TABLES

NOMENCLATURE

Roman Symbols

$\hat{a}_i^j$ normalised polynomial coefficient

A^j coefficient matrix for jth performance parameter

$\tilde{A}_i^j$ normalised polynomial coefficient

B blade number

B_{aero} aerodynamic blockage factor

B_f blockage factor

C_{is} isentropic velocity

c_P specific heat capacity at constant pressure

DRVT LE value of the loading curve

E expected value

f blade wrap angle

f_1 normalised polynomial coefficient

f_2 normalised polynomial coefficient

F_n Fourier coefficient

h static enthalpy

$\dot{m}_1(t)$ instantaneous inlet mass flow rate

$\dot{m}$ mass flow rate

$\dot{m}_{in}$ inlet mass flow rate

$\dot{m}_{out}$ outlet mass flow rate

m meridional coordinate

m_n nondimensionalised meridional coordinate

m^* normalised meridional coordinate

NC streamwise coordinate of the point dividing the loading curve

ND streamwise coordinate of the point dividing the loading curve

P Pressure

P_{01} inlet total pressure

$P_{01}(t)$ instantaneous inlet total pressure

$P_2(t)$ instantaneous outlet static pressure

P_4 outlet static pressure

r radial coordinate

Re Reynolds number

R_n Fourier coefficient

R_{tip} blade tip radius

$r\bar{V}_\theta$ mean swirl velocity

s static entropy

S_1 blade-to-blade streamsurface

S_2 hub-to-tip streamsurface

S_{2m} mean hub-to-tip streamsurface

$S(\alpha)$ periodic sawtooth function

SLOPE slope of the straight line in the loading curve

s^* normalised spanwise coordinate

S_{tr}	Strouhal number
T	Temperature
t	time
T_{01}	inlet total temperature
$T_{01}(t)$	instantaneous inlet total temperature
t_N	normal thickness
t_θ	tangential thickness
U	blade speed or blade tip speed
$\frac{U}{C_{is}}$	velocity ratio or blade to jet speed ratio
U/C_{is}	velocity ratio or blade to jet speed ratio
$\vec{V}$	absolute velocity vector
$\bar{V_y}$	prescribed pitch-averaged tangential velocity
W_1	nozzle gap, meridional inducer width
W_2	meridional exducer width
$\dot{W}_{is}(t)$	instantaneous isentropic power
W_{is}	total isentropic work during one pulse period
$\dot{W}_T(t)$	instantaneous turbine power
W_T	total turbine work during one pulse period
$\vec{W}$	relative velocity vector
x	Cartesian coordinate x
$\hat{x}_i^j$	normalised design parameter
x_i	ith design parameter
X^j	design parameter matrix for jth performance parameter
y	Cartesian coordinate y

$\hat{y}_j$ normalised performance parameter

Y_{hub} meridional hub control point parameter

Y^j performance parameter matrix for jth performance parameter

y^j jth performance parameter

y^+ dimensionless wall distance

Y_{shr} meridional shroud control point parameter

z axial coordinate

Greek Symbols

α blade wrap angle

α_1 nozzle LE absolute flow angle, meridional LE angle

α_2 nozzle TE absolute flow angle, meridional TE angle

α_3 rotor LE absolute flow angle

α_{in} rotor incidence angle

β_3 rotor LE relative flow angle

$\beta_{b,LE}$ rotor LE blade angle

$\delta_P(\alpha)$ periodic Dirac delta function

ΔT pulse period

Δt time lag

ΔP pressure difference between the blade pressure and suction surfaces

$\frac{\partial r\bar{V}_\theta}{\partial m}$ rate of change of the mean swirl velocity along the streamwise direction

η efficiency

η_{t-s} steady total-to-static efficiency

$\eta_{t-s}(t)$ instantaneous total-to-static efficiency

$\bar{\eta}_{t-s}$ cycle-averaged total-to-static efficiency

γ	heat capacity ratio
λ	Monge-Clebsch scalar
μ	Monge-Clebsch scalar
Ω	blade rotational speed
ω	blade rotational speed
Φ	potential function
ϕ	potential function
Ψ	stream function
ψ	stream function
ρ	density
τ	torque
τ_A	timescale of fluid particles passing through the turbine
τ_B	timescale of the unsteadiness of the pulsating flow
θ	circumferential coordinate
$\vec{\Omega}$	vorticity vector

Superscripts

-1	inverse of a matrix
area	area-averaged
mass	mass-averaged
$+$	blade pressure surface
rot	rotary value
$*$	complex conjugation
$-$	blade suction surface
T	transpose of a matrix

Subscripts

0	total or stagnation value
$50k$	50,000 rev/min
$60k$	60,000 rev/min
$70k$	70,000 rev/min
$80k$	80,000 rev/min
$90k$	90,000 rev/min
ave	average
bl	blade
exd	exducer
hub	blade hub
ind	inducer
in	inlet
is	isentropic
out	outlet
ref	reference
shr	blade shroud
T	turbine
tip	blade tip
$t\text{-}s$	total-to-static

Other Symbols

$\overline{\square}$	circumferential mean symbol
$\vec{\square}$	vector symbol
$\widetilde{\square}$	periodic symbol

∇ gradient

$\nabla\cdot$ divergence

$\nabla\times$ curl

$\hat{\square}$ normalised symbol

Acronyms

1D one-dimensional

2D two-dimensional

3D three-dimensional

ADT Advanced Design Technology

ANN artificial neural network

BEP best efficiency point

CAD computer-aided design

CCD Central Composite design

CFD Computational Fluid Dynamics

CO_2 carbon dioxide

CPU central processing unit

CSM computational structural mechanics

CTT Cummins Turbo Technologies

DFT Discrete Fourier Transform

DOE Design of Experiments

DP design point

EA evolutionary algorithm

ER expansion ratio

FEA Finite Element Analysis

GA genetic algorithm

IDFT Inverse Discrete Fourier Transform

LHS left-hand side, Latin Hypercube sampling

LE leading edge

MCA Mass and Circumferentially Averaged

MFP mass flow parameter

MFT mixed-inflow turbine

MOGA multi-objective genetic algorithm

MOI moment of inertia

MRF multiple reference frame

NACA National Advisory Committee for Aeronautics

NASA National Aeronautics and Space Administration

NSGA-II Non-dominated Sorting Genetic Algorithm-II

OLHS Optimal Latin Hypercube Sampling

PTC Parametric Technology Corporation

RANS Reynolds-averaged Navier-Stokes

RBF radial basis function

RFM Radial Filament Modification

RFT radial-inflow turbine

RHS right-hand side

RPM revolution per minute

RPS revolution per second

RSM response surface model

SP speed parameter

SST shear stress transport

TE trailing edge

TRACE Turbomachinery Research Aerodynamics Computational Environment

t-s total-to-static

CHAPTER 1

INTRODUCTION

A turbine is a rotating machine which extracts energy from the fluid and converts it into useful work. The fluid can be a gas or liquid depending on the application. Many types of turbines, such as gas turbine, steam turbine, wind turbine and water turbine have been widely used for different applications.

A turbocharger consists basically of a compressor and a turbine coupled on a common shaft. The turbocharger turbine, which consists of a turbine wheel and a turbine housing, converts the engine exhaust gas into mechanical energy to drive the compressor. A pressure and temperature drop between the inlet and the outlet of the turbine is converted into kinetic energy to drive the turbine wheel.

Turbines can be different types including axial, radial and mixed-inflow. The axial turbine through which the flow is only in the axial direction is fitted to large turbochargers. In radial-inflow turbines which are fitted to small turbochargers, gas inflow is in the radial direction at the inlet and axial direction at the outlet. A mixed-inflow turbine can be viewed as a design between an axial and a radial turbine, since the inlet flow of a mixed-inflow turbine is at an angle between the complete axial and radial design.

In this study what we are going to investigate are radial and mixed-inflow turbines used in the turbochargers of heavy duty vehicles.

1.1 Radial and Mixed-inflow Turbines for Turbochargers

The radial-inflow turbine is a work producing device which contains two essential parts: a fixed and swirl generating component in which the working fluid is expanded and turned to be given a circumferential velocity about the rotating axis and a rotor through which the flow passes and does work by doing so. The swirl generating component must be able to turn the inlet flow and distribute it around the circumference of the turbine. To do this the casing is made in a spiral shape with a cross-sectional area which is maximum at the inlet and decreases with the azimuth angle about the turbine rotational axis. Such a casing is called volute or scroll.

The radial turbine can be divided into two types by the existence of a stator (or called vane or nozzle blade). The function of the stator is to remove any circumferential non-uniformities in the flow, give the flow swirl or tangential velocitiy and accelerate the flow before it enters the rotor. Due to the requirements of reducing manufacturing cost and installation size, especially for turbocharger applications, the omission of the nozzle ring is another option in which case the swirl must be generated by the volute alone. A schematic of radial-inflow turbines is shown in Figure 1.1.

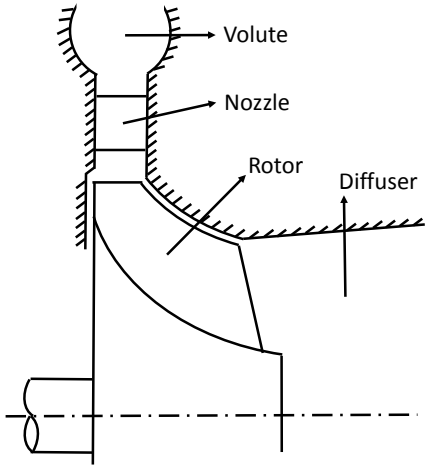

Fig. 1.1 Schematic of radial-inflow turbines

The main advantage of a radial turbine is that it can employ a relatively higher expansion ratio for low mass flow rate (low specific speed) applications compared

to axial turbines. The work produced by a single stage of a radial turbine is equivalent to that of two or more stages in an axial turbine. Another advantage of the radial turbine over axial turbines is its small and compact size especially for the vehicle applications. An axial-flow turbine with the same flow conditions as a radial-inflow turbine would have a larger relative clearance (percentage of the rotor exit passage height, Futral and Holeski [1970]) which will result in more leakage loss. Therefore, the shroud clearance of a radial turbine has a smaller effect on the performance. By considering all these factors, the best option for small gas turbine application is radial-inflow turbines rather than axial turbines.

The main disadvantage of radial turbines is that the flow in the rotor is fully 3D and complicated which results in lower maximum efficiency for radial-inflow turbines compared to that of axial turbines. Only when the Reynolds number (Re) becomes low enough ($10^5 - 10^6$), the efficiency of the axial turbine is less than that of a radial-inflow turbine according to Boyce [2002].

Automotive turbochargers are almost entirely equipped with radial turbines. Due to the increasing demand for improving fuel economy and fast response of automotive turbochargers, a turbine which can extract more energy at high expansion ratio (ER), low rotating speed and has lower inertia is desirable. It is found that the peak efficiency of radial turbines always occurs in the U/C_{is} of around 0.7. Blade to jet speed ratio U/C_{is} is defined by Equation 1.1 (Whitfield and Baines [1990]). However, at very high ER and low rotating speed where $U/C_{is} < 0.7$, the radial turbine experiences high positive incidence which results in lower efficiency. To overcome the efficiency loss in the low U/C_{is} and achieve lower turbine inertia, mixed-inflow turbines have been proposed and studied for decades since 1950s.

$$\frac{U}{C_{is}} = \frac{\omega R_{tip}}{\sqrt{2c_P T_{01}\left[1 - \left(\frac{P_2}{P_{01}}\right)^{(\gamma-1)/\gamma}\right]}} \tag{1.1}$$

One of the earliest mixed-flow concept in the turbomachinery was reported by Hamrick et al. [1950]. They proposed a method to analyse the compressible flow in an arbitrary mixed-flow impeller. Rajoo and Martinez-Botas [2008] provided a comprehensive review of the past 50 years' research into mixed-inflow turbines. The meridional plane of a mixed-inflow turbine can be seen in Figure 1.2. The radial and mixed-inflow turbines are distinguished by the cone angle which is the

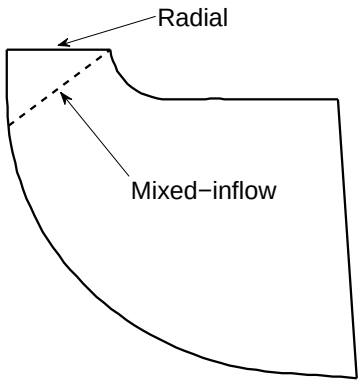

Fig. 1.2 Meridional plane of radial and mixed-inflow turbines

angle between blade LE and the radial direction. For radial turbines, the cone angle is always equal to 90°. For mixed-inflow turbines, the cone angle is less than 90°.

The main advantage of a mixed-inflow turbine as mentioned above is that it results in a shift of peak efficiency to lower U/C_{is} compared to a traditional radial turbine as shown in Figure 1.3. For automotive turbocharger applications, the flow is always in the pulsating condition with varying pressure and temperature at the turbine inlet and most of the exhaust energy is available in the high pressure and temperature region which corresponds to high values of C_{is}. The change of the rotating speed of the turbine is negligible during its operation. Therefore, it becomes important to extract more energy in the low U/C_{is} region for the turbine and the mixed-inflow turbine has shown improved efficiency in this region.

It should also be noted that the definition of the blade tip speed U for a mixed-inflow turbine is different from that for a radial turbine. There is no problem for the radial turbine, since $U = \omega R_{tip}$ and R_{tip} is constant along the LE. However, for a mixed-inflow turbine, R in the LE varies from the hub to the shroud ($R_{hub} < R_{shr}$). Different methods of defining the average tip radius (R_{ave}) for mixed-inflow turbines have been used. For example, $R_{ave} = (R_{hub} + R_{shr})/2$ or $R_{ave} = \sqrt{(R_{hub}^2 + R_{shr}^2)/2}$. By this definition even for the same C_{is}, rotating speed and blade tip radius (R_{shr}), the U/C_{is} of mixed-inflow turbines shifts towards lower values compared to that of radial turbines.

Another advantage of mixed-inflow turbines over radial turbines is the reduction of the MOI. As it can be seen in Figure 1.2, compared to the radial turbine, the LE of a mixed-inflow turbine which has the largest radius in the blade is

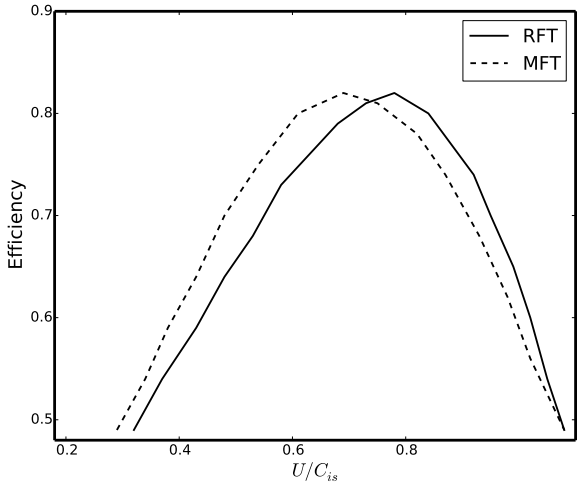

Fig. 1.3 Turbine efficiency as a function of velocity ratio for radial and mixed-inflow turbines (Watson and Janota [1982])

trimmed off which significantly reduces the turbine MOI . The turbine with lower inertia has a faster response to the engine exhaust change and therefore achieves better transient performance. It is also reported by Wallace and Pasha [1972] that mixed-inflow turbines have better swallowing capacity in the high speed and high pressure ratio region compared to radial turbines. This makes it possible to apply a smaller mixed-inflow turbine for a given performance target.

1.2 Design Challenges

The traditional design method for the turbine blades which is called direct design method is a 'trial and error' process. The blade geometry is defined by the meridional shape, the camber line (blade angle or wrap angle) and the thickness distribution at different blade layers. The blade meridional shape, blade angle and thickness distribution are controlled by B-spline, Bézier or polynomial curves. This design process contains around 50 design parameters or even more in total. When the blade geometry is ready, CFD and FEA simulations will be used to evaluate the turbine's aerodynamic and mechanical performance. If the turbine's aerodynamic or mechanical performance does not meet the requirements, the designer has to modify the large number of design parameter and repeat this process until the final design which meets all the design targets is obtained. However, for the designer there are no simple rules on how to modify the blade to improve both

the aerodynamic and mechanical performance simultaneously. Since the designer does not know which parameters need to be changed and how to change them, before the final design is obtained hundreds of design loops need to be done.

The main challenges we are facing now when designing the radial/mixed-inflow turbines are:

1) The design process using the direct design method is time consuming and computationally expensive;

2) The temperature of the exhaust gas enters the turbine is extremely high (around 600 - 1000°C) which reduces the yield strength of the material significantly and the maximum turbine tip speed is extremely high (around 500 - 600 m/s) which results in very high centrifugal stress on the blades. The maximum blade stress has to be less than the quite low material strength by a certain level to ensure the turbine's durability. Therefore, it is very challenging to design turbine blades with low stress. To reduce the stress, the turbine blade is always radial filament or radial fibred using the direct design method. Its disadvantage is that the blade design space is constrained to a small region (radial filament blading only) compared to the very large space with non-radial filament or 3D blading which may potentially provide better aerodynamic performance;

3) The same turbocharger may be used for different engines which requires the turbine has high efficiencies at different operating conditions. However, the blade is normally designed for a fixed condition, called the design point (DP), and the designer has no direct control over the turbine performance at other operating points;

4) The turbine's unsteady performance becomes more and more important since the turbocharger turbine inlet always encounters pulsating flow from the internal combustion engine. It is found that most of the exhaust gas energy is in the low U/C_{is} region. Therefore, it is very critical to improve the efficiency in the low U/C_{is}. Again, since the direct design method is DP locked it is difficult to improve the efficiencies at off-design points (low U/C_{is}) and maintain the efficiency in the DP which usually is also the best efficiency point (BEP, $U/C_{is} \approx 0.7$);

5) More and more rigorous engine emission standards require a quick response of the turbocharger which is governed by the MOI of the rotor, and in particular the turbine wheel, which is the heaviest part of the rotor assembly. The turbine with low MOI is desirable;

6) The turbine blades are not only experiencing high thermal and centrifugal loads, but also dynamic loads caused by the blade vibration modes and the nozzle vane excitation which can lead to damages of the blade. It is desirable for the turbine blade to have high eigenfrequencies to avoid any possible resonance caused by the engine/shaft order excitation, the rotor blade passing excitation and the nozzle blade passing excitation;

7) To sum up, the design of radial/mixed-inflow turbines is a multidisciplinary, multi-objective and multipoint design problem which requires the optimisation since it is almost impossible to achieve the multiple design criteria by using manual design. The DOE, surrogate models and MOGA have been used for the optimisation of turbine blades. However, the large number of design parameters used by the direct design method requires a larger number of design points sampled in the DOE which requires tremendous mount of time and computational resources. The accuracy of the surrogate model decreases when the number of design parameters increases. The performance of the optimal design obtained based on a poor surrogate model cannot be guaranteed which may result in the failure of the optimisation process.

A different method called inverse design method (initially referred to as inverse approach) has been proposed by Hawthorne et al. [1984]. Unlike the direct design method, the basic idea of the inverse design method is that the blade geometry is calculated iteratively based on a prescribed flow field. The advantages of the inverse design method are:

1) By investigating the flow physics and the loss mechanism in the flow field, the design parameters can be directly related to the performance and used to guide the design process;

2) 3D blades or partially radial filament blades can be generated using the inverse design method which can provide additional benefit in terms of the aerodynamic performance;

3) The number of design parameters required for the inverse design method is much smaller which reduces the number of sampling points for the DOE and surrogate models;

4) In the inverse design method, the specific Euler work of the rotor is fixed since the change of rV_θ between the LE and the trailing edge (TE) is predefined. However, the specific work for the designs in the DOE using the direct design method varies since the blade angles are sampled randomly in the design space.

1.3 Scope and Objective

To fulfil the gap between the current design method and all the design challenges listed above, this study is aimed to develop a systematic design approach which integrates the inverse design method with DOE, RSM and multi-objective and multidisciplinary optimisation method to design radial and mixed-inflow turbines for turbochargers. A baseline turbine design which has been highly optimised is provided by the sponsor (CTT). The new turbine designed must satisfy the following criteria:

1) Higher efficiency to extract more energy form the exhaust gas compared to the baseline design;

2) Flow capacity should be controlled between 95% to 105% compared to the baseline value;

3) Higher vibration frequencies compared to the baseline design;

4) Lower MOI compared to the baseline design;

5) Lower maximum principle stress to make sure that turbine blade will not fail at the same working condition compared to the baseline design.

1.4 Thesis Structure

This thesis is organised to report the work which has been carried out to achieve all the objectives listed above in the following structure:

Chapter 2 presents a literature review covering three topics including 3D inverse design methods, pulsating flow analysis of turbocharger turbines and surrogate models. It is impossible to review all the papers for these three topics due to their extremely broad range and long history. However, the most important and the most relevant work have been reviewed and cited.

Chapter 3 illustrates the analysis methods including CFD and FEA used to evaluate the baseline design's aerodynamic and mechanical performance. The predicted efficiency and mass flow rate values are validated through the comparison with the experimental results for the baseline turbine. The CFD and FEA results of the baseline are used as a reference to assess and rank any new design.

Chapter 4 explains the inverse design method used for the blade generation including the meridional geometry, the grid generation, the blade thickness, flow specifications, boundary conditions, blade loading parameters, stacking parameters and the blade update algorithm. A simplified flow chart for the inverse design method is shown. More detailed derivation of this method and all the equations can be found in Appendix A.

Chapter 5 shows a systematic optimisation methodology using the inverse design method, DOE, RFM, Kriging approximation and MOGA. An optimal design, design 10535, with improved aerodynamic and mechanical performance is obtained.

Chapter 6 discusses the generation of turbine blades with a backswept LE using the direct design and inverse design method. The blades with a backswept LE shows improvement in the efficiency in the low U/C_{is} which is beneficial for the turbine's unsteady performance.

Chapter 7 performs a new optimisation (Optimisation 2) using the similar methodology shown in Chapter 5 but modified ranges of design parameters and RFM2 to obtain design 12651 with significant improvement in almost all aspects, especially total-to-static efficiency at RPM = 50,000 ($\eta_{t-s,50k}$), maximum stress and first mode vibration frequency (f_1).

Chapter 8 summaries the most important achievements in this thesis and proposes several suggestions for the future work.

Appendix A presents the detailed description and derivation of all formulations used in the inverse design method (Circulation Method).

CHAPTER 2

LITERATURE REVIEW

In the previous chapter, a brief introduction about the design challenges of radial and mixed-inflow turbines and the objective of this study have been clearly presented and defined. In this chapter, a comprehensive literature review is carried out concentrating on the following three topics:

1) 3D inverse design methods;

2) pulsating flow analysis of turbocharger turbines;

3) surrogate models used for the optimisation of turbomachinery blades.

It should be noted that in spite of the fact that it is impossible to review all the papers related to these three topics, the most important and the most relevant work have been reviewed and cited.

2.1 3D Inverse Design Methods

A number of two-dimensional (2D) inverse design methods have been developed and used in the turbomachinery blade design by different authors such as Conformal Transformation (Mapping) Method (Costello [1950]; Costello et al. [1952]; Lighthill [1945]), Hodograph Method (Cantrell and Fowler [1959]; Garabedian and Korn [1976]; Hobson [1974]; Korn [1978]; Sanz [1983]; Sanz et al. [1985]; Uenishi [1971]), Streamline Curvature Method (Jansen and Kirschner [1974]; McBride [1979];

Wright and Novak [1960]), Potential/Stream Function Method (Beauchamp and Seebass [1985]; Cedar and Stow [1985]; Sator [1977]; Sobieczky and Dulikravich [1982]; Wang [1985]) and so on.

Only a few of inverse design methods can be or have been extended to 3D. In this section, four main 3D inverse design methods which are available in the literature are reviewed.

2.1.1 Singularity/Circulation Methods

This approach models the flow field by using a distribution of sources, sinks, vortices or a combination of them. The flow field can be determined by the strength of these singularities and the blade shape can be determined by the boundary condition that the flow is assumed to be tangential to the blade surface.

Hawthorne et al. [1984] presented a method applied to the design of 2D cascades. The flow is assumed to be incompressible and inviscid. The blades are assumed to be thin with zero thickness. The blade is represented by a distributed bound vorticity whose strength is given by the prescribed tangential velocity $\bar{V_y}$ (which is related to the circulation). The velocity induced by the bound vortices is obtained by a conventional Biot-Savart method which is the same as Betz and Flügge-Lotz [1939]. Using the blade surface boundary condition, the blade profile is obtained iteratively. Another method based on the Clebsch formulation (or called Monge-Clebsch decomposition) of steady rotational flows to solve the velocity field is also demonstrated. The advantage of this Clebsch approach is that it can be easily extended to 3D and compressible flow problems.

The approach mentioned above has been extended to the design of 3D annular cascades of infinitely-thin blades with constant hub and tip diameters by Tan et al. [1984]. In this method, the mean swirl velocity $r\bar{V_\theta}$ is prescribed and the flow field is split into circumferentially averaged and periodic components. It should be noted that the specified mean swirl $r\bar{V_\theta}$ is only a function of the axial distance z. The Stokes stream function is used to compute the circumferentially averaged axial and radial velocities, while Clebsch formulation is used to compute the periodic velocity. The blade profile is computed iteratively by computing the flow field and applying the inviscid blade boundary condition.

Borges [1986] applied Tan's method to the design of low speed (incompressible) turbomachinery with an arbitrary meridional geometry and a general $r\bar{V}_\theta$ distribution (function of r and z) using a finite difference multi-grid technique and a transformation of coordinates from the physical plane to a body fitted computational plane. A low speed radial-inflow turbine was designed whose experimental results show higher total-to-static (t-s) efficiency over a wide range compared to a turbine designed by the direct design method (Borges [1990a] and Borges [1990b]). Ghaly [1986] extended this method to the design of radial-inflow turbines for subsonic compressible flow and the numerical scheme is implemented based on a finite element method. Ghaly [1990] performed a parametric study to investigate the effect of the mean swirl schedule $r\bar{V}_\theta$, the number of blades B and the blade stacking location on the blade shape or blade wrap angle f.

Zangeneh-Kazemi [1986] and Zangeneh [1991] developed Ghaly's method and approximated the effect of the blade thickness using a blockage factor B_f in the mean flow continuity equation. A finite difference method was used to solve governing equations numerically. A small high speed radial-inflow turbine impeller was obtained and experimental results showed improvement in the t-s efficiency compared to a conventional design. But structural analysis results showed that the maximum principle stress near the hub trailing edge of the 3D blade was much higher than the material yield strength.

Yang [1991] and Yang et al. [1993] applied a similar method to Zangeneh's to the design of small high speed radial turbines using a finite element method to solve flow equations. Yang performed a parametric study including the mean swirl schedule, the stacking position, the lean along the stacking line, the slip factor (the leading edge incidence), blockage effects, the number of blades, the exit swirl and hub/shroud profiles. The results showed excellent agreement between the specified swirl distribution and those obtained from the Euler and Navier-Stokes solvers. Tjokroaminata [1992] and Tjokroaminata et al. [1996] extended Yang's method to the design of radial-inflow turbines with splitter blades in the 3D flow. The main and splitter blades were represented by two vorticity sheets in the formulation. The use of splitter blades resulted in the reduction of 'inviscid reverse flow' region on the blade pressure side and also resulted in blades with nearly radial blade filament.

The Hawthorne and Tan's method is now commonly referred to as Circulation ($r\bar{V}_\theta$) Method. Dang [1992, 1993] used a finite volume technique with a shock-

capturing capability to extend Circulation Method into the transonic flow regime for 2D and 3D blades. The flow is assumed to be inviscid and blades have zero thickness. This method was extended to handle blades with a finite thickness in the 2D flow by Jiang and Dang [1994] using two bound-vortex sheets to represent the blade upper and lower surfaces. The primary inputs for this method are inflow and outflow pitch-averaged tangential velocities ($\bar{V_y}$), the pressure loading distribution on the blade (ΔP) and the blade tangential thickness distribution. The output will be the blade mean camber line. Yang [1997] extended this method further to the application of 3D blades with arbitrary thickness and transonic flow. The blade pressure and suction surfaces were modelled by using two periodic bound vorticity sheets. Yang used a mean swirl distribution $r\bar{V_\theta}$ and a splitting function which was used to separate the mean swirl distribution into two fractions to give two different strength of bound vortex sheets (one for the pressure surface and one for the suction surface) instead of ΔP as inputs.

2.1.2 Taylor Series Methods

In this approach, the flow is specified on a mean streamline (or streamsurface). The equations of motion are solved by a pitchwise (tangential) expansion of flow variables in a Taylor series around the mean streamline.

Wu and Brown [1952] first applied this method to the 2D cascade design for the compressible flow. They specified the inlet and exit flow angles, the blade thickness distribution and a desirable mean streamline shape. Then the flow along the mean streamline is calculated and is extended in the pitchwise direction by a second-order (first three terms) Taylor series expansion. The blade shape is determined by the given mass flow. Novak and Haymann-Haber [1983] used a fourth-order Taylor series expansion to solve the flow equations for a mixed-flow cascade.

Zhao et al. [1985] extended this technique to 3D domain consisting of two intersecting families of streamsurfaces (S_1 and S_2 planes), where S_1 is the blade-to-blade streamsurface and S_2 is the hub-to-tip streamsurface. In their method, the meridional geometry, the rV_θ distribution on the mean hub-to-tip streamsurface (S_{2m}) and the blade circumferential thickness are specified. The shape of the S_{2m} surface is calculated from the specified S_{2m} flow and a Taylor series expansion is then used

with the irrotationality and continuity equations to give the shapes of the family of S_2 surfaces progressing from S_{2m}. The extreme two surfaces of the family of S_2 surfaces are the upper and lower surfaces of the blade which define the blade geometry. Wang [1988] reported a similar technique applied to the design of 3D axial flow blades. The main development of this method was summarised by Cai [1984].

The accuracy of the Taylor series method is limited by the number of terms used in the series expansion (Zhao used the first three terms and Wang used up to five terms). As a result this method is accurate only for high solidity (chord to pitch ratio) blades and it cannot cope with stagnation points.

2.1.3 Potential and Stream Function/Plane Methods

In the potential and stream function/plane method, the inverse design problem is tackled by a transformation from physical plane (x, y) to the potential-stream plane (ϕ, ψ), where ϕ is the potential function and ψ is the stream function. The blade surface consists of lines of constant ψ.

Stanitz [1952] first proposed this method to the design of 2D channels with prescribed velocity distribution along the channel walls. The irrotationality and continuity equations in the (ϕ, ψ) plane are solved to find the flow field which satisfies the prescribed boundary conditions. Having solved the flow in the (ϕ, ψ) plane, the definition of the stream function ψ is then used to obtain the channel shape between the blades. The shortcoming of this method is that it cannot cope with stagnation points. Stanitz [1980] extended this method to 3D by introducing a second stream function and solving the problem in the (ϕ, ψ_1, ψ_2) plane. This 3D method can be used in a wide range of channels and ducts but restricted to the subsonic flow.

Schmidt and Berger [1986] modified Stanitz's method to compute the transonic flow for 2D supercritical compressor cascades. The inverse design method they presented shows accurate results compared with complete measurements and computations from other methods. Lower loss and therefore higher efficiency were obtained in comparison with conventional National Advisory Committee for Aeronautics (NACA) blading. Bonataki et al. [1993] followed Schmidt's work and extended the application to the design of quasi-3D turbomachinery

cascades including stator and rotor blades. The flow is considered irrotational and compressible in the absolute frame of reference. The given data are the streamtube geometry, the number of blades, the inlet flow conditions and the pressure and suction surface velocity distributions. The output of the computation is the blade shape which satisfies the above data.

A potential function method and a stream-function-coordinate method for solving 3D inverse and hybrid problems were proposed by Chen et al. [1990, 1995]. Hybrid problems referred to as inverse problems where only a portion of the blade geometry is unknown and the remainder is known. The unknown portion can be predicted or calculated by a prescribed velocity distribution. Chen's method cannot be used to tackle transonic and viscous flows.

2.1.4 Time-marching/Time-dependent Methods

In the Time-marching/Time-dependent method, the unsteady (time-dependent) Euler (or Navier-Stokes) equations are iterated forward in time until a steady state solution is reached. It can be used in both subsonic and supersonic or mixed subsonic/supersonic regimes. The flow is not assumed to be irrotational and this technique can cope with strong shock waves. However, for low speed flows the convergence rate is very slow and may not reach steady state solution in some cases.

One of the first applications of this method to the inverse design was given by Thompkins and Tong [1982] and Tong and Thompkins [1983]. They used the surface pressure distribution and geometric constraints as inputs. If a geometry satisfying both the surface pressure distribution and constraints cannot be found, a solution satisfying the constraints and a relaxed pressure distribution will be found.

Meauzé [1982] provided another inverse design method and applied it to 2D turbomachinery cascades and duct corresponding to a given velocity distribution using solutions of the unsteady Euler equations. The velocity distribution can be assigned over the whole of the suction and pressure surfaces or over only a part of them, the remaining parts being already known. The second version of this design method allowed the blade thickness to be prescribed and the velocity on the suction side to be assigned. Later Meauzé and Lesain [1984] extended this

method to the design of cascades with a large variation of radius. Zannetti [1980] developed a similar method and applied it to inviscid compressible subsonic or transonic, 2D or axisymmetric flows with arbitrary prescribed pressure distribution at the walls. Zannetti and Ayele [1987] extended it to fully 3D turbomachinery blades. Only the suction surface of the blade is designed and the pressure surface is determined by subtracting the fixed thickness from the suction surface.

Singh [1986] proposed an inverse design method based on Denton [1983]'s time-marching scheme with a prescribed pressure distribution around the blade surfaces. The method can be used either to generate entire blade shapes or to modify regions of suction and pressure surfaces. The method enables a reduction in the overall aerodynamic design time.

All the time marching methods mentioned above are based on the prescribed velocity or pressure distribution on the blade surfaces. There is another type of time marching method which is based on the prescribed blade loading distribution. The blade loading (ΔP) is defined as the pressure difference between the blade pressure and suction surfaces which is also related to the rate of change of the mean swirl velocity along the streamwise direction ($\frac{\partial r\bar{V}_\theta}{\partial m}$).

This method was first demonstrated by Dang and Isgro [1995] for 2D cascades. In Circulation Method (subsection 2.1.1), the blades are represented as bound vortex sheets and the equations of motion are cast in terms of Monge-Clebsch variables ($r\bar{V}_\theta$ and α, α is the wrap angle of blade surfaces) used in the potential flow equations. Dang and Isgro [1995] reformulated Circulation Method in terms of conservative variables using an existing time-marching algorithm (cell-centered finite volume Runge-Kutta time-stepping scheme proposed by Jameson et al. [1981]) for the 2D inviscid Euler equations. The presence of the blades is represented by a periodic array of discrete body forces. The blade body force is zero everywhere except on the blades and must point in the direction normal to the blade surface. Dang et al. [2000] extended this 2D Euler-based inverse method to 3D. In this new method, the primary prescribed quantities are the blade pressure loading (ΔP), the blade tangential thickness distribution (including rounded leading and trailing edges) and a stacking line.

Tiow and Zangeneh [1998] proposed another 2D ΔP-based inverse design method using a 2D unsteady (time-marching) Euler flow solver for viscous transonic flows. The viscous effects were modelled using a body force distribution as proposed by

Denton [1986]. The method was extended to 3D by Tiow and Zangeneh [2000] based on prescribed mass averaged swirl ($r\tilde{V}_\theta$) distribution. The viscous effects were modelled using the log-law and the mixing length model as described by Denton [1992]. The method was used to redesign NASA (National Aeronautics and Space Administration) rotor 67 blade and validated using the experimental data of NASA rotor 67.

2.2 Pulsating Flow Analysis of Turbocharger Turbines

Due to the pulsating nature of the exhaust gas from the internal combustion engines, turbocharger turbines always encounter highly unsteady flows with varying pressure and temperature at the turbine inlet. A large number of experimental and numerical work have been done to investigate and determine the turbine unsteady performance and how turbines work during a pulsatile flow.

2.2.1 Experimental Investigations

A very early attempt to experimentally investigate the performance of radial-inflow turbines under pulsating flow conditions was made by Kosuge et al. [1976]. They used the quasi-steady assumption to estimate the transient mass flow rate since the exact measurement of the transient mass flow rate was not possible by the measurement technique at that time. For the turbine unsteady performance analysis, it is important to accurately measure the instantaneous total pressure and the instantaneous total temperature at the turbine inlet, the instantaneous inlet and outlet mass flow rates, the instantaneous turbine rotating speed and the instantaneous turbine power (or shaft torque). However, it is very difficult to measure the instantaneous total temperature directly since the transient response of the thermocouple is very poor compared to the quick temperature change during a real pulse flow. Two methods have been used. One is to assume a constant inlet total temperature by using the measured average temperature value (see Arcoumanis et al. [1995]; Baines et al. [1994]; Dale and Watson [1986]; Kosuge et al. [1976]; Winterbone et al. [1990]). The other one is to assume an isentropic relation between pressures and temperatures and instantaneous total temperature $T_{01}(t)$

is calculated by using instantaneous total pressure $P_{01}(t)$, average pressure $P_{1,ave}$ and average temperature $T_{1,ave}$ as shown in Equation 2.1 (see Capobianco and Gambarotta [1990]; Capobianco and Marelli [2011]; Chen et al. [1996]; Hakeem et al. [2007]; Karamanis and Martinez-Botas).

$$T_{01}(t) = T_{1,ave}\left[\frac{P_{01}(t)}{P_{1,ave}}\right]^{(\gamma-1)/\gamma} \tag{2.1}$$

Another point that should be noted is the time shift between the isentropic power which is measured at the volute inlet and the actual turbine power which is measured at the rotor (or the shaft). The instantaneous turbine t-s efficiency is defined by Equation 2.2, where Δt is the time lag. The turbine rotating speed Ω is treated as constant since the experimental measurement of the rotating speed shows very small fluctuation (1-2%) (Capobianco and Marelli [2010]).

$$\begin{aligned}\eta_{t-s}(t) &= \frac{\dot{W}_T(t+\Delta t)}{\dot{W}_{is}(t)} \\ &= \frac{\Omega\tau(t+\Delta t)}{\dot{m}_1(t)\,c_P T_{01}(t)\left[1-\left(P_2(t)/P_{01}(t)\right)^{(\gamma-1)/\gamma}\right]}\end{aligned} \tag{2.2}$$

This time lag Δt is the finite time which is needed by the unsteady flow to propagate from the volute inlet to the turbine rotor. Several different methods have been proposed to estimate Δt by using the length from the volute inlet to the turbine rotor and different flow velocities including the sonic velocity (Arcoumanis et al. [1995]; Dale and Watson [1986]), the bulk flow velocity (Baines et al. [1994]; Winterbone et al. [1991]) and the summation of both (Rajoo and Martinez-Botas [2010]). Padzillah et al. [2012] calculated Δt by matching the peak isentropic power to the peak turbine power (or peak torque). Some simple one-dimensional (1D) models have been developed based on the experimental results. Chen et al. [1996, 1990] proposed a 1D model for vaneless radial turbines and vaneless mixed flow turbines. The vaneless casing is treated as a tapered pipe with a certain length and the rotor is modelled by a quasi-steady flow method which assumes the rotor acts like under steady flow condition at every time step and 1D steady flow equations are solved. The quasi-steady assumption is only valid when the Strouhal number (S_{tr}) (defined in Equation 2.3, where τ_A is the timescale of the fluid particles passing through the turbine and τ_B is the timescale of the unsteadiness of the pulsating flow (Chen et al. [1990])) which describes the degree of unsteadiness is much smaller than 1. Abidat et al. [1998] modified Chen's method by modelling

the volute as a curved pipe but retaining the quasi-steady assumption on the rotor. The unsteady 1D conservation equations are solved in the curved pipe and improved results compared to Chen's earlier work are obtained. Costall et al. [2006, 2011] extended Abidat's method to the prediction of a twin entry turbocharger instantaneous unsteady performance. Chiong et al. [2012] applied Costall's method in a single entry mixed flow turbine with a meanline model.

$$S_{tr} = \frac{\tau_A}{\tau_B} \tag{2.3}$$

2.2.2 Numerical Simulations

Another way to tackle the turbine unsteady performance is to solve the complete 3D time-dependent Navier-Stokes equations. The first attempt can be found in the literature was made by Lam et al. [2002] using commercial CFD software FLUENT. The whole turbine stage including a volute, a nozzle ring and a turbine rotor is modelled and multiple reference frame (MRF, often referred to as frozen rotor) is used for the interface between the stationary and the rotating domain. The relative motion of two domains is not taken into account which results in the main limitation of MRF which is that it is only meaningful for the steady flow and not suitable to model the unsteady flow. Padzillah et al. [2012] performed a 3D unsteady numerical study on a nozzled mixed flow turbine by using commercial 3D CFD solver ANSYS CFX. The transient rotor-stator model is used for the interface between the stationary domain of nozzles and the rotating domain of the rotor. CFD results were validated against the experimental data and showed a reliable prediction. More 3D unsteady numerical studies on the turbocharger turbines with the experimental validation can be found in Copeland et al. [2002]; Galindo et al. [2013]; Hamel et al. [2012]; Hamidreza et al. [2012]; Tabatabaei et al. [2013].

For turbocharger manufactures, the key question is how to improve the turbine cycle-averaged t-s efficiency rather than the instantaneous t-s efficiency. The turbine cycle-averaged t-s efficiency ($\bar{\eta}_{t-s}$) is defined by Equation 2.4, where $\Delta T = 1/f$ and f is the frequency of the inlet pulse, W_T is the total turbine work during one pulse period (ΔT) and W_{is} is the total isentropic work during ΔT. In other words, the most important point is how to extract more energy from the exhaust gas during one pulse cycle for a given pulse shape. However, there

is limited study on how to design or modify the turbine geometry to improve its unsteady performance in the literature. The pulsating engine exhaust gas with the high pressure and temperature (low U/C_{is}) carries more energy than the high U/C_{is} region. Therefore, it is important to improve the turbine efficiency in the low U/C_{is} region which can be achieved by using radial turbines with a backswept LE (see Barr and McNally [2006]; Barr et al. [2009]; Huang et al. [2012]; Walkingshaw et al. [2011]).

$$\begin{aligned}\bar{\eta}_{t-s} &= \frac{W_T}{W_{is}} \\ &= \frac{\int_t^{t+\Delta T} \dot{W}_T(t)\,dt}{\int_t^{t+\Delta T} \dot{W}_{is}(t)\,dt} \\ &= \frac{\int_t^{t+\Delta T} \Omega\tau(t)\,dt}{\int_t^{t+\Delta T} \dot{m}_1(t)\,c_P T_{01}(t)\left[1-\left(P_2(t)/P_{01}(t)\right)^{(\gamma-1)/\gamma}\right]dt}\end{aligned} \tag{2.4}$$

2.3 Surrogate Models

The main challenge for the multidisciplinary and multi-objective optimisation of turbomachinery blades are the time consuming meshing, CFD, static structural and modal analysis which require a tremendous amount of computational resources (CPU time and computer memory). To accelerate and improve the optimisation process, surrogate models have been widely used. The terms surrogate model, approximation model, response surface and metamodel are used as synonym in the literature. The surrogate model is constructed based on data from known designs (usually from DOE) and provides fast approximation and evaluation of objectives for different design parameters at new design points. The most commonly used surrogate models are polynomial approximation, artificial neural network (ANN) or radial basis function (RBF) and Kriging. A detailed review of these methods can be found in Queipo et al. [2005].

2.3.1 Polynomial Approximation

The polynomial approximation, or polynomial regression, is a methodology that studies the quantitative association between a function y and n basic variables x_i, where there are m sampling values of function y_j. For each observation of

function y_j, a linear polynomial can be written down using Equation 2.5:

$$y_j = \sum_{i=1}^{n} a_i^j x_i^j + \varepsilon_j, \quad E(\varepsilon_j) = 0, \quad V(\varepsilon_j) = \sigma^2 \tag{2.5}$$

The error ε_j has zero expected value and σ^2 is its variance. A second-order polynomial can be expressed by:

$$\hat{y} = a_0 + \sum_{i=1}^{n} a_i x_i + \sum_{i \neq j}^{n} a_{ij} x_i x_j + \sum_{i=1}^{n} a_{ii} x_i^2 \tag{2.6}$$

Equation 2.5 can be written down in the matrix form as:

$$Y^j = X^j A^j + \varepsilon_j \tag{2.7}$$

where Y^j is $m \times 1$ matrix of y_j, X is $m \times N$ matrix of x_i^j, A is $N \times 1$ matrix of a_i^j. N is the total number of polynomial coefficients a_i^j. To determine the coefficient parameters a_i^j, the number of sampling points m has to be equal to or greater than N. The estimated parameters $\hat{A}^j$ can be determined by least square method by Equation 2.8:

$$\hat{A}^j = \left(X^{jT} X^j\right)^{-1} X^{jT} Y^j \tag{2.8}$$

Dornberger et al. [2000] compared the polynomial approximation and the neural network. They concluded that exponential functions often cannot be represented sufficiently with response surfaces based on the polynomial approximation compared to the neural network. Lian and Liou [2005] developed a multi-objective optimisation approach using the second-order polynomial response surface model and evolutionary algorithm (EA). The proposed system was used in the redesign of a single-stage turbopump, a two-stage turbopump and the NASA rotor 67 blade. Goel et al. [2007] presented a systematic approach to approximate the Pareto optimal front by a quadratic polynomial response surface approximation. The methodology was applied to design a single element injector of the liquid-rocket engine with four design parameters. Bonaiuti and Zangeneh [2009] coupled the inverse design method with the quadratic polynomial RSM approximation for the multi-objective, multipoint optimisation design of compressor blades. The improvements in the efficiency and flow range were obtained. Kim et al. [2010] used second-order polynomial approximation as a surrogate model and Non-dominated Sorting Genetic Algorithm-II (NSGA-II) to improve total efficiency and torque of

an axial fan blade. The blade was parametrised by Bézier curves and in total six design variables were selected.

The advantage of the polynomial approximation is that it can be easily implemented. However, for the turbomachinery blade design, the first- and second-order polynomials are too simple and cannot be used to express the very high order and non-linear relation between the design and performance parameters accurately. The minimum number of designs needed which is $(n+1)(n+2)/2$ (n is the number of design parameters) for the second-order polynomial approximation becomes too large when n increases.

2.3.2 Artificial Neural Network (ANN) or Radial Basis Function (RBF)

In the computer science, ANN is a computational model which is capable of machine learning and pattern recognition. It has been used to construct the response surface due to its ability of approximating non-linear functions. RBF is one type of artificial neural networks. A RBF is a real-valued function whose value depends only on the distance from the origin, or alternatively on the distance from some other point c, called a centre. RBF approximation is an artificial neural network (ANN) that uses radial basis function as activation functions. The output of the network is a linear combination of radial basis functions of the inputs and neuron parameters.

Verstraete et al. [2007] used a genetic algorithm and ANN to find a compromise between the conflicting demands of high efficiency and low centrifugal stresses for micro gas turbine blades. Pierret [2005] and Pierret et al. [2007] used a genetic algorithm (GA) and radial basis function network for the shape optimisation of 3D compressor blades. The blade geometry is parametrised using B-spline. Roclawski et al. [2012] used the neural network method to construct a metamodel to replace the time consuming CFD and modal analysis. Curves in the meridional plane can be modified by cubic splines with control points. It is found that qualitatively better designs were obtained, but the quantitative agreement for the new virtual designs with the recalculated real designs was not good. Chahine et al. [2012] and Mueller et al. [2013] replaced the computationally expensive tools for CFD and computationally structural mechanics (CSM) with ANN and got rapid but

less accurate predictions to evaluate the large number of geometries. The hub and shroud curves, the blade angle and the thickness distribution are defined by B-spline curves with 24 optimisation parameters.

2.3.3 Kriging

Kriging is a method of interpolation which was first proposed by a South African statistician and mining engineer Danie G. Krige and used to predict the location of unknown mineral resources. The basic idea of Kriging is that the value at an unknown point should be the average of the known values at its neighbours, weighted by the neighbour's distance to the unknown point. The detail of Kriging implementation is explained in Chapter 5. It is not widely used in the optimisation of turbomachinery blades due to its numerically expensive matrix inversion and difficulty in minimising Equation 5.30 compared to the polynomial approximation.

Chung and Alonso [2004] combined the micro-GA and Kriging approximation technique to optimise a supersonic business jet design. Siller et al. [2009] implemented the Kriging model in their optimisation software called AutoOpti for a transonic axial compressor. Blade is parametrised by B-spline curves. Turbomachinery Research Aerodynamics Computational Environment (TRACE), a finite volume Reynolds-averaged Navier–Stokes (RANS) solver is used. The stall margin is remained and the efficiency is improved by 2.5%.

2.4 Summary

In this chapter, different inverse design methods, the pulsating flow analysis of turbocharger turbines and different surrogate models used for the turbomachinery blade optimisation have been reviewed.

Among all these inverse design methods reviewed above, Zangeneh [1991]'s method has been the most widely applied for the industrial applications. This method has been successfully used to design and optimise different types of turbomachinery blades including turbines (Watanabe et al. [2004]; Zangeneh [1990]; Zhang and Zangeneh [2015]; Zhang et al. [2014]), compressors (Zangeneh et al. [2010]), fans (Okamoto et al. [2009]), pumps (Ashihara and Goto [2000]), nozzles (Watanabe

and Harada [1999]) and diffusers (Zangeneh and Roduner [2002]). It also has been extended to real gas applications and used in the design of supercritical CO_2 compressor and turbines (Zhang et al. [2017]), recently.

It is not difficult to find that there is still a gap in the research field that needs to be fulfilled, which is how to systematically design radial and mixed-inflow turbines with improved cycle-averaged aerodynamic performance and mechanical performance. In this work, 3D steady and unsteady CFD simulations will be used to show the improved steady efficiency in the low U/C_{is} region and cycle-averaged efficiency of backswept turbine blades designed using the inverse design method compared to the conventional turbine blades with zero LE blade angle. For the first time, both the first-order polynomial and Kriging approximation methods are combined and applied to the optimisation of radial and mixed-inflow turbine blades. The first-order polynomial is used to reduced the number of design parameters and Kriging is used to construct a more accurate response surface for the new design parameters. The comparison of optimisation results using Kriging approximation, second-order polynomial and RBF based on the same DOE results shows that Kriging is more suitable for the prediction of the performance of turbomachinery blades.

CHAPTER 3

EVALUATION OF BASELINE TURBINE PERFORMANCE

In this chapter, the aerodynamic and mechanical performance of the baseline turbine design will be evaluated and investigated by using steady CFD and FEA analysis.

3.1 Baseline Design Geometries

The baseline design geometries provided by CTT are a volute, a single nozzle blade and a rotor blade. The volute geometry and nozzle shape will not be modified in this study since the objective of this project is to optimise the rotor blade shape.

3.1.1 Rotor

The meridional shape and dimensional parameters of the baseline rotor blade are shown in Figure 3.1 and Table 3.1. The total number of rotor blades is 11. The blades are designed to be radial fibred to reduce the centrifugal bending stress. Radial fibred or radial filament blade means the blade wrap angles from the shroud to the hub are identical at the same axial position and each part of the blade is supported by the blade beneath. The wrap angle distribution of the baseline rotor blade can be seen in Figure 3.2.

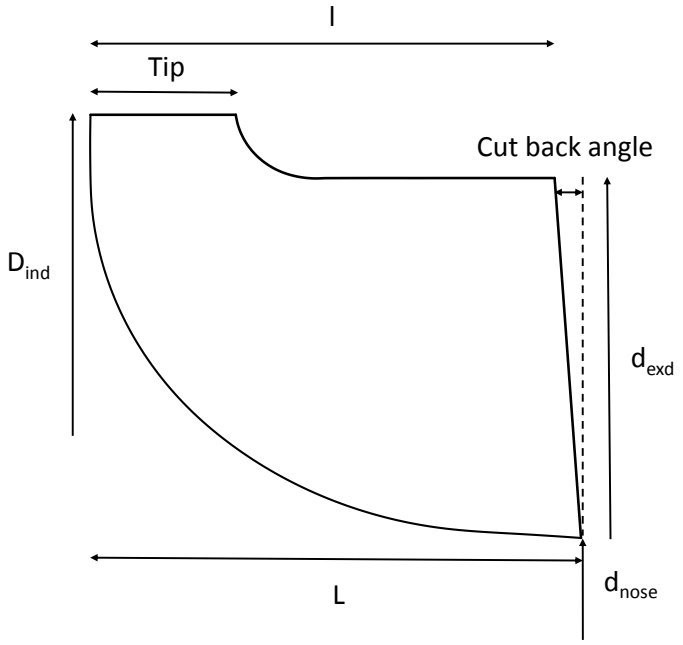

Fig. 3.1 Meridional plane of the baseline rotor blade

Table 3.1 Meridional dimensions of the baseline rotor blade

D_{ind}	d_{nose}	d_{exd}	l	L	Tip	Cut back angle
$[mm]$						$[^{\circ}]$
76	22.5	67	27	28.5	7.941	3.86

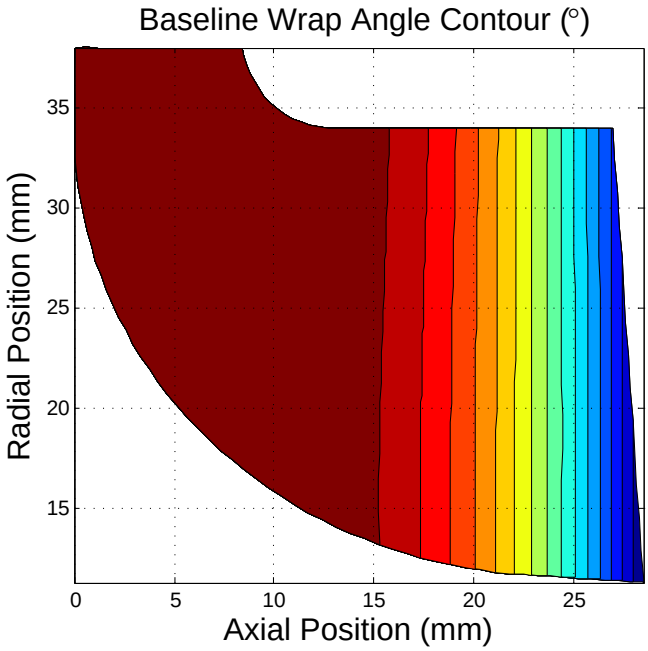

Fig. 3.2 Wrap angle contour of the baseline rotor blade

3.1.2 Nozzle

The geometry of the nozzle blades is illustrated in Figure 3.3 and Table 3.2. The nozzle is electronically actuated in the axial direction, with a shroud plate to prevent the leakage over the top of the guide vanes, as depicted in Figure 3.6. The function of the nozzle blades is to guide the flow at the optimal incidence angle before it enters the rotor blade LE, thereby maximising the turbine t-s efficiency.

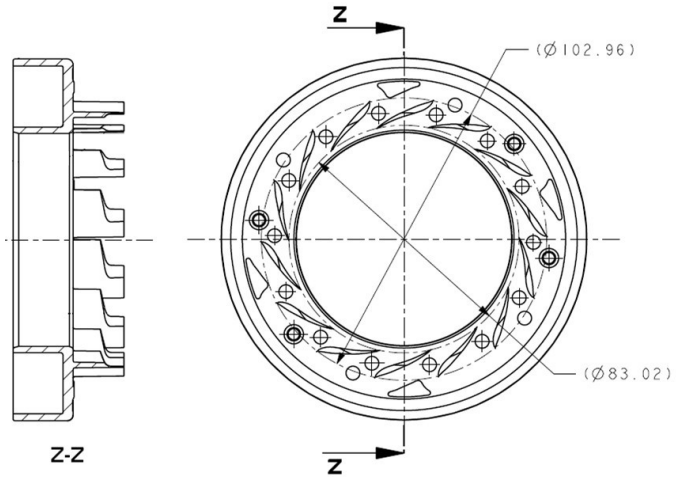

Fig. 3.3 Baseline nozzle geometry

Table 3.2 Baseline nozzle geometry

Number of Vanes	14
Vane Type	Cambered
Chord Length	22.2 mm
Vane LE Angle	30°
Vane LE Diameter	102.96 mm
Vane TE Angle	83°
Vane TE Diameter	83.02 mm

3.1.3 Volute

The baseline volute geometry is shown in Figure 3.4.

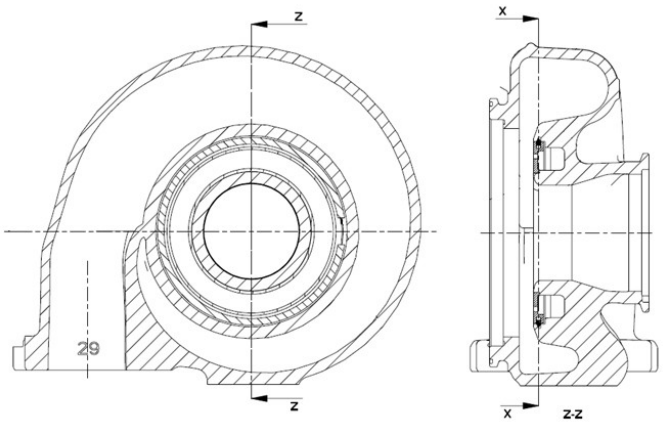

Fig. 3.4 Baseline volute geometry

3.1.4 Turbine Assembly

The assembly of the turbine housing, the variable nozzle ring and the turbine wheel is shown in Figure 3.5 and its section view is shown in Figure 3.6. In Figure 3.6 the red part denotes the turbine housing. The yellow part denotes the variable nozzle ring which can move in the axial direction and be used to control

the flow capacity. The purple part denotes the fixed nozzle shroud plate. The nozzle gap is defined as the distance from the fixed shroud plate to the deck of the nozzle ring. The flush condition is defined as the nozzle gap at which the deck aligns with the turbine housing volute. The blue part denotes the turbine wheel and the clearance between the blade shroud and the turbine housing is 0.5 mm. The green parts denote the flow domain of the volute and the nozzle ring. The black parts denote sealing rings.

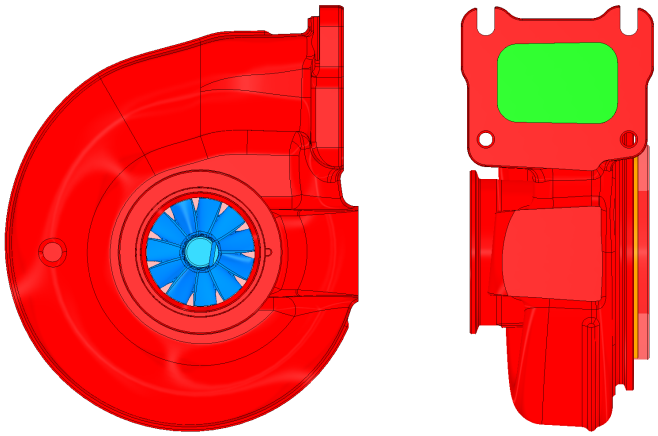

Fig. 3.5 Assembly of baseline turbine geometries

3.2 Steady CFD Simulation

This section will explain how the turbine aerodynamic performance parameters including mass flow parameter (MFP), torque (τ) and t-s efficiency (η_{t-s}) are evaluated by using the commercial CFD software, ANSYS CFX. First of all, it is necessary to examine the accuracy of the CFD model and determine whether the CFD model is suitable for the prediction of the aerodynamic performance parameters. It also should be noted that all the experimental and numerical results shown in this thesis are scaled or normalised due to the confidentiality requirements from the sponsor (CTT).

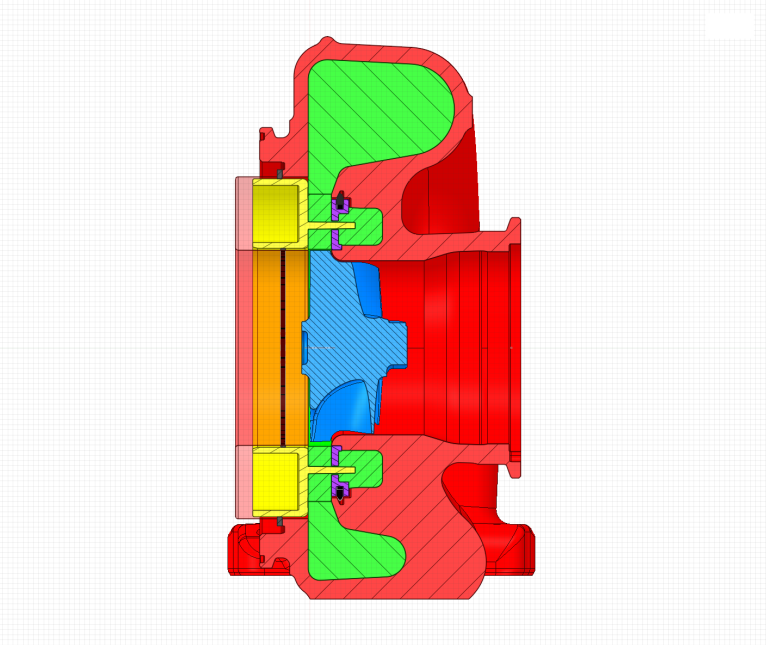

Fig. 3.6 Schematic of the variable geometry turbine at the 'flush' condition

3.2.1 Validation with Experimental Data

The mesh or computational domain used for the validation of the CFD model is shown in Figure 3.7, where the nozzle gap = 9.09 mm. The volute is not included in the model due to the purpose of simplifying the problem and saving computational resources and time. The nozzle mesh is unstructured and generated using ANSYS Meshing. The total number of elements for the nozzle mesh is 1,284,000. The inflation layers are applied on all the nozzle walls with a near wall element distance of 0.001 mm to capture the boundary layer effects. The rotor mesh is structured (hexahedron) and generated using ANSYS TurboGrid. The total number of elements for the rotor mesh is around 750,000. The first element offset is also 0.001 mm. There are 20 layers of elements in the shroud clearance.

The nozzle domain is stationary and the rotor domain is rotating with a constant speed. Inlet boundary conditions are total pressure and total temperature. Inlet absolute flow angle is 40° from the tangential direction. Outlet boundary condition is atmospheric static pressure (1.0 bar). Rotational periodical boundary conditions are applied on all the periodic surfaces of the nozzle and rotor domains. The Stage (or mixing plane) method is used for the interface between the stator and the rotor. The Stage model performs a circumferential averaging of the fluxes through

the interface and passes it to the component downstream. The turbulence model used is the shear stress transport (SST) $k - \omega$ (Menter [1993]). The working fluid is assumed to be ideal gas with $\gamma = 1.4$ (specific heat index or specific heat capacity ratio) since the experiments are performed using the air rather than the combustion products whose γ is around 1.333. RANS equations are solved iteratively to obtain the whole flow field.

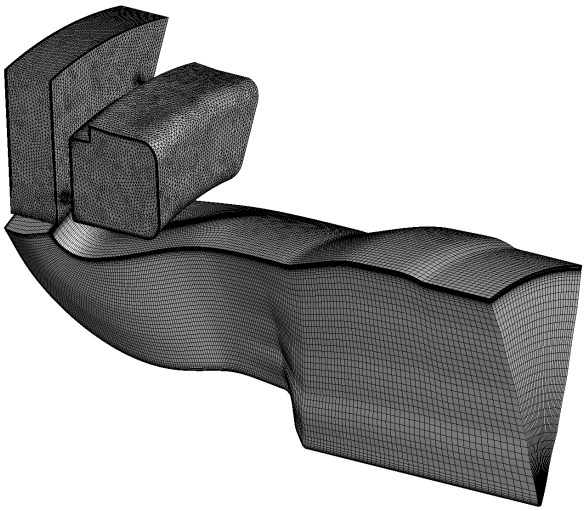

Fig. 3.7 Computational domain of the nozzle and rotor single passage

The comparison of the mass flow and the efficiency between the experimental data (pers. comm. with Palmer [2012-02-17] through email) and CFD results are shown in Figure 3.8, Figure 3.9 and summarised in Table 3.3. From Figure 3.8 it can be seen that the mass flow matches very well (around 1-2%) near the design point (ER = 2.2, 2.6 and 3.0) and the mass flow at off-design points (very low and very high ER) are underestimated by 5-9%. Similarly from Figure 3.9 it can be seen that efficiencies obtained from the experiment and CFD match well at most of ER but at very low ER = 1.4 where the difference is about 7%. The discrepancy in the mass flow and the efficiency prediction can be explained as the simplified CFD model fails to model and capture certain flow phenomenon in the turbine at very low ER. The constant efficiency difference (around 1.5%) between CFD and the experiment near the design point (ER = 2.2, 2.6 and 3.0) can be explained by that the CFD model does not include the total pressure/friction loss in the volute, the heat transfer loss, the leakage loss caused by the scallop backplate

and the turbine fillet blockage loss and as such gives higher efficiencies. It can be concluded that the CFD model is sufficient to predict the turbine performance and a design with improved efficiency from CFD will perform better in reality compared to the baseline turbine at the design point.

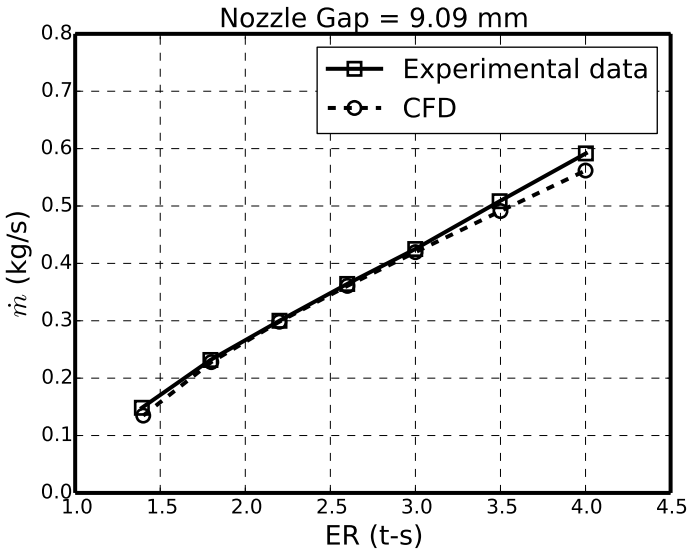

Fig. 3.8 Comparison of the experimental data and CFD results for mass flow

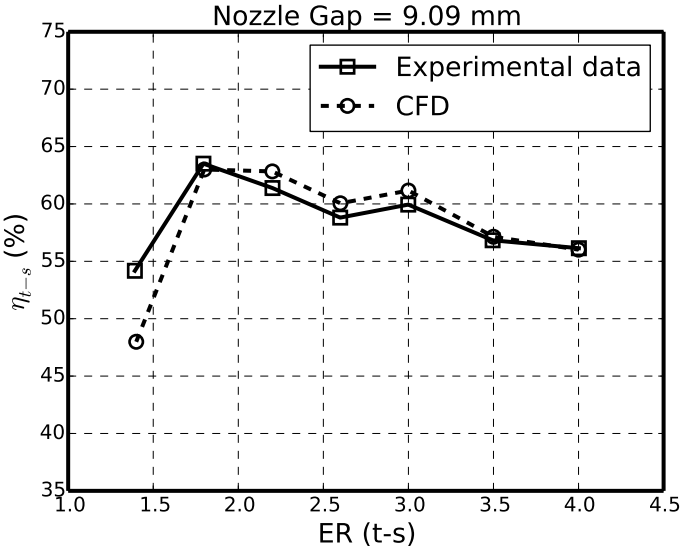

Fig. 3.9 Comparison of the experimental data and CFD results for t-s efficiency

Table 3.3 Comparison of the experimental data and CFD results

Case	RPM	Experimental Data			CFD		
		ER (t-s)	$\dot{m}$	η_{t-s}	ER (t-s)	$\dot{m}$	η_{t-s}
[-]	[rev/min]	[-]	[kg/s]	[%]	[-]	[kg/s]	[%]
1	60,943	1.392	0.148	54.18	1.4	0.135	47.99
2	61,492	1.795	0.232	63.51	1.8	0.228	63.00
3	58,315	2.201	0.300	61.38	2.2	0.298	62.83
4	57,644	2.599	0.364	58.81	2.6	0.361	60.06
5	63,041	2.999	0.425	59.94	3.0	0.419	61.17
6	59,359	3.495	0.508	56.83	3.5	0.491	57.14
7	60,654	4.002	0.592	56.14	4.0	0.562	56.02

3.2.2 Mesh Dependency Analysis

The CFD model shown in Figure 3.7 is simplified by removing the extra nozzle flow chamber since the main objective of this study is to optimise the turbine rotor blade with a fixed nozzle geometry. The computational domain of the simplified CFD model is shown in Figure 3.10. A mesh dependency analysis is performed by running CFD simulations with different number of elements but same boundary conditions for this model. The element type of the unstructured mesh in the nozzle is tetrahedron and generated using ANSYS Meshing. The element type of the rotor mesh is structured (hexahedron) and generated using ANSYS TurboGrid. Inlet boundary conditions are total pressure (2.2 bar) and total temperature (403K). Outlet boundary condition is atmospheric static pressure (1.0 bar). The rotor is rotating at a constant speed of 70,000 rev/min. The SST $k-\omega$ turbulence model is used and y^+ of near wall elements is around 1. Rotational periodical boundary conditions are also applied for the single passage simulation. The Stage model is used for the interface between the stator and the rotor.

The results are illustrated in Figure 3.12, where $\dot{m}_{in}$ and $\dot{m}_{out}$ are the turbine inlet and outlet mass flow rates and τ is the turbine torque. All these values are normalised based on their values obtained using the finest mesh (around 8.1 million). It can be seen that the effect of the mesh size changing on the selected parameters are little. The maximum error is less than 2% with the coarsest mesh. To save computational time and guarantee the accuracy, the mesh with 1.5 million elements is selected.

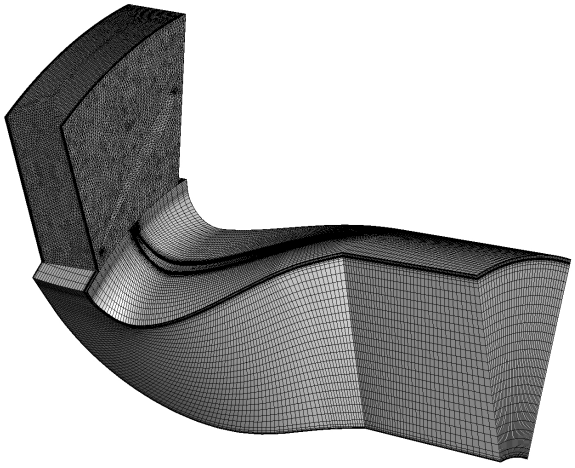

Fig. 3.10 Computational domain of the single stator-rotor passage

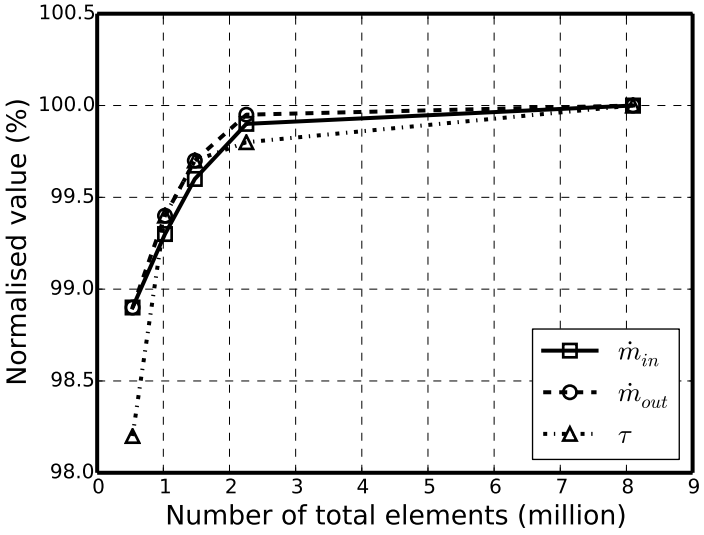

Fig. 3.11 Mesh dependency analysis

3.2.3 Nozzle Gaps

In this subsection, the effect of nozzle gaps on the turbine aerodynamic performance will be investigated using the simplified CFD model.

The nozzle gap (W_1) is defined as the width (or the height) of the nozzle blade as shown in Figure 3.12. The throat area of nozzle blades can be controlled by changing the nozzle gap W_1. The 'flush' condition is defined when $W_1 = 8.441$ mm since it is equal to 7.941 mm (baseline rotor tip width) + 0.5 mm (rotor shroud tip clearance). When the nozzle is in the 'non-flush' position, the non-matching area between the nozzle and the rotor is defined as the wall as depicted in Figure 3.18.

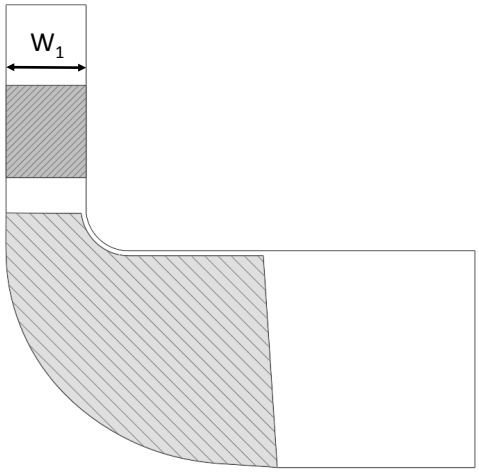

Fig. 3.12 Definition of the nozzle gap W_1

Figure 3.13, Figure 3.14 and Figure 3.15 show the comparison of MFP, torque and η_{t-s} for different nozzle gaps with the same boundary conditions ($P_{01} = 2.2$ bar, $T_{01} = 403.2$K and $P_4 = 1.0$ bar). The turbine MFP and speed parameter (SP) are defined by Equation 3.1 and Equation 3.2, where $\dot{m}$ is the mass flow rate, P_{01} and T_{01} are the inlet total pressure and total temperature and RPS (revolution per second) is the turbine rotational speed. The turbine MFP and torque increases with the increasing of W_1 for the same RPM. The higher W_1 gives greater nozzle throat area and allows the nozzle to pass more flow. Consequently more mass flow will produce more torque on the rotor blade. Nozzle gap in the 'flush' condition (8.441 mm) gives the highest η_{t-s}.

$$Mass\ Flow\ Parameter = \frac{\dot{m}\sqrt{T_{01}}}{P_{01}} \tag{3.1}$$

$$Speed\ Parameter = \frac{RPS}{\sqrt{T_{01}}} \tag{3.2}$$

T-s efficiency is defined by Equation 3.3 and subscripts 1 and 4 denote different turbine stage stations, the stator/nozzle inlet and the rotor outlet, respectively. All the parameters in this equation are constant except for the mass flow rate ($\dot{m}$) and the torque (τ). Therefore, the η_{t-s} is determined by the value of $\frac{\tau}{\dot{m}}$ for different nozzle gaps for a given speed. The torque of $W_1 = 11$ mm is higher than that of $W_1 = 8.441$ mm but the mass flow rate of $W_1 = 11$ mm is also higher than that of $W_1 = 8.441$ mm. The increment of the mass flow is greater than the increment of the torque for $W_1 = 11$ mm compared to $W_1 = 8.441$ mm. Therefore, the η_{t-s} of $W_1 = 11$ mm is lower than $W_1 = 8.441$ mm.

$$\eta_{t-s} = \frac{\dot{W}_T}{\dot{W}_{is}} = \frac{\omega\tau}{\dot{m}c_P T_{01}\left[1 - \left(\frac{P_4}{P_{01}}\right)^{(\gamma-1)/\gamma}\right]} \tag{3.3}$$

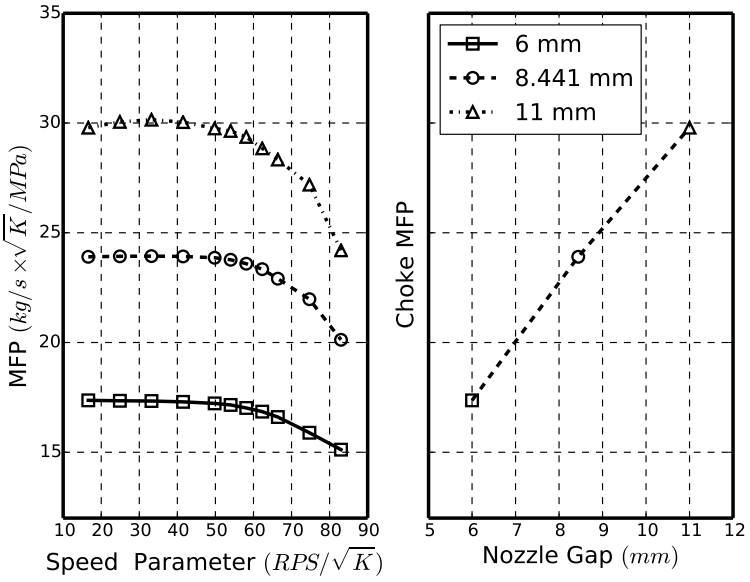

Fig. 3.13 Comparison of MFP for different nozzle gaps

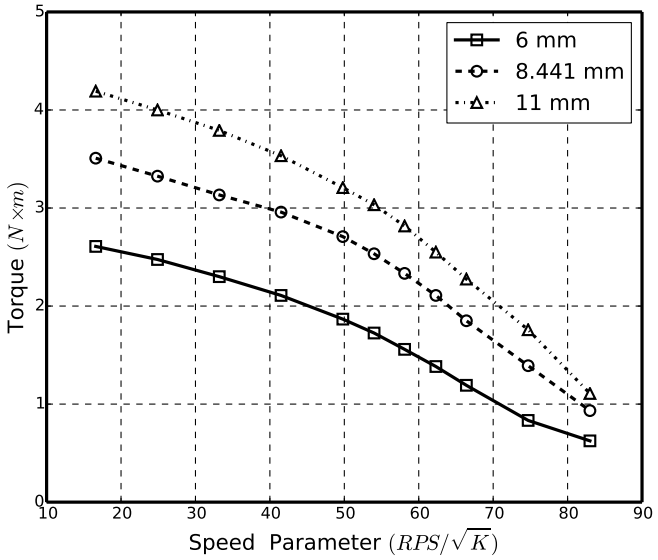

Fig. 3.14 Comparison of torque for different nozzle gaps

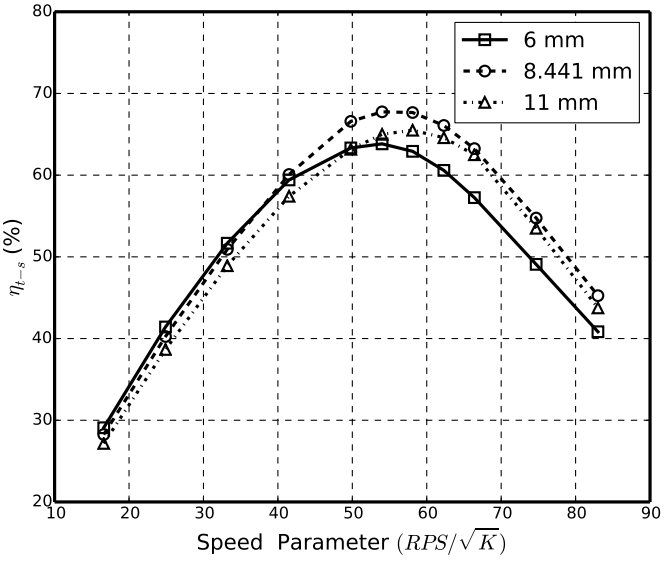

Fig. 3.15 Comparison of η_{t-s} for different nozzle gaps

The absolute flow angle α_i is defined by Equation 3.4, where $i = 1$, 2 and 3 denotes different streamwise locations (nozzle LE, nozzle TE and rotor LE) which are shown as black surfaces in Figure 3.16, $V_{i\theta}$ is the mass averaged tangential velocity

and V_{im} is the mass averaged meridional velocity in the location i.

$$\alpha_i = \arctan\left(\frac{V_{i\theta}}{V_{im}}\right) \tag{3.4}$$

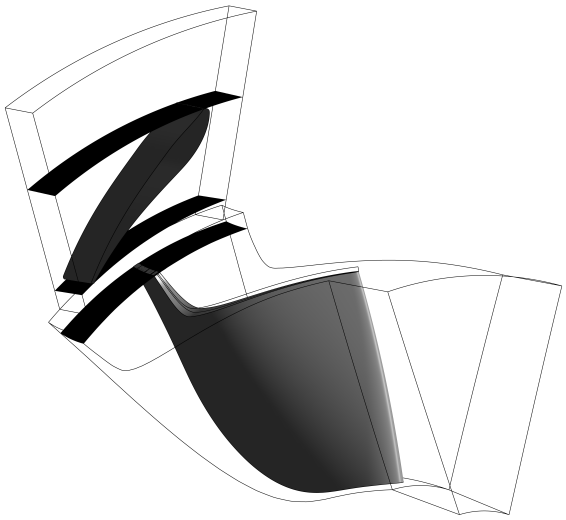

Fig. 3.16 Locations where the absolute flow angle α_i is measured

The nozzle LE absolute flow angle α_1 for different nozzle gaps W_1 is plotted in Figure 3.17. It can be seen that α_1 for $W_1 = 6$ and 8.441 mm are almost identical and α_1 for $W_1 = 11$ mm is much greater. This can be explained using Figure 3.18. In Figure 3.18, the flow angle at the nozzle inlet boundary is constant. For cases of $W_1 = 6$ and 8.441 mm, the nozzle width (or height) between the nozzle inlet and the nozzle LE does not change so the flow angle remains the same as the flow angle at the inlet boundary. For the case of $W_1 = 11$ mm, it can be seen that the flow expands in the axial direction from the nozzle inlet to the nozzle LE since the flow area increases. The increasing flow area will result in the decreasing of V_{1m}. Using Equation 3.4 it can be obtained that α_1 will be higher than the flow angle specified in the inlet boundary.

The nozzle TE absolute flow angle α_2 is shown in Figure 3.19. It can be seen that the variation of α_2 for different nozzle gaps is very small ($67.5° - 68.4°$) after the guidance of nozzle vanes. The rotor LE absolute flow angle α_3 is shown in Figure 3.20. Looking at Figure 3.18 again from the nozzle TE to the rotor LE the flow area increases for nozzle gap = 6 mm and decreases for nozzle gap = 11 mm.

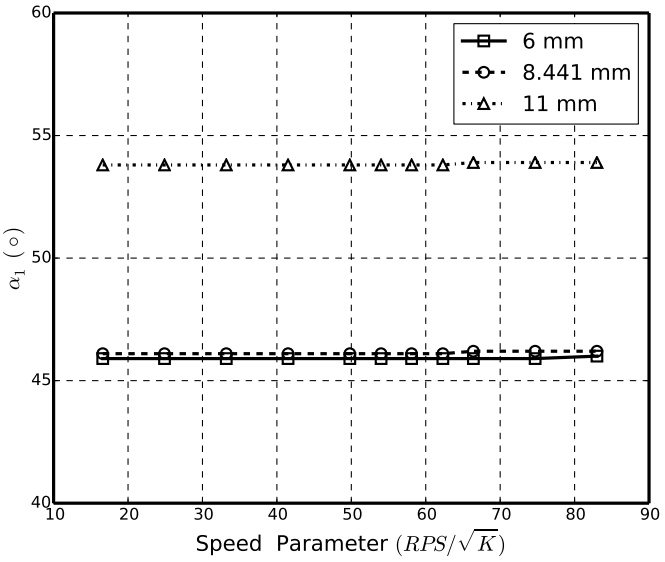

Fig. 3.17 Comparison of nozzle LE flow angle α_1 for different nozzle gaps

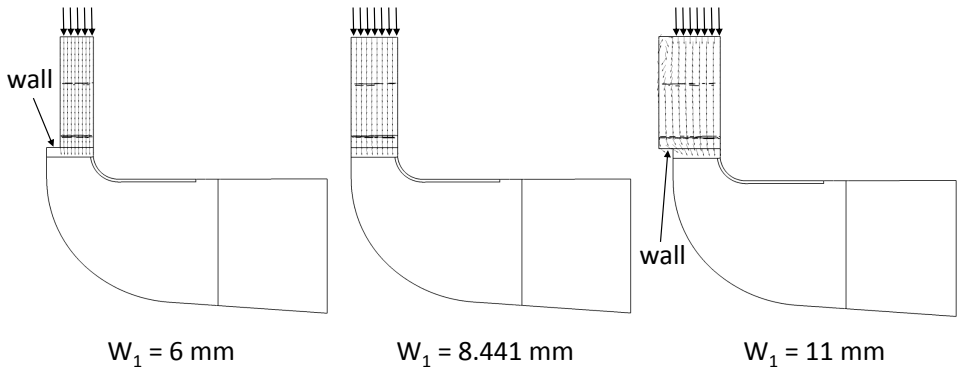

Fig. 3.18 Nozzle velocity vectors in the meridional plane for different nozzle gaps

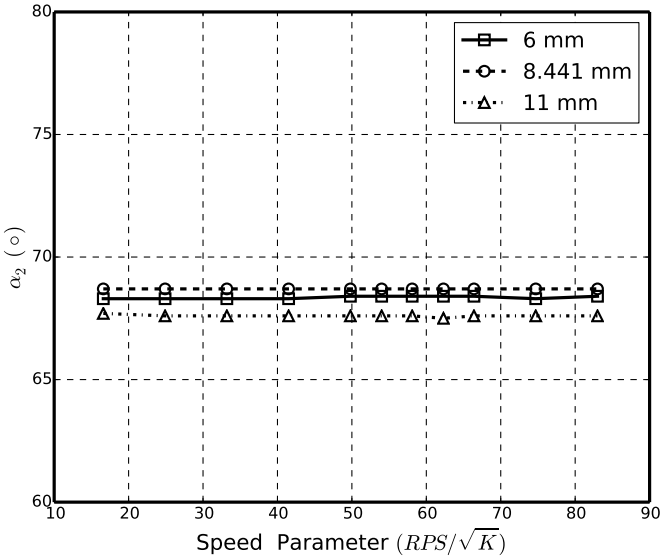

Fig. 3.19 Comparison of nozzle TE flow angle α_2 for different nozzle gaps

Therefore, the meridional velocity V_m will decrease for nozzle gap = 6 mm and increase for nozzle gap = 11 mm. Using Equation 3.4 again α_3 will increase for nozzle gap = 6 mm, remain the same for nozzle gap = 8.441 mm and decrease for nozzle gap = 11 mm which is exactly what has been shown in Figure 3.20.

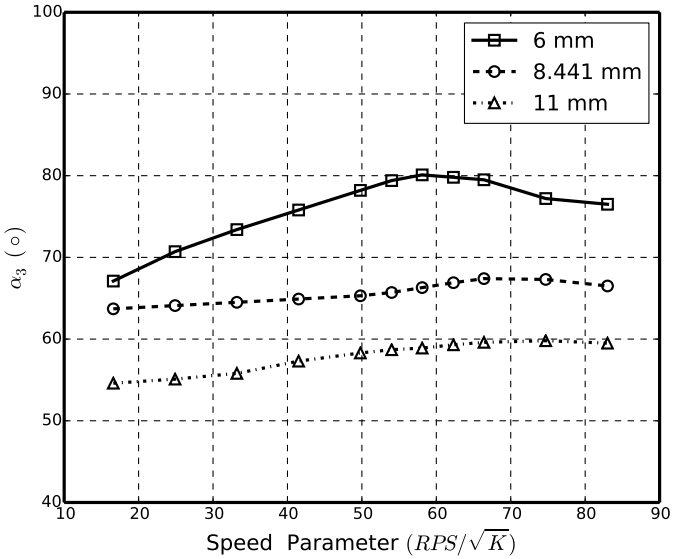

Fig. 3.20 Comparison of rotor LE flow angle α_3 for different nozzle gaps

Substituting Equation 3.5 which states that the torque is equal to the time rate of the change of the angular momentum between the rotor LE and the rotor TE into Equation 3.3 to obtain Equation 3.6, where r_3 and r_4 are the rotor LE and TE radius, $V_{3\theta}$ and $V_{4\theta}$ are LE and TE absolute circumferential flow velocity. Therefore, for given ER, T_{01} and turbine rotating speed ω, t-s efficiency is only determined by the change of rV_θ between the rotor LE and TE. The change of rV_θ from the rotor LE to TE ($r_3V_{3\theta} - r_4V_{4\theta}$) is shown in Figure 3.21.

$$\tau = \dot{m}\left(r_3V_{3\theta} - r_4V_{4\theta}\right) \tag{3.5}$$

$$\eta_{t-s} = \frac{\omega\left(r_3V_{3\theta} - r_4V_{4\theta}\right)}{c_PT_{01}\left[1 - \left(\frac{P_4}{P_{01}}\right)^{(\gamma-1)/\gamma}\right]} \tag{3.6}$$

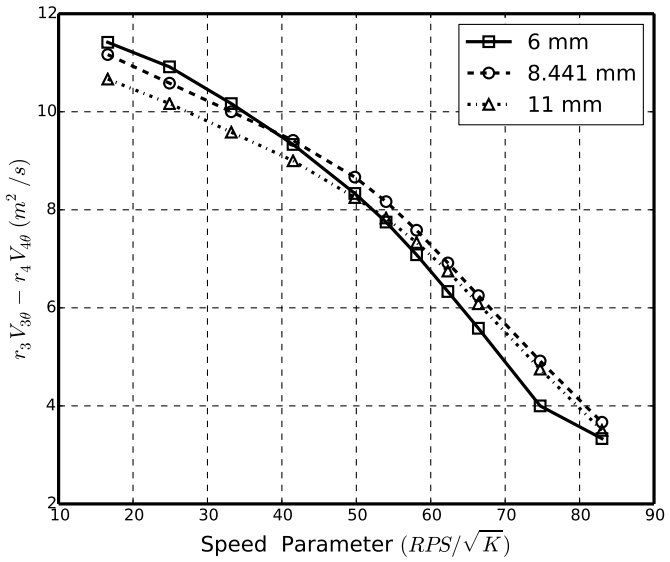

Fig. 3.21 Comparison of rotor rV_θ change for different nozzle gaps

Figure 3.22 shows the meridional plane contours of Mass and Circumferentially Averaged (MCA) static entropy generation for different nozzle gaps at RPM = 70,000 which is the peak efficiency point. The static entropy (s) is defined by Equation 3.7 , where T and P are static temperature and static pressure. It can be clearly seen that the entropy generation of 'non-flush' cases (W_1 = 6 and 11 mm) near the rotor-stator interface (hub) is much greater than that in the 'flush'

case ($W_1 = 8.441$ mm). The non-matching rotor and stator width ('non-flush' condition) increases the flow non-uniformity when the flow enters the rotor from the stator exit thereby generates extra entropy and mixing losses.

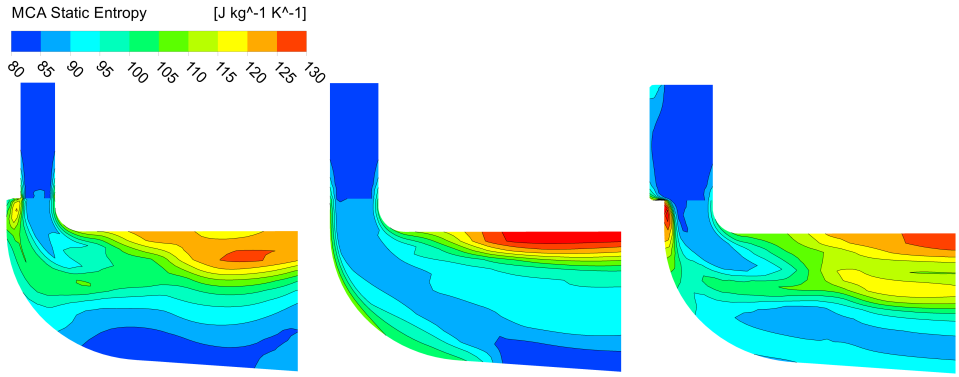

Fig. 3.22 MCA static entropy contours in the meridional plane for different nozzle gaps @ RPM = 70k (left - $W_1 = 6$ mm, middle - $W_1 = 8.441$ mm, right - $W_1 = 11$ mm)

$$
\begin{aligned}
s - s_{ref} &= c_p \ln \frac{T}{T_{ref}} - R \ln \frac{P}{P_{ref}} \\
T_{ref} &= 298.15 \quad K \\
P_{ref} &= 1 \quad bar \\
s_{ref} &= 0 \quad J/kg/K
\end{aligned} \tag{3.7}
$$

It can be concluded that:

1) The changing of nozzle gaps helps to control the flow capacity and shifts the location of the peak efficiency values;

2) The maximum t-s efficiency is achieved in the 'flush' condition.

3.2.4 Nozzle Angles

In this subsection, the effect of nozzle angles on the turbine aerodynamic performance will be investigated. The nozzle gap used in this subsection is fixed ('flush' condition, $W_1 = 8.441$ mm). The nozzle angle is defined in Figure 3.23 where the rotational axis is fixed and can be used to control the nozzle throat area and the

exit flow angle. If the nozzle blade is rotated in the anticlockwise direction, the rotating angle will be positive. If the rotating direction is clockwise, the nozzle angle will be negative. The nozzle throat is shown in the Figure 3.24 and defined as the location where the distance between two adjacent nozzle blades reaches the minimum value.

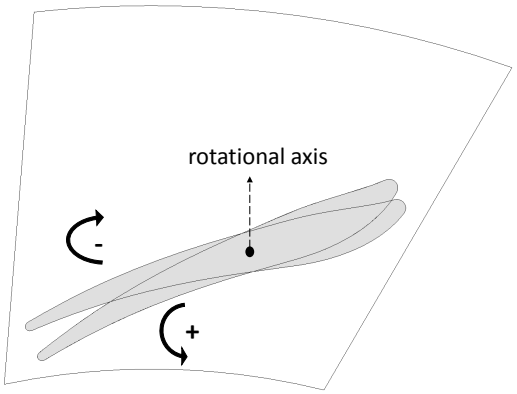

Fig. 3.23 Pivoted nozzle blades (view from the shroud to the hub)

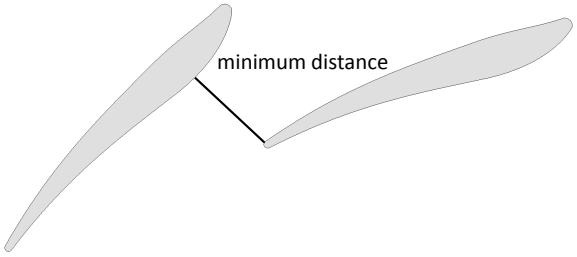

Fig. 3.24 Nozzle throat

Figure 3.25 shows MFP comparison for different nozzle angles. The CFD boundary conditions are the same as those used in the last subsection. Baseline design is the case with nozzle angle = 0°. It can be seen that with the increasing nozzle angles (from −4° to 4°), the nozzle throat is opened further and the throat area is increased which results in the increasing of the mass flow rate passing through the turbine for a given ER.

Figure 3.26 shows that the turbine rotating speed has little effect on the nozzle TE absolute flow angle α_2 for a given nozzle angle since the rotating speed in the downstream will not impact on the flow in the upstream (nozzle exit). When

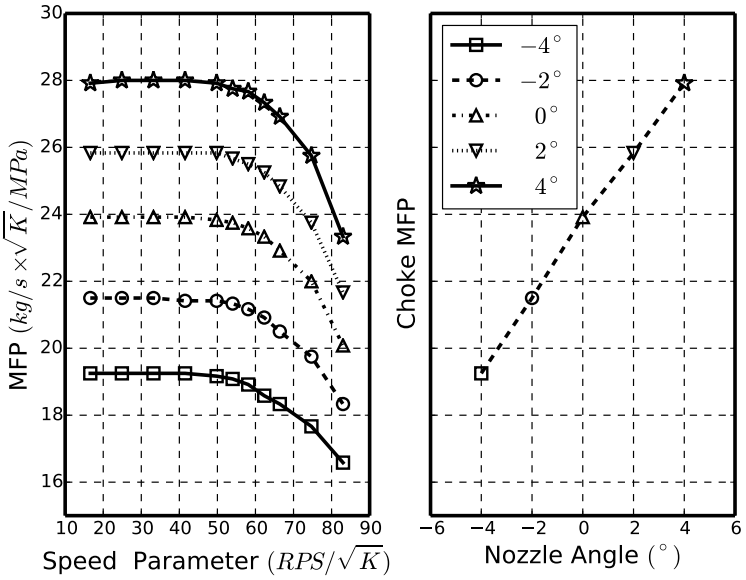

Fig. 3.25 Comparison of MFP for different nozzle angles

the nozzle angle increases, $V_{2\theta}$ at the nozzle TE decreases and V_{2m} increases. Therefore, α_2 decreases according to Equation 3.4.

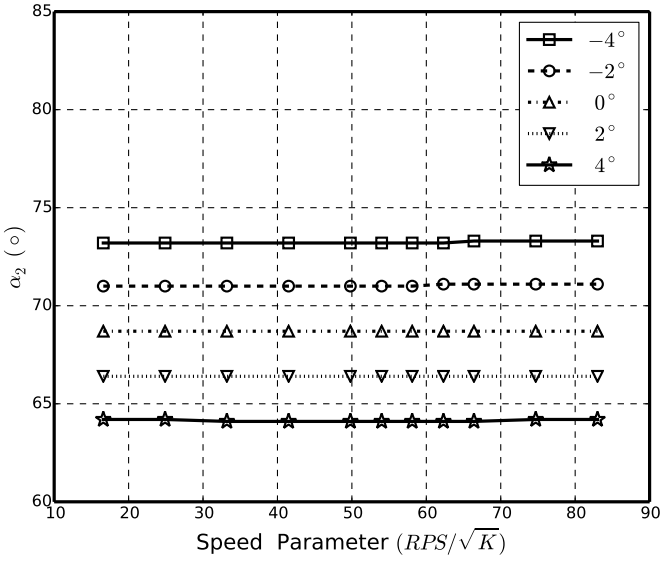

Fig. 3.26 Comparison of nozzle TE flow angle α_2 for different nozzle angles

The turbine η_{t-s} versus the rotor incidence angle α_{in} for different nozzle angles is plotted in Figure 3.27. The incidence angle α_{in} is defined as the difference

between the relative flow angle at the rotor LE (β_3) and the rotor LE blade angle ($\beta_{b,LE}$) (see Equation 3.8). Since the baseline rotor blade has zero LE blade angle ($\beta_{b,LE} = 0$), α_{in} will be equal to β_3 for all the cases. It can be seen that with the increasing nozzle angles, the whole efficiency curve moves from the right side (high α_{in}) to the left (low α_{in}). The α_{in} corresponding to the peak η_{t-s} decreases from 20° to −6° for nozzle angles ranging from −4° to 4°.

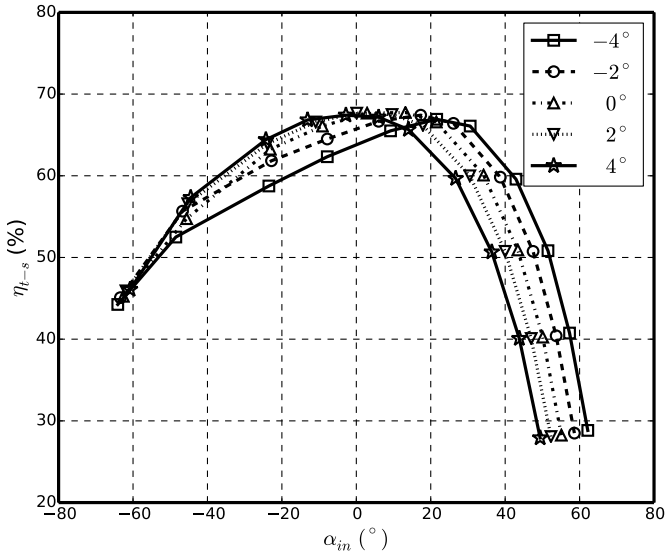

Fig. 3.27 η_{t-s} versus α_{in} for different nozzle angles

$$\alpha_{in} = \beta_3 - \beta_{b,LE} \tag{3.8}$$

It can be concluded that:

1) The mass flow rate, the nozzle TE flow angle (α_2) and the rotor incidence angle (α_{in}) can be controlled by changing the nozzle angle;

2) Changing of nozzle angles does not change the value of the peak efficiency but changes the α_{in} corresponding the peak efficiency.

3.3 FEA Simulation

In this section the method used to evaluate the turbine mechanical performance parameters including the maximum principle stress, 1^{st} and 2^{nd} mode natural frequencies and MOI by using ANSYS Mechanical is described.

3.3.1 Whole Wheel Geometry and Mesh Generation

The blade geometry used in the steady CFD simulation is just a single blade which is not enough for the static structural and the modal analysis of the turbine wheel. To get accurate evaluation of the stress value and vibration characteristics during the turbine's rotation it is necessary to create the whole turbine wheel geometry from the single turbine blade by using Pro/ENGINEER which is a commercial CAD (computer-aided design) software now known as PTC Creo. Variable radius fillet is generated between the blade root and the hub to reduce the stress concentration. The minimum fillet radius has to be greater than 1 mm due to the manufacture restrictions and the adjacent fillets must not contact each other. To reduce the MOI of the rotor the back face is scalloped by removing metal between the blades in the inducer region. (See Figure 3.28).

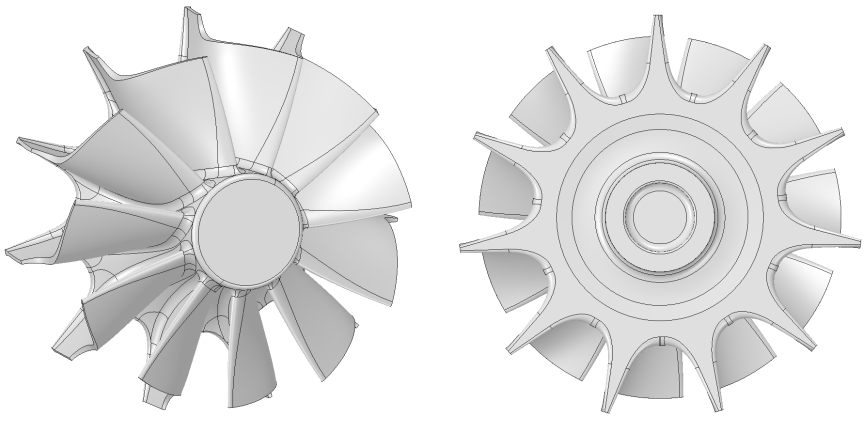

Fig. 3.28 Whole wheel geometry of the baseline design

The mesh is generated by using ANSYS Meshing as shown in Figure 3.29 and the total number of unstructured elements is around 150,000. Only one blade mesh is refined (element size = 0.6 mm) to save computational resource and time since the whole wheel geometry is axisymmetric. The mesh in the hub fillet and

the blade trailing edge is refined further (element size = 0.3 mm) since they are locations where the maximum stress occurs.

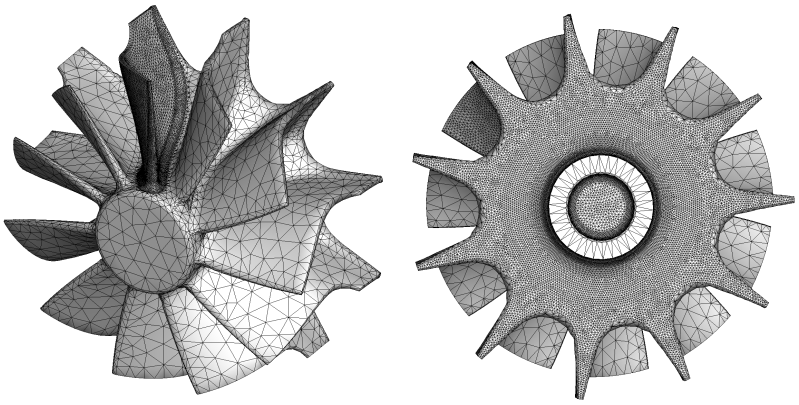

Fig. 3.29 Mesh of baseline whole wheel geometry

3.3.2 Turbine Material and Boundary Conditions

The material used to manufacture the turbine is Inconel 713C. The physical and mechanical properties of Inconel 713C are omitted due to the confidentiality requirements from CTT.

The wheel MOI ($8.8342 \times 10^{-5}\ kg \cdot m^2$) can be obtained directly through ANSYS Mechanical once the geometry is imported.

For the static structural analysis the boundary conditions applied are the rotational velocity (A in Figure 3.30) and the cylindrical support (B in Figure 3.30) provided by the shaft connected to the compressor. The rotating speed is 130,000 rev/min which is the maximum working speed of the turbine. The cylindrical support constrains the turbine wheel in the tangential direction and it is free in the radial and axial directions.

For the modal analysis the boundary conditions applied is only the cylindrical support without pre-stress consideration.

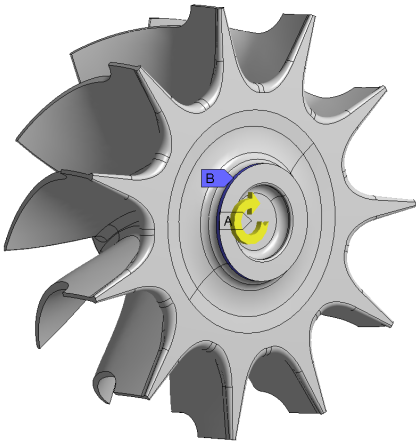

Fig. 3.30 Rotational velocity (A) and cylindrical support (B)

3.3.3 Static Structural and Modal Analysis Results

Figure 3.31 shows the maximum principle stress contour of the turbine wheel at RPM = 130,000. The legend of the stress contour is normalised due to the requirement from the sponsor (CTT). The stress is increasing from the shroud to the hub and the maximum stress location is always in the fillet which is the joint of the blade root and the wheel hub. The stress level at the concentration point can be reduced by increasing the fillet radius locally.

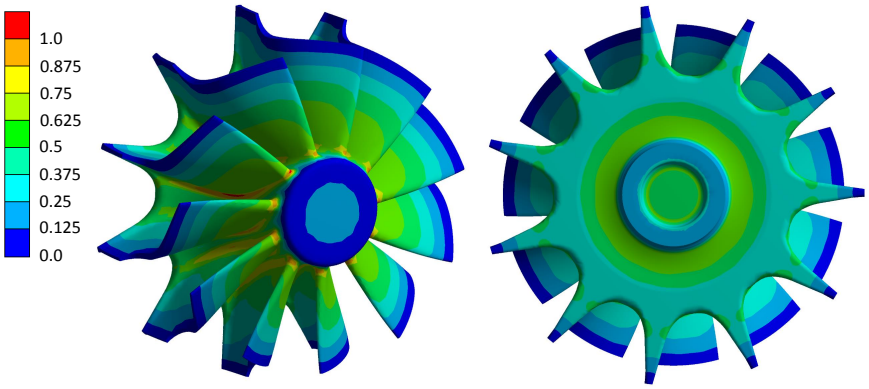

Fig. 3.31 Maximum principle stress (scaled) contour

Figure 3.32 shows the 1^{st} and 2^{nd} mode shapes of the turbine wheel vibration. The 1^{st} mode shape is always exducer flex and 2^{nd} mode shape is always inducer and exducer flex. The calculation of 1^{st} and 2^{nd} vibration natural frequencies is the average value of vibration frequencies which have the similar mode shapes

as shown in Figure 3.33. A Campbell digram of the baseline rotor is shown in Figure 3.34. It can be seen that the 1^{st} mode frequency is higher than the 4 times of RPS across the turbine operating RPM. The circles indicate the possible resonance operating conditions.

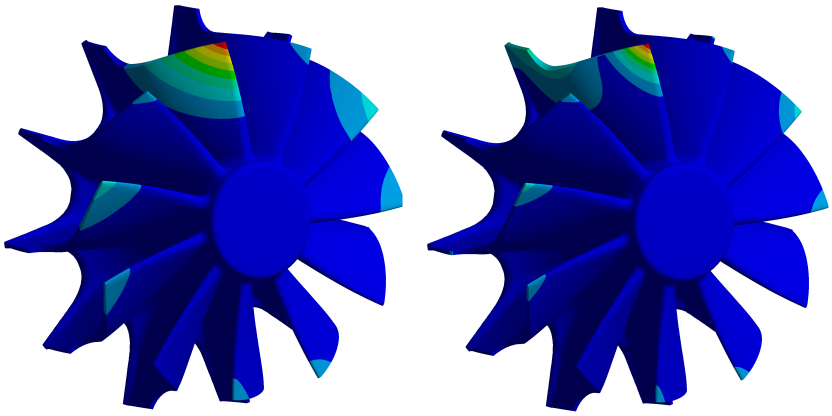

Fig. 3.32 1^{st} (left) and 2^{nd} (right) vibration mode shapes

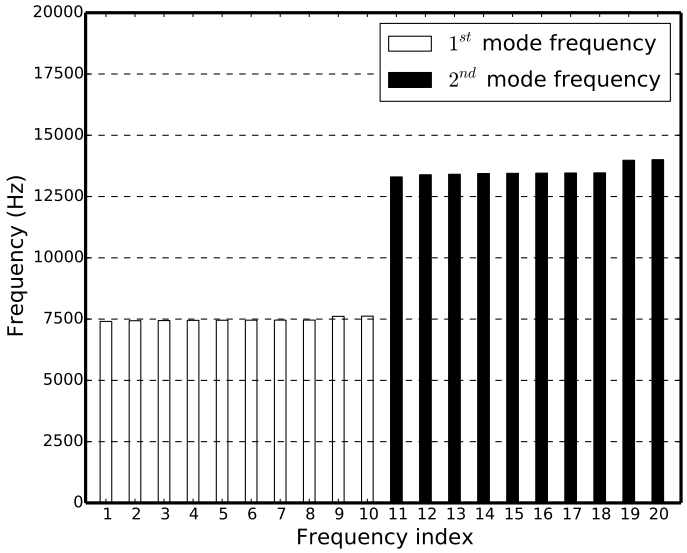

Fig. 3.33 Baseline vibration frequencies

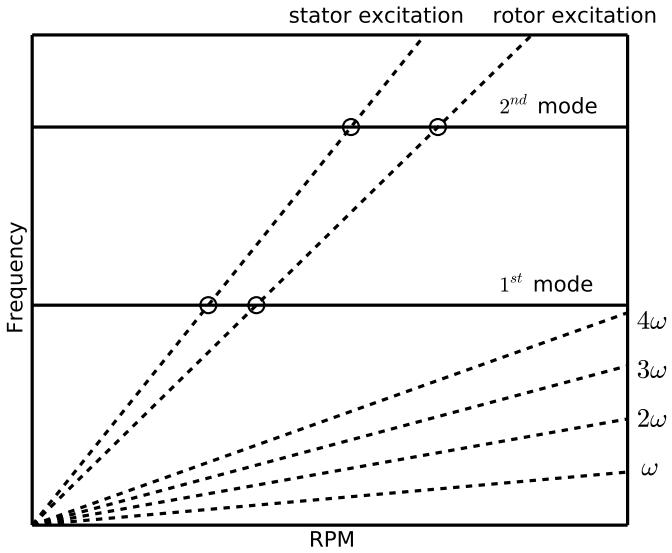

Fig. 3.34 Baseline Campbell diagram

3.4 Summary

In this chapter, the baseline turbine volute, nozzle ring and rotor blade geometries are introduced first and the CFD model is validated against the experimental results for the baseline turbine. The effect of the nozzle gap, the nozzle angle, the inlet total temperature on the turbine aerodynamic performance have been investigated through steady CFD simulations. The boundary conditions and mesh generation used for the steady CFD, the static structural and the modal analysis of the baseline geometry have been illustrated.

All the aerodynamic and mechanical performance parameters of the baseline design are summarised in Table 3.4. The stress values shown in this thesis are all non-dimensionalised.

Table 3.4 Performance parameters of the baseline design

$\eta_{t-s,50k}$	59.9 %
$\eta_{t-s,60k}$	66.5 %
$\eta_{t-s,70k}$	67.4 %
$\eta_{t-s,80k}$	63.3 %
$\eta_{t-s,90k}$	54.7 %
MFP_{50k}	23.9 $kg/s \cdot \sqrt{K}/MPa$
MFP_{60k}	23.9 $kg/s \cdot \sqrt{K}/MPa$
MFP_{70k}	23.6 $kg/s \cdot \sqrt{K}/MPa$
MFP_{80k}	22.9 $kg/s \cdot \sqrt{K}/MPa$
MFP_{90k}	22.0 $kg/s \cdot \sqrt{K}/MPa$
Maximum Principle Stress	0.99
1^{st} Frequency	7479 Hz
2^{nd} Frequency	13535 Hz
Moment of Inertia	8.8342 $\times 10^{-5}$ $kg \cdot m^2$

CHAPTER 4

BLADE GENERATION USING INVERSE DESIGN METHOD

This chapter will explain the procedures of the blade generation using the inverse design method proposed by Zangeneh [1991]. It is found that the derivation of this method is difficult to follow in the original paper. Therefore, to help readers understand this method more clearly, the detailed derivation of this method is illustrated in Appendix A.

4.1 Blade Meridional Geometry

The first step is to define the blade meridional shape. The blade meridional shape is the projection of the 3D blade on the meridional plane ((r, z) plane). As shown in Figure 4.1, the blade meridional geometry is divided into three parts by the blade LE and TE: the inlet domain, the blade domain and the outlet domain. The shapes of these three domains are controlled by two curves called hub and shroud. The hub and shroud curves are independent to each other and are defined by a cubic spline interpolation method based on two sets of points as shown in Figure 4.1.

To create the blade meridional geometry, coordinates of two sets of hub and shroud curve definition points have to be predefined. The detailed cubic spline interpolation method used for this curve generation is illustrated below. Only the

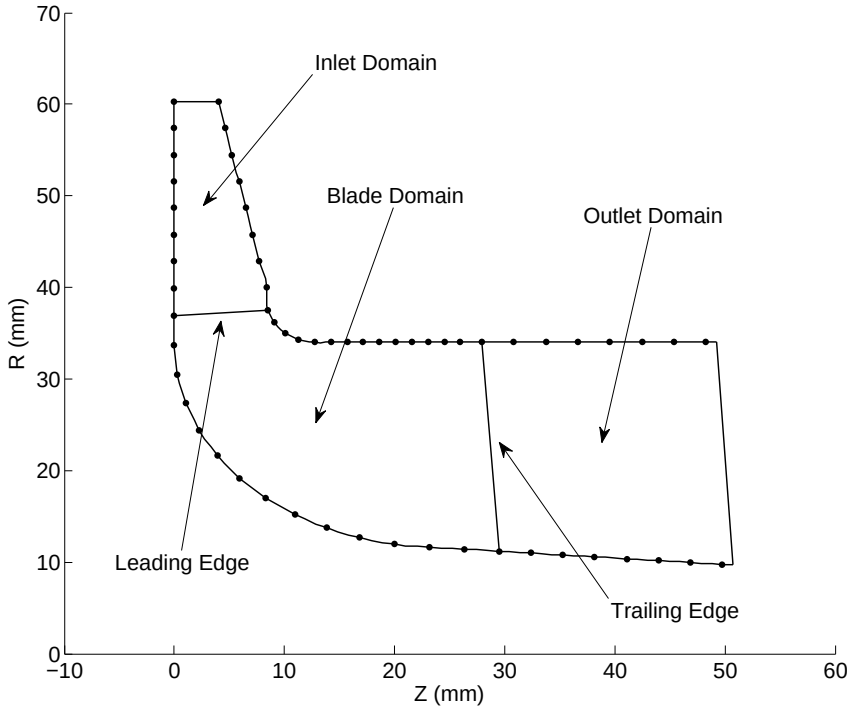

Fig. 4.1 Blade meridional geometry

hub curve generation is explained since the shroud curve generation uses the same method.

The coordinates of the i^{th} predefined hub point are r_i and z_i $(1 \leq i \leq N)$, where N is the total number of points. The aim is to determine $(N-1)$ cubic spline functions f_i $(i \in [1, N-1])$ used to connect two neighbouring points.

1) Calculate meridional distance m_i using Equation 4.1:

$$m_i = m_{i-1} + \sqrt{(r_i - r_{i-1})^2 + (z_i - z_{i-1})^2} \quad (i \in [2, N], m_1 = 0) \tag{4.1}$$

2) The cubic spline function $f_i(m)$ between two neighbouring points is defined by Equation 4.2:

$$f_i(m) = a_i(m - m_i)^3 + b_i(m - m_i)^2 + c_i(m - m_i) + d_i \quad (m \in [m_i, m_{i+1}], i \in [1, N-1]) \tag{4.2}$$

3) Calculate the first- and second-order derivatives of $f_i(m)$ using Equation 4.3 and Equation 4.4:

$$f_i^{'}(m) = 3a_i(m - m_i)^2 + 2b_i(m - m_i) + c_i \quad (m \in [m_i, m_{i+1}], i \in [1, N-1]) \tag{4.3}$$

$$f_i^{''}(m) = 6a_i(m - m_i) + b_i \quad (m \in [m_i, m_{i+1}], i \in [1, N-1]) \tag{4.4}$$

There are $(4N - 4)$ unknowns (a_i, b_i, c_i, d_i) in total in these equations.

4) Take m_i and r_i as an example. To meet the continuity and the smoothness conditions for the cubic spline functions f_i at the knots, the following equations must be satisfied:

$$f_i(m_i) = r_i \quad (i \in [1, N-1]) \tag{4.5}$$

$$f_i(m_{i+1}) = r_{i+1} \quad (i \in [1, N-1]) \tag{4.6}$$

$$f_i^{'}(m_{i+1}) = f_{i+1}^{'}(m_{i+1}) \quad (i \in [1, N-2]) \tag{4.7}$$

$$f_i^{''}(m_{i+1}) = f_{i+1}^{''}(m_{i+1}) \quad (i \in [1, N-2]) \tag{4.8}$$

5) However, only $(4N - 6)$ equations are placed above and two extra equations are needed to solve all the $(4N - 4)$ unknowns (a_i, b_i, c_i, d_i). Equation 4.9 and Equation 4.10 are added by applying the 'Natural Spline' condition at the first and last knots. The 'Natural Spline' condition is defined as that the spline will take the form of a straight line with $f^{''} = 0$ along the left of the leftmost knot and the right of the rightmost knot.

$$f_1^{''}(m_1) = 0 \tag{4.9}$$

$$f_{N-1}^{''}(m_{N-1}) = 0 \tag{4.10}$$

6) Substitute Equation 4.5, Equation 4.6, Equation 4.7, Equation 4.8, Equation 4.9 and Equation 4.10 into Equation 4.2, Equation 4.3 and Equation 4.4. The values of all unknowns (a_i, b_i, c_i, d_i) and the cubic spline functions between neighbouring points $f_i(r, m)$ can be calculated. The $f_i(z, m)$ can be obtained similarly. The hub curve function is given by Equation 4.11.

$$\begin{cases} r_{i,hub}(m) = f_i(r, m) \\ z_{i,hub}(m) = f_i(z, m) \end{cases} \quad (m \in [m_i, m_{i+1}], \quad i \in [1, N-1]) \tag{4.11}$$

4.2 Grid Generation

In the case of the meridional geometry of a radial or mixed-inflow turbine, the blade boundaries, especially the hub and the shroud, are highly curved and are not coincident with the coordinate lines in the (r, z) plane. To implement the boundary conditions on the grid points nearest to the boundary, the interpolation between points not coincident with the boundaries has to be used which introduces inaccuracies into the solution when solving the partial differential equations.

A transformation of the coordinate system from (r, z) to (ξ, η) is used to reduce the errors in the implementation of the boundary conditions. In the new curvilinear coordinate system the coordinate lines are coincident with all the boundaries. This means that the hub and the shroud coincide with lines of $\eta = constant$, while the inlet and the outlet boundaries coincide with lines of $\xi = constant$. The new transformed coordinate system is called 'boundary-fitted coordinate system' by Thompson et al. [1977]. For the grid generation in the meridional plane of a radial turbine, quasi-orthogonal lines from the hub to the shroud and quasi-streamlines from the inlet to the outlet divide the quasi-orthogonals into equal parts as shown in Figure 4.2. The algebraic expressions for the evaluation of derivatives of functions in the (ξ, η) plane is derived by Thompson et al. [1977]. The flow equations in the θ direction are solved using Inverse Discrete Fourier Transform (IDFT). Therefore, no numerical grid is needed in the θ direction.

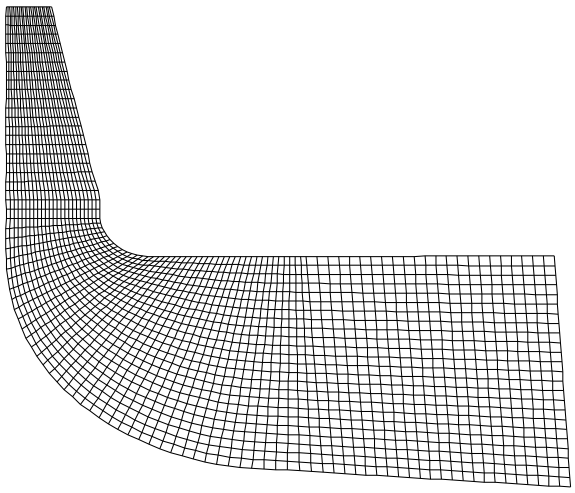

Fig. 4.2 Body-fitted grid in the meridional plane

4.3 Blade Thickness

The blade thickness can be defined by normal thickness (t_N) or tangential thickness (t_θ) using Equation 4.12, Equation 4.13, Equation 4.14 and is illustrated in Figure 4.3. Where r, z and m are blade radial, axial and meridional coordinates, θ^+ and θ^- are wrap angles on the blade pressure and suction surfaces, f or θ is the wrap angle of the blade camber line.

$$t_\theta(r,z) = r\theta^+(r,z) - r\theta^-(r,z) \tag{4.12}$$

$$f(r,z) = \theta(r,z) = \frac{\theta^+(r,z) + \theta^-(r,z)}{2} \tag{4.13}$$

$$\begin{aligned} t_N(r,z) &= \frac{t_\theta(r,z)}{\sqrt{1 + r^2\left[\frac{\partial f(r,z)}{\partial r}\right]^2 + r^2\left[\frac{\partial f(r,z)}{\partial z}\right]^2}} \\ &= \frac{t_\theta(r,z)}{\sqrt{1 + r^2\left[\frac{\partial f(r,z)}{\partial m}\right]^2}} \end{aligned} \tag{4.14}$$

The blade thickness can be controlled by a thickness file which defines the blade thickness values from the LE to the TE (streamwise location $0 \leq m^* \leq 1$) and

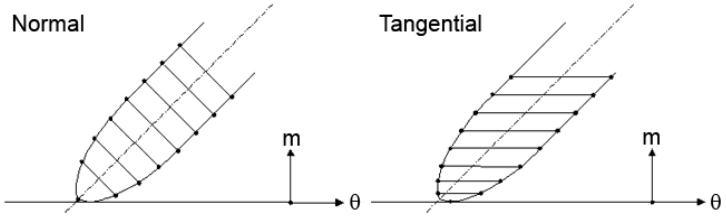

Fig. 4.3 Normal thickness (t_N) and tangential thickness (t_θ)

from the hub to the shroud (spanwise location $0 \leq s^* \leq 1$) as shown in Figure 4.4. The whole blade thickness distribution can be obtained through an interpolation.

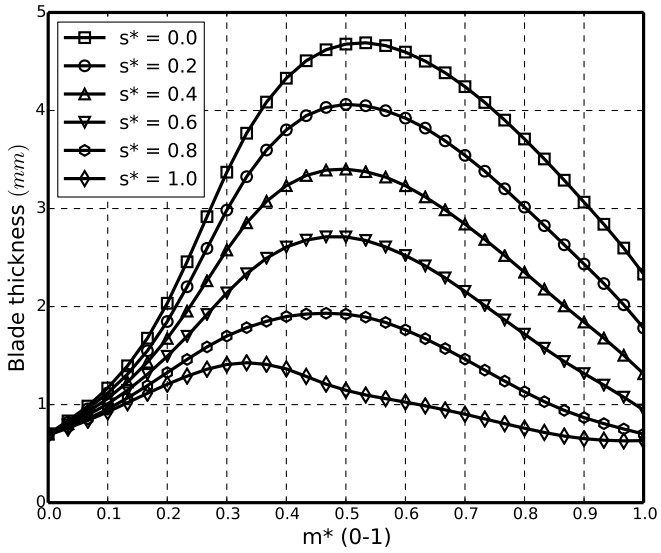

Fig. 4.4 Blade thickness distribution for different spanwise locations

4.4 Flow Specification and Boundary Conditions

The flow properties (stagnation density, gas constant and specific heat ratio) and the design inlet boundary conditions (volume flow rate and total temperature) are specified in Table 4.1. The inlet stagnation density ρ_{01} is calculated using the equation of state for the ideal gas (Equation 4.15). The design rotating speed RPM is calculated based on velocity ratio $\dfrac{U}{C_{is}} = 0.69$ and $R_{tip} = 0.038$ m (Equation 4.16).

Table 4.1 Design specifications

Inlet stagnation density ρ_{01}	1.9005 kg/m^3
Gas constant R	287.1 $J/(kg \times K)$
Specific heat ratio γ	1.4
Rotational speed	70,000 rev/min
Blade number	11
Inlet volume flow rate	0.211 m^3/s
Inlet total temperature T_{01}	403.2K

$$\rho_{01} = \frac{P_{01}}{RT_{01}} \tag{4.15}$$

$$\begin{aligned} RPM &= \frac{U}{C_{is}} C_{is} \frac{1}{R_{tip}} \frac{30}{\pi} \\ &= 0.69 \times \frac{30 C_{is}}{\pi R_{tip}} \\ &= 0.69 \times \frac{30\sqrt{2c_P T_{01}\left[1 - \left(\frac{P_2}{P_{01}}\right)^{(\gamma-1)/\gamma}\right]}}{\pi R_{tip}} \\ &= 0.69 \times \frac{30\sqrt{\frac{2\gamma R T_{01}}{\gamma-1}\left[1 - \left(\frac{P_2}{P_{01}}\right)^{(\gamma-1)/\gamma}\right]}}{\pi R_{tip}} \end{aligned} \tag{4.16}$$

4.5 Blade Loading and Stacking

For the steady inviscid compressible flow, the specific enthalpy jump across the blade Δh can be expressed by Equation 4.17.

$$\Delta h = h^+ - h^- = \frac{2\pi}{B} W_{m,bl} \frac{\partial r\bar{V}_\theta}{\partial m} \tag{4.17}$$

Where h^+ and h^- are the specific enthalpy on the blade pressure and suction surfaces, B is the number of blades, $W_{m,bl}$ is the relative meridional velocity on the blade surface (mean of the pressure and suction surfaces) and $\frac{\partial r\bar{V}_\theta}{\partial m}$ is the derivative of $r\bar{V}_\theta$ along the meridional direction m. Circumferentially averaged

swirl velocity $r\bar{V_\theta}$ is defined by Equation 4.18.

$$r\bar{V_\theta} = \frac{B}{2\pi}\int_0^{2\pi/B} rV_\theta d\theta \tag{4.18}$$

For the incompressible flow, Equation 4.17 can be rewritten to express the static pressure jump across the blade ΔP using Equation 4.19, where P^+ and P^- are the static pressure on the blade pressure and suction surfaces and ρ is the density.

$$\Delta P = P^+ - P^- = \frac{2\pi}{B}\rho W_{m,bl}\frac{\partial r\bar{V_\theta}}{\partial m} \tag{4.19}$$

According to Borges [1990a] $W_{m,bl}$ should smoothly vary from the LE to the TE in a well-designed turbomachine. Therefore, $\frac{\partial r\bar{V_\theta}}{\partial m}$ will approximately vary in the same way as Δh or ΔP from the LE to the TE along streamlines. In the inverse design method, $\frac{\partial r\bar{V_\theta}}{\partial m}$ is defined as the blade loading.

The three segments method by Zangeneh et al. [1996] is used to define the blade loading distribution as illustrated In Figure 4.5. The horizontal axis is the normalised meridional coordinate m^* defined by Equation 4.20, where M is the maximum meridional length, in the LE $m^* = 0$ and in the TE $m^* = 1$.

$$m^* = \frac{m}{M} \tag{4.20}$$

The vertical axis is the non-dimensional blade loading $\frac{\partial r\bar{V_\theta}^*}{\partial m_n}$ defined by Equation 4.21, where L is the reference length, U is the reference velocity, $r\bar{V_\theta}$ is nondimensionalised by LU and m is nondimensionalised by L.

$$\frac{\partial r\bar{V_\theta}^*}{\partial m_n} = \frac{\partial\left(\frac{r\bar{V_\theta}}{LU}\right)}{\partial\left(\frac{m}{L}\right)} = \frac{1}{U}\frac{\partial r\bar{V_\theta}}{\partial m} \tag{4.21}$$

This method divides the loading distribution into three separate parts by two points NC and ND on the meridional line. Parabolas are used to define the distribution for the first and last segment and the middle segment is specified by a straight line with a given slope (SLOPE). The loading value at the LE is specified by DRVT. Typically by defining $\frac{\partial r\bar{V_\theta}^*}{\partial m_n}$ in this way at two spanwise locations (hub and shroud) and $r\bar{V_\theta}^*$ in the LE and TE (Table 4.2), the $r\bar{V_\theta}$ distribution in the whole blade channel can be computed.

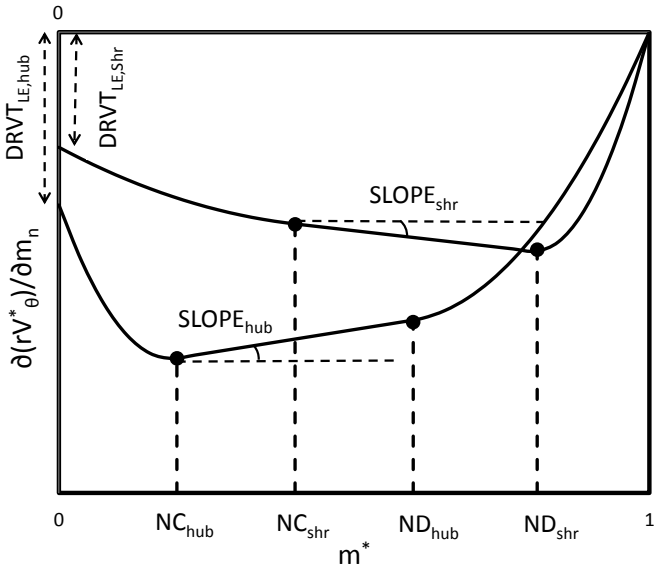

Fig. 4.5 Three segments method used to define the blade loading

Table 4.2 Blade loading parameters

	hub	shroud
LE $r\bar{V_\theta}^*$	$r\bar{V_\theta}^*_{LE,hub}$	$r\bar{V_\theta}^*_{LE,shr}$
TE $r\bar{V_\theta}^*$	$r\bar{V_\theta}^*_{TE,hub}$	$r\bar{V_\theta}^*_{TE,shr}$
NC	NC_{hub}	NC_{shr}
ND	ND_{hub}	ND_{shr}
SLOPE	$SLOPE_{hub}$	$SLOPE_{shr}$
LE $\frac{\partial r\bar{V_\theta}^*}{\partial m_n}$	$DRVT_{LE,hub}$	$DRVT_{LE,shr}$

The following points should be taken into account for choosing the blade loading distribution:

1) $r\bar{V}_\theta$ change between the turbine inlet and outlet should be equal to the turbine specific work (see Equation 4.22);

$$\frac{\tau}{\dot{m}} = r\bar{V}_{\theta,LE} - r\bar{V}_{\theta,TE} \tag{4.22}$$

2) $r\bar{V}_{\theta TE}^{*}$ should be minimised to reduce the exit swirl velocity (kinetic energy loss) and therefore to maximise the turbine t-s efficiency (η_{t-s}). The ideal value of $r\bar{V}_{\theta TE}^{*}$ should be 0;

3) $\frac{\partial r\bar{V}_\theta^{*}}{\partial m_n}$ at LE ($DRVT_{LE}$) can be used to control the flow incidence condition. When $DRVT_{LE} = 0$, it gives zero incidence. When $DRVT_{LE} < 0$, it gives positive incidence. When $DRVT_{LE} > 0$, it gives negative incidence;

4) $\frac{\partial r\bar{V}_\theta^{*}}{\partial m_n}$ at TE is always set to zero to satisfy Kutta-Joukowsky condition (Anderson [2007]).

The stacking or stacking condition of the blade is the initial values of the blade camber along a quasi-orthogonal and is necessary for integrating and solving the partial differential equations regarding the blade camber. For radial turbine applications, it is common to define zero stacking in the blade LE which means the blade LE wrap angle is zero.

4.6 Blade Generation

The simplified flow chart of the inverse design method used to generate the 3D blade geometry is illustrated in Figure 4.6.

The initial blade camber f^0 is obtained by assuming zero periodic and uniform mean velocity along quasi-orthogonals. The flow field $\vec{V}$ for a given blade camber f^{n-1} is computed by splitting the velocity field into the circumferentially averaged component $\overline{\vec{V}}$ and the periodic component $\widetilde{\vec{V}}$ as shown in Equation 4.23. The mean flow equation is solved using Stokes stream function for 3D axisymmetric flow. The periodic flow equation is solved using potential flow theory, Monge-Clebsch

decomposition and IDFT.

$$\overrightarrow{V}(r,\theta,z) = \overline{\overrightarrow{V}}(r,z) + \widetilde{\overrightarrow{V}}(r,\theta,z) \tag{4.23}$$

Once the flow field has been determined, the new blade camber f^n can be computed by using the blade surface boundary condition. This condition can be expressed as that the relative velocity vector on the blade surface must align to the blade surface using Equation 4.24.

$$\begin{aligned} \vec{W}_{bl} \cdot \nabla\alpha &= 0 \\ \frac{\left(\vec{W}_{bl}^{+} + \vec{W}_{bl}^{-}\right)}{2} \cdot \nabla\alpha &= 0 \end{aligned} \tag{4.24}$$

Where α is the blade surface, $\nabla\alpha$ is the vector normal to the blade surface, $\vec{W}_{bl}$ is the relative velocity at the blade mean surface, $\vec{W}_{bl}^{+}$ and $\vec{W}_{bl}^{-}$ are the relative velocities on the blade pressure and suction surfaces. Expand Equation 4.24 to get :

$$\left(\bar{V}_r + \tilde{V}_{r,bl}\right)\frac{\partial f^n}{\partial r} + \left(\bar{V}_z + \tilde{V}_{z,bl}\right)\frac{\partial f^n}{\partial z} = \frac{r\bar{V}_\theta}{r^2} + \frac{\tilde{V}_{\theta,bl}}{r} - \omega \tag{4.25}$$

Where f^n is the new blade camber and can be obtained through the integration of Equation 4.25 using the initial stacking conditions. If the maximum difference between the new blade camber f^n and the blade camber f^{n-1} from the previous iteration is less than the specified tolerance, the program is treated as converged. Otherwise, the program will go to the next iteration and update the flow field for the new blade shape f^n. The program will stop when the number of iterations reaches the maximum value.

4.7 Summary

A thorough explanation of the key aspects for the inverse design method has been presented in this chapter including the meridional geometry defined by the cubic spline method, 2D 'boundary-fitted' grid, the blade thickness definition, design specifications, the blade loading defined by the three segments method,

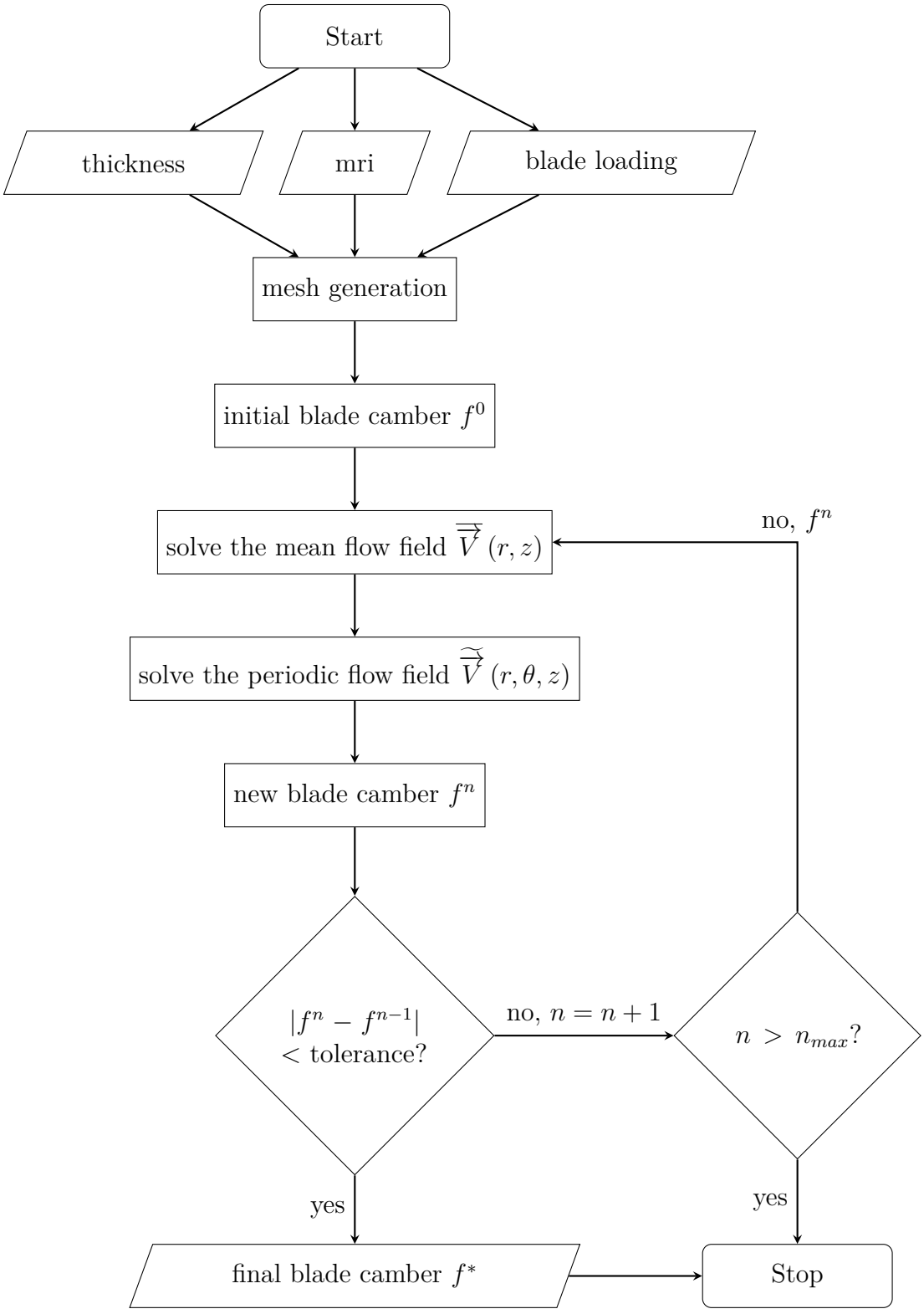

Fig. 4.6 Simplified flow chart of the blade generation using inverse design method

the stacking and the simple blade update algorithm. A step by step derivation of all formulations for the inverse design method can be found in Appendix A which will help readers understand the beautiful nature of this method from both aerodynamic and mathematical points of view.

CHAPTER 5

OPTIMISATION WITH IMPROVEMENT IN HIGH U/C_{is}

In this chapter the inverse design method, DOE theory, the response surface approximation model and MOGA are coupled and a systematic approach used to design radial and mixed-inflow turbines which meet multidisciplinary, multi-objective and multipoint optimisation targets is presented. The flow chart of the optimisation process is shown in Figure 5.1.

1) To generate a blade geometry using the inverse design method, the meridional geometry, the thickness distribution and the blade loading distribution are necessary inputs. The parametrisation of all these inputs and their ranges of the variation have to be specified first during an optimisation process. The output parameters including the aerodynamic performance parameters and the mechanical performance parameters shown in Table 3.4 of any new designs in the optimisation will be evaluated using the same method stated in Chapter 3.

2) The sensitivity study in step 4) requires a linear (first-order polynomial) RSM model. Therefore, the minimum number of $n+1$ designs are generated using the inverse design method and Optimal Latin Hypercube Sampling (OLHS) method within the specified ranges of all design parameters, where

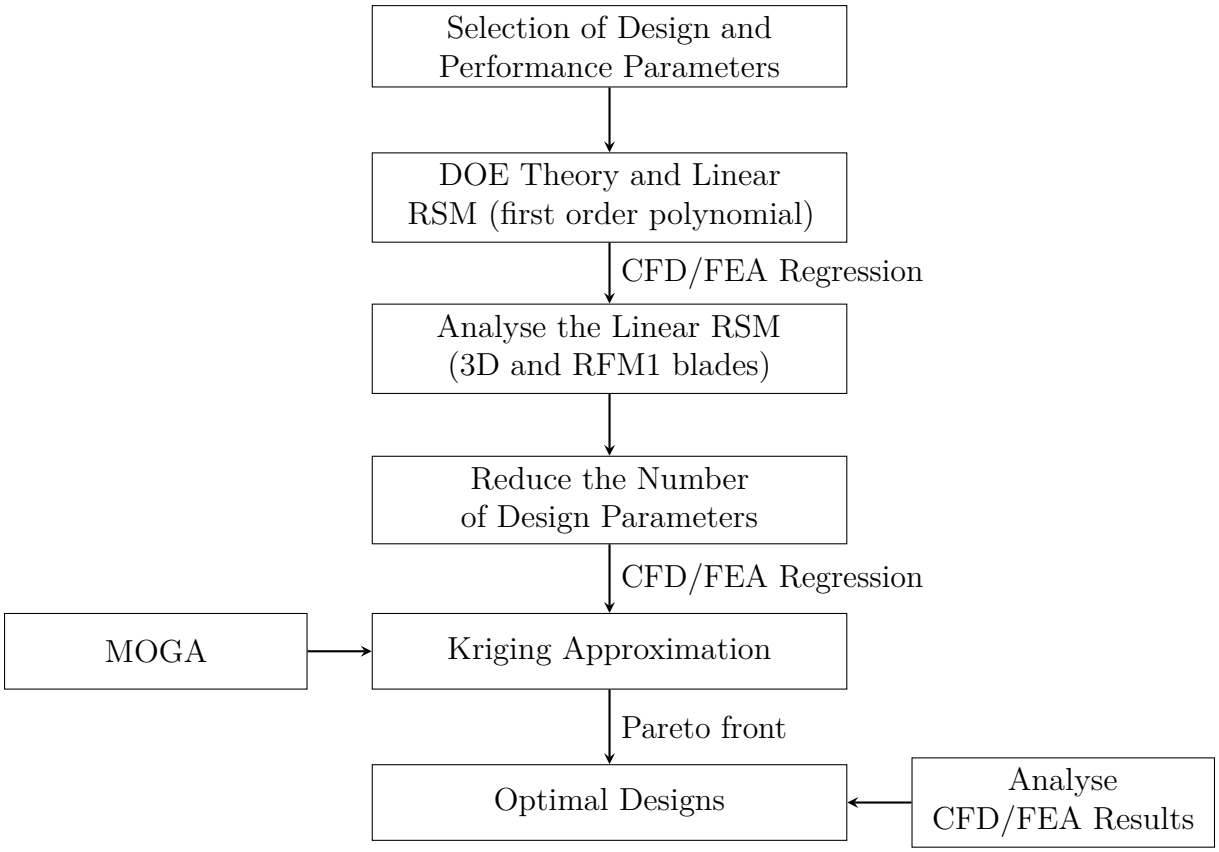

Fig. 5.1 Flow chart of the optimisation process

n is the number of design parameters selected in step 1). The performance of all these 3D blades are evaluated using CFD and FEA simulations.

3) The stress level of 3D blades is found to be much higher compared to the baseline value and the material strength, which is caused by the non-radial blading of 3D blades generated using the inverse design method. A Radial Filament Modification method (RFM1) is proposed to reduce the stress on the 3D blades and the new blade after the modification is designated RFM1 blade. Through the comparison of the performance values of a set of 3D and RFM1 blades with the same design parameters, it is found that the RFM1 blades have much lower stress and do not necessarily sacrifice other performance parameters. Therefore, RFM1 will be applied to all the designs in the following optimisation process.

4) A linear RSM model is generated based on the design parameters and performance parameters of RFM1 blades using first-order polynomial regression. The number of the design parameters is reduced based on the sensitivity analysis which compares the normalised coefficients of the linear polynomial and the most significant design parameters are selected whose variation have a larger effect on the performance parameters.

5) A new DOE with more designs is generated for the new selected design parameters with RFM1 modification and their performance parameters are evaluated using CFD and FEA simulations. The Kriging approximation is used to build the Kriging RSM based on the new DOE results.

6) A Pareto front is generated through searching the optimal designs on the Kriging RSM quickly using MOGA and several optimal designs can be selected from the Pareto Front. The performance parameters of these optimal designs are validated against CFD and FEA calculations.

5.1 Selection of Design and Performance Parameters

The design parameters consist of 6 meridional geometry parameters, 10 blade loading parameters and 1 thickness parameter.

It is shown in Figure 5.2 that five control points A, B, C, D and E are used to create the hub curve and the shroud curve is created similarly using A', B', C', D'and E'. Both hub and shroud curves are created by the cubic spline method which has been explained in section 4.1. The radial coordinate of point B'(maximum tip radius) is fixed (38 mm) while the axial coordinate of point B is also fixed (0 mm). Point D is fixed in both axial and radial directions to make sure all the blades have the same blade length and shaft radius as the baseline which are design constraints from CTT. The 6 design parameters used to define the blade meridional geometry are the inducer width W_1, the exducer width W_2, the LE angle α_1, the TE angle α_2, the hub and shroud control points Y_{hub} and Y_{shr}.

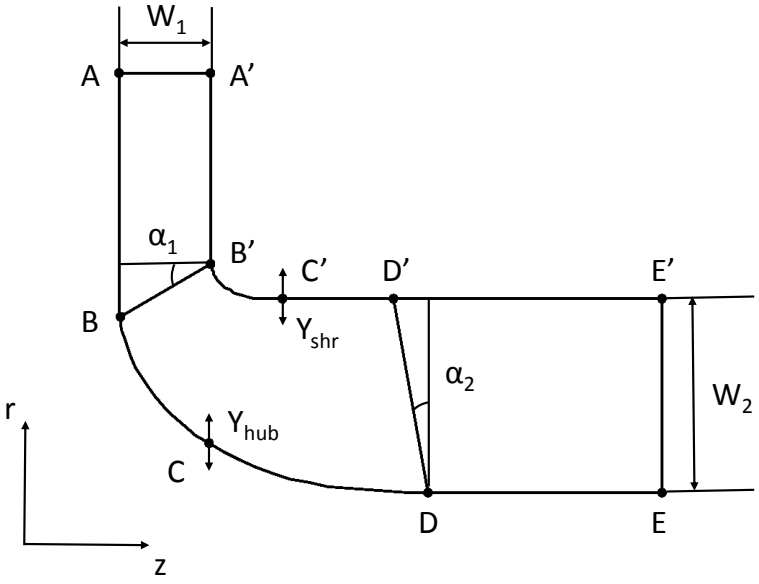

Fig. 5.2 Meridional plane parameters

The 10 blade loading parameters are shown in Table 4.2 while $r\bar{V}^*_{\theta LE,hub}$ and $r\bar{V}^*_{\theta LE,shr}$ are not design parameters and set as constants to meet the turbine specific work requirement.

The blade thickness is controlled by one non-dimensional factor called thickness parameter (Figure 5.3) which is greater than 0.9 and less than 1.2. The profile thickness distribution of the baseline blade can be seen in Figure 4.4. The thickest part of the blade is always in the middle hub section. To create a new thickness distribution using the thickness parameter, the shroud thickness (t_{shr}) remains the same and the hub thickness (t_{hub}) is multiplied by the thickness parameter.

The thickness between the hub and the shroud sections is recalculated through linear interpolation.

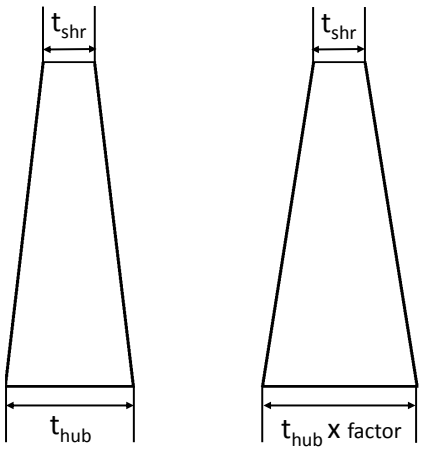

Fig. 5.3 Thickness parameter

For an optimisation process, it is desirable to explore the design space as much as possible, this requires a wide variation of all the design parameters in order to increase the chance that the global optimal design can be found. However, if the range of design parameters is too big, a large number of poor designs have to be evaluated which will significantly increase the complexity and the cost of the optimisation process. Therefore, the range of all the 17 design parameters are carefully selected and are shown in Table 5.1. The range of W_1, W_2, α_1 and α_2 are selected to make sure that they cover the value of the baseline design. The range of the radial coordinate of the hub control point Y_{hub} is selected to make sure a reasonable curvature and hub shape. It is difficult to define Y_{shr} for the shroud control point in a similar way since the radial position of point D' is changing. Therefore, Y_{shr} is defined as a non-dimensional parameter by Equation 5.1. The resulting possible meridional shape is shown in Figure 5.4 compared to the baseline

Table 5.1 Ranges of design parameters and baseline values

Design Parameters	min	max	baseline
W_1 (mm)	7	11	8.441
W_2 (mm)	15	24	22.25
α_1 $(^\circ)$	0	40	0
α_2 $(^\circ)$	0	10	3.86
Y_{hub} (mm)	16.5	21	—
Y_{shr}	0.2	0.4	—
$r\bar{V}_{\theta TE,hub}$	0	0.04	—
$r\bar{V}_{\theta TE,shr}$	0.06	0.1	—
NC_{hub}	0.05	0.2	—
NC_{shr}	0.05	0.4	—
ND_{hub}	0.6	0.85	—
ND_{shr}	0.6	0.85	—
$SLOPE_{hub}$	1	2.5	—
$SLOPE_{shr}$	-5	-1	—
$DRVT_{LE,hub}$	-1	-0.1	—
$DRVT_{LE,shr}$	-1	-0.1	—
$Thickness\ Parameter$	0.9	1.2	1.0

and a large variation can be seen.

$$\begin{aligned} Y_{shr} &= \frac{r_{C'} - r_{D'}}{r_{B'} - r_{D'}} \\ &= \frac{r_{C'} - (r_D + W_2)}{r_{B'} - (r_D + W_2)} \\ &= \frac{r_{C'} - (11.25 + W_2)}{38 - (11.25 + W_2)} \\ &= \frac{r_{C'} - W_2 - 11.25}{26.75 - W_2} \end{aligned} \tag{5.1}$$

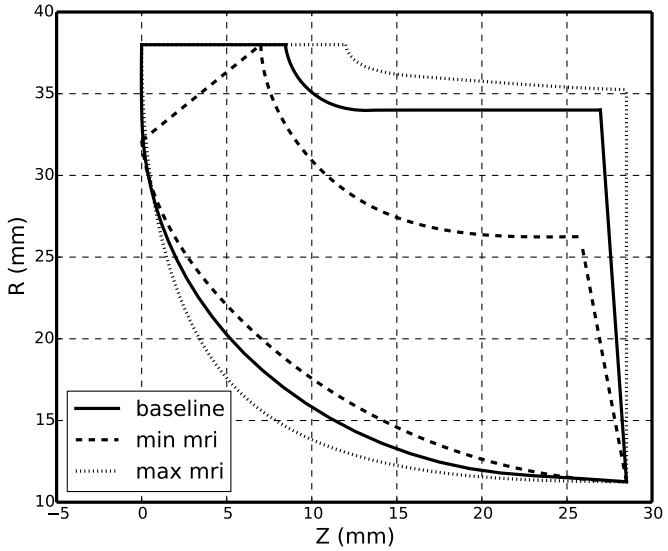

Fig. 5.4 Range of meridional shapes compared to the baseline

The blade loading parameters are carefully selected to make sure the hub is always fore-loaded. The circumferential distance between the pressure surface and the suction surface of two adjacent blades $d(m^*)$ for a constant spanwise location (e.g. hub) can be expressed using Equation 5.2, where r is the radius, B is the number of blades and t_θ is the blade tangential thickness. In the hub from the blade LE ($m^* = 0$) to TE ($m^* = 1$), $r(m^*)$ is decreasing from the largest value to the smallest value and t_θ is increasing until $m^* = 0.5$ then starts decreasing. Therefore, the value of $d(m^*)$ is decreasing along the streamwise direction in the hub which can be clearly seen in Figure 5.5. The pressure from the suction surface of one blade to the pressure surface of another blade must be smoothly distributed.

Therefore, the pressure difference ΔP between two surfaces near the middle and TE must be smaller than that in the fore-part of the blade. The pressure difference is proportional to the blade loading (Equation 4.19) which means the hub blade loading has to peak in the fore-part of the blade which is called fore-loaded. A small value of NC_{hub} and positive $SLOPE_{hub}$ will make sure the hub is always fore-loaded. It also should be noted that the blade loading may be greater than 0 if the $SLOPE_{hub}$ is to high which is not physically feasible. There is no special requirement for the shroud loading since the change of $r(m^*)$ and $t_\theta(m^*)$ along the shroud is very small allowing the loading to be an arbitrary shape.

$$d\left(m^*\right) = \frac{2\pi r\left(m^*\right)}{B} - t_\theta\left(m^*\right) \tag{5.2}$$

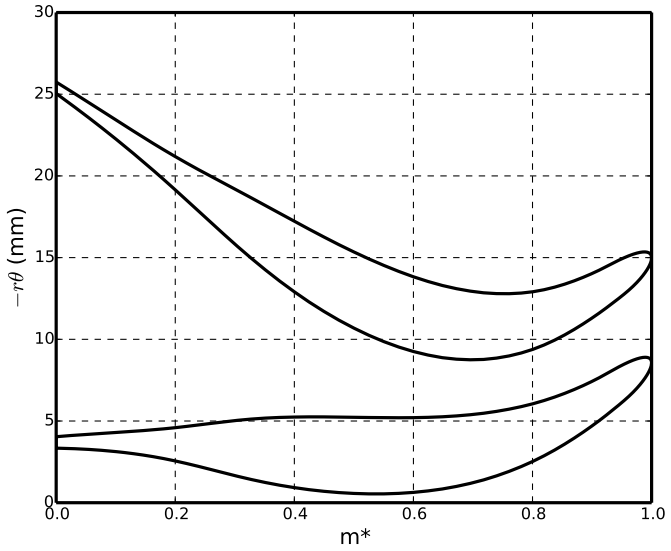

Fig. 5.5 Hub blade-to-blade view of a radial turbine

The range of all design parameters and their baseline values are summarised in Table 5.1. All 14 performance parameters and their baseline values have been summarised in Table 3.4 and the performance of any new design will be evaluated using the same CFD and FEA set up as the baseline design.

5.2 DOE Theory and Linear RSM Analysis

For any design problem the performance parameters (y_j) can be expressed by a function of design parameters (x_i):

$$y_j = f_j(x_i), \quad i \in [1, n], \quad j \in [1, m] \tag{5.3}$$

Where n is the number of design parameters and m is the number of performance parameters. The optimisation process is to find the optimal design $y_j \in R^m$ which satisfies all design criteria by exploring the design space $x_i \in R^n$. In most cases, f_j is unknown or impossible to get an analytic expression and a surrogate or response surface model ($\widetilde{f}_j$) then can be used to approximate f_j:

$$\widetilde{f}_j \approx f_j \tag{5.4}$$

The most widely used response surface models (RSM) are polynomial, Radial Basis Function (RBF) and Kriging. A detailed review of these three methods can be found in Queipo et al. [2005]. To construct a response surface for a design problem a Design of Experiments (DOE) study has to be performed first. DOE is the design technique which aims to study the relation between the inputs (design parameters) and the outputs (performance parameters). The first question before starting a DOE is, "What is the minimum number of designs (or observations) needed to perform such a DOE study?" On one hand, to extract as much information as possible it is desirable to get a large number of different designs. On the other hand, the number of designs needs to be minimised due to the limited time and resources.

The minimum number of designs needed N_{min} for different RSM are defined by Equation 5.5 and plotted in Figure 5.6, where n is the number of design parameters. It can be seen that N_{min} is increasing linearly for the linear polynomial, RBF and Kriging and quadratically for higher order polynomials. The minimum number of designs N_{min} for RBF and Kriging is almost twice of N_{min} for the linear polynomial model. For the case of Optimisation 1, $n = 17$, N_{min} for the linear model is only 18 while for other models this number is between 35 and 205. The linear (first-order) polynomial model requires the least computational resources and can be easily implemented to study the relation between the design parameters and the performance parameter. Therefore, it is used to approximate f_j by Equation 5.6

and will be used in section 5.4 for the sensitivity analysis.

$$N_{min} = \begin{cases} n+1 & (linear) \\ \frac{n^2+3n+2}{2} & (quadratic) \\ \frac{n^2+5n+2}{2} & (cubic) \\ \frac{n^2+7n+2}{2} & (quartic) \\ 2n+1 & (RBF \quad \& \quad Kriging) \end{cases} \tag{5.5}$$

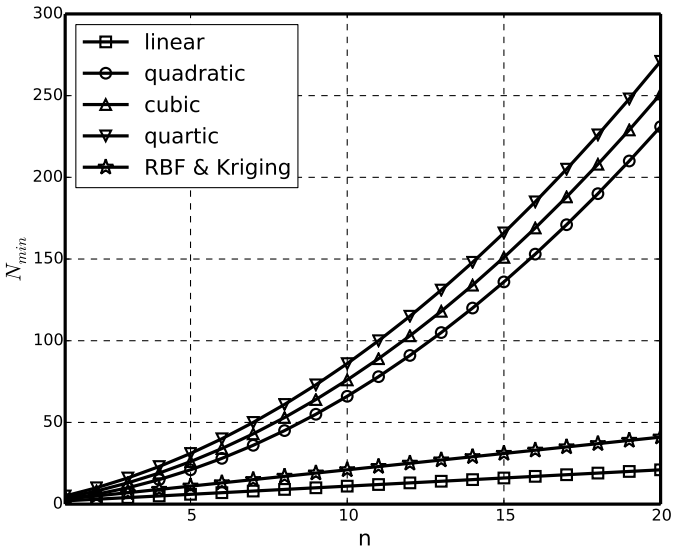

Fig. 5.6 Minimum number of designs needed for different RSM

$$f_j(x_i) \approx \widetilde{f}_j(x_i) = y_j = a_0^j + \sum_{i=1}^{n} a_i^j x_i^j \tag{5.6}$$

There are n+1 unknown polynomial coefficients a_i in Equation 5.6 whose values can be determined by a standard least-square regression as shown in Equation 2.7. At least n+1 design points are needed to perform the least-square regression.

The next question needed to be answered is how to choose these (at least $n+1$) discrete design points in the continuous design space which contains infinite designs and combinations of design parameters. Different methods are available including Parametric Study, Full Factorial, Fractional Factorial, Orthogonal Array, Central

Composite, Latin Hypercube and Optimal Latin Hypercube. The advantages and disadvantages of all these methods are reviewed and compared below.

In a Parametric Study, each design parameter is varying over the specified range while other design parameters are held at the specified baseline values. The number of designs needed for a Parametric Study is defined by Equation 5.7, where n is the number of design parameters x_i and l_i is the number of levels or values for different x_i. An example of the Parametric Study of two parameters is shown in Figure 5.7. In this case, n = 2 and $l_1 = l_2 = 5$. Therefore, 9 designs are generated. Its advantage is a small number of design points are enough to evaluate independent effects of each design parameter. While the disadvantage is that the interactions between different design parameters are not taken into account.

$$N = \sum_{i=1}^{n} l_i - n + 1 \tag{5.7}$$

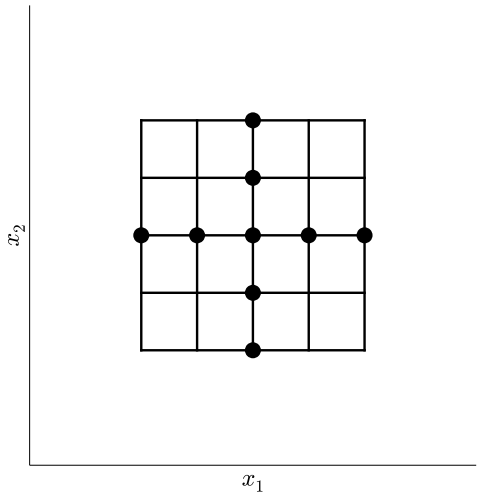

Fig. 5.7 Parametric Study for two design parameters (x_1 and x_2)

In a Full Factorial design, the number of discrete levels l_i for each design parameters x_i have to be specified. For such an experiment, all the combinations of all the parameters at all levels will be evaluated. The number of all the combinations is given by Equation 5.8. An example is given in Figure 5.8. The advantage is

that the effect of each design parameter on the performance parameters can be investigated, as well as the effects of all the interactions between design parameters on the performance parameters. For l_i levels, the effects up to $(l_i - 1)$ order can be evaluated. The disadvantage is the cost is very expensive since N is increasing exponentially with n. For the case of Optimisation 1, $n = 17$, even each design parameter only has two levels, the total number of designs needed will be 2^{17} which is not feasible.

$$N = \prod_{i=1}^{n} l_i \tag{5.8}$$

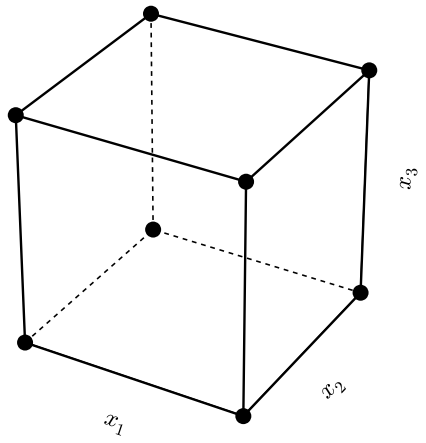

Fig. 5.8 Full Factorial design for three design parameters (x_1, x_2 and x_3)

A Fractional Factorial design is an experimental design consisting of a carefully chosen subset of a Full Factorial design. The number of designs is l^{n-m} (Equation 5.9), where m is the size of the fraction ($\frac{1}{m}$) of the Full Factorial. Figure 5.9 is a 2^{3-1} Fractional Factorial design and it is $\frac{1}{2^1}$ of the Full Factorial design shown in Figure 5.8. It is more efficient than Full Factorial, but less effect can be observed compared to a Full Factorial design.

$$N = l^{n-m} \tag{5.9}$$

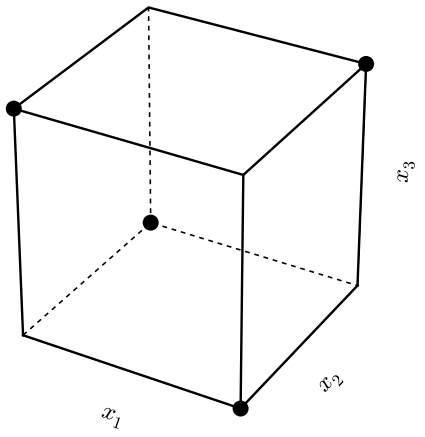

Fig. 5.9 Fractional Factorial design for three design parameters (x_1, x_2 and x_3)

An Orthogonal Array is a special Fractional Factorial design which maintains the orthogonality among the different design parameters and their interaction. Table 5.2 shows a L_9 Orthogonal Array design for three design parameters with three levels. Select any two columns from this table for example column A and C. For all the rows, the frequency of the pair (A_i, C_j) is the same time (once in this case), where $i \in [1, 3]$ and $j \in [1, 3]$. The same feature is held for column A and B, B and C and arrays with this feature are called Orthogonal Arrays. This can also be seen in Figure 5.10. To investigate the interaction between parameters, new parameter like AB, BC and AC can be defined. The advantage of this method is large saving in the experimental effort compared to a Full Factorial design. The disadvantage is that high-order interactions are neglected in the design matrix.

A Central Composite design (CCD) is a 2-level Full Factorial design plus a central point and two additional points for each design parameter as shown in Figure 5.11. The total number of designs N is defined by Equation 5.10. In spite of the fact that CCD requires a significant number of designs, more than a 2-level Full Factorial design, the covered design space is expanded and more information can be obtained.

$$N = 2^n + 2n + 1 \tag{5.10}$$

Table 5.2 L_9 Orthogonal Array for three design parameters (A, B and C) with three levels

Design	A	B	C
1	A_1	B_1	C_1
2	A_1	B_2	C_2
3	A_1	B_3	C_3
4	A_2	B_1	C_2
5	A_2	B_2	C_3
6	A_2	B_3	C_1
7	A_3	B_1	C_3
8	A_3	B_2	C_1
9	A_3	B_3	C_2

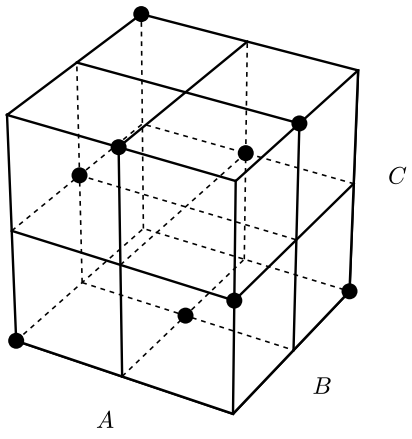

Fig. 5.10 L_9 Orthogonal Array for three design parameters (A, B and C)

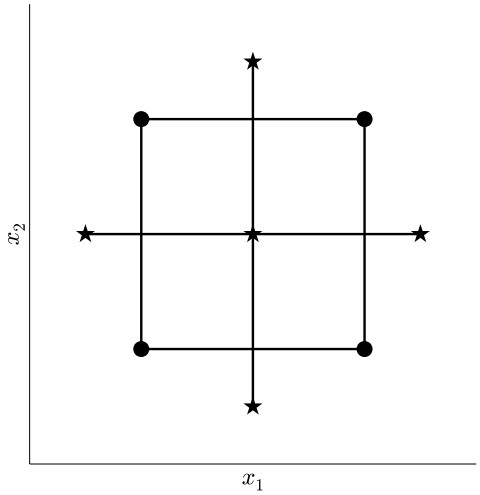

Fig. 5.11 Central Composite design for two design parameters (x_1 and x_2)

Latin Hypercude sampling (LHS) is a statistical method which can be used to create a random sampling of multiple parameters. The number of designs N has to be equal to the number of levels for each design parameters l and greater than the number of the design parameters n as shown in Equation 5.11. Figure 5.12 shows an example of LHS of 9 designs for two parameters with 9 levels. The main advantage of this method is that it allows more levels and more combinations to be included in the design matrix.

$$N = l \geq n + 1 \tag{5.11}$$

Optimal Latin Hypercube sampling (OLHS) is a special LHS where all the design points are equally spaced. This can be clearly seen by comparing Figure 5.12 and Figure 5.13. The disadvantage of OLHS is that it requires more time to generate the design matrix compared to LHS.

To sum up, for some of the methods above, the number of designs needed N is increasing exponentially with the number of design parameters n or the level of design parameters l. For some methods, the levels of design parameters l is restricted to be 2 or 3. Only LHS and OLHS allow the use of a large number of levels l with a reasonable number of design points N. OLHS provides a more

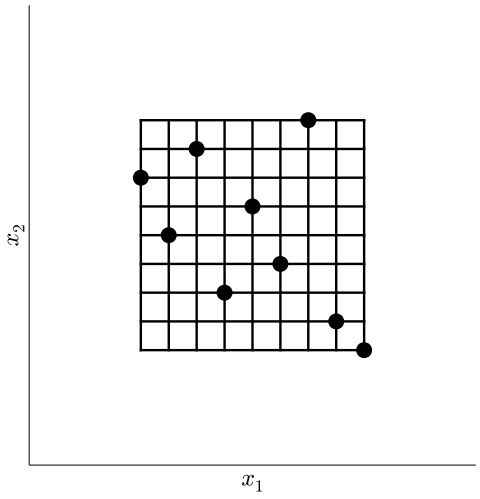

Fig. 5.12 Latin Hypercube sampling for two design parameters (x_1 and x_2)

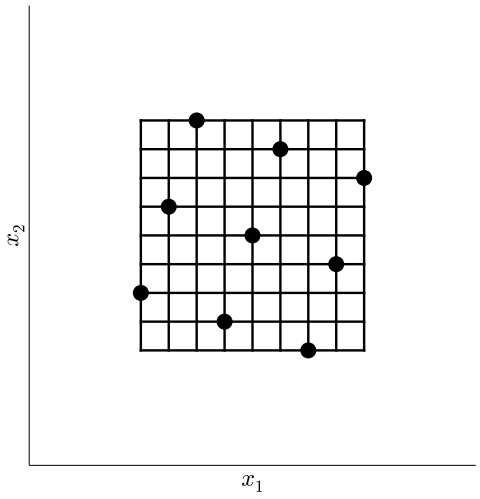

Fig. 5.13 Optimal Latin Hypercube sampling for two design parameters (x_1 and x_2)

uniform sampling of the design space. Therefore, OLHS is selected to generate the design points (matrix) for the linear RSM.

The 25 design points are generated for the 17 design parameters with 25 different levels (the range specified in Table 5.1) using OLHS and allow several designs to diverge and fail to create geometries. Finally 19 designs converge and generate blade geometries using the inverse design method which is sufficient for the linear regression. The design matrix including the design parameters and the performance parameters of all 19 designs is called the linear DOE.

5.3 Comparison of 3D and RFM1 Blades

5.3.1 Stress

As it has been mentioned in subsection 2.1.1, 3D radial turbine blades designed using the inverse design method show 2-3% (validated against numerical and experimental results by Zangeneh-Kazemi [1986]) higher efficiency than the conventional radial fibre design. However, their stress values are much higher than the material strength. An example can be seen in Figure 5.22 where the square symbols denote the stress values for the 19 3D inverse designed blades in the linear DOE. It can be seen that the stress value for most of the 3D blades is greater than 2.0, some designs may reach as high as 4.7. The stress level for the baseline design is only 0.99. To reduce the stress level of the 3D blades, a blade modification method called Radial Filament Modification method 1 (RFM1) is introduced.

Radial Filament Modification method 1 is illustrated in Figure 5.14 which shows the meridional shape of a 3D turbine blade. The LE wrap angle distribution of this 3D blade is expressed using Equation 5.12 and its shroud wrap angle distribution is defined by Equation 5.13. It can be seen that the original shroud wrap angle distribution $f_{shr}^{3D}(z)$ is only defined for $z \in [z_1, z_2]$. It can be extrapolated to get a new function $f_{shr,new}^{3D}(z)$ (Equation 5.14) defined for a wider range $z \in [z_1, z_{max}]$ using high-order polynomial interpolation. An example can be seen in Figure 5.15, where square dots are $f_{shr}^{3D}(z)$ and the solid line is $f_{shr,new}^{3D}(z)$. The wrap angle of the new RFM1 blade $f^{RFM1}(r, z)$ is calculated using Equation 5.15. For the left part of the blade ($z < z_1$) the new RFM1 wrap angle is calculated from $f_{LE}^{3D}(z)$

and for the right part of the blade ($z \geq z_1$) the new RFM1 wrap angle is calculated from $f^{3D}_{shr,new}(z)$. In the inverse design method, the blade LE stacking is specified as 0 which is exactly the LE wrap angle distribution $f^{3D}_{LE}(z)$. Therefore, it is expected that the wrap angle of the left part of the RFM1 blade ($z < z_1$) will be 0.

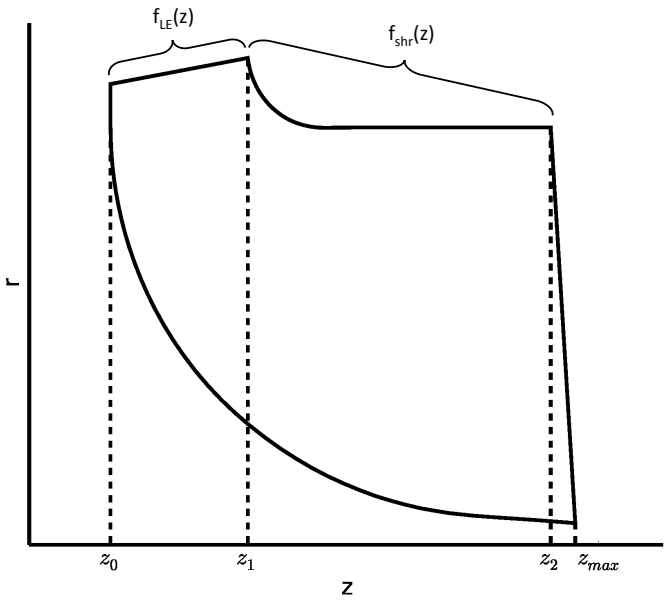

Fig. 5.14 Illustration of Radial Filament Modification method 1

$$f^{3D}_{LE}(z), \quad z \in [z_0, z_1] \tag{5.12}$$

$$f^{3D}_{shr}(z), \quad z \in [z_1, z_2] \tag{5.13}$$

$$f^{3D}_{shr,new}(z), \quad z \in [z_1, z_{max}] \tag{5.14}$$

$$f^{RFM1}(r,z) = \begin{cases} f^{3D}_{LE}(z) & z_0 \leq z < z_1 \\ f^{3D}_{shr,new}(z) & z_1 \leq z \leq z_{max} \end{cases} \tag{5.15}$$

Figure 5.16 shows the wrap angle distribution of one 3D blade from the linear DOE and its RFM1 blade in the hub, mid-span and shroud sections. It can be seen that the 3D blade has very different wrap angles at different spanwise locations

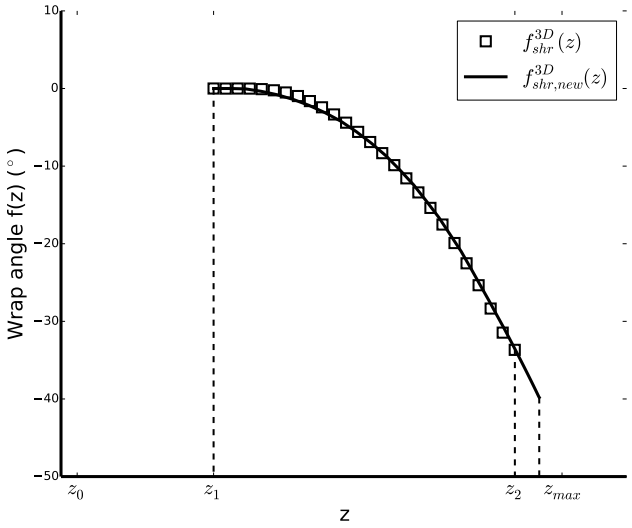

Fig. 5.15 $f^{3D}_{shr}(z)$ and $f^{3D}_{shr,new}(z)$

while RFM1 blade has exactly the same wrap angle at the same axial location (z) for different spanwise locations. The comparison of blade-to-blade view at three different spanwise locations are also shown in Figure 5.17, Figure 5.18 and Figure 5.19. A clear radial filament wrap angle distribution can also be seen in Figure 5.20 for the RFM1 blade which shows the comparison of the wrap angle contours.

A comparison of stress contours of a 3D and a RFM1 blade at a constant axial (z) cross-section is shown in Figure 5.21. When the blade is rotating at very high speed, the very different wrap angles from the hub to the shroud of the 3D blades cause extra centrifugal bending stress on the blade suction surface (red area). There is no such extra bending stress for the RFM1 blade since each part of the blade is supported by the part beneath. To validate this conclusion the static structural analysis is performed for 19 3D blade designs in the linear DOE and their RFM1 blades. The results are compared and shown in Figure 5.22. The stress for the 3D blades is much greater than the baseline value and the material yield strength. The stress value for the RFM1 blades oscillates around the baseline value. Therefore, it can be concluded that RFM1 helps to significantly reduce the stress level compared to the original 3D blade stress.

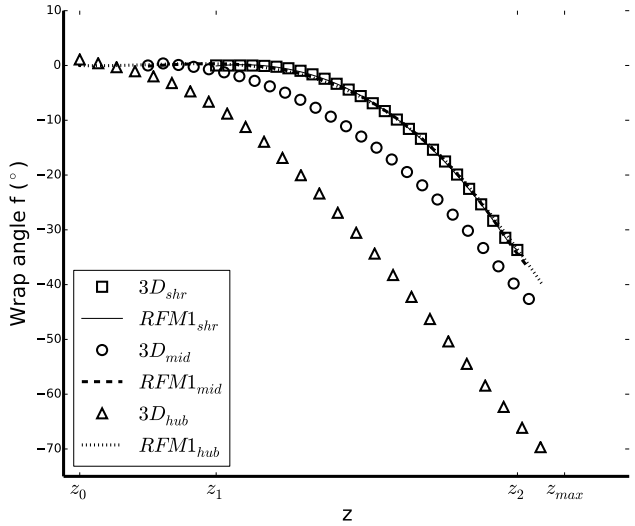

Fig. 5.16 Wrap angle comparison of 3D and RFM1 blades in the hub, mid-span and shroud

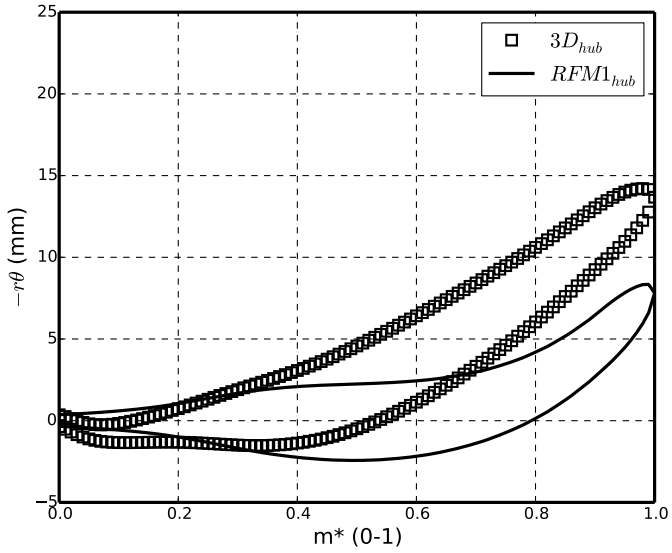

Fig. 5.17 blade-to-blade view comparison of 3D and RFM1 blades in the hub

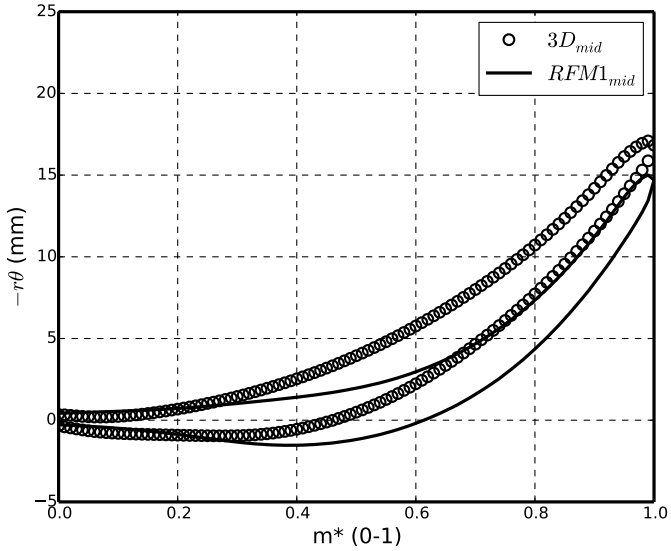

Fig. 5.18 blade-to-blade view comparison of 3D and RFM1 blades in the mid-span

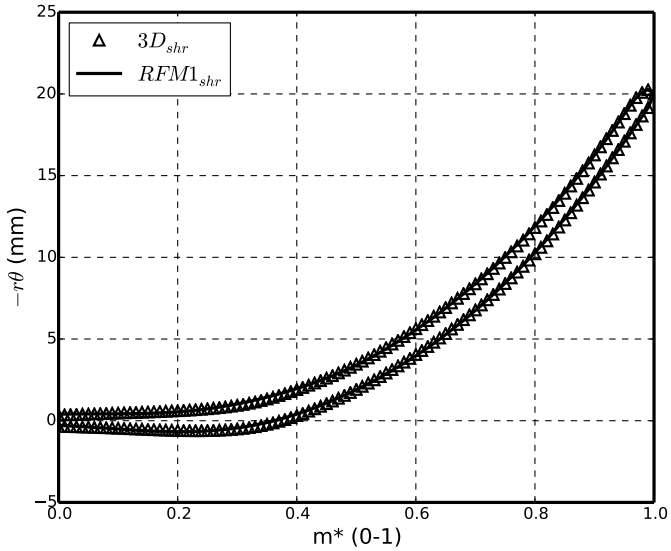

Fig. 5.19 blade-to-blade view comparison of 3D and RFM1 blades in the shroud

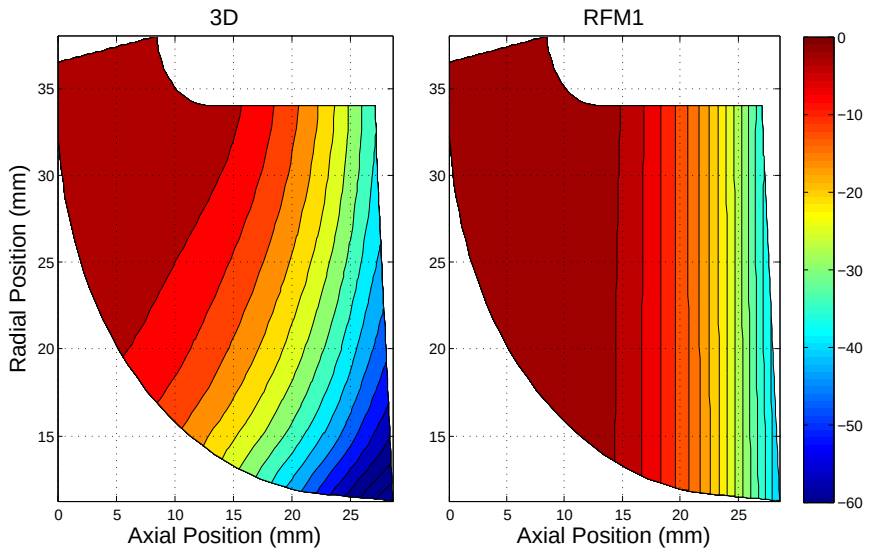

Fig. 5.20 Wrap angle contours of 3D and RFM1 blades

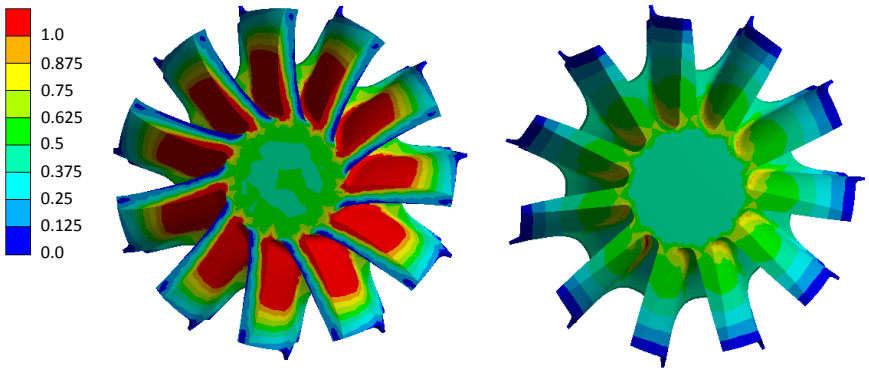

Fig. 5.21 Comparison of stress contours of 3D (left) and RFM1 (right) blades at a constant z cross-section

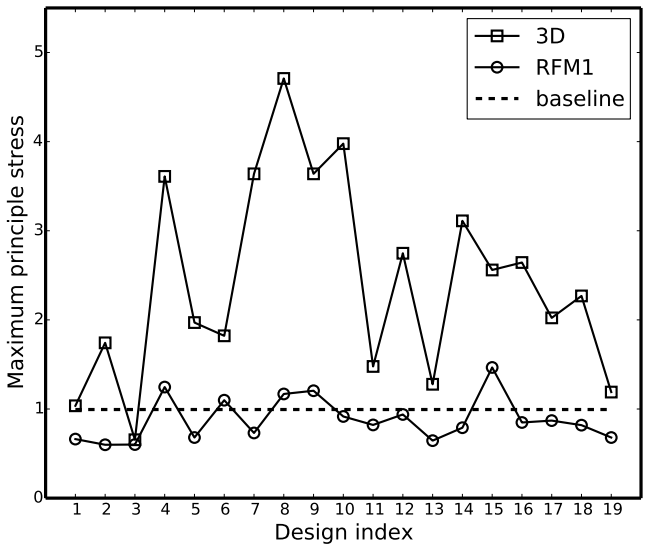

Fig. 5.22 Stress (scaled) comparison of 3D and RFM1 blades

5.3.2 Performance Parameters excluding Stress

The question needs to be raised now is that what is the effect of this Radial Filament Modification on the other turbine performance parameters? For example, will the RFM1 blade be less efficient or less stiff? To answer these questions CFD simulation and modal analysis are performed for 19 3D and RFM1 blades. The results are summarised and compared in Figure 5.23 to Figure 5.35.

Figure 5.23 shows MOI comparison of 3D and RFM1 blades. Since the RFM does not change the turbine meridional shape and the blade normal thickness distribution, 73.7% (14 out of 19) of RFM1 blades have almost the same moment of inertia as 3D blades. Only 5 RFM1 blades (design 4, 8, 9, 10 and 15) have slightly lower moment of inertia compared to the corresponding 3D blades. MOI of most (14 out of 19) RFM1 and 3D blades are reduced significantly compared to the baseline value.

Figure 5.24 and Figure 5.25 show 1^{st} and 2^{nd} mode vibration frequency comparison of 3D and RFM1 blade. Around 52.6% (10 out of 19) of RFM1 blades have same or higher 1^{st} mode frequency and 47.4% (9 out of 19) of RFM1 blade have same or higher 2^{nd} mode frequency compared to 3D blades. Around 89.5% (17 out of

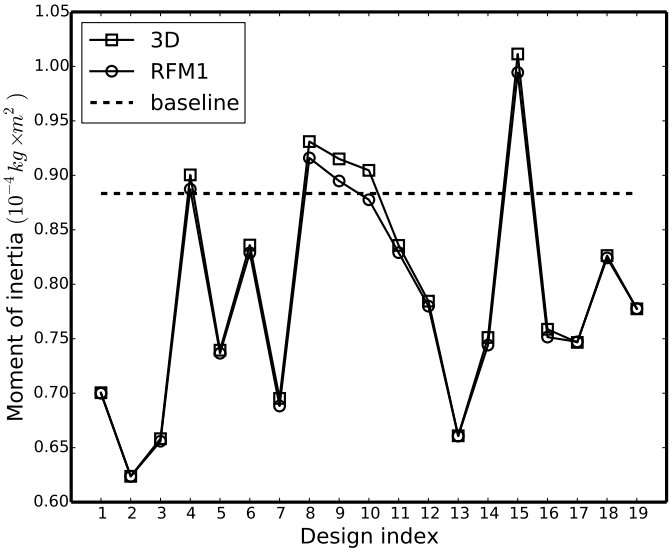

Fig. 5.23 Moment of inertia comparison of 3D and RFM1 blades

19) of RFM1 blades have higher 1^{st} mode frequency and 68.4% (13 out of 19) of RFM1 blades have higher 2^{nd} mode frequency compared to the baseline.

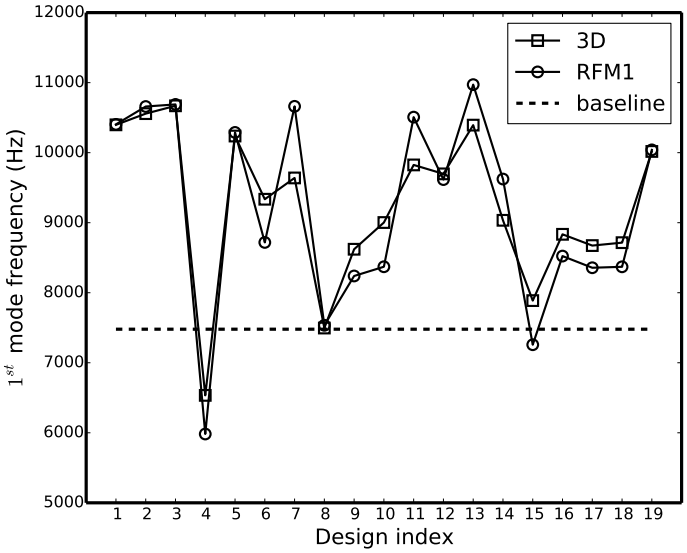

Fig. 5.24 1^{st} mode vibration frequency comparison of 3D and RFM1 blades

Figure 5.26 to Figure 5.30 show the t-s efficiency comparison of 3D and RFM1 blades for different turbine rotating speeds. Around 47.4% - 63.2% of RFM1

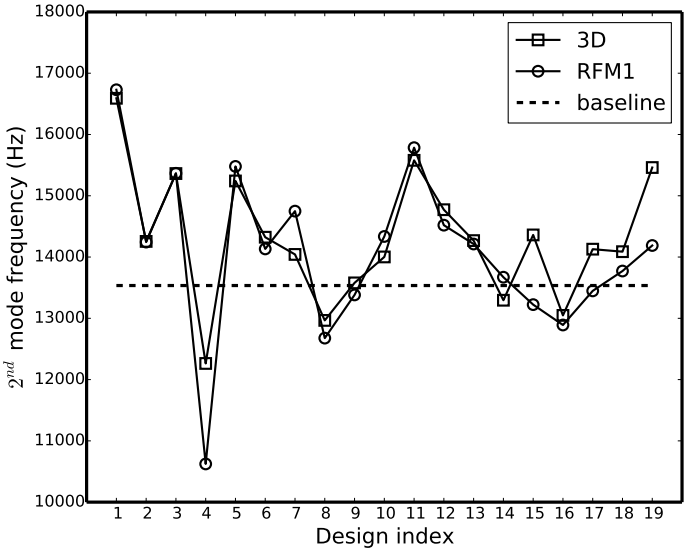

Fig. 5.25 2^{nd} mode vibration frequency comparison of 3D and RFM1 blades

blades have same or higher efficiencies for different RPM compared to 3D blades. It should be noted that at lower RPM (50k, 60k and 70k) the efficiencies of most (84.2% - 89.5%) 3D and RFM1 blades are lower than the baseline value while at higher RPM (80k and 90k) the efficiencies of 57.9% - 68.4% of 3D and RFM1 blades are higher than the baseline. It shows that the efficiencies at the lower RPM of most designs in the linear DOE are not improved compared to the baseline design.

Figure 5.31 to Figure 5.35 show the mass flow parameter comparison of 3D and RFM1 blades for different turbine rotating speeds. Almost all the RFM1 blades have the same MFP at different RPM as 3D blades and the values of MFP are evenly distributed along the baseline value.

To sum up, it can be concluded that Radial Filament Modification method 1 can reduce the maximum blade stress of 3D blades generated by the inverse design method and does not necessarily sacrifice the aerodynamic and other mechanical performance.

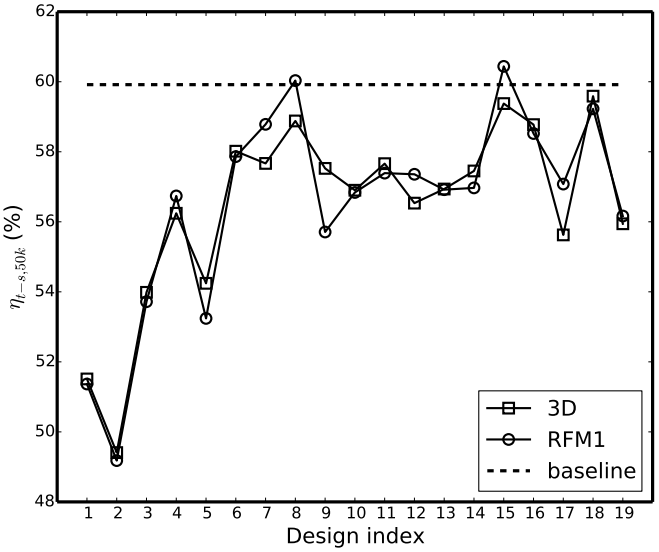

Fig. 5.26 $\eta_{t-s,50k}$ comparison of 3D and RFM1 blades

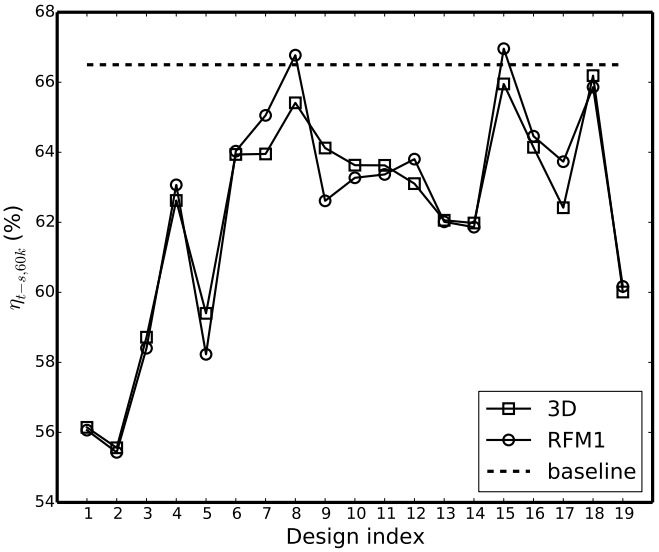

Fig. 5.27 $\eta_{t-s,60k}$ comparison of 3D and RFM1 blades

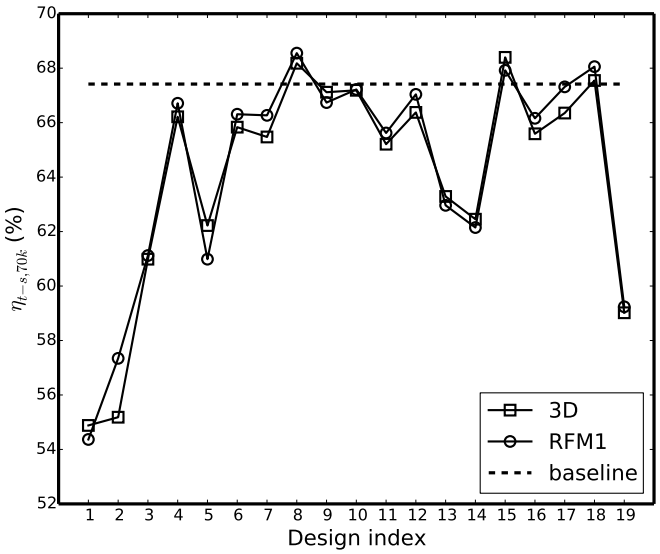

Fig. 5.28 $\eta_{t-s,70k}$ comparison of 3D and RFM1 blades

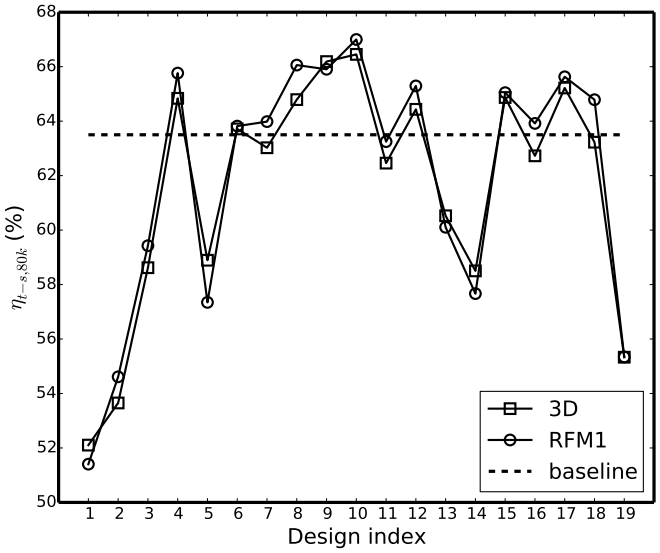

Fig. 5.29 $\eta_{t-s,80k}$ comparison of 3D and RFM1 blades

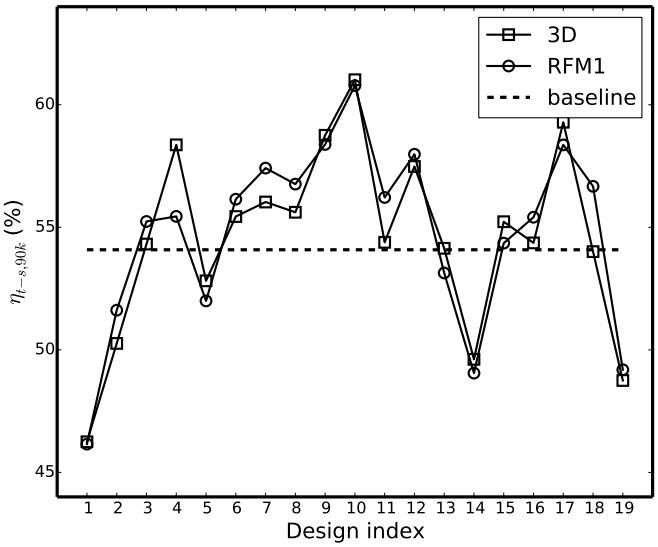

Fig. 5.30 $\eta_{t-s,90k}$ comparison of 3D and RFM1 blades

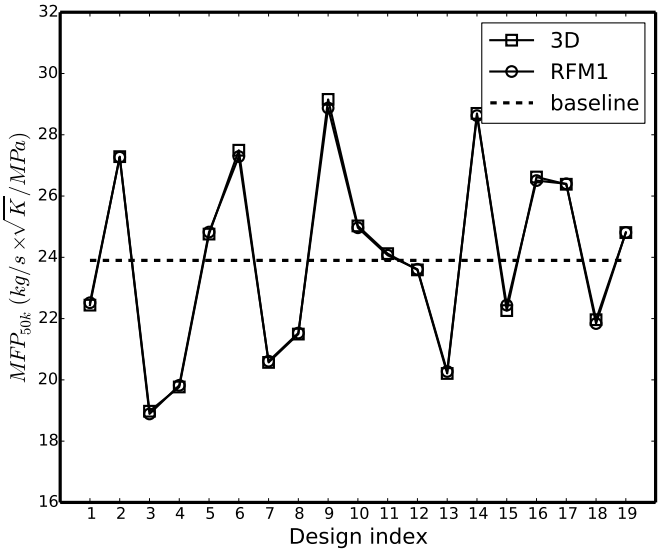

Fig. 5.31 MFP_{50k} comparison of 3D and RFM1 blades

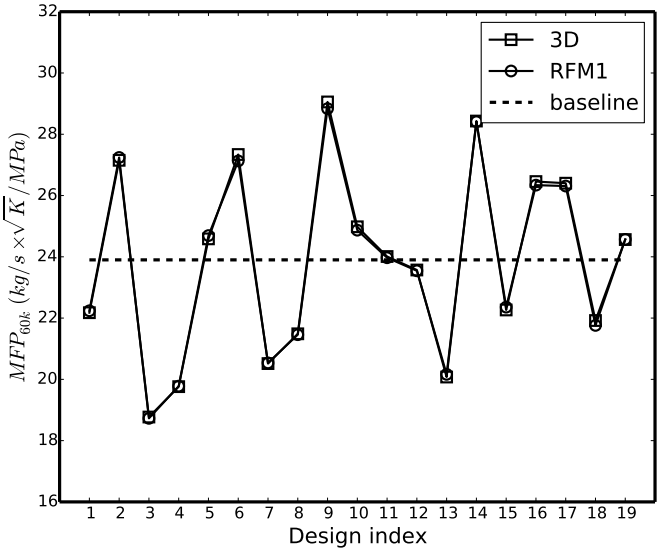

Fig. 5.32 MFP_{60k} (scaled) comparison of 3D and RFM1 blades

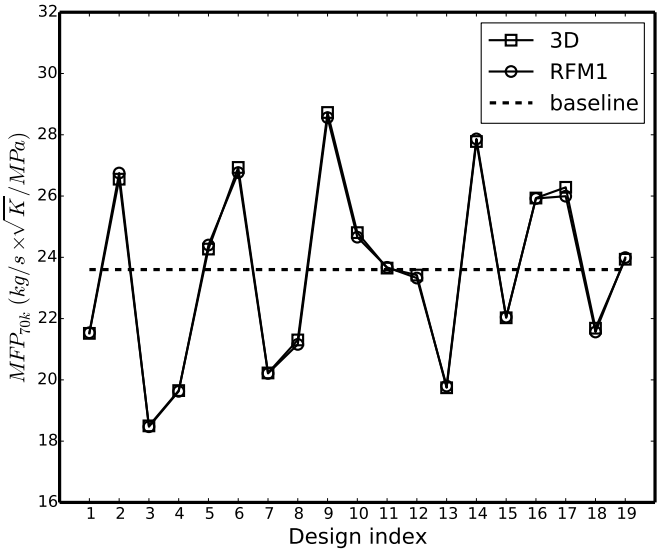

Fig. 5.33 MFP_{70k} comparison of 3D and RFM1 blades

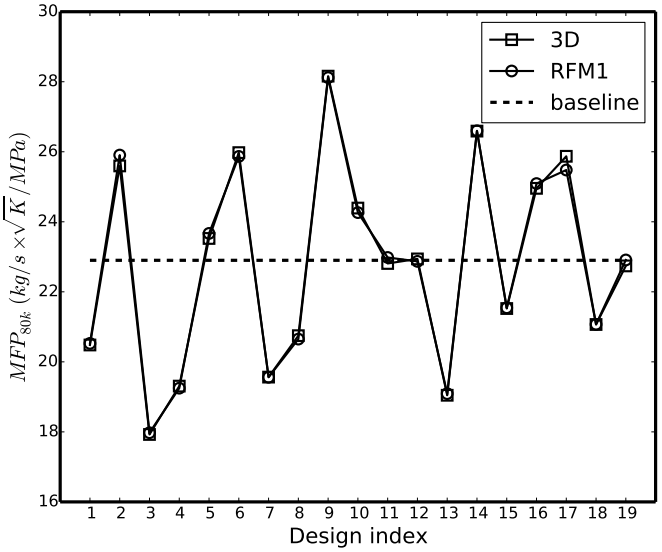

Fig. 5.34 MFP_{80k} comparison of 3D and RFM1 blades

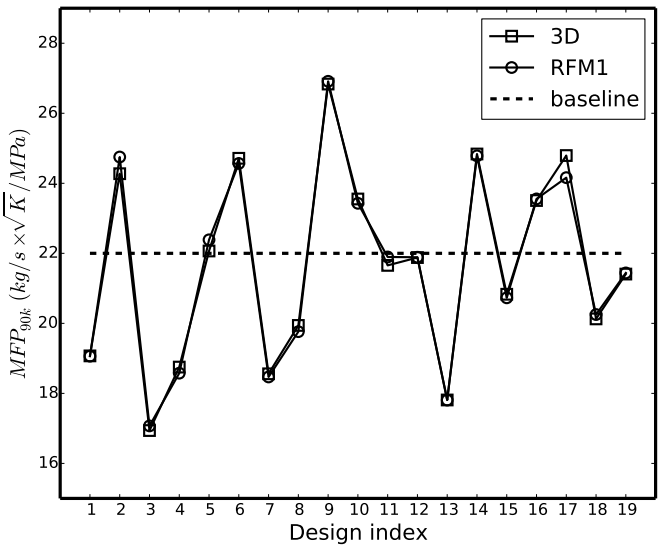

Fig. 5.35 MFP_{90k} comparison of 3D and RFM1 blades

5.4 Reduction of the Number of Design Parameters

To reduce the number of design parameters ($n = 17$), a sensitivity analysis is performed by comparing the value of normalised polynomial coefficients ($\hat{a}_i^j$) which is shown in Equation 5.16. Equation 5.16 is very similar to Equation 5.6. However, x_i^j and y_j are normalised to the range of 0 - 1 corresponding the minimum and maximum values in Equation 5.16 and the polynomial coefficient a_i^j become normalised $\hat{a}_i^j$. The normalised $\hat{x}_i^j$ and $\hat{y}_j$ can be calculated using Equation 5.17.

$$\hat{y}_j = \hat{a}_0^j + \sum_{i=1}^{n} \hat{a}_i^j \hat{x}_i^j \tag{5.16}$$

$$\begin{cases} \hat{x}_i^j = \frac{x_i^j - \min\left(x_i^j\right)}{\max\left(x_i^j\right) - \min\left(x_i^j\right)} \\ \hat{y}_j = \frac{y_j - \min\left(y_j\right)}{\max\left(y_j\right) - \min\left(y_j\right)} \end{cases} \tag{5.17}$$

Equation 5.16 can be rewritten in the form of a matrix as Equation 5.18, where j indicates different performance parameters and $1 \leq j \leq 14$, $\hat{Y}_j$ is a matrix of 1×19 , $\hat{A}^j$ is a matrix of 1×18 and $\hat{X}^j$ is a matrix of 18×19 and the first row values are always 1.

$$\hat{Y}_j = \hat{A}^j \hat{X}^j \tag{5.18}$$

From previous two subsections the values of design parameters (x_i^j) and performance parameters (y_j) of 19 RFM1 blade designs are known through CFD and FEA calculations and then $\hat{X}^j$ and $\hat{Y}_j$ can be calculated using Equation 5.17. By substituting $\hat{X}^j$ and $\hat{Y}_j$ into Equation 5.18 and using a standard least-square regression, the normalised coefficient matrix $\hat{A}^j$ for different performance parameters can be obtained.

A sensitivity analysis is then performed by comparing the normalised coefficients $\tilde{A}_i^j$ defined in Equation 5.19. The comparison of the normalised coefficients $\tilde{A}_i^j$ is

shown in Table 5.3.

$$\tilde{A}_i^j = \frac{\hat{a}_i^j}{\max\left(\left|\hat{a}_i^j\right|\right)} \times 100 \tag{5.19}$$

The range of $\tilde{A}_i^j$ is from -100 to 100. For a particular performance parameter y_j (j is constant), the greater the absolute value of $\tilde{A}_i^j$ is, the more significant the corresponding design parameter x_i is. When $\tilde{A}_i^j$ is greater than 0, it means the performance parameter y_j increases with the increasing of this design parameter x_i. When $\tilde{A}_i^j$ is less than 0, it means the performance parameter y_j decreases with the increasing of the design parameter x_i.

For MFP_{50k}, MFP_{60k}, MFP_{70k}, MFP_{80k} and MFP_{90k}, the most significant parameter is W_1 since the values of $\tilde{A}_i^j$ are 100. It can be easily understood by looking at Figure 5.2 and the increasing of W_1 results in the increase of the nozzle throat area and more flow can enter the nozzle. Therefore, the flow capacity of the turbine is improved. For the 1^{st} and 2^{nd} frequency, if W_2 which is the blade exducer height is increased the blade will become higher. Therefore, the blade stiffness is reduced and 1^{st} and 2^{nd} frequency will drop (the corresponding $\tilde{A}_i^j$ are -100). Similarly for the MOI, increasing of W_2 and Y_{hub} increases the blade inertia and the wheel hub inertia. Therefore, the total MOI will increase. This explains that $\tilde{A}_i^j$ of W_2 and Y_{hub} have the largest absolute values (100 and 45) for the performance parameter MOI. For the efficiencies, the most significant parameter is W_2 since increasing W_2 will significantly reduce the turbine exit kinetic energy loss.

The most significant design parameters are selected based on the summation of all the absolute values of $\tilde{A}_i^j$ as shown in Figure 5.36. The number of the significant parameters selected is directly related to the size (or the dimension) of the design space and the computational cost. The larger this number is, the more likely the optimal design can be found while more sampling points and computational resource are needed. Therefore, the 8 most significant design parameters are selected which are α_1, NC_h, ND_h, $RVT_{TE,s}$, $SLOPE_s$, W_1, W_2 and Y_h (highlighted in grey in Table 5.3 and Figure 5.36). The variation of these 8 design parameters have much larger effect on the performance parameters compared to the other design parameters. Different weighting numbers can be applied for different performance parameters during this summation process and

Table 5.3 Comparison of normalised coefficients $\tilde{A}_i^j$ (most significant parameters highlighted)

		x_1	x_2	x_3	x_4	x_5	x_6	x_7	x_8	x_9	x_{10}	x_{11}	x_{12}	x_{13}	x_{14}	x_{15}	x_{16}	x_{17}
		α_1	α_2	$DRVT_{LE,h}$	$DRVT_{LE,s}$	NC_h	NC_s	ND_h	ND_s	$RVT_{TE,h}$	$RVT_{TE,s}$	$SLOPE_h$	$SLOPE_s$	Th	W_1	W_2	Y_h	Y_s
y_1	$\eta_{t-s,50k}$	-2	-1	16	0	80	-3	-34	14	-9	-49	-36	43	-14	-17	100	-64	2
y_2	$\eta_{t-s,60k}$	20	5	0	-4	49	-11	-30	15	-16	-34	-11	36	-5	-10	100	-53	-19
y_3	$\eta_{t-s,70k}$	64	-5	-6	-6	52	-10	-30	21	-16	-34	-15	31	-3	-4	100	-53	-15
y_4	$\eta_{t-s,80k}$	95	6	-17	-4	52	-18	-50	27	-27	-40	-4	35	-8	-10	100	-57	-20
y_5	$\eta_{t-s,90k}$	100	1	-22	-5	48	-25	-31	26	-19	-34	2	33	-1	-6	73	-42	-25
y_6	MFP_{50k}	-17	-8	9	6	9	10	11	-10	7	-2	-16	-3	0	100	-3	2	11
y_7	MFP_{60k}	-16	-8	8	5	9	9	11	-9	7	-2	-15	-3	1	100	-1	2	10
y_8	MFP_{70k}	-12	-10	8	4	10	8	12	-8	6	-2	-16	-3	1	100	3	1	10
y_9	MFP_{80k}	-5	-10	5	3	11	5	10	-6	4	-3	-13	-2	2	100	11	0	8
y_{10}	MFP_{90k}	-4	-13	4	2	9	3	16	-8	6	0	-13	-3	5	100	19	5	7
y_{11}	$Stress$	51	26	-28	-20	-6	-12	-74	25	-27	-24	17	17	8	-7	100	-17	-16
y_{12}	$1^{st}freq$	5	-11	-17	-36	19	-27	8	8	-8	21	7	32	28	8	-100	-8	-24
y_{13}	$2^{nd}freq$	23	15	2	-10	39	14	33	-6	-11	-4	-39	47	69	31	-100	29	-13
y_{14}	MOI	-28	-9	3	6	-6	6	0	-7	6	-1	-2	-2	25	-4	100	45	19
	$Summation$	442	128	145	111	399	161	350	190	169	247	206	290	170	597	910	378	199

this will result in different collections of most significant design parameters. In this study the weighting numbers for different performance parameters are assumed to be identical.

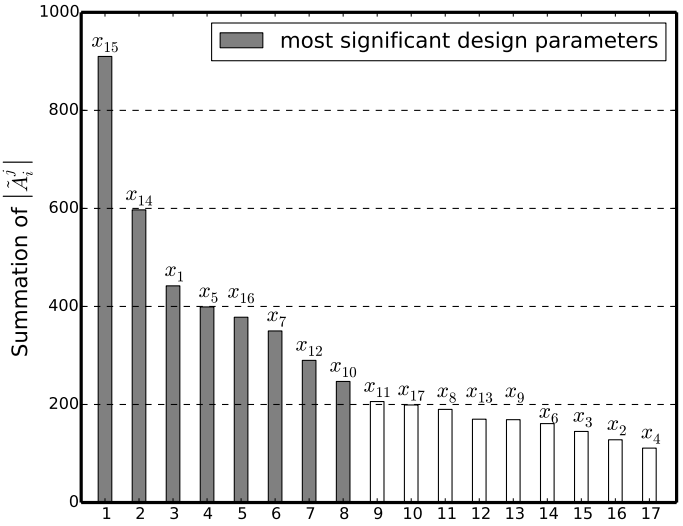

Fig. 5.36 Most significant design parameters selected based on the summation of $\left|\tilde{A}_i^j\right|$

In this subsection, the number of design parameters has been successfully reduced from 17 to 8 by a sensitivity analysis based on the linear DOE results. A more accurate approximation method (Kriging) will be used for these new 8 design parameters and MOGA will be used to search the design space to obtain the optimal design which meets multiple objectives and constraints in the following subsections.

5.5 Kriging Approximation

Three basic assumptions for the implementation of Kriging approximation are shown as following:

1) Assume M design points $(\vec{x}_1, y_1)$, $\cdots$, $(\vec{x}_M, y_M)$ are known, where $\vec{x}_i$ is a N-dimensional design parameter vector and y_i is the response parameter. Design parameters can be written in the form of a $N \times 1$ vector using

Equation 5.20. The response parameter can be written in the from of a $M \times 1$ vector using Equation 5.21;

$$\vec{x}_i = (x_{i,1}, \cdots, x_{i,N}) \quad i \in [1, M] \tag{5.20}$$

$$\vec{y}_s = (y_1, \cdots, y_M) \tag{5.21}$$

2) A regression model $Y(\vec{\beta}, \vec{x})$ which is a linear combination of basis functions $f_1, \cdots, f_M$ is used (see Equation 5.22). The $\vec{f}(\vec{x})$ is assumed to be a column vector of length M which is filled with ones ($\vec{f}(\vec{x}) = \vec{1}$);

$$Y\left(\vec{\beta}, \vec{x}\right) \simeq \beta_1 f_1(\vec{x}) + \cdots + \beta_M f_M(\vec{x}) = \vec{\beta}\vec{f}(\vec{x}) \tag{5.22}$$

3) A correlation function $R(\vec{x}_i, \vec{x}_j)$ is defined by Equation 5.23. The $R(\vec{x}_i, \vec{x}_j) \in (0, 1]$ is the correlation between the responses at $\vec{x}_i$ and $\vec{x}_j$. In the case of $\vec{x}_i = \vec{x}_j$, they are the same point in the design space with the same response. Therefore, their responses have the strongest correlation and $R(\vec{x}_i, \vec{x}_j) = 1$. When the distance between two points $\vec{x}_i$ and $\vec{x}_j$ is far enough, their correlation function will be close to 0.

$$R(\vec{x}_i, \vec{x}_j) = exp\left(-\sum_{k=1}^{N} \theta_k |x_{i,k} - x_{j,k}|^{p_k}\right) \quad i, j \in [1, M], k \in [1, N] \tag{5.23}$$

The correlation function can be written in the form of $M \times M$ symmetrical matrix R and its each element R_{ij} is calculated by Equation 5.24. In most cases matrix R is ill conditioned and may generate numerical instability. A regularisation matrix λI is added to improve the numerical stability and get a regularised correlation matrix $\widehat{R}$ as shown in Equation 5.25, where λ is a constant greater than 0 and I is a $M \times M$ unit matrix. The $\vec{r}(\vec{x})$ is the correlation vector between $\vec{x}$ and all sampling points $\vec{x}_i$ which is defined by Equation 5.26. The prediction function $\widehat{y}(\vec{x})$ for an unknown point $\vec{x}$ is given by Equation 5.27, where β^* is estimated using the generalised least squares method in Equation 5.28.

$$R_{ij} = R(\vec{x}_i, \vec{x}_j) \quad i, j \in [1, M] \tag{5.24}$$

$$\widehat{R} = R + \lambda I \quad \lambda > 0 \tag{5.25}$$

$$\vec{r}(\vec{x}) = \left[\widehat{R}(\vec{x}, \vec{x}_1), \widehat{R}(\vec{x}, \vec{x}_2), \cdots, \widehat{R}(\vec{x}, \vec{x}_M)\right] \tag{5.26}$$

$$\widehat{y}\left(\vec{x}\right) = \beta^* + \vec{r}^T\left(\vec{x}\right)\widehat{R}^{-1}\left(\vec{y}_s - \beta^*\vec{1}\right) \tag{5.27}$$

$$\beta^* = \frac{\vec{1}^T\widehat{R}^{-1}\vec{y}_s}{\vec{1}^T\widehat{R}^{-1}\vec{1}} \tag{5.28}$$

It is noted that β^*, $\vec{r}(\vec{x})$, $\widehat{R}$ are all functions of λ, θ_k and p_k. The values of λ, θ_k and p_k are obtained by maximising the likelihood function (Equation 5.29) or minimising Equation 5.30 over the interval $\lambda > 0$, $\theta_k > 0$ and $p_k > 0$. Both of them are equivalent. The global model variance σ^2 is defined by Equation 5.31. The mean squared error of the prediction $s^2\left(\vec{x}\right)$ is given by Equation 5.32. Since there are $2N + 1$ unknown parameters (λ, θ_k and p_k) in total, the number of sampling points M has to be $\geq 2N + 1$ to determine all λ, θ_k and p_k.

$$-\frac{1}{2}\left(M\ln\sigma^2 + \ln\left|\widehat{R}\right|\right) \tag{5.29}$$

$$\sigma^2\left|\widehat{R}\right|^{1/M} \tag{5.30}$$

$$\sigma^2 = \frac{1}{M}\left(\vec{y}_s - \beta^*\vec{1}\right)^T\widehat{R}^{-1}\left(\vec{y}_s - \beta^*\vec{1}\right) \tag{5.31}$$

$$s^2\left(\vec{x}\right) = \sigma^2\left[1 - \vec{r}^T\left(\vec{x}\right)\widehat{R}^{-1}\vec{r}\left(\vec{x}\right) + \frac{\left(1 - \vec{1}^T\widehat{R}^{-1}\vec{r}\left(\vec{x}\right)\right)^2}{\vec{1}^T\widehat{R}^{-1}\vec{1}}\right] \tag{5.32}$$

The accuracy of the Kriging RSM is directly related to the number of the sampling points and the sampling method. The more points are used to build the Kriging RSM, the more accurate the model will be. In total 60 designs are generated by the OLHS method for the 8 new selected design parameters whose ranges are shown in Table 5.4. The values of other design parameters are set as medial value or same as the baseline value since they have little effect on the performance parameters. The 53 of 60 designs converge and generate blade geometries using the inverse design method. Radial Filament Modification method 1 is performed for these 53 blade geometries to get RFM1 blades. CFD and FEA calculations are run for these 53 new RFM1 blades and their performance parameter ranges are shown in Table 5.5. CFD and FEA results of these 53 designs are shown in Figure 5.37 to Figure 5.50.

A Kriging RSM then can be constructed using the design and performance parameters of these 53 designs. The performance parameters of any new designs

Table 5.4 Ranges of design parameters for Kriging DOE

Design Parameters	min	max
α_1 (°)	0	28
NC_{hub}	0.05	0.18
ND_{hub}	0.6	0.85
$r\bar{V}_{\theta TE,shr}$	0.06	0.1
$SLOPE_{shr}$	-5	-1
W_1 (mm)	7	11
W_2 (mm)	15	23.7
Y_{hub} (mm)	16.5	21

Table 5.5 Ranges and baseline value of performance parameters for Kriging DOE

Performance Parameters	min	max	baseline
$\eta_{t-s,50k}$ (%)	49.8	61.3	59.9
$\eta_{t-s,60k}$ (%)	53.6	66.9	66.5
$\eta_{t-s,70k}$ (%)	52.8	69.1	67.4
$\eta_{t-s,80k}$ (%)	49.3	69.0	63.3
$\eta_{t-s,90k}$ (%)	43.1	63.3	54.7
MFP_{50k} $(kg/s \cdot \sqrt{K}/MPa)$	19.7	29.3	23.9
MFP_{60k} $(kg/s \cdot \sqrt{K}/MPa)$	19.6	28.9	23.9
MFP_{70k} $(kg/s \cdot \sqrt{K}/MPa)$	19.4	28.4	23.6
MFP_{80k} $(kg/s \cdot \sqrt{K}/MPa)$	19.0	27.4	22.9
MFP_{90k} $(kg/s \cdot \sqrt{K}/MPa)$	18.0	26.3	22.0
$Stress$ (scaled)	0.61	1.81	0.99
$1^{st} freq$ (Hz)	5419	12318	7479
$2^{nd} freq$ (Hz)	9514	16257	13535
MOI $(\times 10^{-4} kg \cdot m^2)$	0.6167	1.0000	0.8834

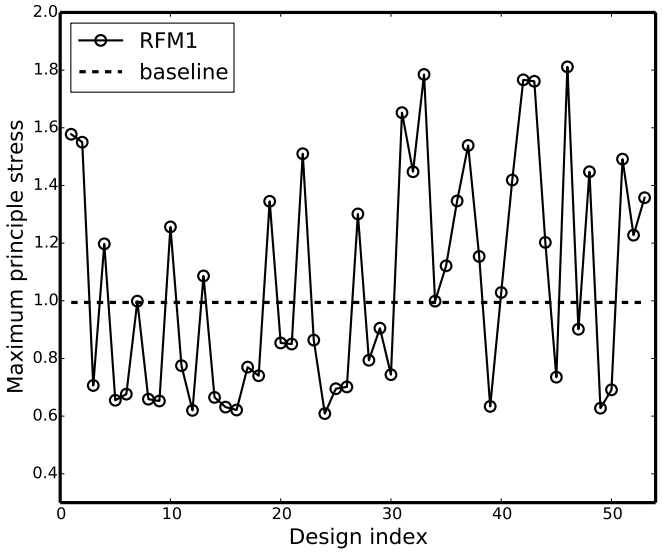

Fig. 5.37 Stress (scaled) comparison of RFM1 blades and baseline for Kriging DOE

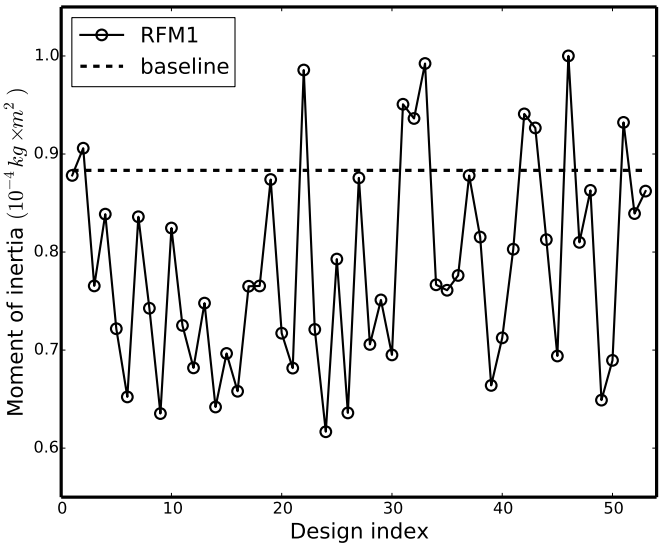

Fig. 5.38 Moment of inertia comparison of RFM1 blades and baseline for Kriging DOE

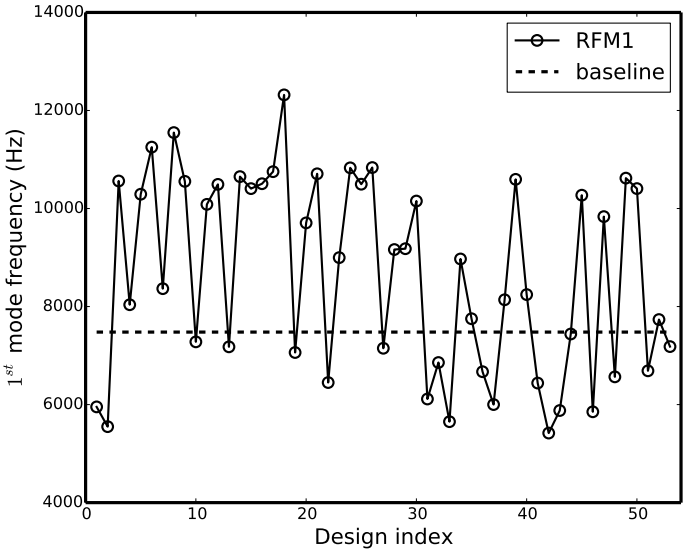

Fig. 5.39 1^{st} vibration mode frequency comparison of RFM1 blades and baseline for Kriging DOE

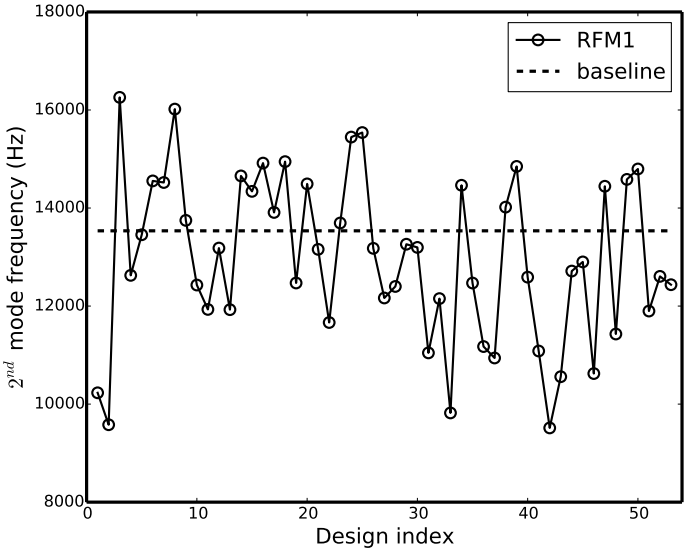

Fig. 5.40 2^{nd} vibration mode frequency comparison of RFM1 blades and baseline for Kriging DOE

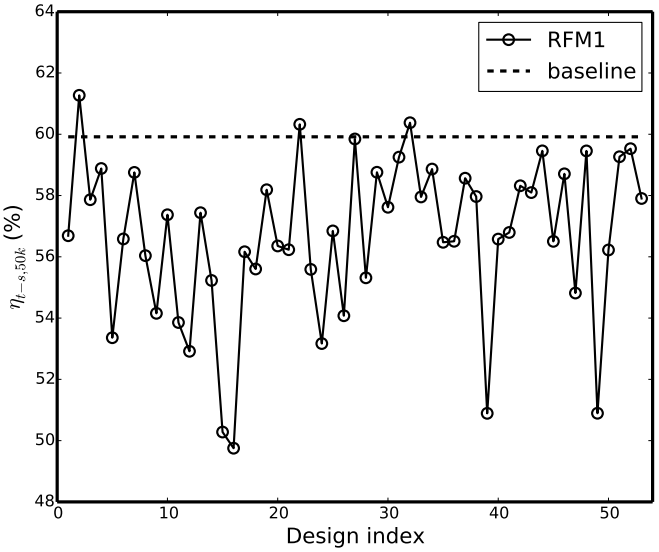

Fig. 5.41 $\eta_{t-s,50k}$ comparison of RFM1 blades and baseline for Kriging DOE

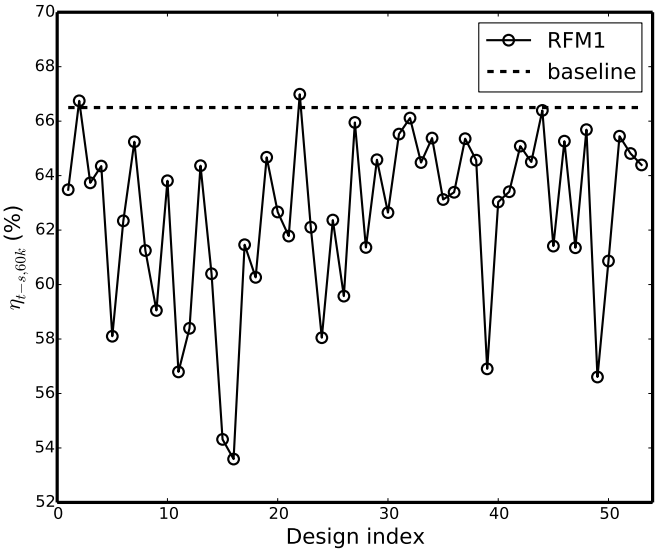

Fig. 5.42 $\eta_{t-s,60k}$ comparison of RFM1 blades and baseline for Kriging DOE

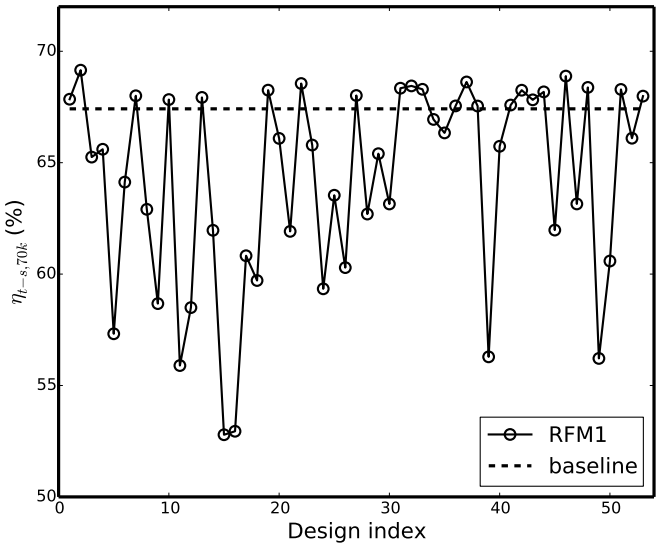

Fig. 5.43 $\eta_{t-s,70k}$ comparison of RFM1 blades and baseline for Kriging DOE

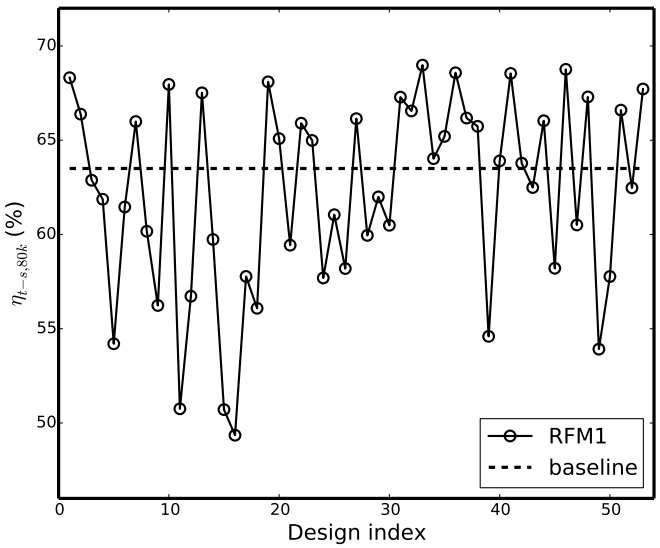

Fig. 5.44 $\eta_{t-s,80k}$ comparison of RFM1 blades and baseline for Kriging DOE

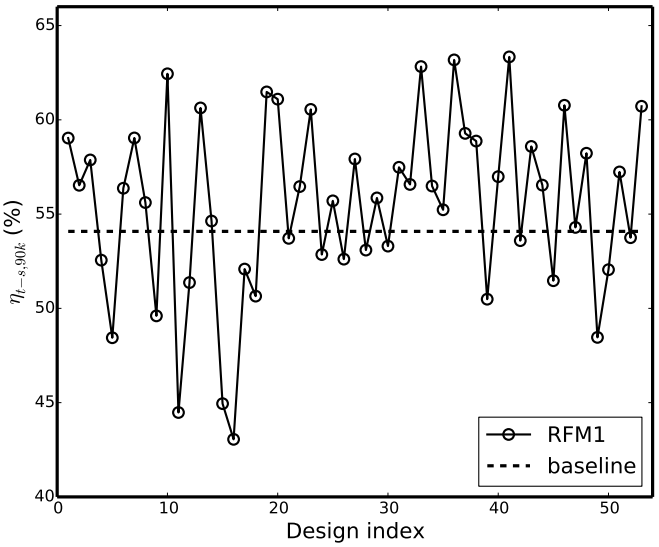

Fig. 5.45 $\eta_{t-s,90k}$ comparison of RFM1 blades and baseline for Kriging DOE

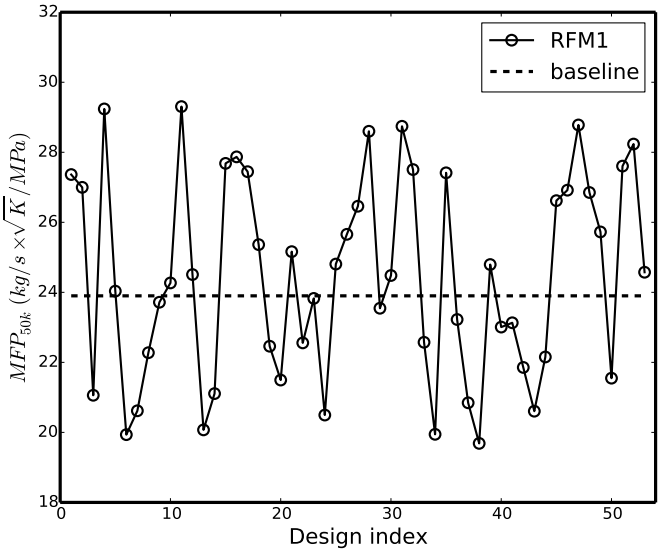

Fig. 5.46 MFP_{50k} comparison of RFM1 blades and baseline for Kriging DOE

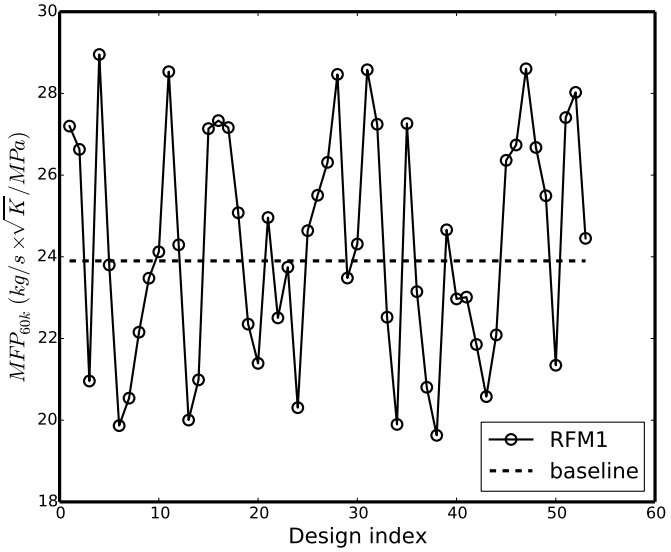

Fig. 5.47 MFP_{60k} comparison of RFM1 blades and baseline for Kriging DOE

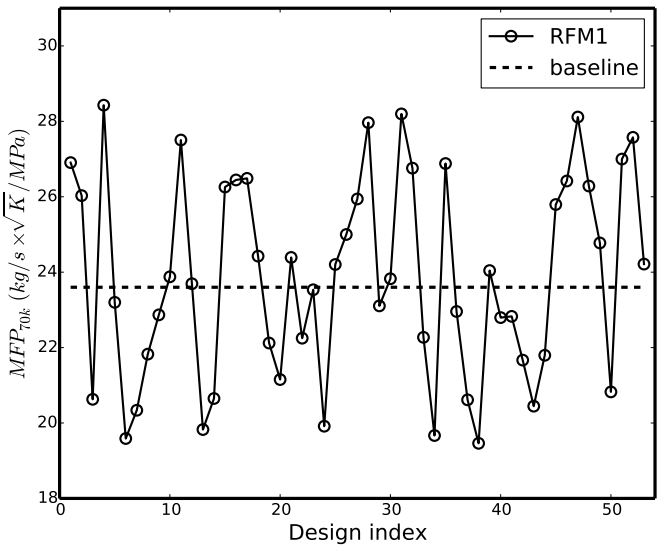

Fig. 5.48 MFP_{70k} comparison of RFM1 blades and baseline for Kriging DOE

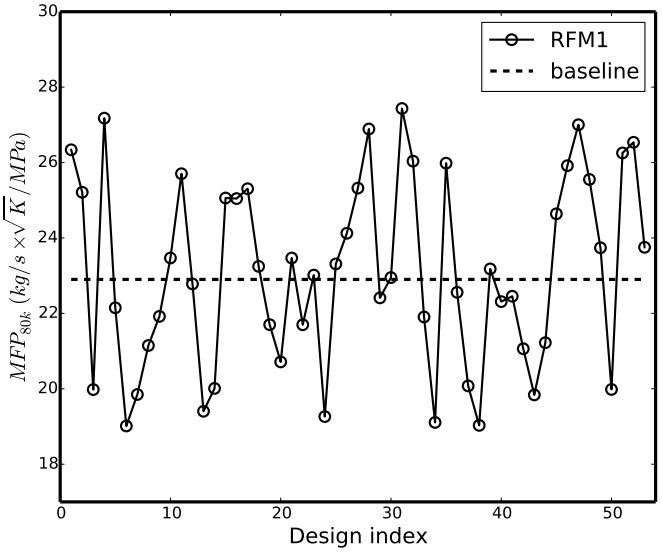

Fig. 5.49 MFP_{80k} comparison of RFM1 blades and baseline for Kriging DOE

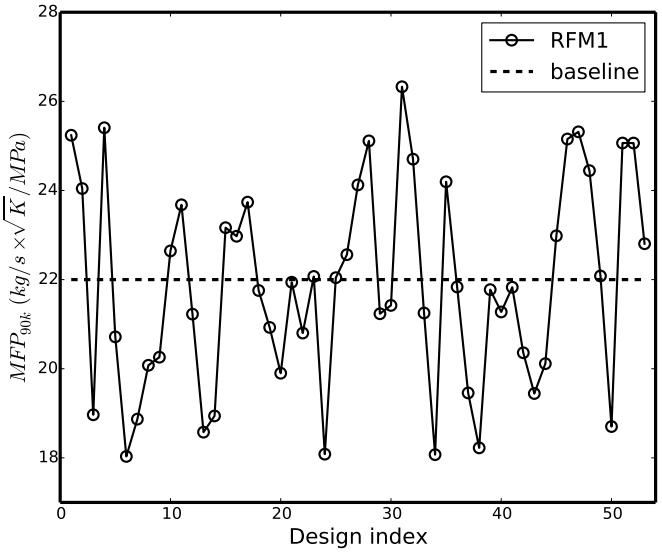

Fig. 5.50 MFP_{90k} comparison of RFM1 blades and baseline for Kriging DOE

in the optimisation shown in the next subsection can be evaluated quickly through the Kriging RSM instead of the expensive CFD and FEA simulation.

5.6 Optimisation 1 Using MOGA

NSGA-II (Non-dominated Sorting Genetic Algorithm-II) is a multi-objective genetic algorithm (MOGA) which was first proposed by Deb et al. [2000]. It is well-suited for highly non-linear design spaces. Each objective is treated separately and a Pareto front is constructed by selecting feasible non-dominated designs.

The ranges of design parameters are the same as they are in Table 5.4. The constraints and objectives of Optimisation 1 are summarised in Table 5.6 and Table 5.7. The constraints are chosen based on the consideration that all the performance parameters of the optimal design have to be improved compared to the baseline value. Objectives are maximising $\eta_{t-s,70k}$ and minimising Stress.

Table 5.6 Constraints of Optimisation 1

	Constraints
$\eta_{t-s,50k}$	> 0.599
$\eta_{t-s,60k}$	> 0.665
$\eta_{t-s,80k}$	> 0.633
$\eta_{t-s,90k}$	> 0.547
MFP_{50k}	> 23.3
$1^{st}freq$	> 7479
$2^{nd}freq$	> 13535
MOI	$< 8.8342 \times 10^{-5}$

Table 5.7 Objectives of Optimisation 1

	Objectives
$\eta_{t-s,70k}$	Maximise
Stress	Minimise

NSGA-II is then used to search the design space based on the constraints and objectives specified above. The performance parameters are evaluated through the Kriging approximation model which is much faster compared to the time consuming CFD and FEA simulations. The population size is set as 100 and the number of generations is set as 120. In total 12,000 designs are generated and their aerodynamic and mechanical performance values can be evaluated in 10 minutes. The flow chart of MOGA optimisation based on RSM is shown in Figure 5.51. A Pareto front is plotted in Figure 5.52 and a trade-off between $\eta_{t-s,70k}$ and Stress can clearly be seen. Three optimal designs along the Pareto front are selected and their CFD and FEA results will be used to validate the Kriging approximation model in the next subsection.

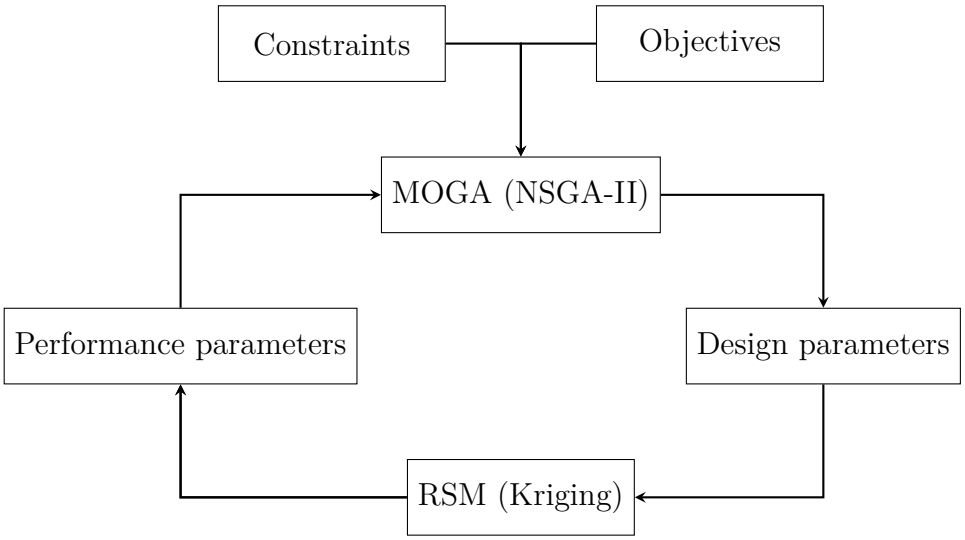

Fig. 5.51 The flow chart of MOGA optimisation based on RSM

Kriging in Figure 5.51 is replaced by quadratic polynomial and RBF approximation. The optimisation is repeated using the same data, same objectives and constraints. 2D scatter plots of $\eta_{t-s,70k}$ versus Stress are shown in Figure 5.53 and Figure 5.54. A Pareto front can be obtained for the quadratic polynomial approximation. However, the range of $\eta_{t-s,70k}$ is between 69.7% and 71.7% which seems overestimated, since the maximum value of $\eta_{t-s,70k}$ in the Kriging DOE (Figure 5.43) is only 68.7%. For the RBF model, no feasible design is found using MOGA. The possible reason is that the optimisation is over-constrained for the RBF model. On the other hand, it shows that RBF is less accurate than Kriging since it fails to generate a better (feasible) design compared to Kriging.

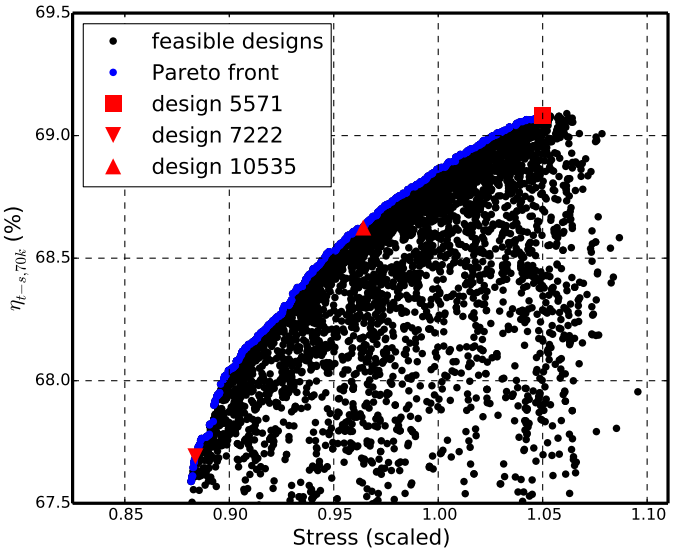

Fig. 5.52 2D scatter plot of $\eta_{t-s,70k}$ versus Stress (scaled) for Kriging approximation

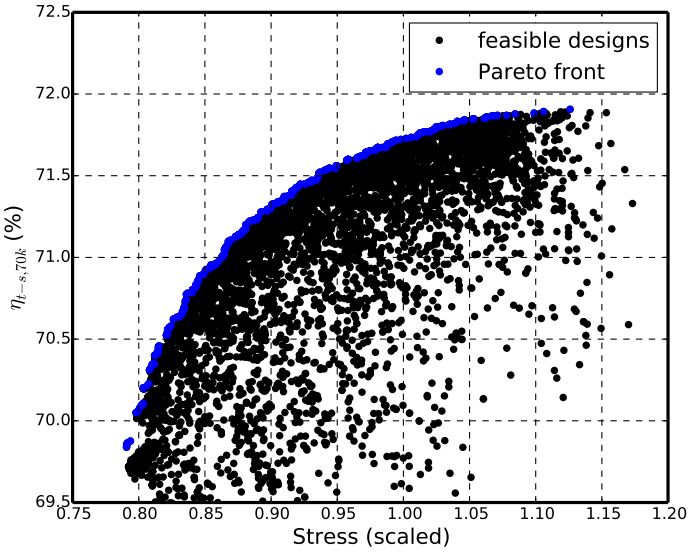

Fig. 5.53 2D scatter plot of $\eta_{t-s,70k}$ versus Stress (scaled) for quadratic polynomial approximation

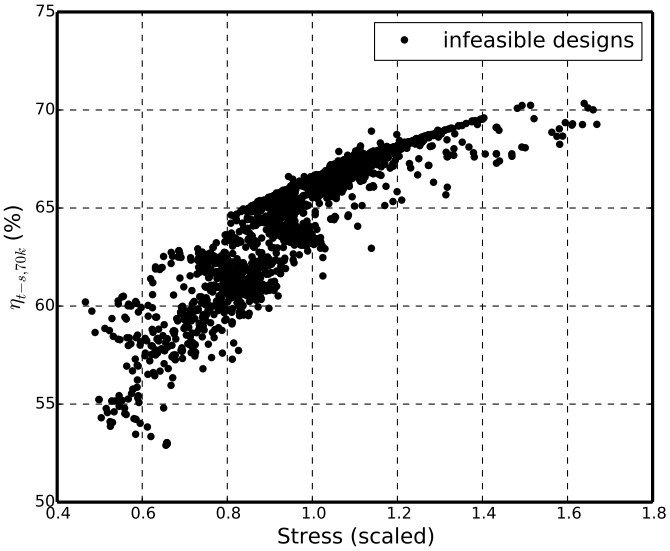

Fig. 5.54 2D scatter plot of $\eta_{t-s,70k}$ versus Stress (scaled) for RBF approximation

5.6.1 CFD and FEA Results

Three designs, design 5571, design 7222 and design 10535, are selected from the Pareto front in Figure 5.52. To validate the accuracy of the Kriging model, their performance values obtained through CFD and FEA simulations are compared with the prediction values through the Kriging model in Table 5.8.

The error between the Kriging prediction and CFD/FEA validation for MFP_{50k}, MFP_{60k} and MFP_{70k} is between 0.8% and 2.2% and the error for MFP_{80k} and MFP_{90k} is slightly higher (3.1% - 4.4%). The error for most efficiencies is less than 2.0% and it increases to 3-4% for several efficiency values. The error for most of the mechanical performance parameters ($1^{st}f$, $2^{nd}f$, MOI and $Stress$) is between 1.4% and 5.7%. However, the largest error is observed for $1^{st}f$ of design 7222 (8.7%) and $Stress$ of design 7222 (-10.5%). The possible explanation is that design 7222 has very high $1^{st}f$ and low $Stress$ compared to other designs and the Kriging model has poor accuracy in this region.

A trade-off between $\eta_{t-s,70k}$ and $Stress$ can be observed from Kriging Pareto front (Figure 5.52). Design 5571 is predicted to have the highest $\eta_{t-s,70k}$ and $Stress$ through the Kriging approximation, while design 7222 is predicted to have the lowest $\eta_{t-s,70k}$ and $Stress$. The same trend is captured through CFD/FEA

Table 5.8 Comparison of predicted (Kriging) and validation values for three optimal designs

design		$1^{st}f$	$2^{nd}f$	η_{50k}	η_{60k}	η_{70k}	η_{80k}	η_{90k}	MFP_{50k}	MFP_{60k}	MFP_{70k}	MFP_{80k}	MFP_{90k}	MOI	$Stress$
5571	Kriging	8102	14342	60.3%	67.2%	69.1%	67.0%	58.6%	24.1	24.0	23.8	23.4	22.3	8.5399e-5	1.05
	CFD/FEA Validation	7987	13563	60.1%	66.3%	68.8%	67.9%	60.6%	23.9	23.7	23.3	22.6	21.4	8.0849e-5	1.08
	error	1.4%	5.7%	0.4%	1.4%	0.4%	-1.4%	-3.3%	0.8%	1.1%	2.0%	3.4%	4.4%	5.6%	-2.5%
	Compared to baseline	6.8%	0.2%	0.3%	-0.4%	2.1%	7.3%	10.7%	0.0%	-0.7%	-1.1%	-1.2%	-2.9%	-8.5%	8.8%
7222	Kriging	9355	14422	60.0%	66.5%	67.7%	64.6%	56.9%	24.4	24.3	24.0	23.4	22.2	8.0975e-5	0.88
	CFD/FEA Validation	8604	14009	59.8%	65.6%	68.0%	66.6%	59.5%	24.1	23.9	23.5	22.7	21.4	7.7700e-5	0.99
	error	8.7%	2.9%	0.4%	1.3%	-0.5%	-3.0%	-4.4%	1.2%	1.6%	2.2%	3.1%	3.5%	4.2%	-10.5%
	Compared to baseline	15.0%	3.5%	-0.2%	-1.3%	0.9%	5.2%	8.8%	0.8%	0.1%	-0.4%	-0.9%	-2.5%	-12.0%	-0.3%
10535	Kriging	8499	14175	60.1%	66.8%	68.6%	66.5%	58.4%	24.1	24.0	23.8	23.4	22.2	8.1654e-5	0.96
	CFD/FEA Validation	8273	13720	59.7%	66.0%	68.6%	67.7%	59.6%	23.9	23.8	23.4	22.7	21.4	7.8590e-5	1.02
	error	2.7%	3.3%	0.7%	1.2%	0.0%	-1.8%	-2.0%	0.8%	0.8%	1.7%	3.1%	3.7%	3.9%	-5.2%
	Compared to baseline	10.6%	1.4%	-0.3%	-0.8%	1.8%	7.0%	9.0%	0.0%	-0.4%	-0.8%	-0.9%	-2.7%	-11.0%	2.7%
baseline	CFD/FEA	7479	13535	59.9%	66.5%	67.4%	63.3%	54.7%	23.9	23.9	23.6	22.9	22.0	8.8342e-5	0.99

validation and the performance improvements for design 5571, design 10535 and design 7222 are plotted in Figure 5.55. As it can be seen that design 5571 has the best efficiency (η_{70k}) but worst mechanical performance ($Stress$, $1^{st}f$, $2^{nd}f$ and MOI). Design 7222 has the best mechanical performance ($Stress$, $1^{st}f$, $2^{nd}f$ and MOI) but worst efficiency (η_{70k}). A clear trade-off between the aerodynamic performance and the mechanical performance is demonstrated. Design 10535 is selected and further analysis will be performed in the following subsections since design 5771 has too high stress and design 7222 has less efficiency improvement.

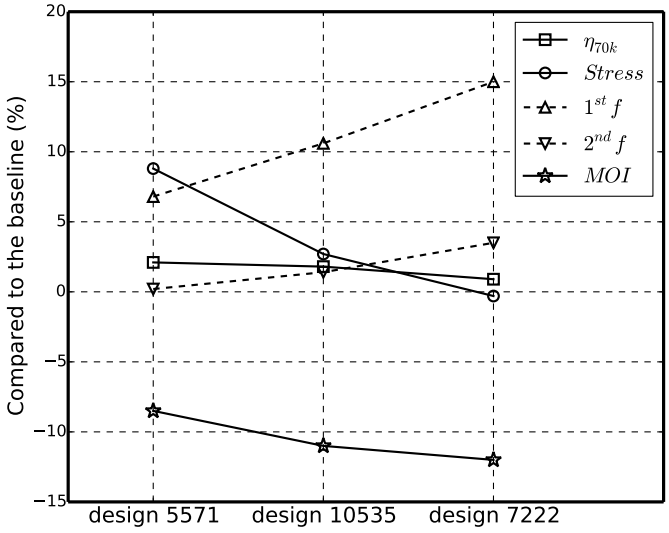

Fig. 5.55 Comparison of performance improvements for design 5571, design 10535 and design 7222

5.6.2 Comparison of Meridional Geometry and Performance Maps (baseline and design 10535)

The meridional geometry comparison between the baseline and design 10535 is shown in Figure 5.56. As it can be seen that the most obvious differences for design 10535 are the increased α_1 and reduced W_2 which are helpful to reduce MOI. The reduced blade exducer height W_2 of design 10535 is helpful to increase the blade stiffness.

The comparison of design parameters is shown in Table 5.9. It can be seen that the values of all the design parameters for design 10535 (the optimal design) are

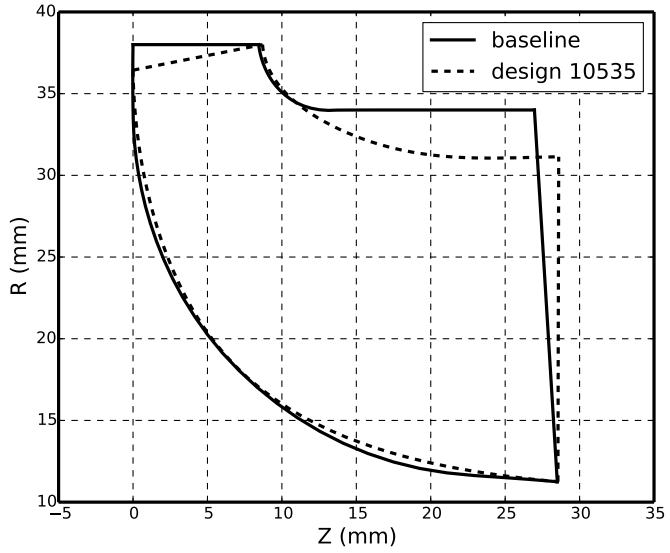

Fig. 5.56 Comparison of meridional geometries

not close to any boundaries (minimum and maximum values) specified in the DOE which indicates that the ranges of the design parameters chosen are reasonable.

Table 5.9 Comparison of design parameters

Design Parameters	baseline	design 10535	min	max
W_1 (mm)	8.441	8.701	7	11
W_2 (mm)	22.25	19.88	15	23.7
α_1 $(^\circ)$	0	10.19	0	28
Y_{hub} (mm)	—	19.185	16.5	21
NC_{hub}	—	0.094	0.05	0.18
ND_{hub}	—	0.721	0.6	0.85
$r\bar{V}_{\theta TE,shr}$	—	0.067	0.06	0.1
$SLOPE_{shr}$	—	-3.46	-5	-1

The MFP and η_{t-s} comparison of the baseline and design 10535 are shown in Figure 5.57 and Figure 5.58. The MFP of design 10535 is slightly higher at U/C_{is} < 0.6 and slightly lower at $U/C_{is} > 0.6$ compared to the baseline. The η_{t-s} of

design 10535 at $U/C_{is} < 0.64$ keeps almost the same as the baseline and is much higher (up to 5 percentage points) at $U/C_{is} > 0.64$.

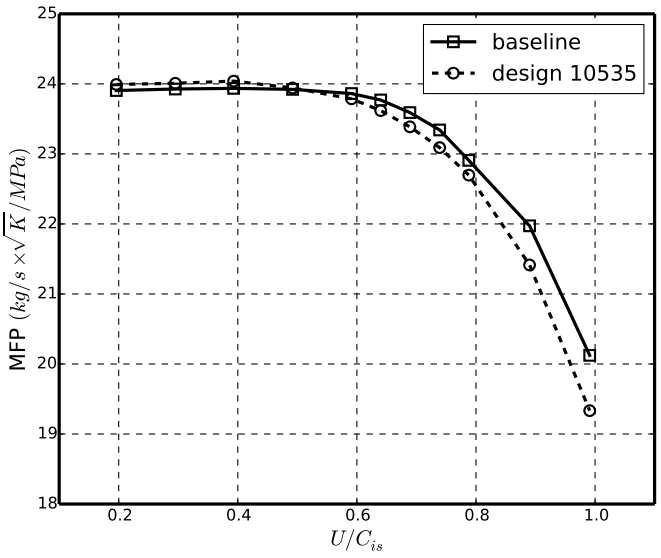

Fig. 5.57 Comparison of MFP

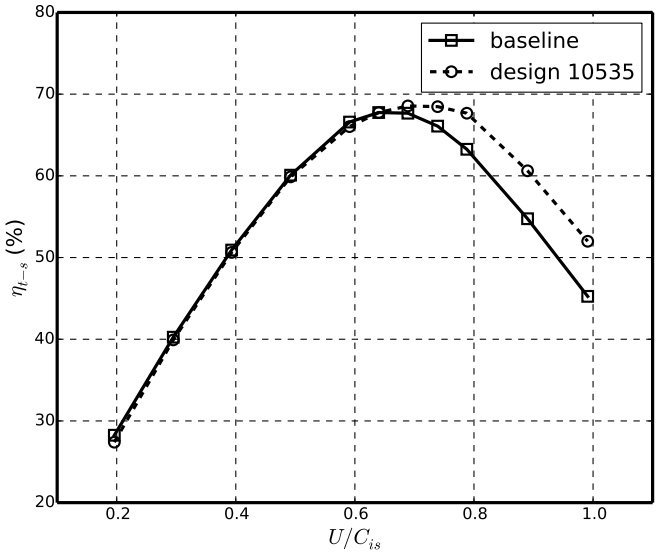

Fig. 5.58 Comparison of t-s efficiency

5.6.3 Comparison of Internal Flow Field (baseline and design 10535 @ RPM = 80k)

In this subsection, the internal flow field details of the baseline and design 10535 at RPM = 80k ($U/C_{is} = 0.79$) where the efficiency improvement is much higher than that at design point (RPM = 70k).

5.6.3.1 Relative Mach Number

The relative Mach number contours of the baseline and design 10535 at different spanwise locations are shown in Figure 5.59, Figure 5.60 and Figure 5.61. The relative Mach number distribution near the hub for the two designs are very similar. Design 10535 has a slightly larger region of low momentum or separation near the blade hub LE pressure side which is caused by the incidence compared to the baseline. In the mid-span and near the shroud, design 10535 has much smaller low momentum region. Near the hub location the relative flow velocity from the middle part of design 10535 is much higher than that of the baseline. This can be explained by that the flow of design 10535 is less diffused since the blade passage area is reduced (reduced W_2). A similar phenomenon can be observed in the mid-span and near the shroud. Another point to note is that the flow separates near the baseline shroud suction side and a large low momentum region exists near the baseline shroud TE which are potentially caused by the complicated leakage flow through the tip clearance. For design 10535, the separation near the suction side is removed and the TE low momentum flow region is improved which indicates that the leakage flow of the new design is improved. The tip leakage flow analysis will be discussed in a subsection later.

The relative Mach number contours of the baseline and design 10535 in the blade LE and TE are shown in Figure 5.62 and Figure 5.63. The LE relative Mach number contours for the two designs are quite similar and uniform with a small variation along the axial direction since the same nozzle blade is used in the upstream to guide the flow and the Stage model is used for the interface between the nozzle and the rotor. The TE relative Mach number for the design 10535 is much higher than that of the baseline, especially near the hub and shroud end walls, same as what have been shown in the contours of the blade-to-blade view.

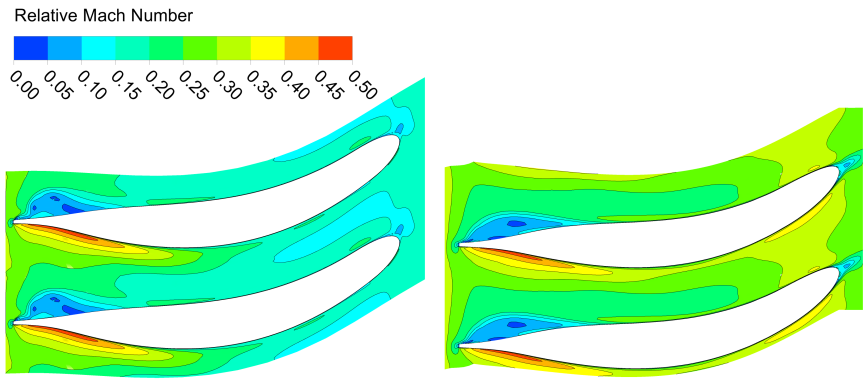

Fig. 5.59 Comparison of relative Mach number contours near the hub ($s^* = 0.1$) @ RPM = 80k (left - baseline, right - design 10535)

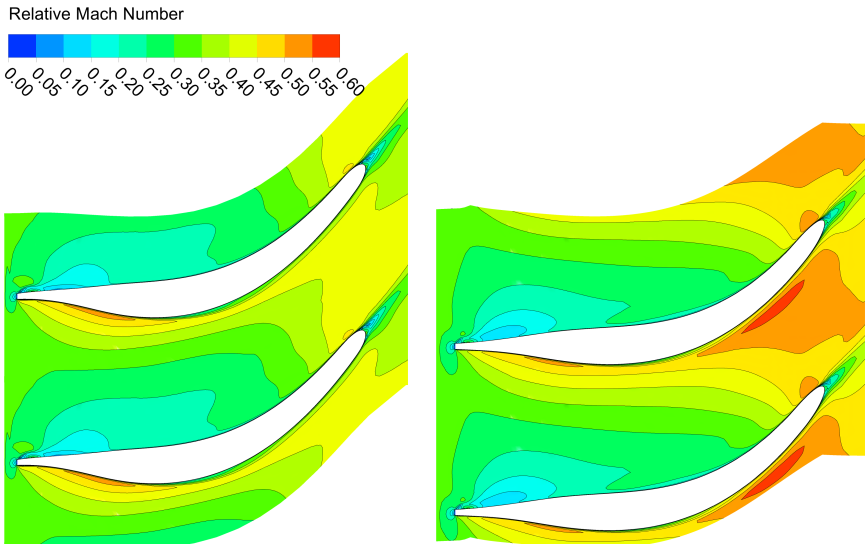

Fig. 5.60 Comparison of relative Mach number contours in the mid-span ($s^* = 0.5$) @ RPM = 80k (left - baseline, right - design 10535)

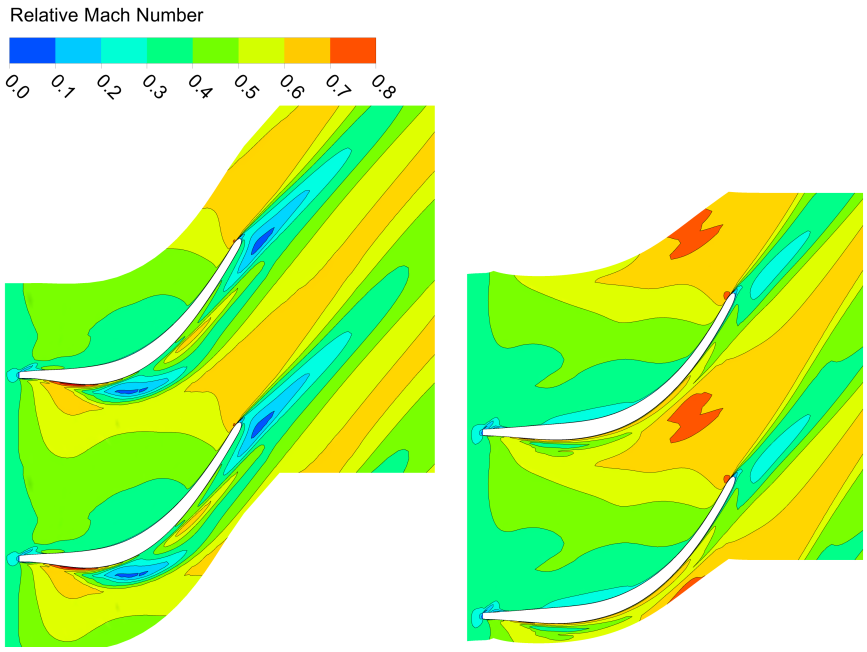

Fig. 5.61 Comparison of relative Mach number contours near the shroud ($s^* = 0.9$) @ RPM = 80k (left - baseline, right - design 10535)

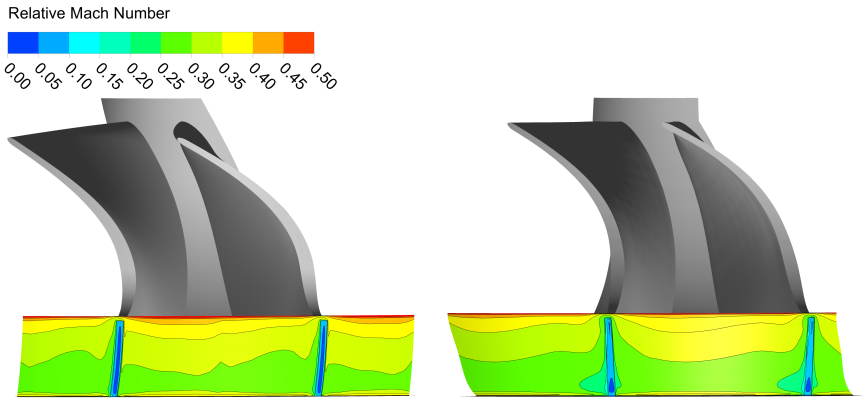

Fig. 5.62 Comparison of relative Mach number contours in the LE @ RPM = 80k (left - baseline, right - design 10535)

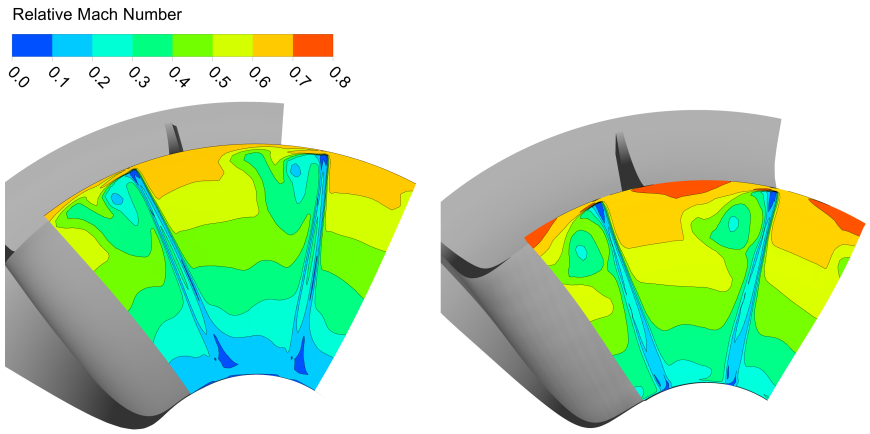

Fig. 5.63 Comparison of relative Mach number contours in the TE @ RPM = 80k (left - baseline, right - design 10535)

5.6.3.2 Blade Surface Pressure

The blade surface pressure comparison for the two designs at different spanwise locations are shown in Figure 5.64, Figure 5.65 and Figure 5.66, where $m^* = 0$ indicates the location of LE and $m^* = 1$ indicates the location of TE. A positive incidence can be seen for the two designs at all three locations while the incidence of design 10535 in the mid-span and near the shroud is reduced. The sudden change of the baseline suction side pressure gradient between $m^* = 0.2$ and $m^* = 0.4$ in Figure 5.66 indicates the existence of the separation which can be seen in Figure 5.61. This separation is removed for design 10535 which can be seen through the improved suction side pressure distribution in Figure 5.66. Both the baseline and design 10535 are fore-loaded near the hub and the blade surface pressure of design 10535 is much higher than that for the baseline on most of the blade. Design 10535 is loaded more at the rear part of the blade ($m^* > 0.5$) from the hub to the shroud compared to the baseline.

5.6.3.3 Aerodynamic Blockage Factor

In the basic theory of the inverse design method, a blockage factor B_f is used in the mean flow continuity equation of a inviscid potential flow field to model the blockage effect caused by the finite blade thickness. While for the 3D viscid flow, an aerodynamic blockage factor is defined as the ratio of the area-averaged meridional velocity to the mass-averaged meridional velocity (Equation 5.33) to

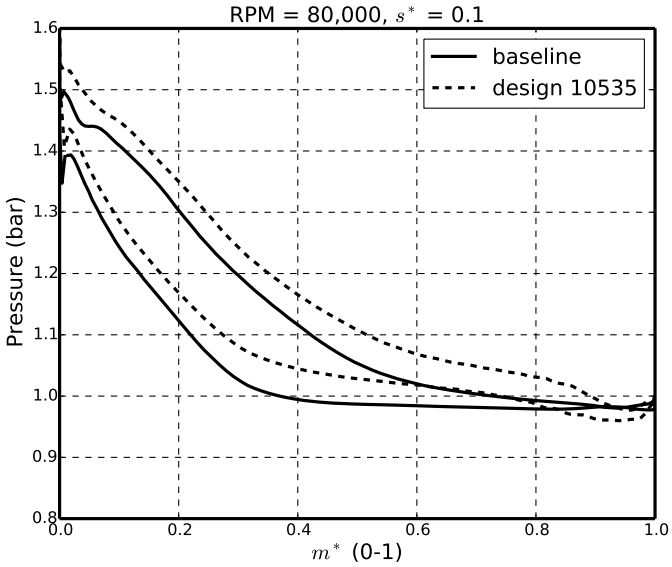

Fig. 5.64 Comparison of blade surface pressure near the hub ($s^* = 0.1$) @ RPM = 80k

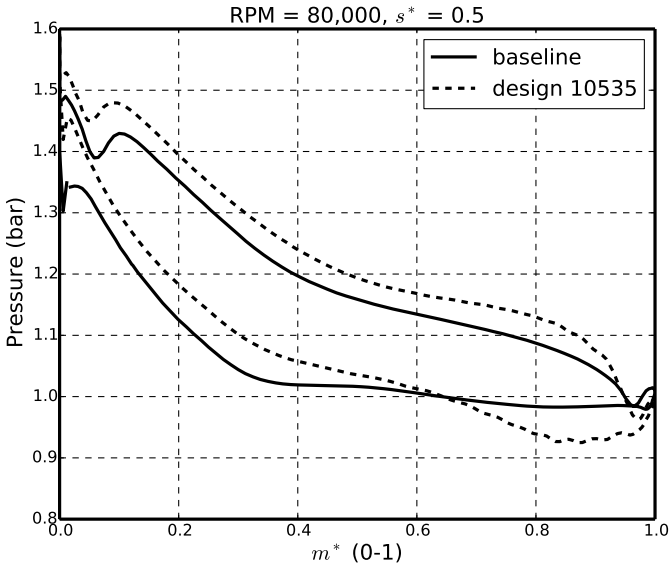

Fig. 5.65 Comparison of blade surface pressure in the mid-span ($s^* = 0.5$) @ RPM = 80k

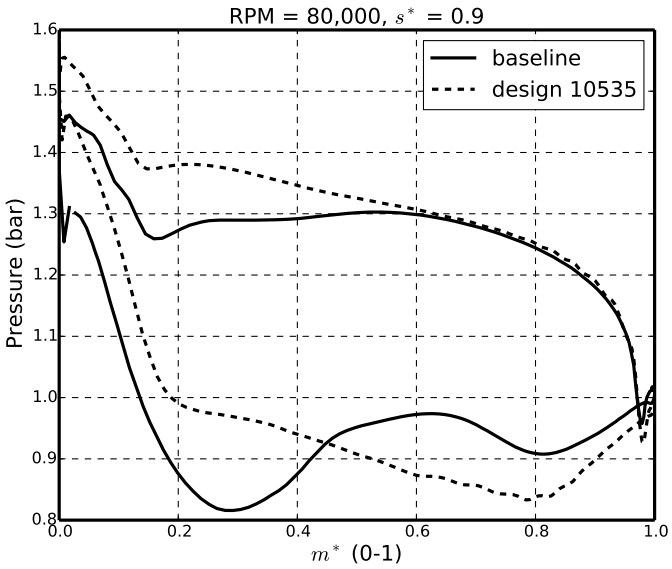

Fig. 5.66 Comparison of blade surface pressure near the shroud ($s^* = 0.9$) @ RPM = 80k

provide a measure of non-uniformity in the flow. The area-averaged meridional velocity $\bar{V}_m^{area}$ and the mass-averaged meridional velocity $\bar{V}_m^{mass}$ are defined by Equation 5.34, where B is the number of blades, V_m is the meridional velocity and ρ is the density. This definition of the aerodynamic blockage is very similar to that suggested by Dring [1984].

$$B_{aero} = \frac{\bar{V}_m^{area}}{\bar{V}_m^{mass}} \tag{5.33}$$

$$\begin{aligned} \bar{V}_m^{area} &= \frac{\int_0^{\frac{2\pi}{B}} V_m r d\theta}{\int_0^{\frac{2\pi}{B}} r d\theta} \\ \bar{V}_m^{mass} &= \frac{\int_0^{\frac{2\pi}{B}} \rho V_m^2 r d\theta}{\int_0^{\frac{2\pi}{B}} \rho V_m r d\theta} \end{aligned} \tag{5.34}$$

The B_{aero} of the baseline and design 10535 at different constant streamwise cross-sections are computed and compared in Figure 5.67, where $m^* = 1$ indicates the location of the rotor inlet and $m^* = 2$ indicates the location of the rotor outlet. As it can be seen that, B_{aero} for the two designs are very close to 1.0 at $m^* = 1$

where the interface between the nozzle and the rotor domain locates which means the flow at the rotor inlet is very uniform. This can be explained by:

1) The Stage interface mixes out the upstream velocity profile and provides a circumferentially uniform flow to the downstream;

2) The flow variation in the 2D nozzle along the axial direction is very small. The flow is also uniform in the axial direction.

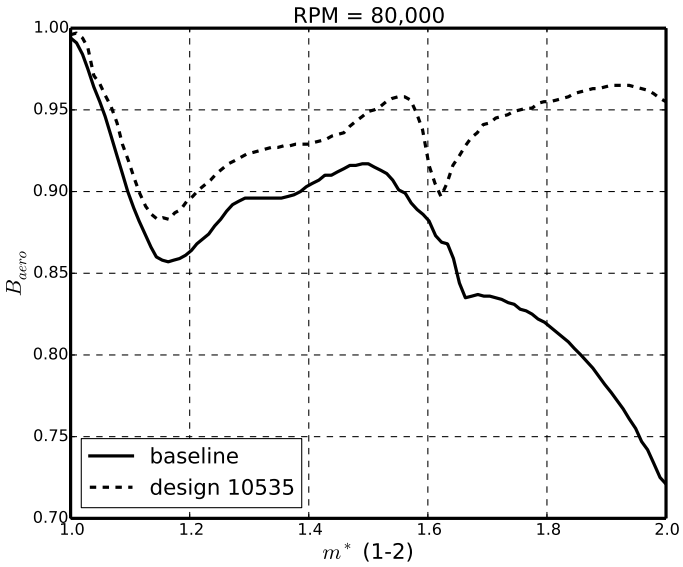

Fig. 5.67 Comparison of B_{aero} from the rotor inlet to the rotor outlet @ RPM = 80k

The trends of B_{aero} for the two designs are very similar between the LE ($m^* = 1.03$) and the TE ($m^* = 1.63$) but very different after the TE. The B_{aero} of design 10535 is always higher than that of the baseline from the rotor inlet to the rotor outlet. At the turbine exit, the flow for design 10535 is more uniform ($B_{aero} = 0.96$) than the baseline whose B_{aero} is only 0.72.

5.6.3.4 Blade Surface Streamline

The blade surface (suction side) streamlines comparison for the two designs is shown in Figure 5.68. One can see that design 10535 has a much better streamline distribution attached on the blade surface, since it has less secondary flow whose direction is from the hub to the shroud compared to the baseline.

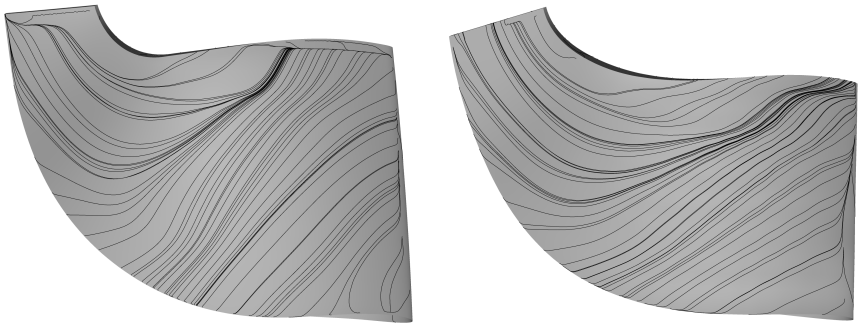

Fig. 5.68 Comparison of blade surface streamlines on the suction side @ RPM = 80k (left - baseline, right - design 10535)

5.6.3.5 Tip Leakage Flow

The tip leakage flow is the flow passing through the tip clearance between the moving rotor and the stationary turbine casing and is one of the most important loss sources in turbomachines. The easiest way to reduce the tip leakage loss is to minimise the tip clearance. However, the value of the tip clearance is limited by a number of factors, for example, the manufacturing cost, the machining accuracy, the blade thermal expansion, the blade deflection caused by the centrifugal loading and so on. In this study, a fixed 0.5 mm clearance is used for the baseline and all the redesigned blades.

The streamlines for the tip leakage flow for the two designs are compared in Figure 5.69. It can be seen that most of the tip leakage flow starts from the blade LE pressure side. The flow direction is from the pressure side to the suction side along the whole chord locations from the LE to the TE. A small leakage vortex is generated near the LE suction side and this vortex grows and mixes with any new leakage flow from the pressure side along the meridional direction. Design 10535 has a better leakage flow structure since the strength of the leakage vortex and its entropy generation for design 10535 is smaller than the baseline. This can be seen more clearly in the next subsection.

5.6.3.6 Entropy Generation

It is well known that entropy is directly related to the loss and the isentropic efficiency of a turbomachine in a compression/expansion process. In this subsection,

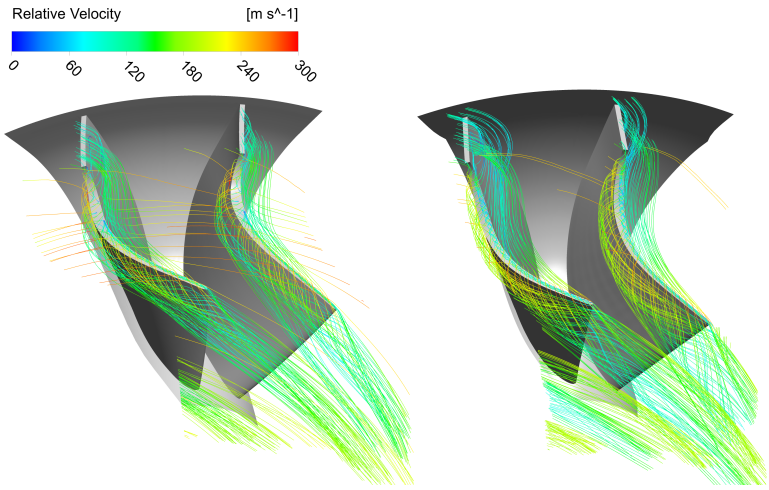

Fig. 5.69 Comparison of streamlines across the tip leakage @ RPM = 80k (left - baseline, right - design 10535)

firstly, the mathematical expression for the entropy generation and the turbine t-s isentropic efficiency is derived. The total entropy s_0 and the static entropy s are defined using Equation 5.35 and Equation 5.36.

$$s_0 - s_{ref} = c_P \ln \frac{T_0}{T_{ref}} - R \ln \frac{P_0}{P_{ref}} \tag{5.35}$$

$$s - s_{ref} = c_P \ln \frac{T}{T_{ref}} - R \ln \frac{P}{P_{ref}} \tag{5.36}$$

Subtracting Equation 5.36 from Equation 5.35 and together using the isentropic flow equations, it can be obtained that the total entropy is always equal to the static entropy (Equation 5.37).

$$s_0 = s \tag{5.37}$$

The total entropy generation between the turbine inlet and the outlet can be written down in the form of Equation 5.38.

$$s_{02} - s_{01} = c_P \ln \frac{T_{02}}{T_{01}} - R \ln \frac{P_{02}}{P_{01}} \tag{5.38}$$

Rearrange Equation 5.38 and Equation 5.39 can be obtained.

$$\frac{T_{02}}{T_{01}} = \left(\frac{P_{02}}{P_{01}} e^{\frac{s_{02}-s_{01}}{R}}\right)^{(\gamma-1)/\gamma} \tag{5.39}$$

Substitute Equation 5.37 and Equation 5.39 into Equation 5.40 to get the final expression for the η_{t-s} (Equation 5.41).

$$\eta_{t-s} = \frac{1 - \frac{T_{02}}{T_{01}}}{1 - \left(\frac{P_2}{P_{01}}\right)^{(\gamma-1)/\gamma}} \tag{5.40}$$

$$\begin{aligned} \eta_{t-s} &= \frac{1 - \left(\frac{P_{02}}{P_{01}} e^{\frac{s_{02}-s_{01}}{R}}\right)^{(\gamma-1)/\gamma}}{1 - \left(\frac{P_2}{P_{01}}\right)^{(\gamma-1)/\gamma}} \\ &= \frac{1 - \left(\frac{P_{02}}{P_{01}} e^{\frac{s_2-s_1}{R}}\right)^{(\gamma-1)/\gamma}}{1 - \left(\frac{P_2}{P_{01}}\right)^{(\gamma-1)/\gamma}} \end{aligned} \tag{5.41}$$

In Equation 5.41, for a fixed ER (P_{01} and P_2), η_{t-s} is determined by the total pressure at the turbine outlet and the static entropy generation between the turbine inlet and the outlet. To maximise η_{t-s}, P_{02} and $(s_2 - s_1)$ need to be minimised.

The comparison of Mass and Circumferentially Averaged (MCA) static entropy from the nozzle inlet ($m^* = 0$) to the rotor outlet ($m^* = 2$) for the baseline and design 10535 is shown in Figure 5.70. The static entropy at the nozzle inlet is the same since the same inlet boundary conditions are applied for both designs. The static entropy for design 10535 is lower than that for the baseline between the rotor inlet ($m^* = 1$) and the rotor outlet. Therefore, the static entropy generation for design 10535 is less than that for the baseline.

The comparison of static entropy contours for the two designs at three different streamwise locations is shown in Figure 5.71 and the last section is located at the TE. As it can be seen that most of the entropy is accumulated near the blade tip suction side where the tip leakage vortex locates. At the same streamwise location, the baseline has higher entropy than design 10535. Especially, in the TE, the baseline has two high entropy regions near the tip while design 10535 only has one. Figure 5.72 shows the baseline has the more complex streamline structure which is the source of the high entropy region. The mass-averaged entropy on the

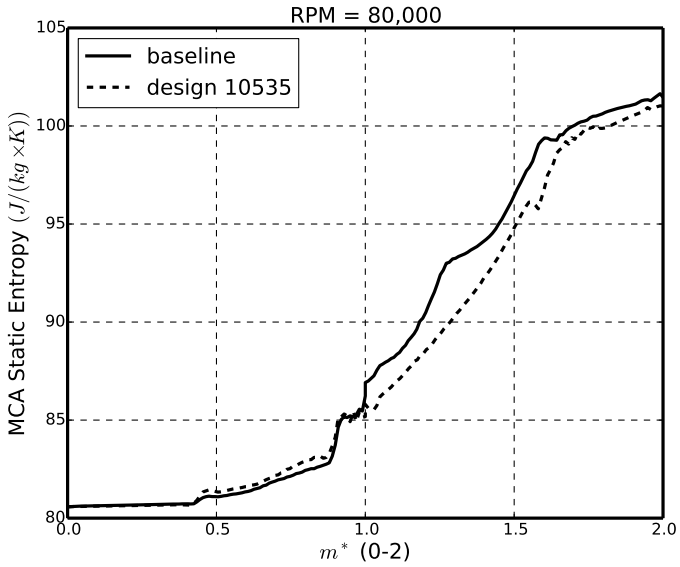

Fig. 5.70 Comparison of MCA static entropy from the nozzle inlet to the rotor outlet @ RPM = 80k

TE plane for the baseline is higher than that for design 10535 which is confirmed in Figure 5.70.

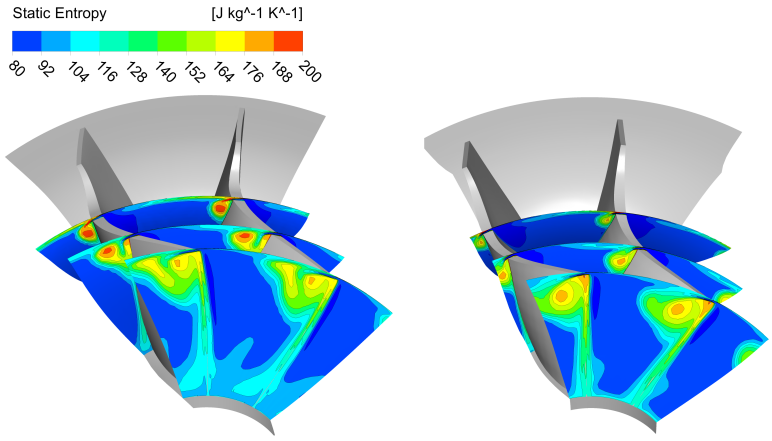

Fig. 5.71 Comparison of static entropy contours at different streamwise locations @ RPM = 80k (left - baseline, right - design 10535)

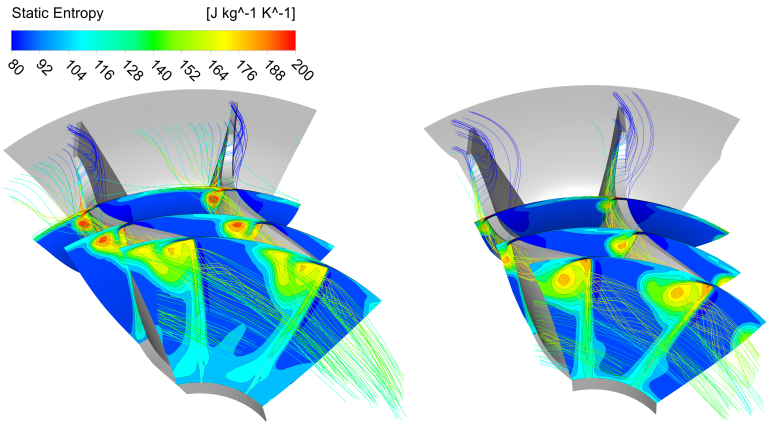

Fig. 5.72 Comparison of streamlines associated with static entropy contours at different streamwise locations @ RPM = 80k (left - baseline, right - design 10535)

5.6.3.7 Exit Kinetic Energy Loss

The exit kinetic energy loss is a very important loss term that needs to be accounted in the calculation of the turbine t-s efficiency, since the kinetic energy at the turbine outlet cannot be recovered and is wasted. The efficiency value corresponding to the kinetic energy loss is defined by Equation 5.42, where V_2 is the absolute flow velocity at the turbine outlet. The calculated η_{exit} for the baseline is 14.7% and η_{exit} for design 10535 is 10.2% at RPM = 80k.

$$\eta_{exit} = \frac{0.5V_2^2}{c_p T_{01}\left[1 - \left(\frac{P_2}{P_{01}}\right)^{(\gamma-1)/\gamma}\right]} \tag{5.42}$$

The meridional velocity, absolute circumferential velocity and absolute velocity contours at the rotor outlet for the two designs are compared in Figure 5.73, Figure 5.74 and Figure 5.75. For the baseline, V_m is distributed uniformly in the circumferential direction and varies in the radial direction., especially V_m near the hub is very low and near the shroud is very high. Design 10535 shows a much more uniform V_m distribution with higher velocity near the hub and lower velocity near the shroud compare to the baseline. This can also be confirmed by the B_{aero} value at $m^* = 2$ in Figure 5.67. Design 10535 removes more swirl and has a smaller tangential velocity near the shroud as shown in Figure 5.74. As a result, design 10535 has a smaller and more uniform velocity profile at the turbine exit compared to the baseline as shown in Figure 5.75.

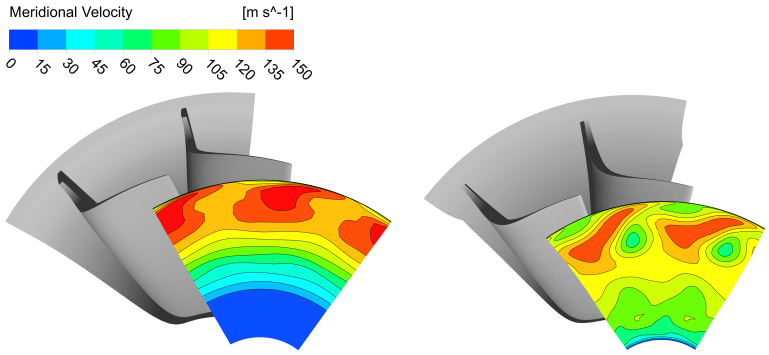

Fig. 5.73 Comparison of meridional velocity contours at the turbine outlet @ RPM = 80k (left - baseline, right - design 10535)

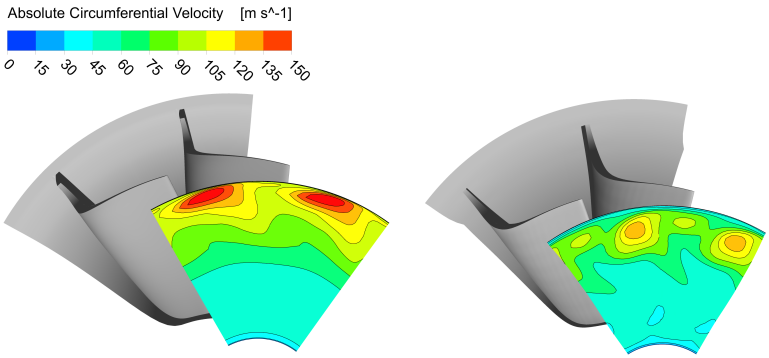

Fig. 5.74 Comparison of absolute circumferential velocity contours at the turbine outlet @ RPM = 80k (left - baseline, right - design 10535)

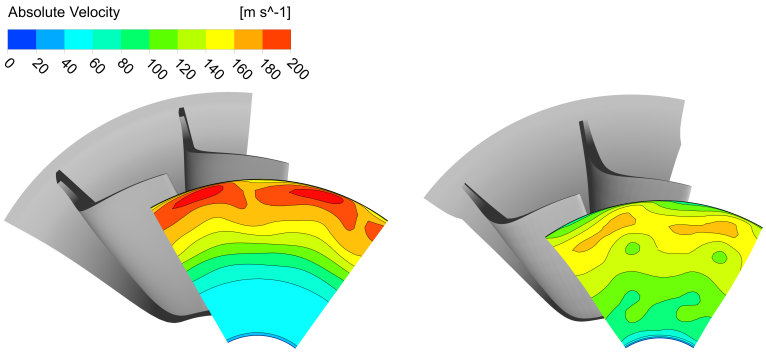

Fig. 5.75 Comparison of absolute velocity contours at the turbine outlet @ RPM = 80k (left - baseline, right - design 10535)

5.6.4 Comparison of Static Structural and Modal Analysis results (baseline and design 10535)

In this subsection, the results of the static structural and modal analysis of the baseline and design 10535 are compared. The MOI of design 10535 has been calculated and shown in Table 5.8 which is reduced by 11% compared to the baseline value.

5.6.4.1 Stress

The comparison of stress contours for the two designs are shown in Figure 5.76, Figure 5.77 and Figure 5.78. The stress distribution on the blade surface and the turbine back face for these two designs are very similar. The stress level in the hub fillet of design 10535 is reduced compared to the baseline. The maximum stress occurs in the same location which is in the TE hub region. The maximum stress of design 10535 is 2.3% higher than the baseline and this can be easily reduced by increasing the fillet radius slightly near the TE.

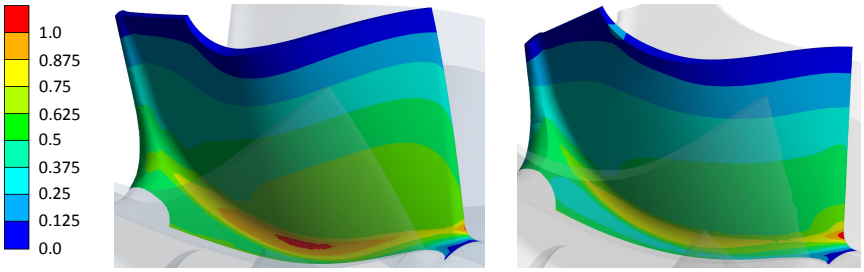

Fig. 5.76 Comparison of maximum principle stress (scaled) contours on the suction surface (left - baseline, right - design 10535)

5.6.4.2 Modal Frequencies

The comparison of 1^{st} and 2^{nd} vibration mode shapes of two designs are shown in Figure 5.79 and Figure 5.80. The frequency for the 1^{st} vibration mode of design 10535 is 10.6% higher and the frequency for the 2^{nd} vibration mode of design 10535 is 1.4% higher than the baseline.

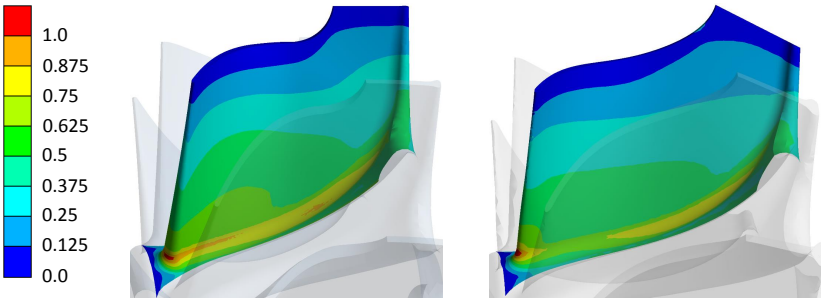

Fig. 5.77 Comparison of maximum principle stress (scaled) contours on the pressure surface (left - baseline, right - design 10535)

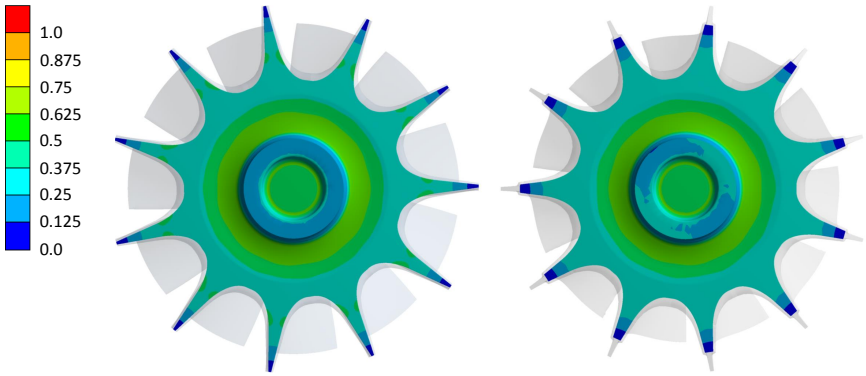

Fig. 5.78 Comparison of maximum principle stress (scaled) contours on the back face (left - baseline, right - design 10535)

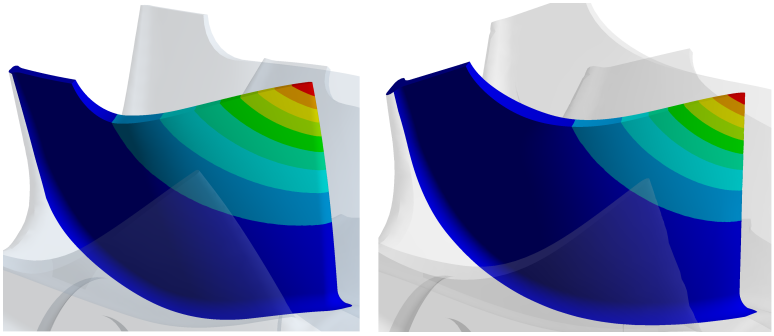

Fig. 5.79 Comparison of 1^{st} vibration mode shapes (left - baseline, right - design 10535)

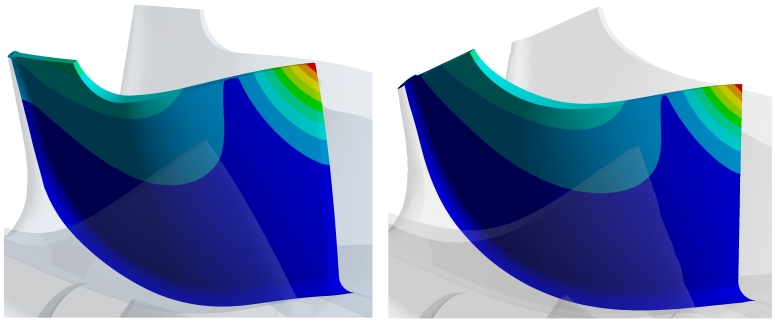

Fig. 5.80 Comparison of 2^{nd} vibration mode shapes (left - baseline, right - design 10535)

5.7 Summary

A systematic optimisation methodology using the inverse design method, DOE, RFM1, Kriging approximation and MOGA is presented in this chapter. The inverse design method is used to generate the 3D blade geometry and Radial Filament Modification method 1 is used to modify the 3D blade shape to reduce the maximum stress. The number of design parameters is reduced from 17 to 8 through a sensitivity analysis based on the linear DOE results. The Kriging is used to construct a more accurate response surface for the new selected design parameters. An optimal design, design 10535, is obtained by searching on the Kriging RSM using MOGA with multiple constraints and objectives. Design 10535 shows better aerodynamic and mechanical performance compared to the baseline design, especially the efficiency at high U/C_{is} and MOI. The improved performance of design 10535 is confirmed by detailed CFD and FEA analysis.

Table 5.10 Performance improvements compared to the baseline

	design 10535
$\eta_{t-s,50k}$	-0.3%
$\eta_{t-s,60k}$	-0.8%
$\eta_{t-s,70k}$	1.8%
$\eta_{t-s,80k}$	7.0%
$\eta_{t-s,90k}$	9.0%
MFP_{50k}	0.0%
MFP_{60k}	-0.4%
MFP_{70k}	-0.8%
MFP_{80k}	-0.9%
MFP_{90k}	-2.7%
Stress	2.7%
1^{st} Frequency	10.6%
2^{nd} Frequency	1.4%
MOI	-11.0%

CHAPTER 6

RADIAL TURBINES WITH A BACKSWEPT LE

As it has been mentioned in Chapter 2, the inlet to a turbocharger turbine encounters highly unsteady flow with varying pressure and temperature due to the pulsating nature of the exhaust gas from the internal combustion engine. It is more important to improve the cycle-averaged t-s efficiency which enables turbines to extract more energy from the exhaust gas during one pulse cycle instead of the instantaneous t-s efficiency. The pulsating engine exhaust gas with high pressure and temperature (low U/C_{is} region) carries more energy than high U/C_{is} region. Therefore, it makes more sense to improve the turbine efficiency in the low U/C_{is} region which can be achieved by using backswept LE turbine blades. Several studies on the backswept turbine blades have been conducted by Barr and McNally [2006], Barr et al. [2009], Walkingshaw et al. [2011] and Huang et al. [2012].

6.1 Definition of Backswept Blades

Conventional radial turbines have zero blade angles in the blade LE, while the backswept turbine blades are different. As it is shown in Figure 6.1, the LE of a backswept blade is swept in the opposite direction of rotation and has a negative blade angle ($\beta_{b,LE} < 0$). All the radial filament designs in the DOE of Chapter

5 including the baseline design are not backswept designs since all of them have zero LE blade angles.

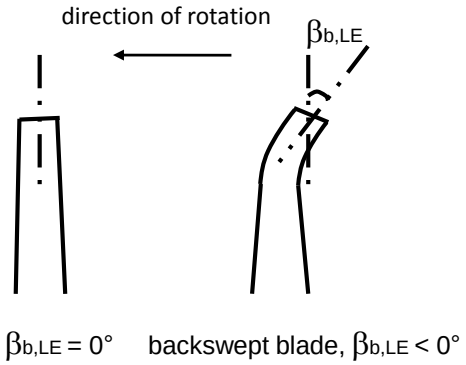

Fig. 6.1 Definition of backswept blades

Figure 6.2 shows the inlet velocity triangles of radial turbines in the low and high U/C_{is}, where C is the absolute flow velocity, U is the blade speed, W is the relative flow velocity, α and β are absolute and relative flow angles. The incidence angle (α_{in}) is the difference between β and $\beta_{b,LE}$ and is defined by Equation 6.1. It can be easily seen that the incidence angle of the backswept blade is smaller than that of a blade with zero $\beta_{b,LE}$ in the low U/C_{is}. The smaller value of the incidence angle results in less incidence loss and gives higher t-s efficiency in the low U/C_{is}.

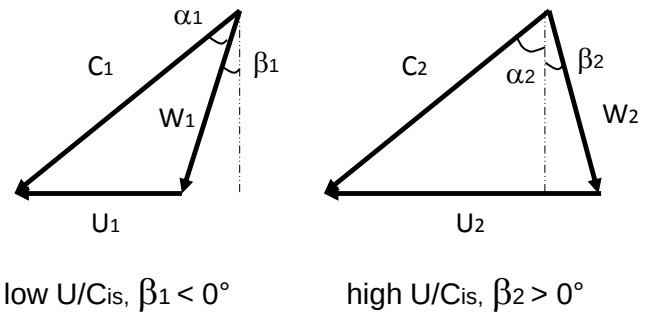

Fig. 6.2 Relative flow angle (β) and velocity triangle in the blade LE

$$\alpha_{in} = \beta - \beta_{b,LE} \tag{6.1}$$

6.2 Backswept Blade Design Using Direct Design Method

Direct design method is used to directly modify the LE wrap angle of the baseline blade and generate two backswept designs which are called backswept-1 and backswept-2 as seen in Figure 6.3, Figure 6.4 and Figure 6.5. The wrap angle contours of the backswept-1 the and backswept-2 are shown in Figure 6.6. Compared to the wrap angle contour of the baseline design (Figure 3.2), the difference in the wrap angle near the blade LE can be clearly seen.

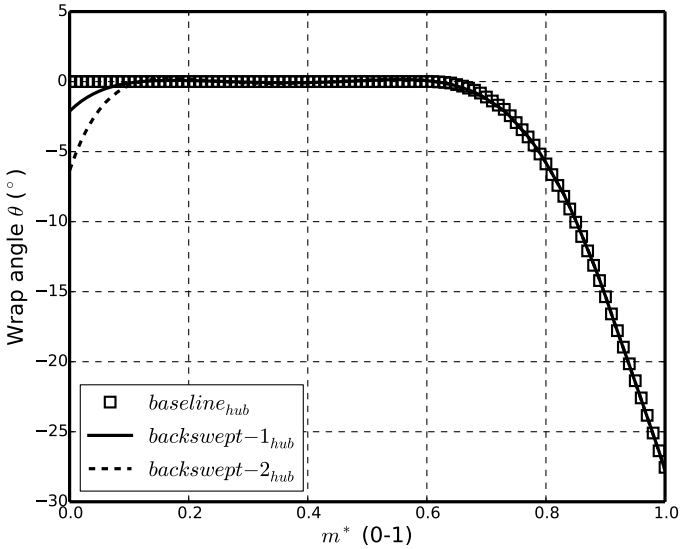

Fig. 6.3 Comparison of wrap angle distribution θ in the hub

The modification of the LE wrap angle distribution results in a change of the LE blade angle which can be seen through the comparison of the blade-to-blade view at three different spanwise locations (Figure 6.7, Figure 6.8 and Figure 6.9). The blade angle β_b is defined by Equation 6.2, where θ is the wrap angle, r is the radial coordinate, m and s are streamwise and spanwise coordinates. The LE of backswept-1 and backswept-2 are swept in the opposite direction of rotation (negative $\beta_{b,LE}$) while the baseline has a straight LE (zero $\beta_{b,LE}$). The comparison of the LE blade angles can be seen more clearly from Figure 6.10, where s^* is the normalised spanwise coordinate. In the hub $s^* = 0$ and in the shroud $s^* =$

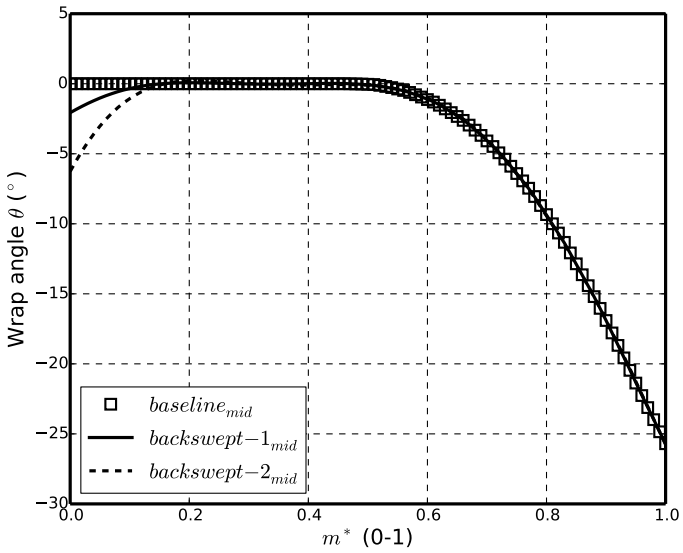

Fig. 6.4 Comparison of wrap angle distribution θ in the mid-span

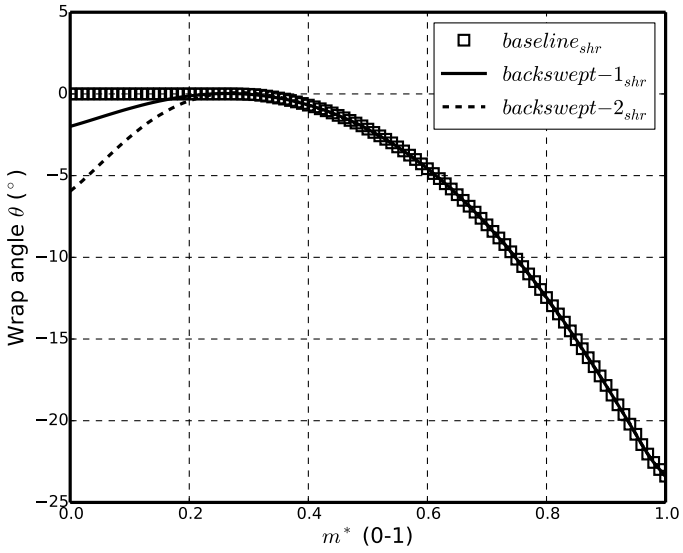

Fig. 6.5 Comparison of wrap angle distribution θ in the shroud

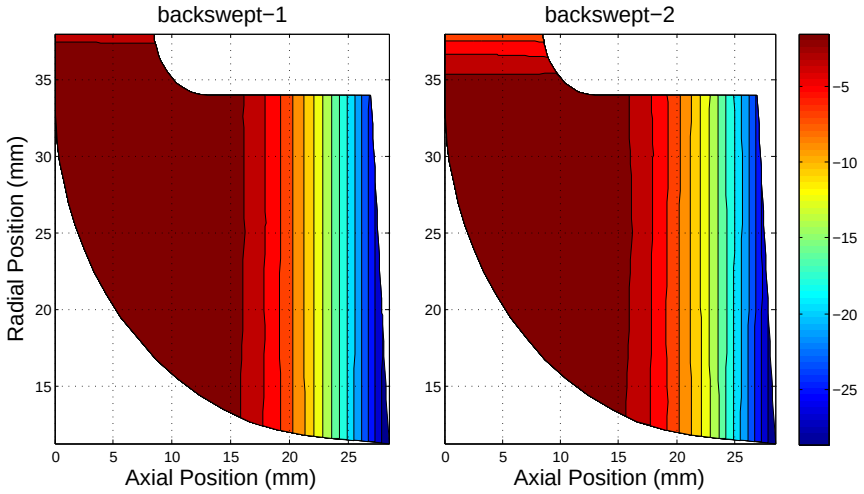

Fig. 6.6 Wrap angle contours of backswept-1 and backswept-2

1. It can be seen that baseline $\beta_{b,LE}$ is 0, backswept-1 $\beta_{b,LE}$ is -32° – -18° and backswept-2 $\beta_{b,LE}$ is -62° – -42°.

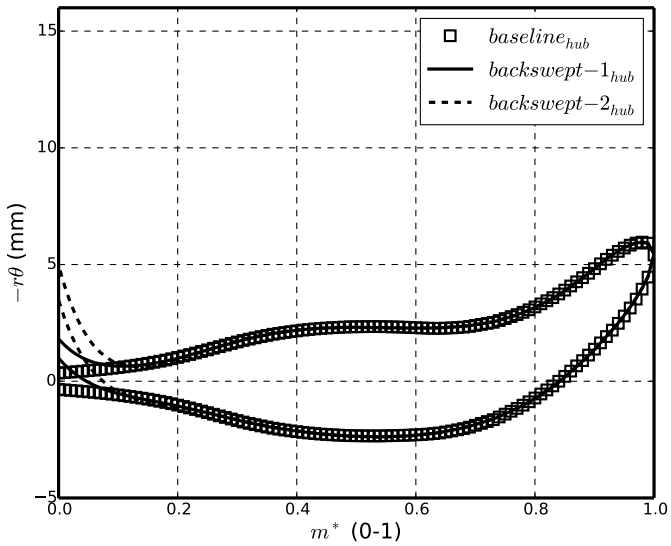

Fig. 6.7 Blade-to-blade view comparison in the hub

$$\beta_b = -\tan^{-1}\left[\frac{r\partial\theta\,(m,s)}{\partial m}\right] \tag{6.2}$$

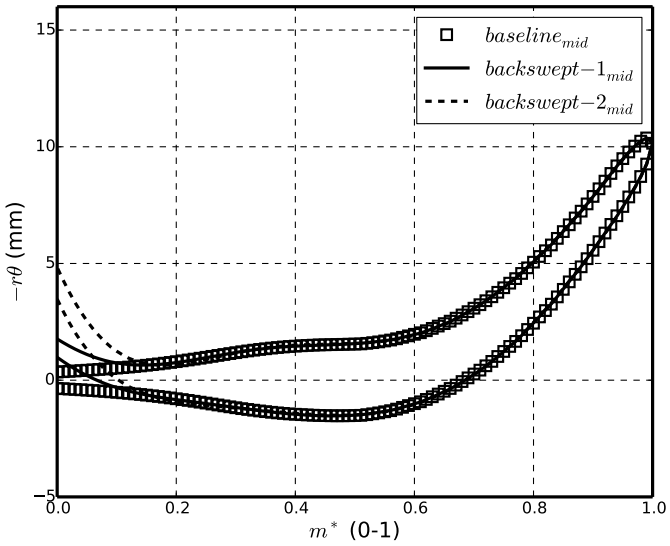

Fig. 6.8 Blade-to-blade view comparison in the mid-span

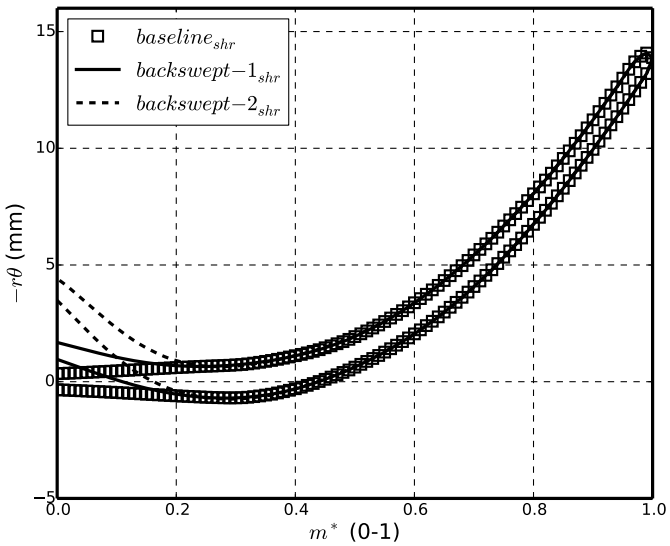

Fig. 6.9 Blade-to-blade view comparison in the shroud

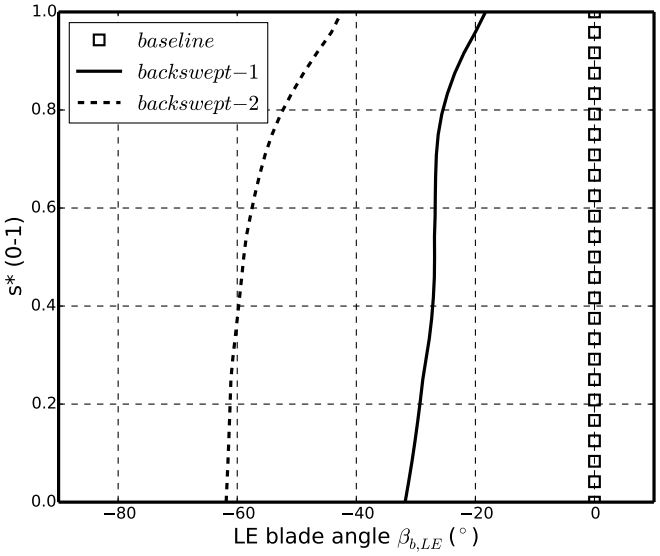

Fig. 6.10 LE blade angle $\beta_{b,LE}$ comparison

The aerodynamic performance of the backswept-1 and the backswept-2 blades are evaluated by running CFD simulations using exactly the same nozzle and boundary conditions as that described in Chapter 3. The MFP and t-s efficiency comparison of the baseline, the backswept-1 and the backswept-2 are shown in Figure 6.11 and Figure 6.12. Compared to the baseline design, backswept blades have slightly higher MFP in the low U/C_{is} and lower MFP in the high U/C_{is}. The t-s efficiency curves of backswept blades shift towards the lower U/C_{is} region compared to the baseline design which results in the efficiency improvement in the low U/C_{is} as expected. The more backswept the blade is, which is equivalent to more negative $\beta_{b,LE}$, the more improvement is achieved. It should be noted that the difference among these three cases is only the LE blade angles ($\beta_{b,LE}$) which can be seen through Figure 6.7, Figure 6.8, Figure 6.9 and Figure 6.10. Therefore, the difference in the aerodynamic performance is only caused by the different LE blade shapes. This can be more easily explained through the comparison of the relative velocity vector plot in Figure 6.13. For all three cases, the LE absolute flow angle α is fixed for different U/C_{is}. When $U/C_{is} = 0.39$, the blade tip speed U is quite low and the calculated relative flow angle β is negative (Figure 6.2). From Figure 6.13 it can be seen that the LE relative flow angles β is negative and almost the same for all three cases. Using Equation 6.1, it can be obtained that $\alpha_{in,backswept-2} < \alpha_{in,backswept-1} < \alpha_{in,baseline}$. For the baseline, the flow starts to separate from the LE due to the large incidence. A region of recirculation and low

momentum can be observed in the LE blade suction side. For backswept-1, the separation region is reduced and the efficiency is improve by 1.1% compared to the baseline since the incidence angle is smaller. For backswept-2, the separation is almost totally removed and the efficiency is 4.2% higher compared to the baseline since the incidence angle is much smaller (close to 0). It can be concluded that backswept blades designed using the conventional method help to improve the turbine efficiency in the low U/C_{is}.

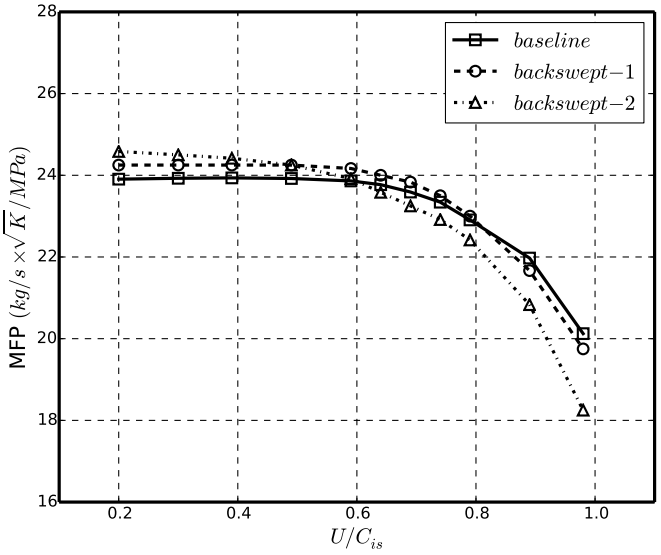

Fig. 6.11 Comparison of MFP

The mechanical performance of these three designs is evaluated through a simple single blade FEA analysis as shown in Figure 6.14. A fixed support is applied on the blade hub surface and the blade is rotating with the maximum speed equal to 130,000 rev/min. The mesh used in the analysis is hexahedral and the number of elements is around 60,000 as it can be seen in Figure 6.15. Figure 6.16 shows the contours of maximum principle stress of the baseline, backswept-1 and backswept-2. The stress distribution of these three designs is very similar except for the inducer part, near the LE, since these blades have the same blade angles over most of the blade. While the maximum local stress in the inducer part is increased with the backsweep. The maximum stress in the inducer for the baseline is around 0.125-0.25. This value is increased to 0.375-0.5 for backswept-1 and >1.0 for backswept-2. The increasing stress values can be explained by: 1) The non-radial filament blading in the inducer part introduces extra bending stress; 2)

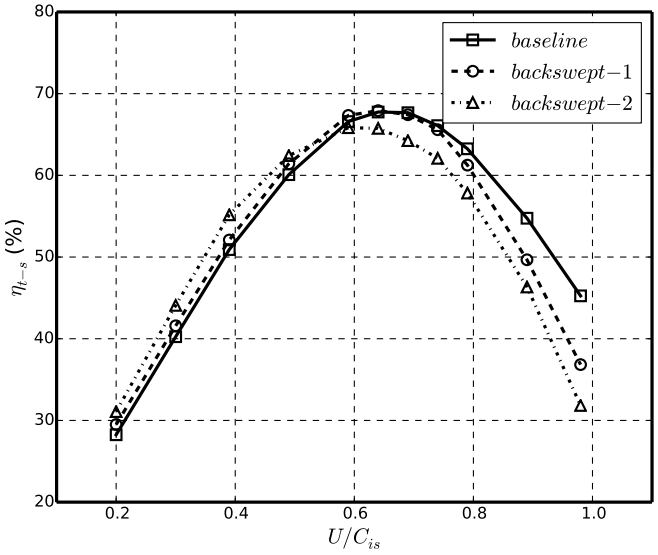

Fig. 6.12 Comparison of t-s efficiency

The rapid change of the blade angle distribution in the inducer causes the local stress concentration which can be seen through the comparison in Figure 6.17, Figure 6.18 and Figure 6.19.

6.3 Backswept Blade Design Using Inverse Design Method

Unlike the direct design method, the inverse design method cannot be used to directly modify the blade wrap and blade angles to create backswept turbine blades. Using the inverse design method the blade angles are computed based on the specified blade loading parameters. In the inverse design method (section 4.5), LE loading parameter $DRVT_{LE}$ can be used to directly control the flow incidence angle. When the LE rV_θ, the inlet volume flow rate $\dot{Q}$ and the meridional shape are fixed, the LE blade angle $\beta_{b,LE}$ can be directly defined by $DRVT_{LE}$ since the relative flow angle β is fixed for the fixed blade rotating speed.

Two different blades are designed using the same meridional shape which is shown in subsection 3.1.1 and different blade loading parameters shown in Table 6.1. The comparison of the loading curves is shown in Figure 6.20. It should be noted

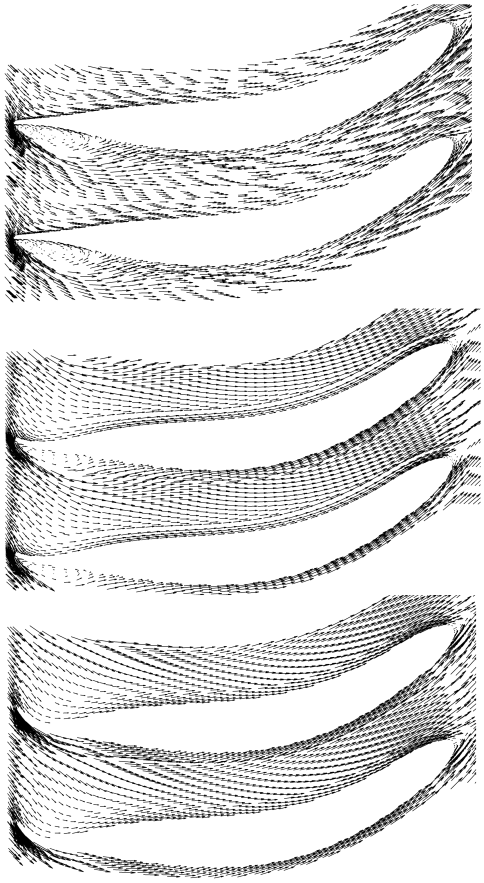

Fig. 6.13 Comparison of relative velocity vector plots near the hub ($U/C_{is} = 0.39$, top - baseline, middle - backswept-1, bottom - backswept-2)

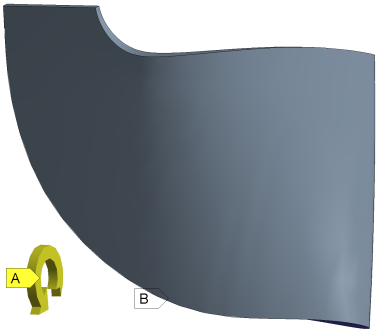

Fig. 6.14 Rotational velocity (A) and fixed support (B)

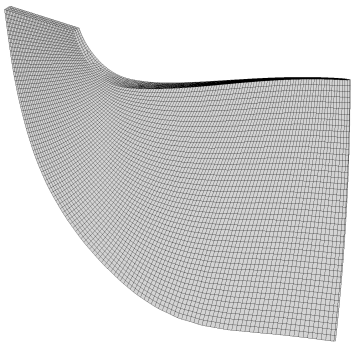

Fig. 6.15 Mesh of single blade geometry

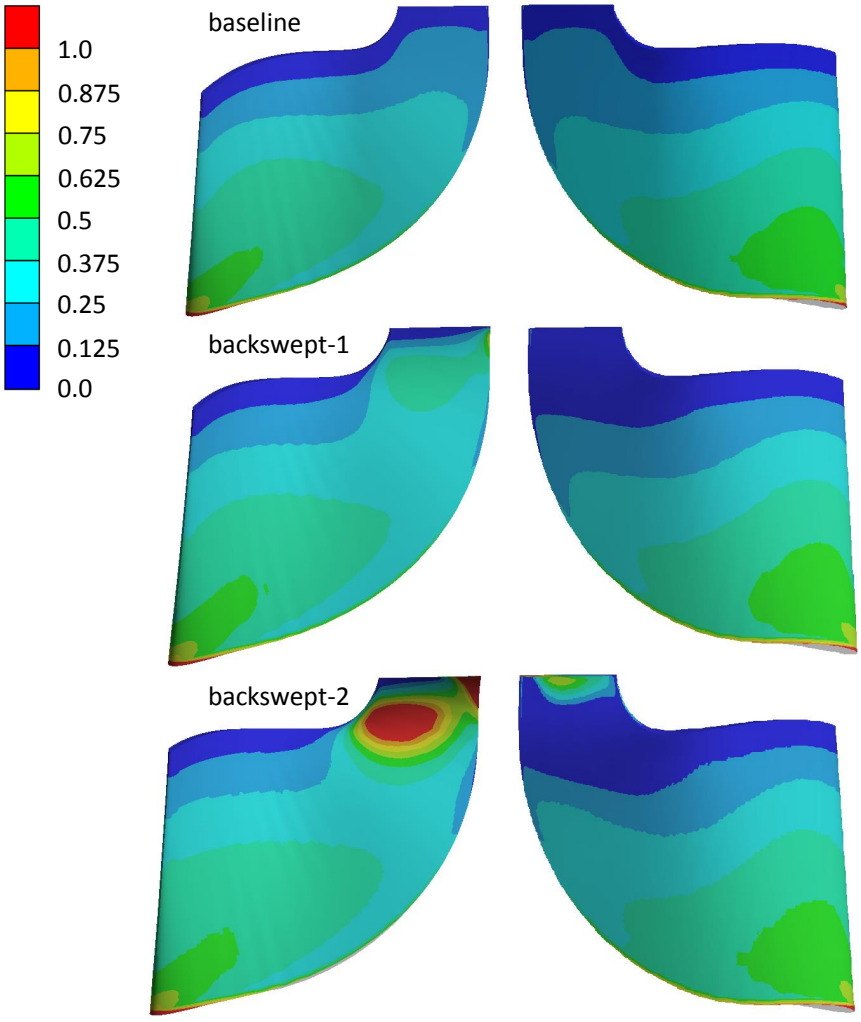

Fig. 6.16 Comparison of maximum principle stress (scaled) contours (left - pressure surface, right - suction surface)

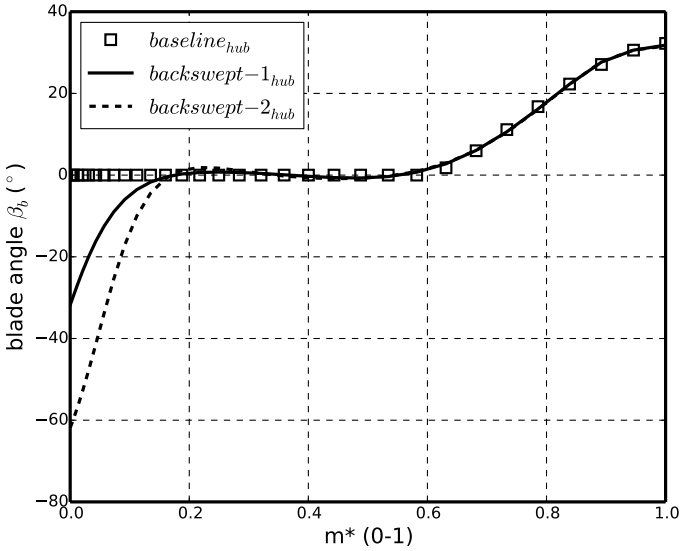

Fig. 6.17 Comparison of blade angle β_b in the hub

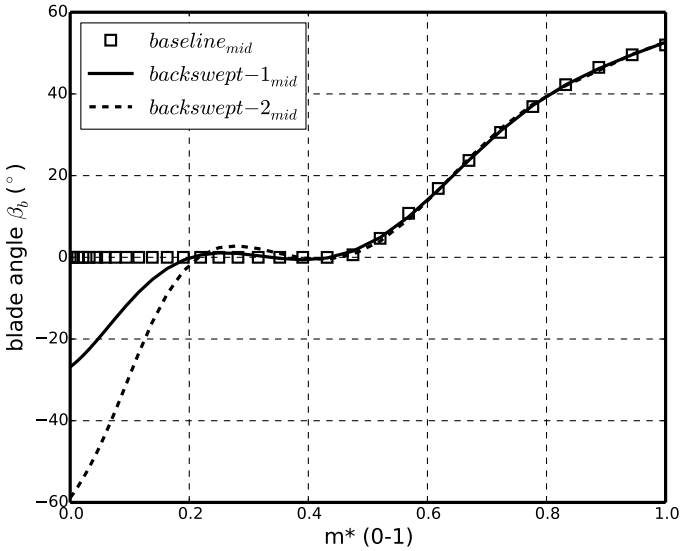

Fig. 6.18 Comparison of blade angle β_b in the mid-span

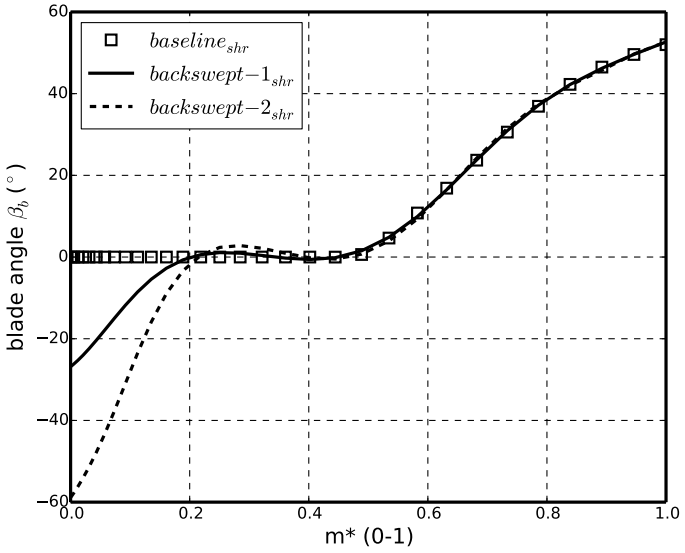

Fig. 6.19 Comparison of blade angle β_b in the shroud

that the only difference between the blade loading of the inverse-baseline and the inverse-baskwept is the LE loading DRVT value. For the inverse-baseline, $DRVT_{LE}$ is less than zero which is similar to the DOE designs in Chapter 5. While $DRVT_{LE}$ of the inverse-backswept design is 0.8. The different LE loading values result in different LE blade angles which can be seen in Figure 6.21. The inverse-backswept has much more negative LE blade angles compared to the inverse-baseline.

However, the blades directly designed using the inverse design method are non radial-filament blades and have very high stress level which have been discussed in subsection 5.3.1. Similar results have been obtained through the FEA analysis of the simple blade model. From Figure 6.22 it can be seen that the stress in the exducer part of the inverse-baseline and the inverse-backswept are extremely high. There is a stress concentration region in the inverse-backswept inducer part which is similar to the conventional backswept blades.

The stress level can be reduced by applying Radial Filament Modification (RFM1). However, the LE blade angle of both inverse-baseline and inverse-backswept will become zero after the Radial Filament Modification method 1 (RFM1) is applied due to the fact that the blade LE stacking angle is zero. This means using the inverse design method and RFM1 cannot generate a backswept blade. To

resolve this problem, a new method called Radial Filament Modification method 2 (RFM2) is proposed and discussed in the next subsection.

Table 6.1 Comparison of blade loading parameters

	inverse-baseline	inverse-backswept
$r\bar{V}^*_{\theta LE,hub}$	0.91	
$r\bar{V}^*_{\theta TE,hub}$	0.07	
$r\bar{V}^*_{\theta LE,shr}$	0.91	
$r\bar{V}^*_{\theta TE,shr}$	0.0013	
NC_{hub}	0.07	
ND_{hub}	0.67	
$SLOPE_{hub}$	1.8	
$DRVT_{LE,hub}$	-0.3	0.8
NC_{shr}	0.336	
ND_{shr}	0.78	
$SLOPE_{shr}$	-3	
$DRVT_{LE,shr}$	-0.8	0.8

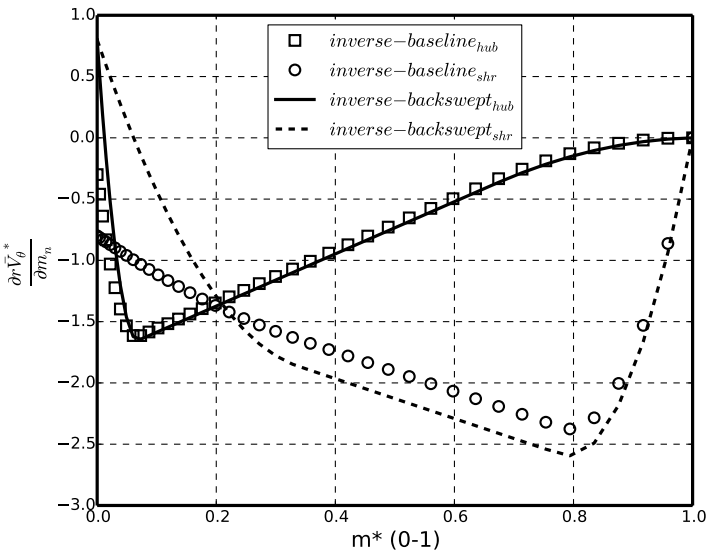

Fig. 6.20 Comparison of blade loading curves

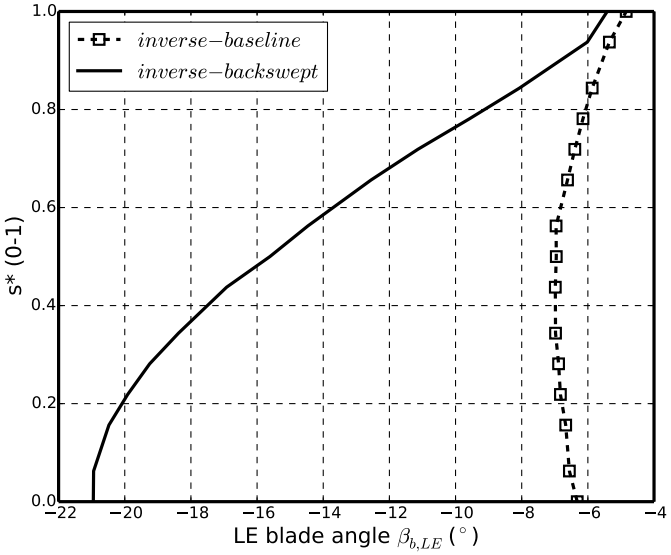

Fig. 6.21 LE blade angle $\beta_{b,LE}$ comparison

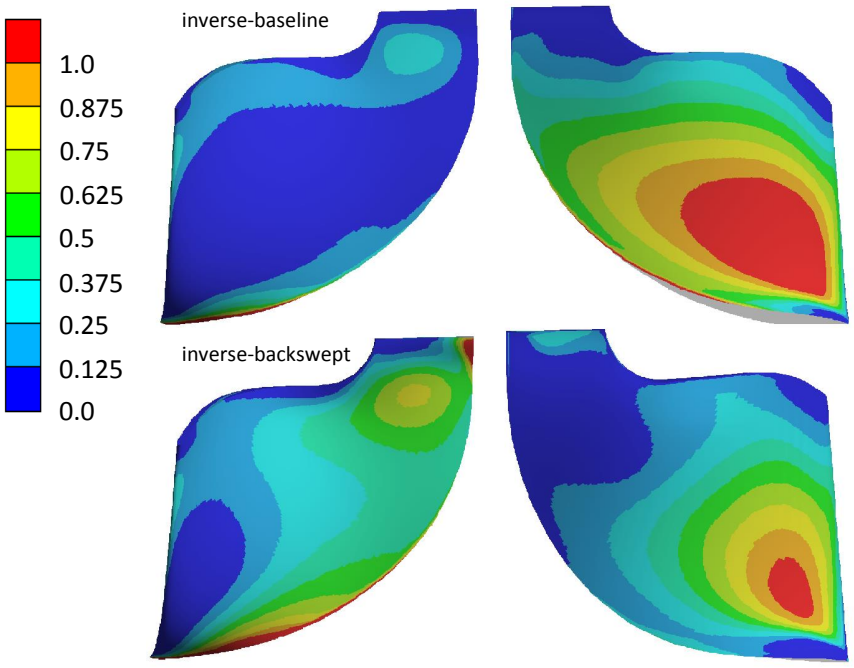

Fig. 6.22 Comparison of maximum principle stress (scaled) contours (left - pressure surface, right - suction surface)

6.3.1 Radial Filament Modification Method 2

Unlike RFM1, RFM2 divides the meridional plane of the turbine rotor into three separate regions as shown in Figure 6.23. Different treatments are applied to the different regions:

Region I: unchanged region. Blade wrap angles (θ) and blade angles (β) remain the same.

Region II: transition region. Blade wrap angles (θ) and blade angles (β) are modified to smoothly connect Region I and Region III.

Region III: radial filament region. Blade wrap angles (θ) are modified to be radial filament based on θ in the shroud ($f_{shr}(z)$), since the maximum stress concentration always occurs near the hub part of the blade exducer.

RFM2 is applied for both inverse-baseline and inverse-backswept blades. Similarly to RFM1, the blade shape in the shroud does not change as it can be seen through the comparison of the blade-to-blade views in Figure 6.26 and Figure 6.29. The blade angles with RFM2 near the LE also remain the same at different spanwise locations which can be clearly seen in Figure 6.24, Figure 6.25, Figure 6.27, and Figure 6.28. The θ distribution in the exducer part (Region III) of blades with RFM2 are radial filament as it is shown in Figure 6.30.

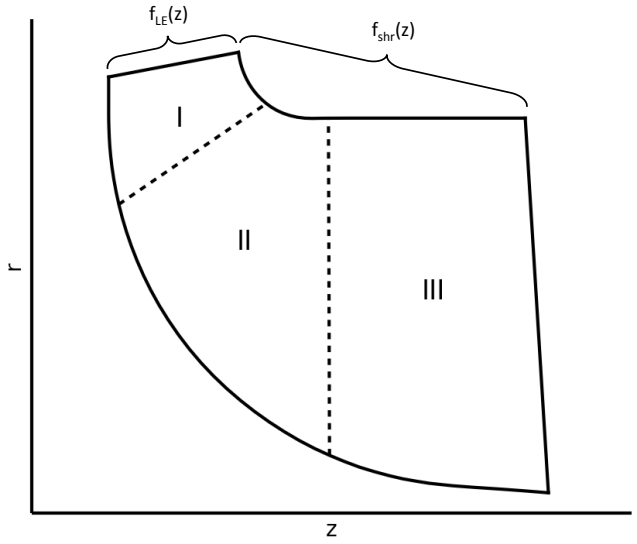

Fig. 6.23 Illustration of Radial Filament Modification method 2

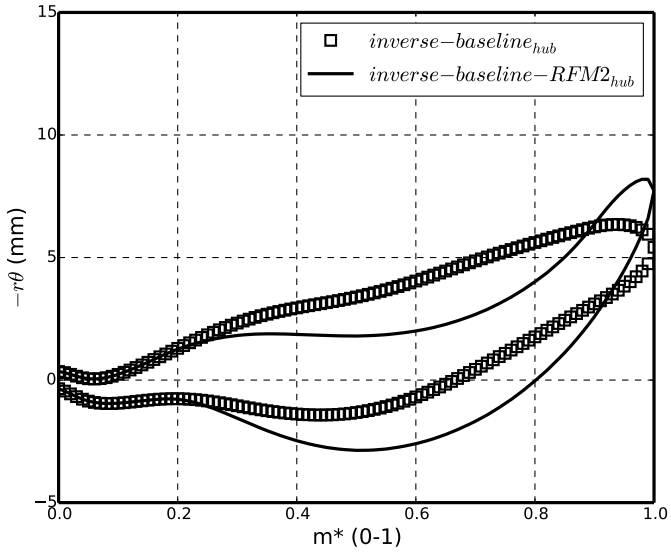

Fig. 6.24 blade-to-blade view comparison of inverse-baseline and inverse-baseline-RFM2 blades in the hub

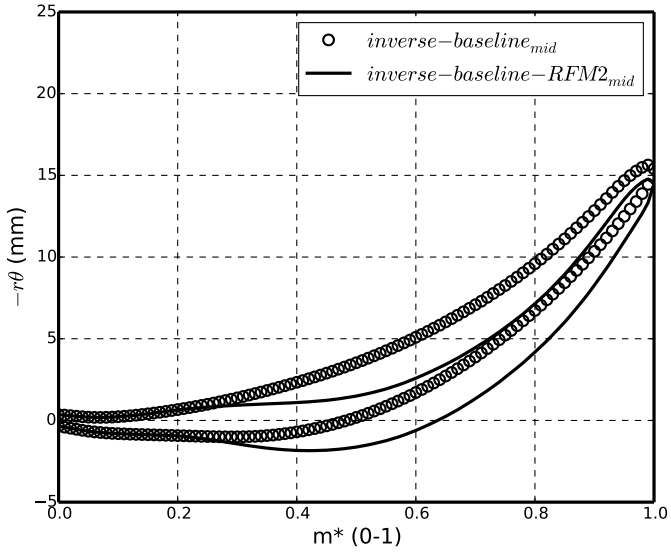

Fig. 6.25 blade-to-blade view comparison of inverse-baseline and inverse-baseline-RFM2 blades in the mid-span

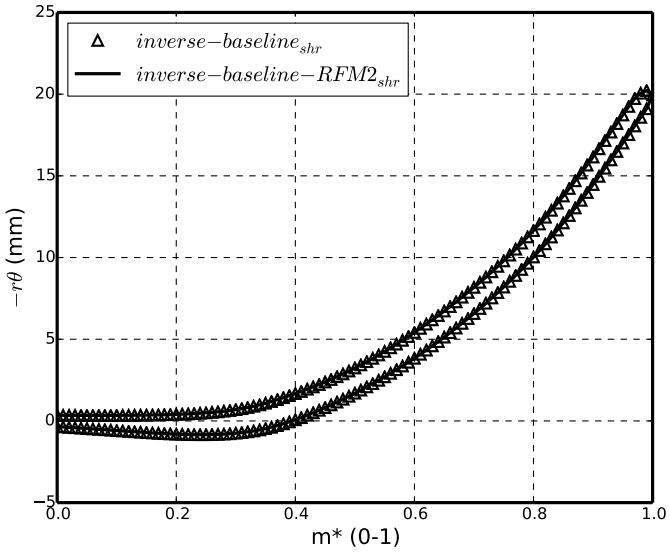

Fig. 6.26 blade-to-blade view comparison of inverse-baseline and inverse-baseline-RFM2 blades in the shroud

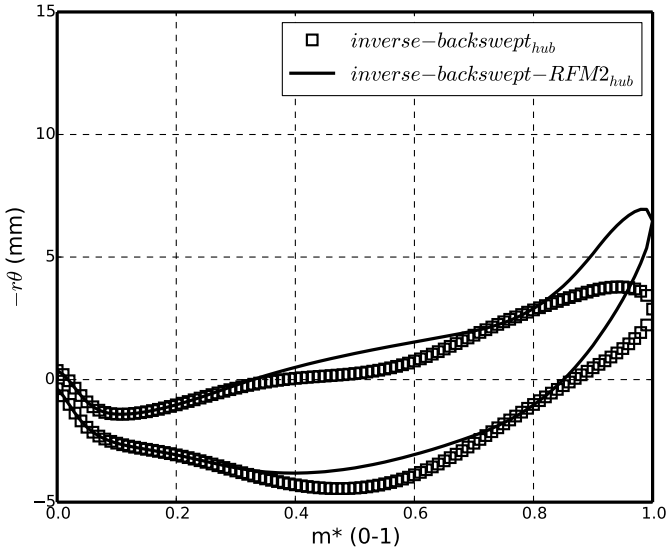

Fig. 6.27 blade-to-blade view comparison of inverse-backswept and inverse-backswept-RFM2 blades in the hub

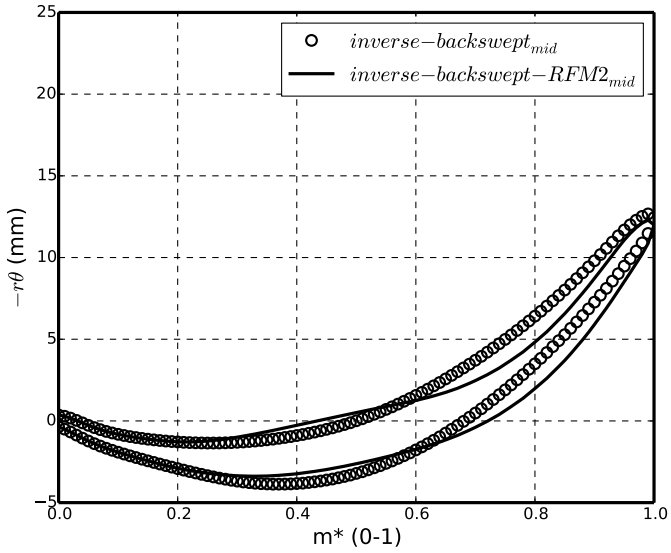

Fig. 6.28 blade-to-blade view comparison of inverse-backswept and inverse-backswept-RFM2 blades in the mid-span

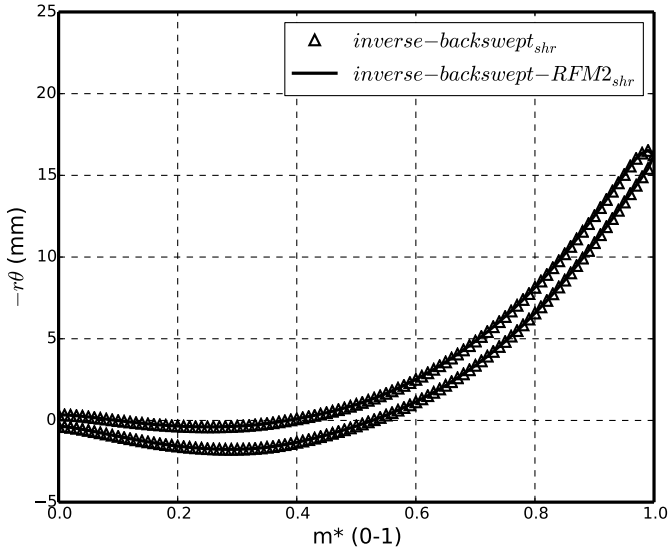

Fig. 6.29 blade-to-blade view comparison of inverse-backswept and inverse-backswept-RFM2 blades in the shroud

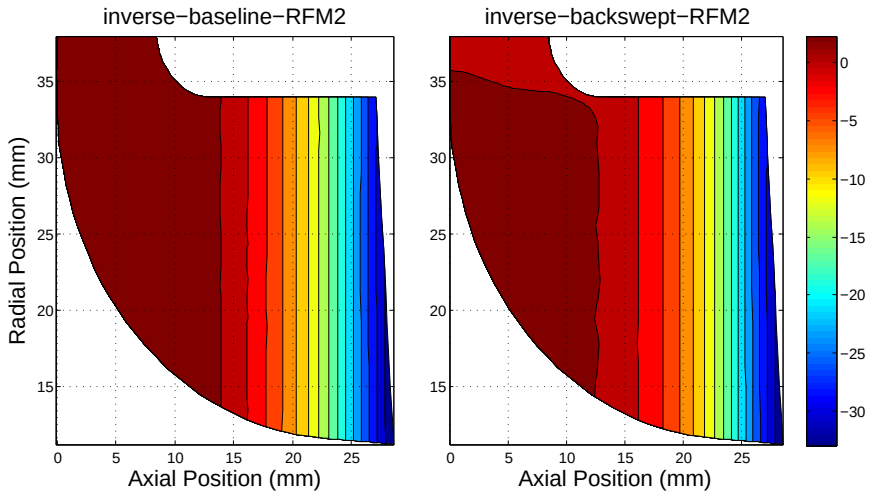

Fig. 6.30 Wrap angle contours of inverse-baseline-RFM2 and inverse-backswept-RFM2

The stress level of the inverse design blades is significantly reduced by applying RFM2 which can be seen through the comparison of maximum principle stress contours in Figure 6.22 and Figure 6.31. The stress concentration (red area) on the blade surfaces is removed after RFM2 especially on the suction surface. The stress on the root (hub) of the RFM2 blades is still quite high due to the limitation of the numerical calculation on the sharp edges which can be removed by applying the fillet in a detailed FEA analysis.

Since RFM2 keeps the same LE blade angle, it is now possible to generate a backswept blade using the inverse design method which maintains a reasonable level of stress. In terms of the aerodynamic performance, the inverse-backswept-RFM2 blade behaves similarly to the backswept blade using conventional design. The t-s efficiency curve of the inverse-backswept-RFM2 blade shifts towards the lower U/C_{is} region as it can be seen in Figure 6.33.

6.4 Increasing Pulse Energy Recovery Using Backswept Blades

An unsteady CFD simulation is performed to compare the unsteady performance of the inverse-baseline-RFM2 and the inverse-backswept-RFM2 in the low U/C_{is} region. The computational domain includes the baseline volute, the whole nozzle

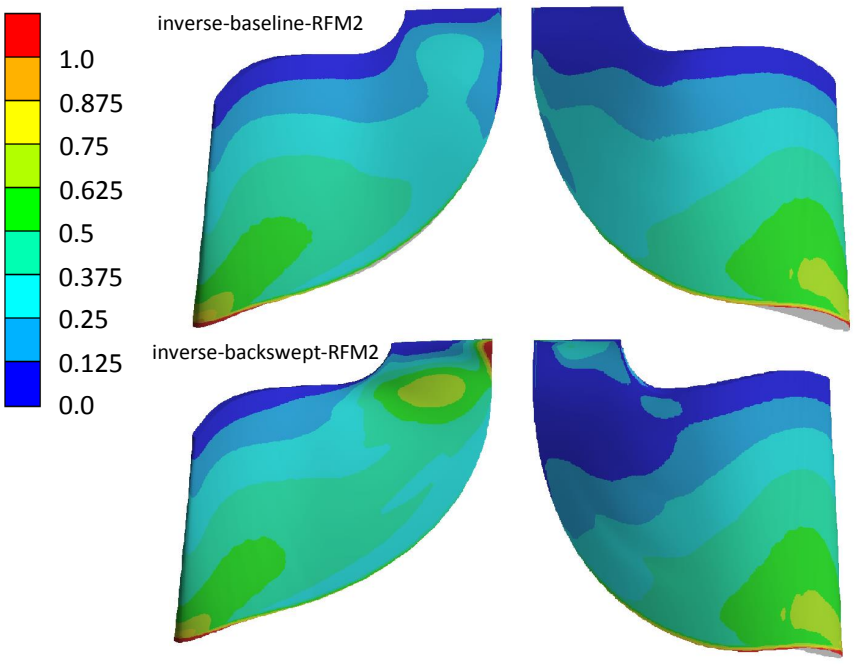

Fig. 6.31 Comparison of maximum principle stress (scaled) contours (left - pressure surface, right - suction surface)

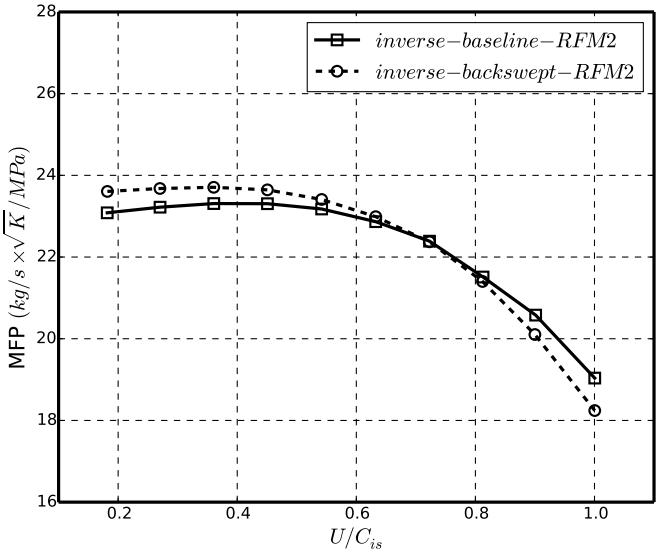

Fig. 6.32 Comparison of MFP

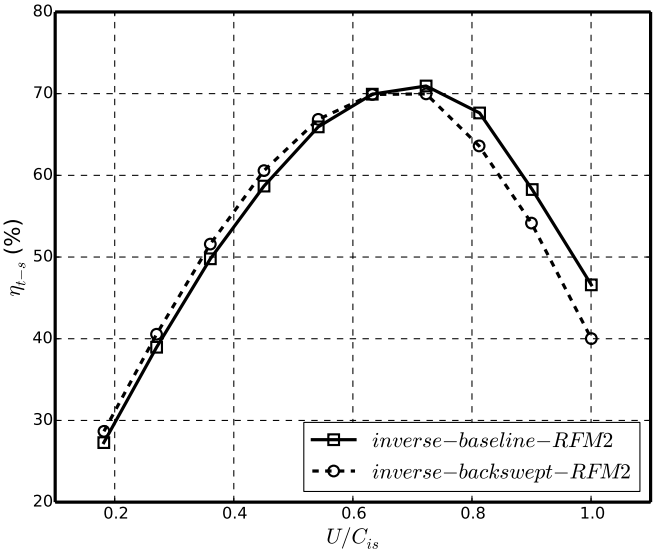

Fig. 6.33 Comparison of t-s efficiency

ring and the whole rotor wheel as shown in Figure 6.34. The total number of elements is around 3,000,000. Inlet boundary conditions are pulsating $P_{01}(t)$ and $T_{01}(t)$ as shown in Figure 6.35 and Figure 6.36. $P_{01}(t)$ is corresponding to an engine RPM of 1,000 as provided by CTT from their engine experimental tests. The measurements of total temperature at the turbine inlet are unreliable due to the thermal inertia of thermocouples. A typical temperature range of 474K - 1066K at the turbine inlet is selected and the similar pressure pulse shape is applied to generate the pulsating inlet total temperature $T_{01}(t)$. The turbine rotating speed ($\Omega = 40,000$ rev/min) and the outlet static pressure ($P_2 = 1.0$ *bar*) are set as constant since their variation are negligible during the pulsating flow. The turbine rotating speed is selected as 40,000 rev/min to make sure the instantaneous velocity ratio $\frac{U}{C_{is}}(t)$ is always less than 0.6. Since P_{01} and T_{01} are not constant in a pulsating flow, U/C_{is} is not constant but a function of time and is defined by Equation 6.3. The time step is set as 1×10^{-4} s. The interface between the nozzle ring and the rotor is modelled by using transient rotor-stator in the ANSYS CFX. CFD results from steady state calculations are used for the initialisation to improve the convergence of the unsteady calculation.

$$\frac{U}{C_{is}}(t) = \frac{\Omega R_{tip}}{\sqrt{2c_p T_{01}(t)\left[1 - \left(\frac{P_2}{P_{01}(t)}\right)^{(\gamma-1)/\gamma}\right]}} \tag{6.3}$$

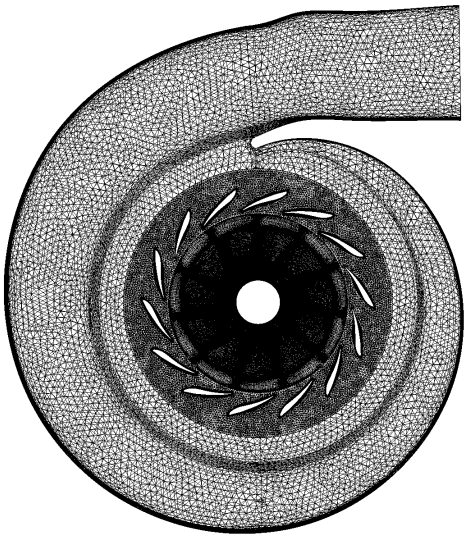

Fig. 6.34 Computational domain of volute + whole nozzle and rotor wheel

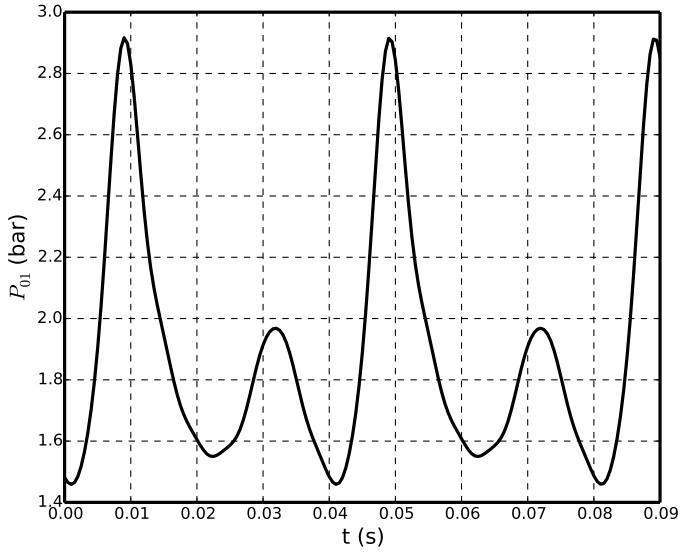

Fig. 6.35 Pulsating inlet total pressure $P_{01}(t)$

The instantaneous isentropic power $\dot{W}_{is}(t)$ (defined by Equation 6.4) and the instantaneous turbine power $\dot{W}_T(t)$ (defined by Equation 6.5) for these two designs are shown in Figure 6.37 and Figure 6.38. The trend of $\dot{W}_{is}(t)$ and $\dot{W}_T(t)$ for inverse-baseline-RFM2 and inverse-backswept-RFM2 are very similar due to the

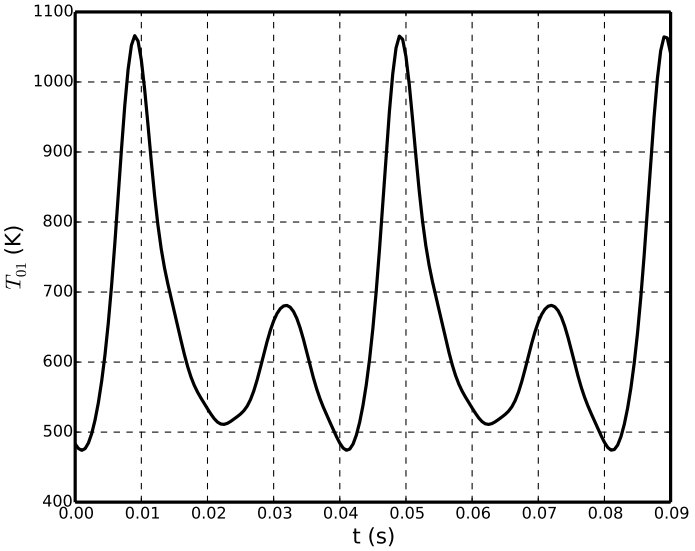

Fig. 6.36 Pulsating inlet total temperature $T_{01}(t)$

same pulsating inlet boundary conditions applied at the turbine inlet. A finite time lag Δt between the peak $\dot{W}_{is}(t)$ and peak $\dot{W}_T(t)$ can be observed since $\dot{W}_{is}(t)$ is calculated at the volute inlet while $\dot{W}_T(t)$ is calculated at the rotor. The exhaust gas requires this finite time lag Δt to travel from the volute inlet to the rotor passage. It is important to accurately determine the value of this time lag Δt when instantaneous t-s efficiency $\eta_{t-s}(t)$ is calculated by Equation 6.6.

$$\dot{W}_{is}\left(t\right) = \dot{m}_1\left(t\right) c_p T_{01}\left(t\right) \left[1 - \left(\frac{P_2}{P_{01}\left(t\right)}\right)^{(\gamma-1)/\gamma}\right] \tag{6.4}$$

$$\dot{W}_T\left(t\right) = \Omega\tau\left(t\right) \tag{6.5}$$

$$\begin{aligned} \eta_{t-s}\left(t\right) &= \frac{\dot{W}_T\left(t+\Delta t\right)}{\dot{W}_{is}\left(t\right)} \\ &= \frac{\Omega\tau\left(t+\Delta t\right)}{\dot{m}_1\left(t\right) c_P T_{01}\left(t\right)\left[1 - \left(P_2\left(t\right)/P_{01}\left(t\right)\right)^{(\gamma-1)/\gamma}\right]} \end{aligned} \tag{6.6}$$

However, cycle-averaged t-s efficiency $\bar{\eta}_{t-s}$ whose calculation does not need the time lag Δt is more important than $\eta_{t-s}(t)$ for the turbocharger unsteady performance. $\bar{\eta}_{t-s}$ is defined by Equation 6.7. Where $\Delta T = \frac{1}{f}$ and f is the frequency of the

inlet pulse, W_T is the total turbine work during one pulse period (ΔT) and W_{is} is the total isentropic work during ΔT. Figure 6.39 and Figure 6.40 show the variation of $\dot{W}_{is}(t)$ and $\dot{W}_T(t)$ versus $\frac{U}{C_{is}}(t)$. It can be seen that most of $\dot{W}_{is}(t)$ and $\dot{W}_T(t)$ are available in the very low U/C_{is} region with high total pressure and total temperature. Therefore, it can be beneficial for the $\bar{\eta}_{t-s}$ to improve the steady t-s efficiency at low U/C_{is} region.

The range of U/C_{is} for this pulse flow is between 0.21 - 0.51 (see Figure 6.39 and Figure 6.40). The inverse-backswept-RFM2 blade has higher steady η_{t-s} at this range of U/C_{is} than inverse-baseline-RFM2 blade (see Figure 6.33). Therefore, it can be predicted that inverse-backswept-RFM2 blade will have better unsteady performance (higher $\bar{\eta}_{t-s}$) compared to inverse-baseline-RFM2 blade. Figure 6.41 shows that inverse-backswept-RFM2 blade does generate higher turbine power than the baseline blade for the same pulse at this low U/C_{is} region. Total isentropic work, total turbine work during one pulse period and cycle-averaged t-s efficiency of these two designs are summarised in Table 6.2. Inverse-backswept-RFM2 blade gives higher 1.33% $\bar{\eta}_{t-s}$.

$$\begin{aligned}\bar{\eta}_{t-s} &= \frac{W_T}{W_{is}} \\ &= \frac{\int_t^{t+\Delta T} \dot{W}_T(t)\,dt}{\int_t^{t+\Delta T} \dot{W}_{is}(t)\,dt} \\ &= \frac{\int_t^{t+\Delta T} \Omega\tau(t)\,dt}{\int_t^{t+\Delta T} \dot{m}_1(t)\,c_P T_{01}(t)\left[1-\left(P_2(t)/P_{01}(t)\right)^{(\gamma-1)/\gamma}\right]dt}\end{aligned} \tag{6.7}$$

Table 6.2 Comparison of $\bar{\eta}_{t-s}$

	inverse-baseline-RFM2	inverse-backswept-RFM2
W_{is} (kJ)	0.8941	0.9129
W_T (kJ)	0.4872	0.5096
$\bar{\eta}_{t-s}$	54.49%	55.82%

Whole turbine wheel geometries for these two designs are generated by adding the variable-radius hub fillets and the backplate with scalloping as shown in Figure 6.42 and Figure 6.43. It can be clearly seen that the LE of inverse-backswept-RFM2 blade is more curved (more backswept) than the LE of inverse-baseline-RFM2

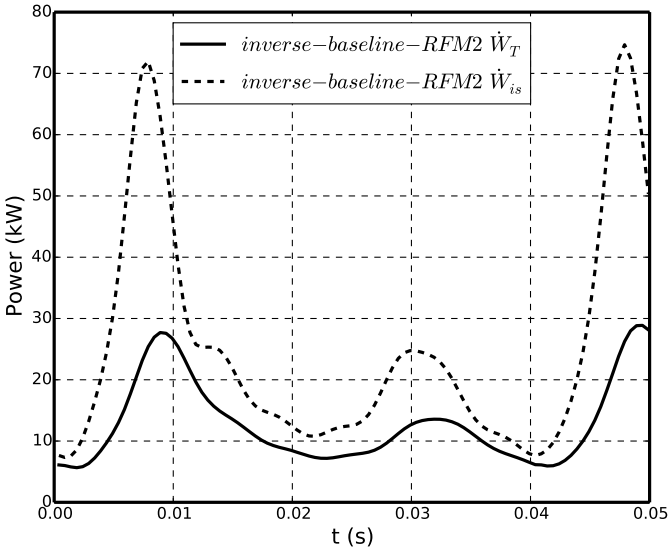

Fig. 6.37 inverse-baseline-RFM2 $\dot{W}_T(t)$ and $\dot{W}_{is}(t)$ versus time

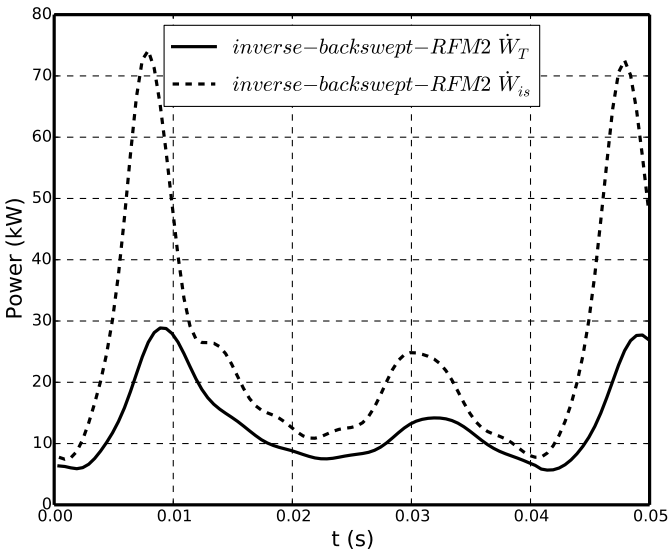

Fig. 6.38 inverse-backswept-RFM2 $\dot{W}_T(t)$ and $\dot{W}_{is}(t)$ versus time

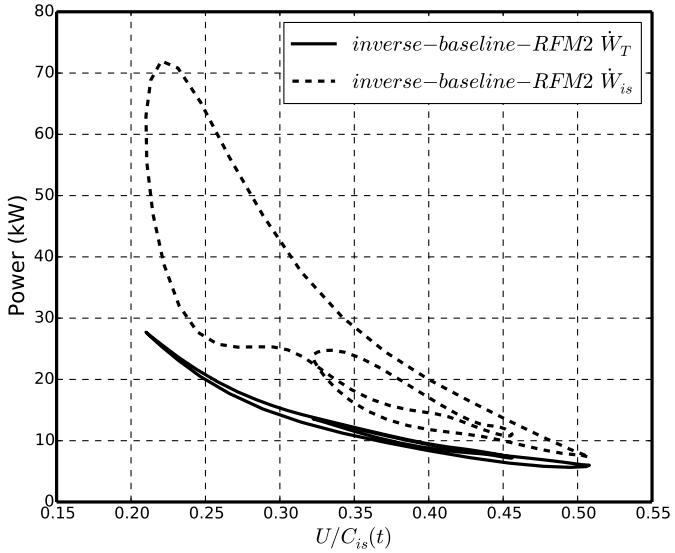

Fig. 6.39 inverse-baseline-RFM2 $\dot{W}_T(t)$ and $\dot{W}_{is}(t)$ versus $\frac{U}{C_{is}}(t)$

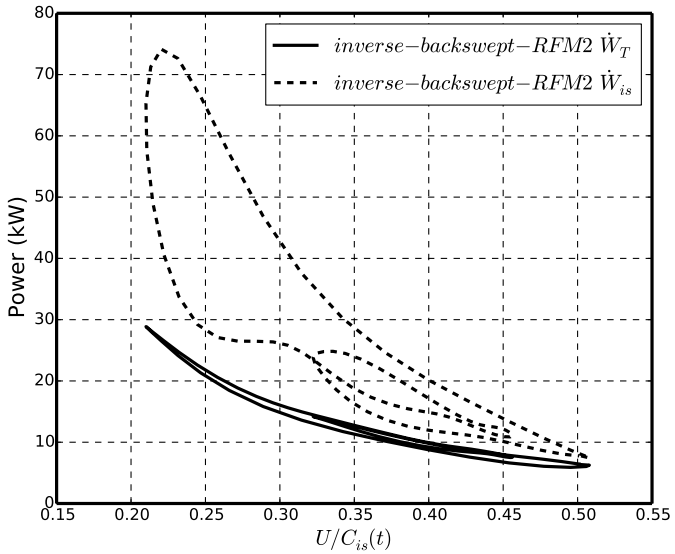

Fig. 6.40 inverse-backswept-RFM2 $\dot{W}_T(t)$ and $\dot{W}_{is}(t)$ versus $\frac{U}{C_{is}}(t)$

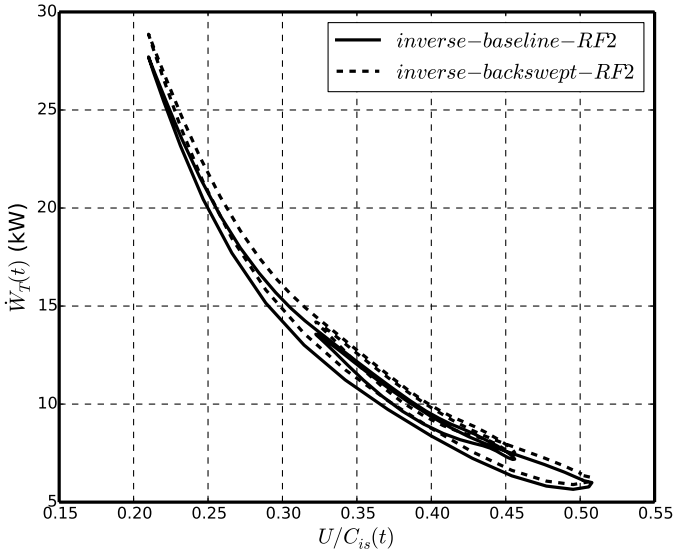

Fig. 6.41 Comparison of $\dot{W}_T(t)$ versus $\frac{U}{C_{is}}(t)$

blade from Figure 6.43. Static structural analysis with similar mesh setting and boundary conditions AS applied in section 3.3 is performed for these two models. The contours of maximum principle stress on the backplate, the blade suction surface and the pressure surface are shown in Figure 6.44, Figure 6.45 and Figure 6.46. The stress contours on the backplate and the blade suction surface are very similar for inverse-baseline-RFM2 and inverse-backswept-RFM2 and no obvious difference can be observed. However, the stress of inverse-backswept-RFM2 is much higher than inverse-baseline-RFM2 especially near the hub inducer part (orange and red areas in Figure 6.46). This stress concentration of inverse-backswept-RFM2 blade is caused by the rapid change of blade angle near THE hub LE which can be seen through the comparison of the blade angle distribution in Figure 6.47. To reduce this maximum stress and maintain a backswept LE shape, the blade meridional shape and blade loading parameters need to be carefully selected through a new optimisation based on DOE and RSM which aims to find the best trade-off between the aerodynamic performance at low U/C_{is} region and the blade mechanical strength which will be illustrated in the next chapter.

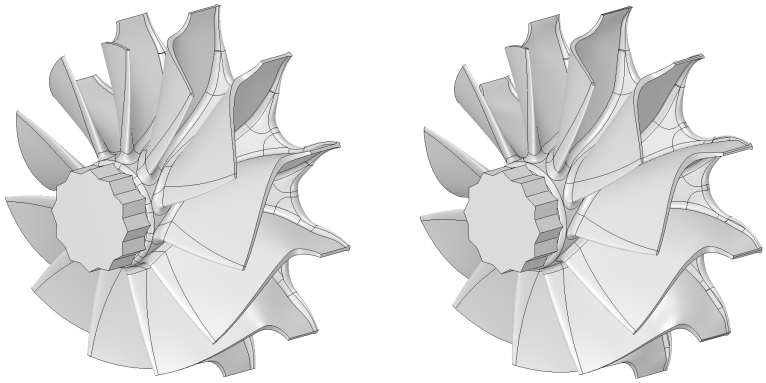

Fig. 6.42 Front view of whole wheel geometry (left - inverse-baseline-RFM2, right - inverse-backswept-RFM2)

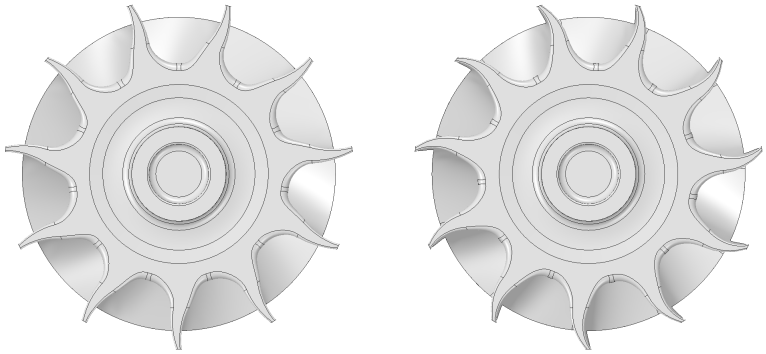

Fig. 6.43 Back view of whole wheel geometry (left - inverse-baseline-RFM2, right - inverse-backswept-RFM2)

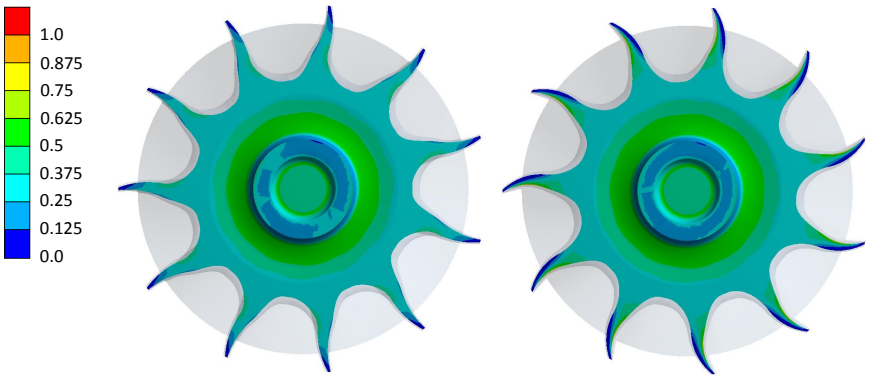

Fig. 6.44 Maximum principle stress (scaled) contour on the back face (left - inverse-baseline-RFM2, right - inverse-backswept-RFM2)

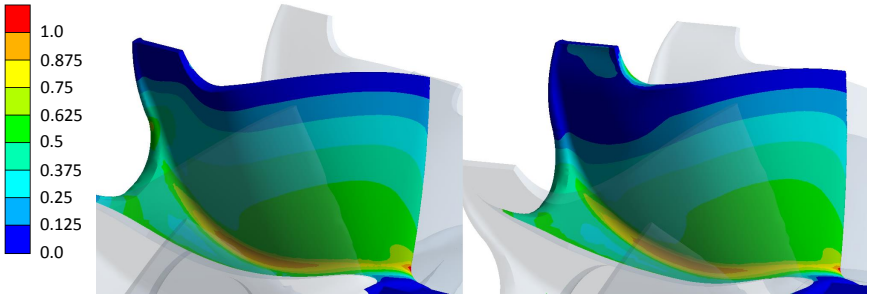

Fig. 6.45 Maximum principle stress (scaled) contour on the blade suction surface (left - inverse-baseline-RFM2, right - inverse-backswept-RFM2)

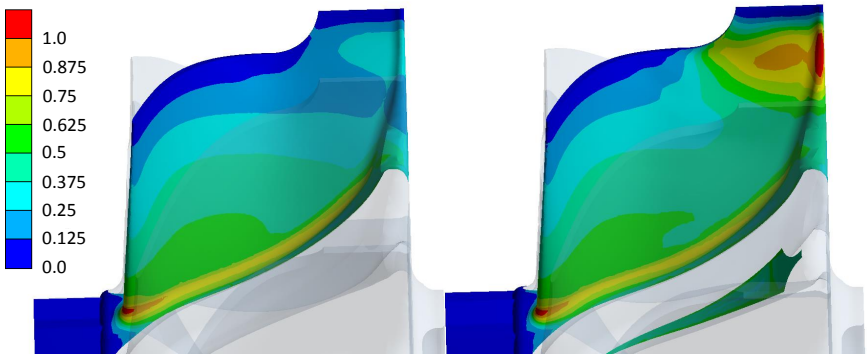

Fig. 6.46 Maximum principle stress (scaled) contour on the blade pressure surface (left - inverse-baseline-RFM2, right - inverse-backswept-RFM2)

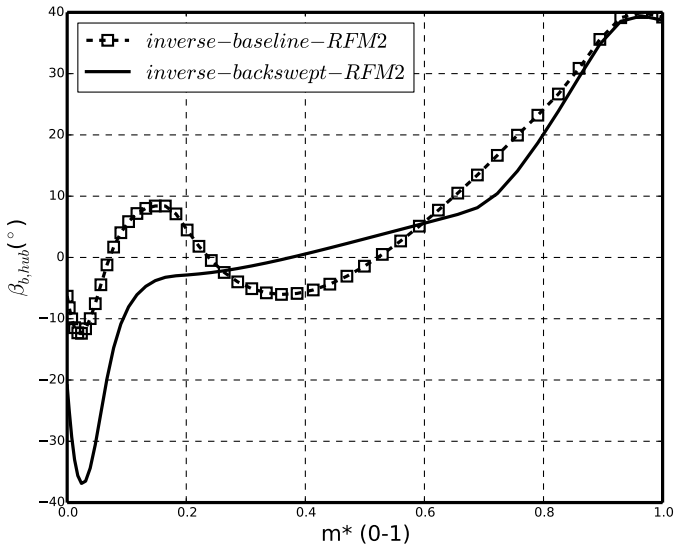

Fig. 6.47 Hub blade angle $\beta_{b,hub}$ comparison

6.5 Summary

Radial turbines with a backswept LE have higher efficiencies at low U/C_{is} region which will improve the turbine unsteady performance compared to conventional turbines with zero LE blade angles. In this chapter, two different methods used to generate radial turbines with backswept LE are first introduced. Using the conventional (direct) method, the blade LE blade (wrap) angle can be directly modified to give a backswept LE. Using the inverse design method, the backswept blade can be generated by specifying a positive LE loading. Backswept designs using both methods show very high stress on the blade surfaces. Especially, inverse-backswept blade has a very high stress concentration on the exducer part due to the non radial-filament blading. To overcome this stress problem and maintain the backswept LE, a new Radial Filament Modification method (RFM2) is introduced. Unsteady CFD simulation shows that inverse-backswept-RFM2 blade has better unsteady performance (1.3% higher $\bar{\eta}_{t-s}$). However, static structural analysis of these two turbine wheel geometries shows stress concentration near the hub LE for the inverse-backswept-RFM2 blade. A new DOE and RSM optimisation is required and will be introduced in the next chapter.

CHAPTER 7

OPTIMISATION FOR UNSTEADY PERFORMANCE

In Chapter 5, Optimisation 1 is used to find an optimal design (design 10535) which achieves most of the efficiency improvement in the high U/C_{is} (RPM = 80k and 90k). However, as discussed in Chapter 2 and Chapter 6, it is more beneficial for the unsteady performance to improve the turbine steady efficiency at low U/C_{is}.

Therefore, a new optimisation (Optimisation 2) using the similar optimisation technique as Optimisation 1 (Figure 5.1) but with a different range of design parameters and a new Radial Filament Modification method (RFM2) is presented. For Optimisation 2 the new design space includes blades with a backswept LE and improved efficiency in the low U/C_{is}.

7.1 New Linear DOE

The range of design parameters for the new linear DOE is shown in Table 7.1. Compared to the previous linear DOE design parameters (Table 5.1), ranges of most design parameters remain the same and ranges of α_1 and Y_{hub} are slightly adjusted based on the previous DOE results. The most obvious difference is that the ranges of LE loading parameters ($DRVT_{LE,hub}$ and $DRVT_{LE,shr}$) are extended

and now positive values are allowed which can generate blades with a backswept LE using the inverse design method as shown in Chapter 6.

Table 7.1 New ranges of design parameters and baseline values

Design Parameters	min	max	baseline
W_1 (mm)	7	11	8.441
W_2 (mm)	15	24	22.25
α_1 $(^\circ)$	0	30	0
α_2 $(^\circ)$	0	10	3.86
Y_{hub} (mm)	16	21	—
Y_{shr}	0.2	0.4	—
$r\bar{V}_{\theta TE,hub}$	0	0.04	—
$r\bar{V}_{\theta TE,shr}$	0.06	0.1	—
NC_{hub}	0.05	0.156	—
NC_{shr}	0.05	0.4	—
ND_{hub}	0.6	0.85	—
ND_{shr}	0.6	0.85	—
$SLOPE_{hub}$	1	2.5	—
$SLOPE_{shr}$	-5	-1	—
$DRVT_{LE,hub}$	-0.8	0.6	—
$DRVT_{LE,shr}$	-0.8	0.6	—
$Thickness\ Parameter$	0.9	1.2	1.0

7.1.1 Comparison of 3D and RFM2 Blades

25 designs are generated for 17 design parameters with the ranges specified in Table 7.1 using OLHS. Finally 21 designs converge and generate 3D blade geometries using the inverse design method. Radial Filament Modification method 2 is applied to these 3D designs to get 21 RFM2 blades. CFD and FEA analysis are performed for both these 3D and RFM2 blades and the results are shown in Figure 7.1 to Figure 7.14.

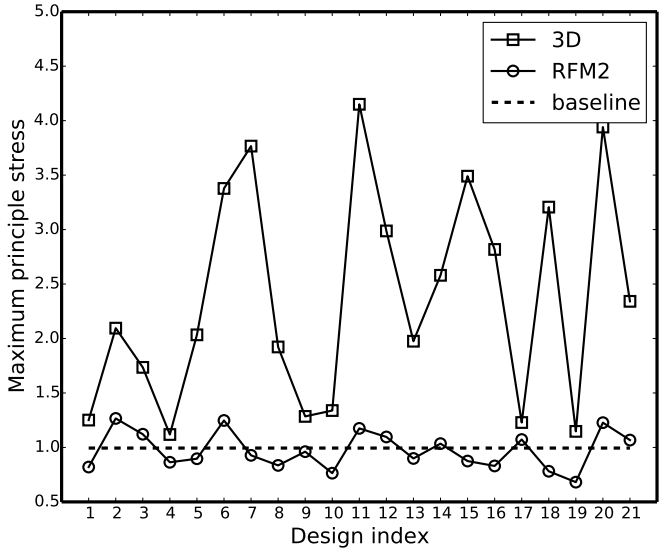

Fig. 7.1 Stress (scaled) comparison of 3D and RFM2 blades

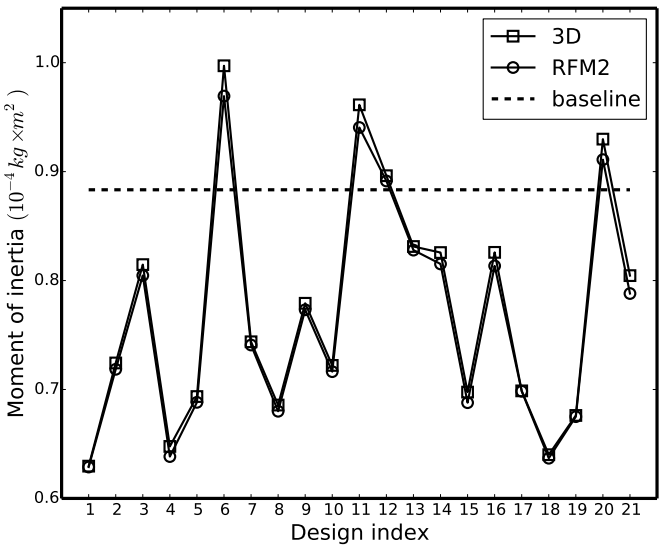

Fig. 7.2 Moment of inertia comparison of 3D and RFM2 blades

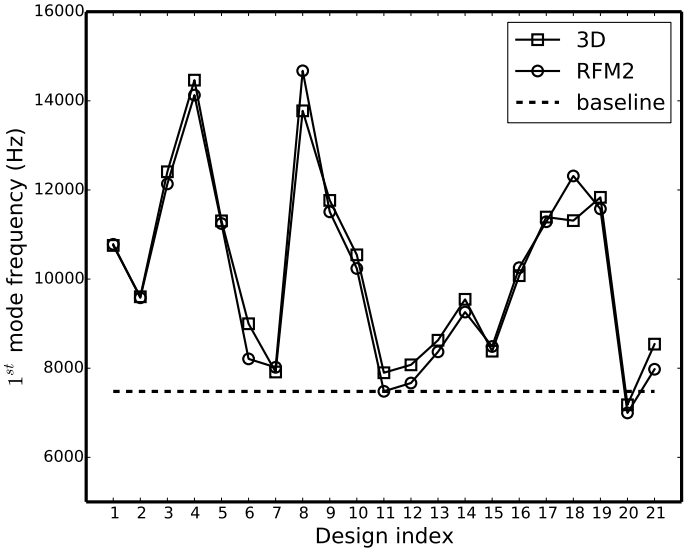

Fig. 7.3 1^{st} vibration mode frequency comparison of 3D and RFM2 blades

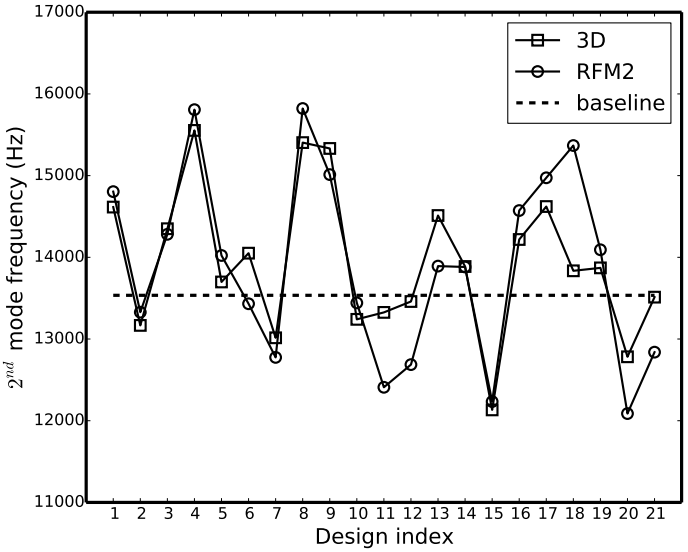

Fig. 7.4 2^{nd} vibration mode frequency comparison of 3D and RFM2 blades

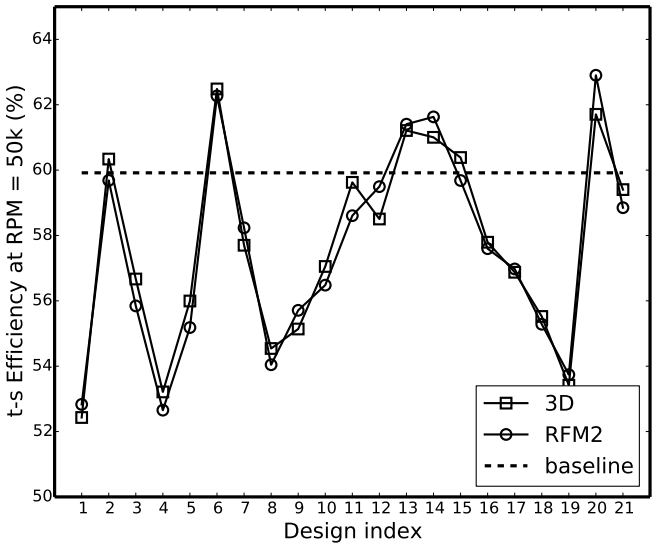

Fig. 7.5 $\eta_{t-s,50k}$ comparison of 3D and RFM2 blades

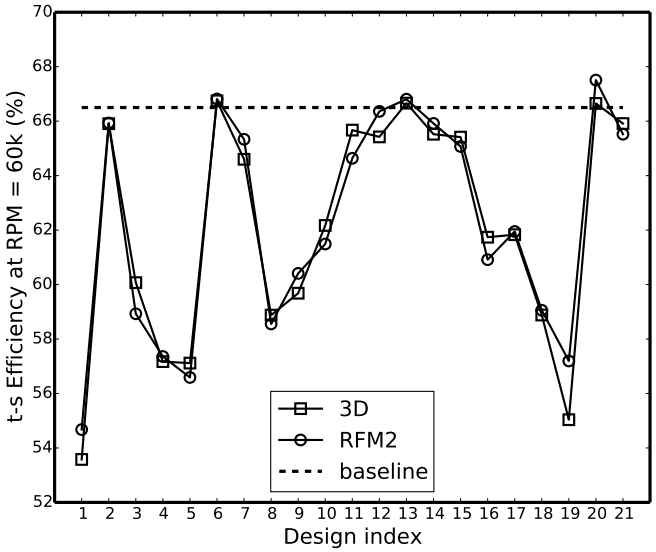

Fig. 7.6 $\eta_{t-s,60k}$ comparison of 3D and RFM2 blades

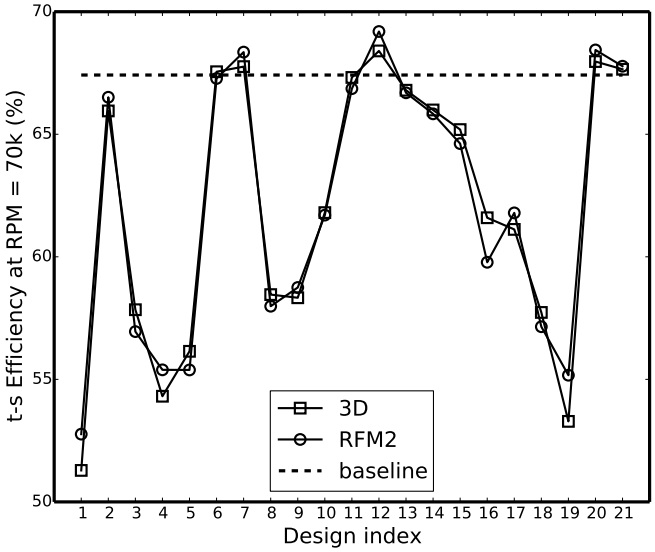

Fig. 7.7 $\eta_{t-s,70k}$ comparison of 3D and RFM2 blades

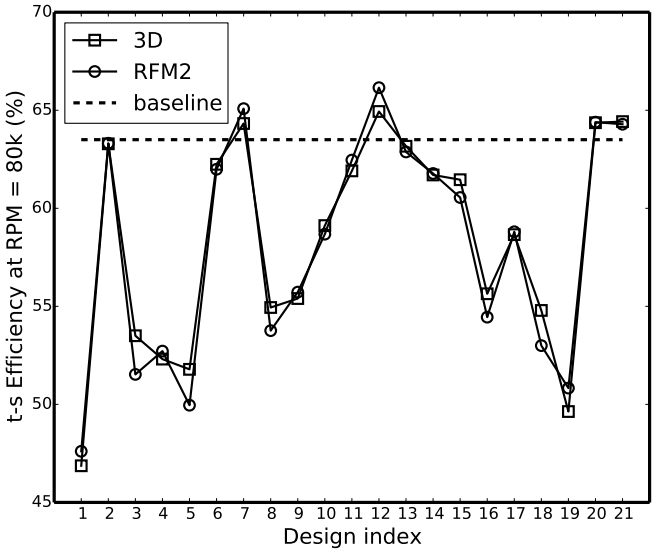

Fig. 7.8 $\eta_{t-s,80k}$ comparison of 3D and RFM2 blades

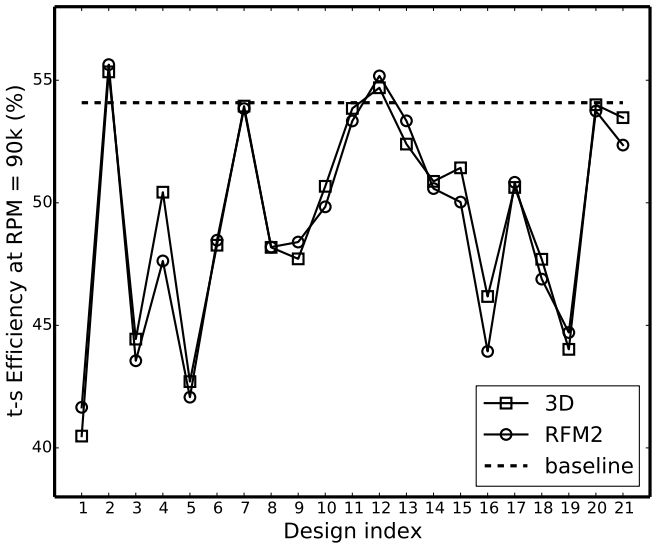

Fig. 7.9 $\eta_{t-s,90k}$ comparison of 3D and RFM2 blades

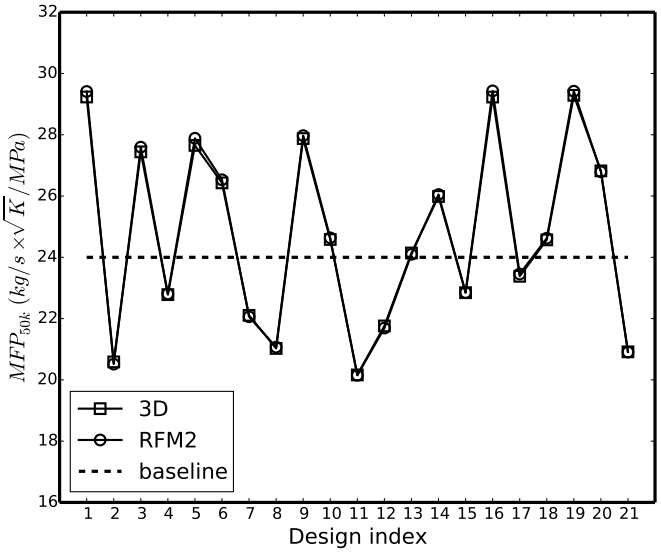

Fig. 7.10 MFP_{50k} comparison of 3D and RFM2 blades

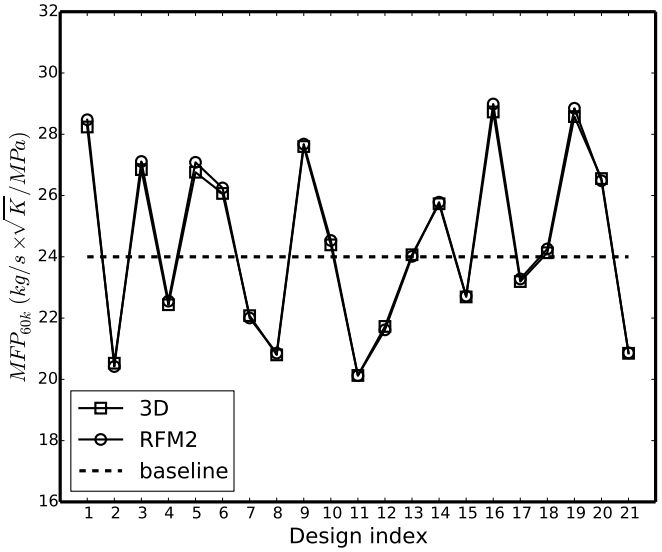

Fig. 7.11 MFP_{60k} comparison of 3D and RFM2 blades

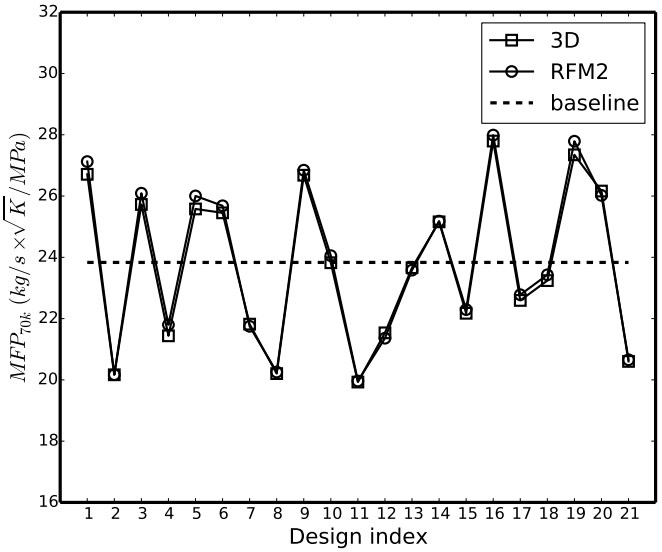

Fig. 7.12 MFP_{70k} comparison of 3D and RFM2 blades

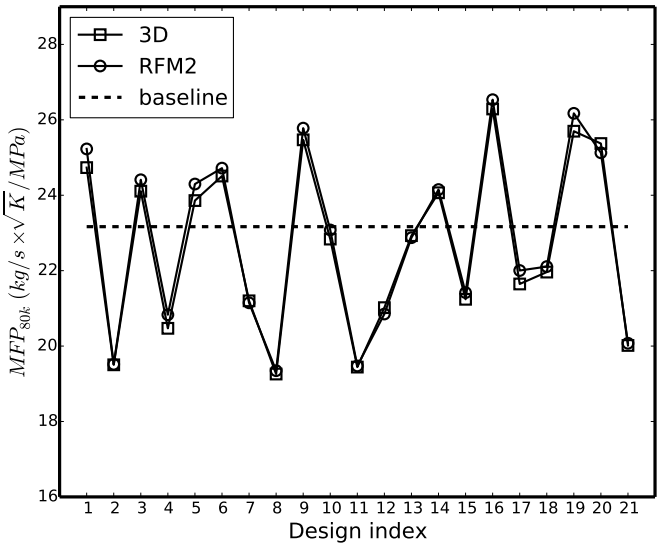

Fig. 7.13 MFP_{80k} comparison of 3D and RFM2 blades

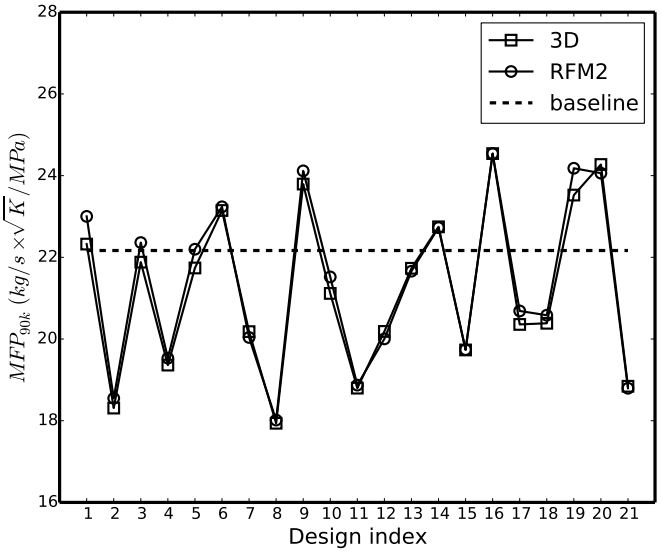

Fig. 7.14 MFP_{90k} comparison of 3D and RFM2 blades

Similarly to RFM1, the stress values of RFM2 blades are successfully reduced to a reasonable level compared to the baseline as shown in Figure 7.1. The MOI, vibration frequencies and efficiencies of RFM2 blades are changed slightly and the MFP of RFM2 bladesare almost kept the same compared to the original 3D blades. By comparing Figure 5.26, Figure 5.30, Figure 7.5 and Figure 7.9, it is noted that RFM2 has more designs with higher $\eta_{t-s,50k}$ and less designs with higher η_{90k} compared to RFM1. This can be explained by that RFM2 and the new ranges of design parameters allow the new design space to contain the blades with a backswept LE which was shown in section 6.3 to improve the efficiency at low U/C_{is}.

7.1.2 Sensitivity Analysis

The 8 most significant design parameters selected in Chapter 5 is based on the sensitivity analysis of the linear DOE results of 19 RFM1 blades and is not applicable to the new linear DOE with the new ranges of design parameters and RFM2. Therefore, a new sensitivity study is performed based on the new linear DOE results of 21 RFM2 blades using the same method and the normalised coefficients $\tilde{A}_i^j$ are shown in Table 7.2.

The most significant design parameters are selected based on the summation of all the absolute values of $\tilde{A}_i^j$ as shown in Figure 7.15. It is desirable to make $(x_3 : DRVT_{LE,h})$ as a significant parameter for the following reasons:

1) It can be used to control the LE blade angle ($\beta_{b,LE}$) to improve the turbine performance at different U/C_{is};

2) It has the biggest effect on the stress since $\tilde{A}_3^{11} = 100$.

There are another 8 design parameters whose summation value of $abs\tilde{A}_i^j$ is greater than that of $DRVT_{LE,h}$ (188) which means they are more important compared to $DRVT_{LE,h}$. Therefore, in total 9 design parameters are selected as the most significant parameters and highlighted in grey in Table 7.2 and Figure 7.15.

Table 7.2 Comparison of normalised coefficients $\tilde{A}_i^j$ (most significant parameters highlighted)

		x_1	x_2	x_3	x_4	x_5	x_6	x_7	x_8	x_9	x_{10}	x_{11}	x_{12}	x_{13}	x_{14}	x_{15}	x_{16}	x_{17}
		α_1	α_2	$DRVT_{LE,h}$	$DRVT_{LE,s}$	NC_h	NC_s	ND_h	ND_s	$RVT_{TE,h}$	$RVT_{TE,s}$	$SLOPE_h$	$SLOPE_s$	Th	W_1	W_2	Y_h	Y_s
y_1	$\eta_{t-s,50k}$	-7	5	23	18	20	-1	13	-22	19	-13	1	13	-23	-2	100	11	10
y_2	$\eta_{t-s,60k}$	15	-5	14	6	24	1	14	-21	24	-9	1	11	-24	-21	100	1	11
y_3	$\eta_{t-s,70k}$	5	-14	-3	2	6	0	8	-7	0	-9	19	13	-21	-28	100	-11	3
y_4	$\eta_{t-s,80k}$	20	-7	0	0	9	-2	6	-10	13	-10	7	12	-20	-42	100	-8	6
y_5	$\eta_{t-s,90k}$	76	32	19	2	38	-40	-6	-19	89	-23	-61	13	-21	-100	72	12	4
y_6	MFP_{50k}	-4	-1	1	3	-1	1	1	1	-3	0	3	-1	0	100	6	1	2
y_7	MFP_{60k}	-1	-3	0	3	2	1	2	0	-1	1	2	0	-1	100	10	1	4
y_8	MFP_{70k}	1	-5	-2	4	2	-1	3	-1	0	-1	3	1	-4	100	18	0	5
y_9	MFP_{80k}	7	-4	-1	6	5	-3	3	-6	7	-2	-3	3	-5	100	24	3	7
y_{10}	MFP_{90k}	15	2	2	10	9	-13	1	-11	20	-6	-17	5	-1	100	25	10	6
y_{11}	$Stress$	76	11	100	36	39	-62	7	-25	58	-51	-55	10	15	-14	43	94	14
y_{12}	$1^{st}freq$	13	16	6	1	13	-17	-3	-8	20	2	-27	5	21	-7	-100	33	-2
y_{13}	$2^{nd}freq$	23	42	10	3	22	-8	-9	-22	22	-9	-31	10	28	-3	-100	49	0
y_{14}	MOI	-27	-5	7	4	-9	-4	-1	1	1	-5	-7	3	43	0	100	56	6
	$Summation$	291	153	188	100	198	153	76	155	279	139	236	102	230	716	899	292	81

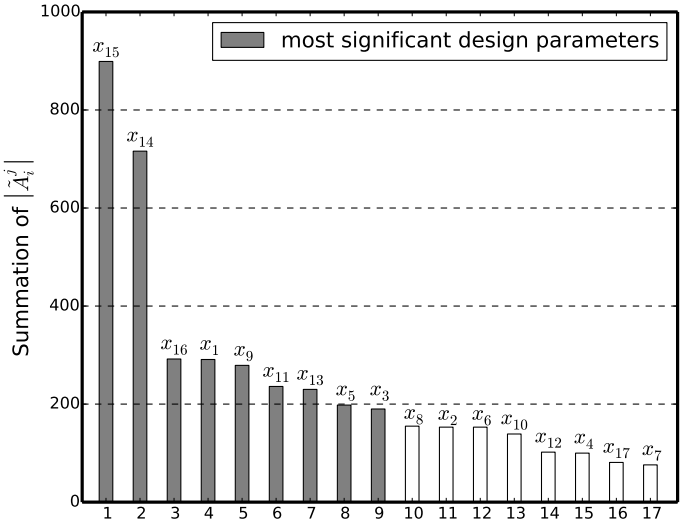

Fig. 7.15 Most significant design parameters selected based on the summation of $\left|\tilde{A}_i^j\right|$

7.2 New Kriging DOE

60 designs (same as Optimisation 1) are generated using the OLHS method for the 9 new design parameters whose ranges are shown in Table 7.3. The values of other design parameters are set as medial value or the same as the baseline value since they have little effect on the performance parameters. 50 out of 60 converge and generate blade geometries using the inverse design method. Radial Filament Modification method 2 is applied to these 50 blade geometries to get RFM2 blades. CFD and FEA calculations are carried out for these 50 RFM2 blades and the results are shown in Figure 7.16 to Figure 7.29.

It can be seen that all the performance parameters of the Kriging DOE of RFM2 blades have a good distribution along the baseline values. Specially, 39.2% of RFM2 blades have higher $\eta_{t-s,50k}$ and 35.3% have higher $\eta_{t-s,60k}$ compared to the baseline. While these numbers are only 5.6% ($\eta_{t-s,50}$) and 3.7% ($\eta_{t-s,60k}$) for the RFM1 Kriging DOE. This suggests that it is possible to achieve designs with improved efficiencies in the low U/C_{is} using the new Kriging DOE. The ranges of all the performance parameters in the new Kriging DOE are shown in Table 7.4.

Table 7.3 Ranges of design parameters for new Kriging DOE

Design Parameters	min	max
α_1 (°)	0	30
$DRVT_{LE,h}$	-0.8	0.6
NC_{hub}	0.05	0.156
$r\bar{V}_{\theta TE,hub}$	0	0.04
$SLOPE_{hub}$	1	2.5
Th	0.9	1.2
W_1 (mm)	7	11
W_2 (mm)	15	24
Y_{hub} (mm)	16	21

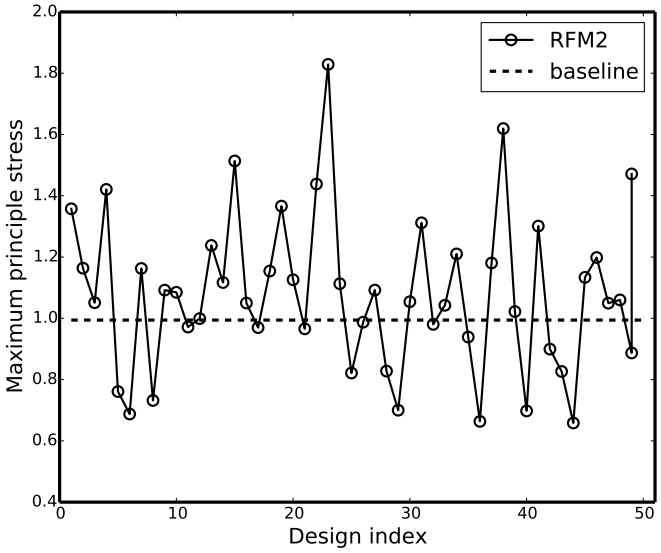

Fig. 7.16 Stress (scaled) comparison of RFM2 blades and baseline for new Kriging DOE

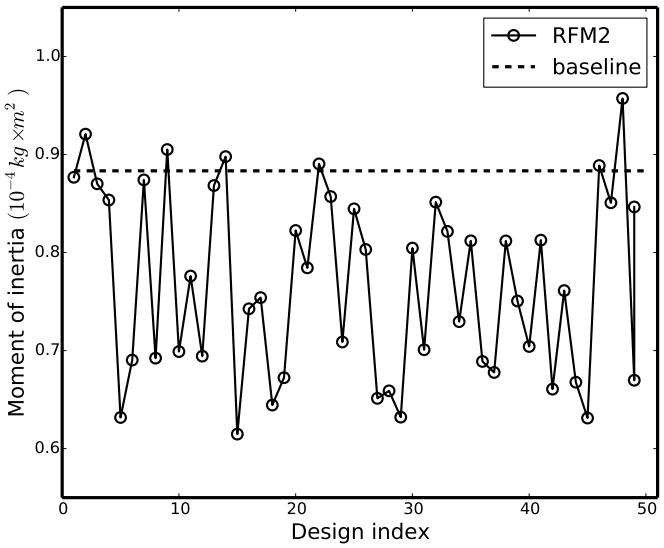

Fig. 7.17 Moment of inertia comparison of RFM2 blades and baseline for new Kriging DOE

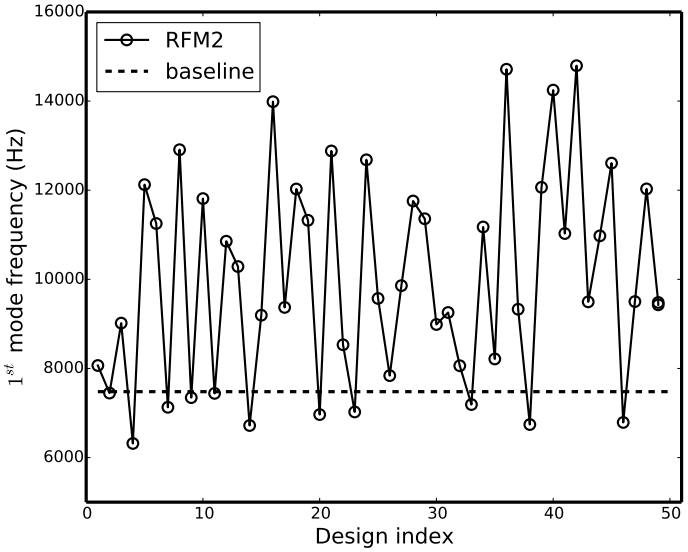

Fig. 7.18 1^{st} vibration mode frequency comparison of RFM2 blades and baseline for new Kriging DOE

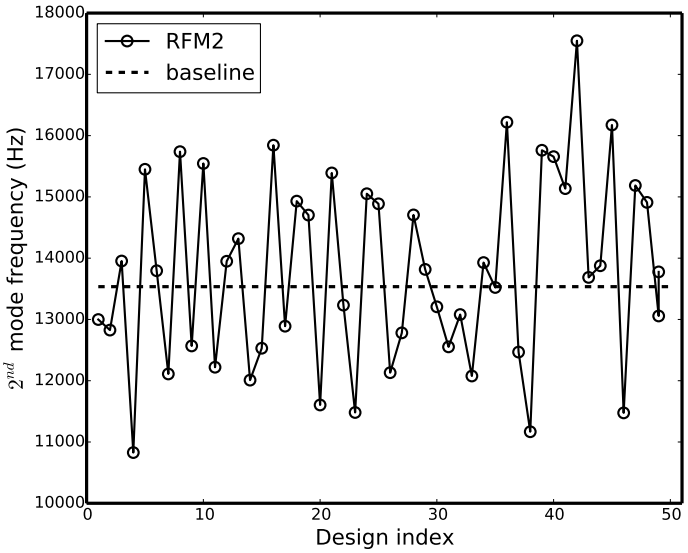

Fig. 7.19 2^{nd} vibration mode frequency comparison of RFM2 blades and baseline for new Kriging DOE

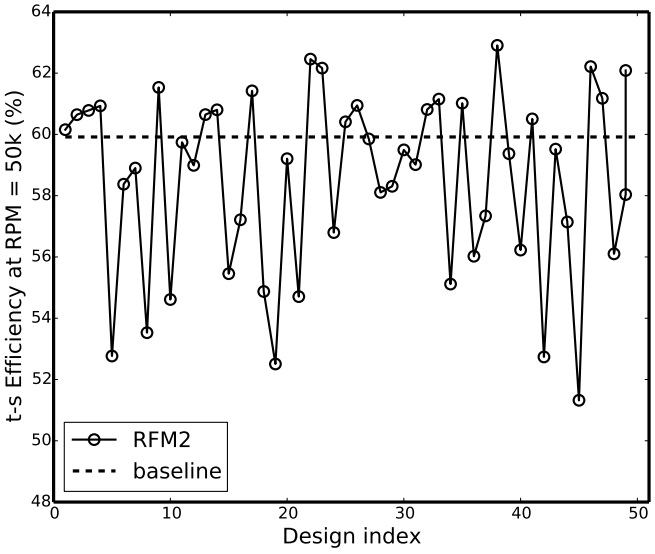

Fig. 7.20 $\eta_{t-s,50k}$ comparison of RFM2 blades and baseline for new Kriging DOE

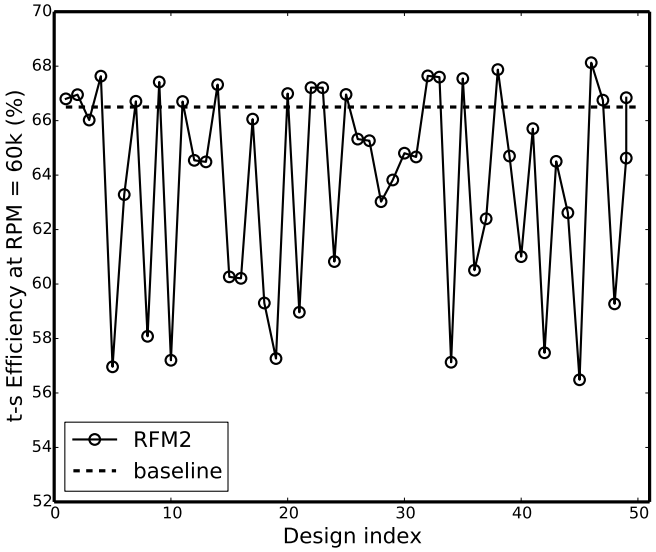

Fig. 7.21 $\eta_{t-s,60k}$ comparison of RFM2 blades and baseline for new Kriging DOE

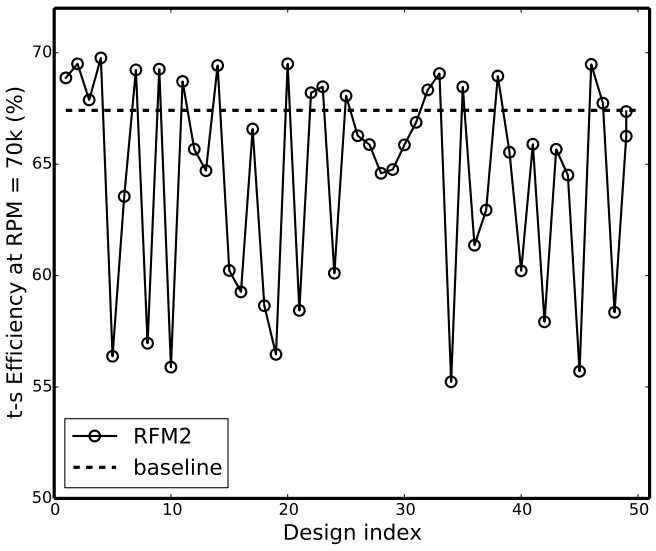

Fig. 7.22 $\eta_{t-s,70k}$ comparison of RFM2 blades and baseline for new Kriging DOE

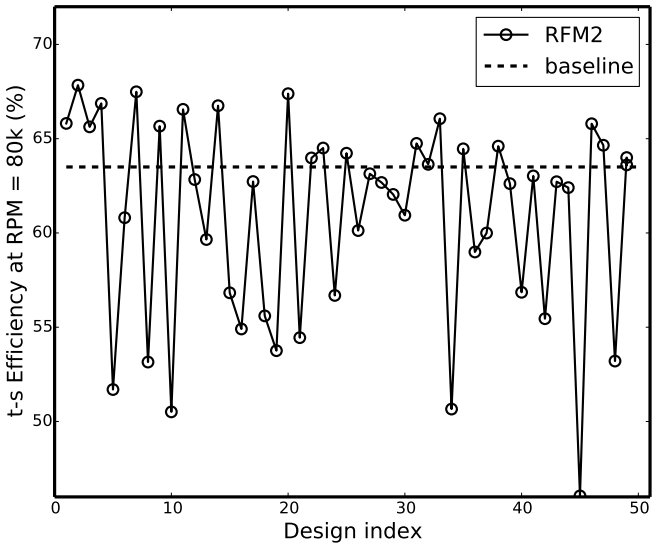

Fig. 7.23 $\eta_{t-s,80k}$ comparison of RFM2 blades and baseline for new Kriging DOE

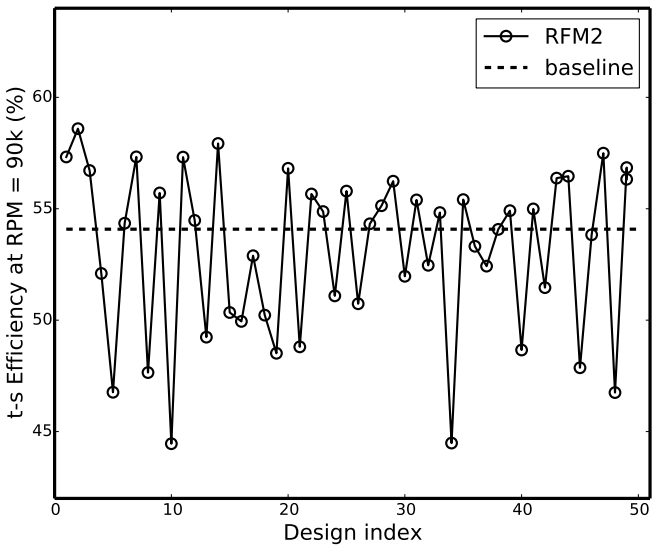

Fig. 7.24 $\eta_{t-s,90k}$ comparison of RFM2 blades and baseline for new Kriging DOE

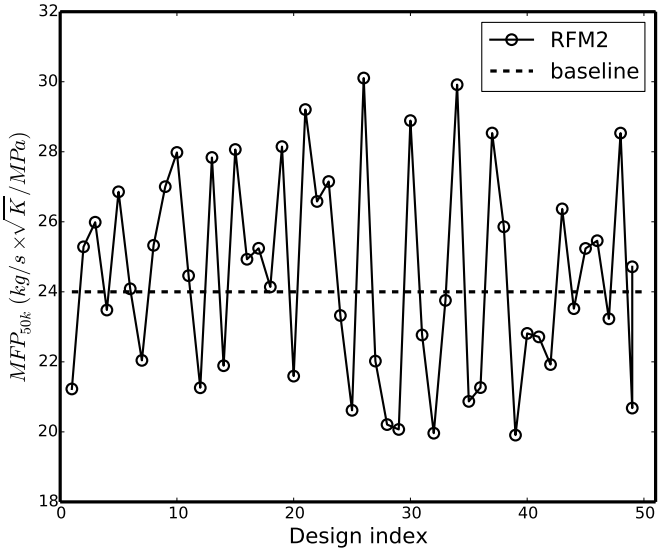

Fig. 7.25 MFP_{50k} comparison of RFM2 blades and baseline for new Kriging DOE

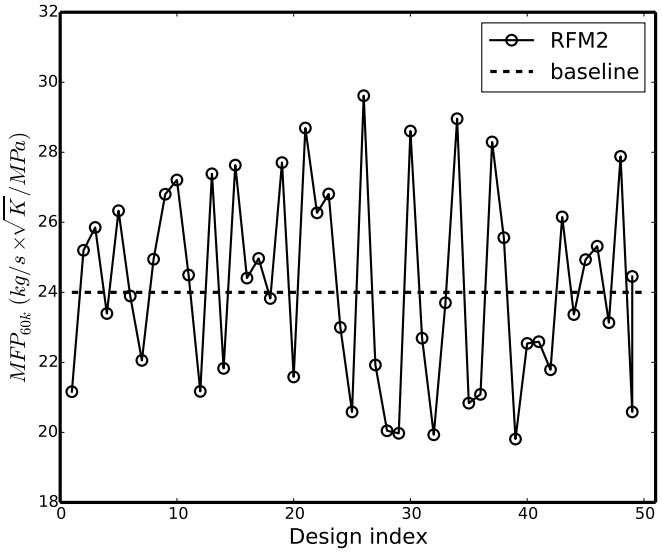

Fig. 7.26 MFP_{60k} comparison of RFM2 blades and baseline for new Kriging DOE

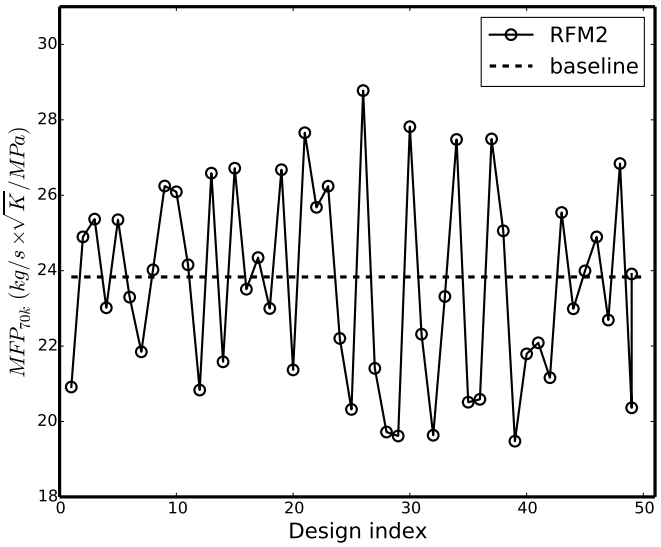

Fig. 7.27 MFP_{70k} comparison of RFM2 blades and baseline for new Kriging DOE

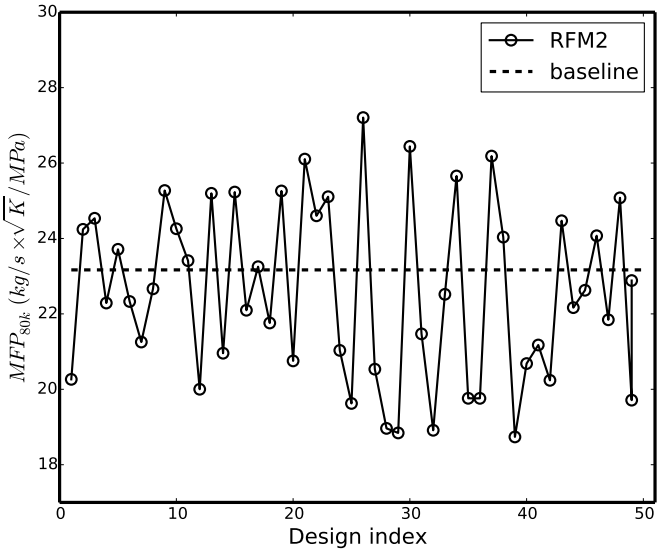

Fig. 7.28 MFP_{80k} comparison of RFM2 blades and baseline for new Kriging DOE

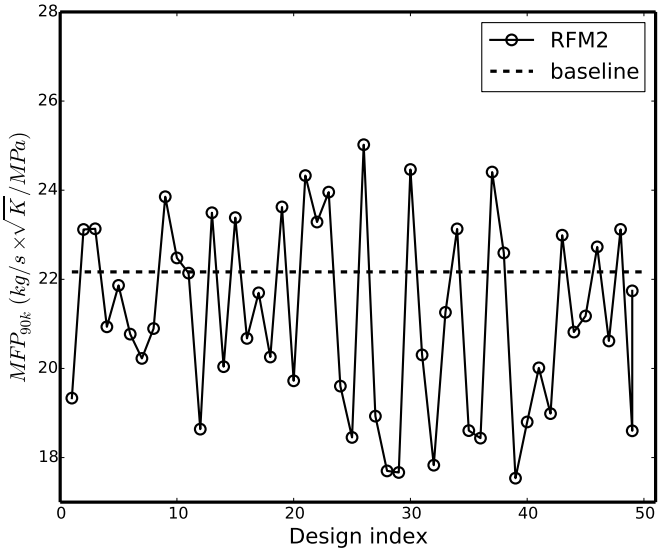

Fig. 7.29 MFP_{90k} comparison of RFM2 blades and baseline for new Kriging DOE

Kriging is then used to construct a RSM which will be used in the Optimisation 2 shown in the following subsection.

7.3 Optimisation 2 Using MOGA

Similarly to that is shown in Figure 5.51, MOGA (NSGA-II) is used to search the optimal designs on the new Kriging RSM for the constraints and objectives specified in Table 7.5 and Table 7.6. It needs to be noted that W_1 is set as 8.441 mm (baseline value) in Table 7.5. The optimisation is initially performed without constraining W_1. W_1 of all the designs on the resulting Pareto front are very close to the baseline value (8.441 mm), with the variation less than 0.1 mm. Therefore, $W_1 = 8.441$ is used as a constraint in Optimisation 2 to make sure exactly the same nozzle is used to compare the performance of the baseline and any new designs. It should also be noted that one of the objectives is changed to maximise $\eta_{t-s,50k}$ compared to Optimisation 1, since the main target of Optimisation 2 is to improve the efficiency in the low U/C_{is} (RPM = 50k).

The resulting 2D scatter plot of $\eta_{t-s,50k}$ versus Stress for Optimisation 2 is shown in Figure 7.30. Black dots denote feasible designs and blue dots denote the designs

Table 7.4 Ranges and baseline values of performance parameters for new Kriging DOE

Performance Parameters	min	max	baseline
$\eta_{t-s,50k}$ (%)	51.3	62.9	59.9
$\eta_{t-s,60k}$ (%)	56.5	68.1	66.5
$\eta_{t-s,70k}$ (%)	55.2	69.8	67.4
$\eta_{t-s,80k}$ (%)	46.1	67.8	63.5
$\eta_{t-s,90k}$ (%)	44.5	58.6	54.1
MFP_{50k} $(kg/s \cdot \sqrt{K}/MPa)$	19.9	30.1	24.0
MFP_{60k}	19.8	29.6	24.0
MFP_{70k}	19.5	28.8	23.8
MFP_{80k}	18.7	27.2	23.2
MFP_{90k}	17.5	25.0	22.2
$Stress$ (scaled)	0.659	1.829	0.99
$1^{st} freq$ (Hz)	6317	14794	7479
$2^{nd} freq$ (Hz)	10827	17548	13535
MOI $(\times 10^{-4} kg \cdot m^2)$	0.6148	0.9572	0.8834

Table 7.5 Constraints of Optimisation 2

	Constraints
$\eta_{t-s,60k}$	> 0.665
$\eta_{t-s,70k}$	> 0.674
$\eta_{t-s,80k}$	> 0.635
$\eta_{t-s,90k}$	> 0.541
MFP_{50k}	> 23.9
MFP_{60k}	> 23.8
MFP_{70k}	> 23.2
MFP_{80k}	> 22.3
MFP_{90k}	> 21.2
$1^{st}freq$	> 7479
$2^{nd}freq$	> 13535
MOI	$< 8.8342 \times 10^{-5}$
W_1	$= 8.441$

Table 7.6 Objectives of Optimisation 2

	Objectives
$\eta_{t-s,50k}$	Maximise
Stress	Minimise

on the Pareto front. Red dots indicate three designs (design 7971, design 12651 and design 13022) selected from the Pareto front whose $\eta_{t-s,50k}$ is greater than 62.0% and their prediction performance values are validated using CFD and FEA simulations in the next subsection.

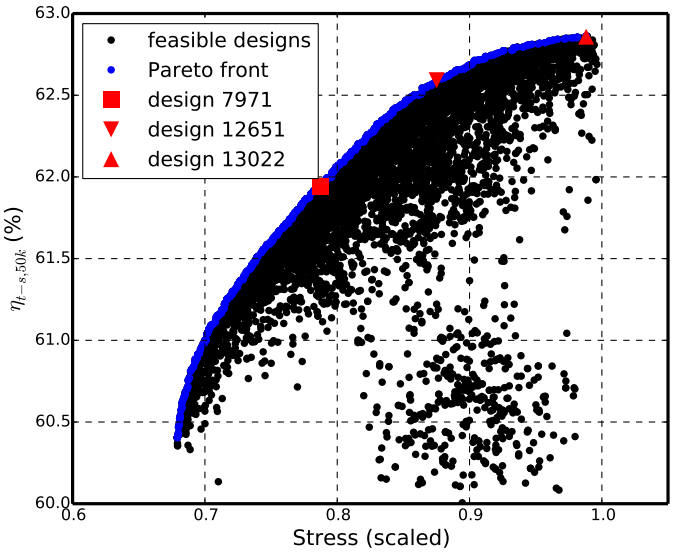

Fig. 7.30 2D scatter plot of $\eta_{t-s,50k}$ versus Stress (scaled) for Optimisation 2 using Kriging approximation

7.3.1 CFD and FEA Results

The blade geometries for design 7971, design 12651 and design 13022 are generated using the inverse design method and their performance parameters are calculated using CFD and FEA simulations. The error between the prediction value and the validation value and the improved performance compared to the baseline of these three designs are summarised in Table 7.7.

The error between the Kriging prediction and CFD/FEA validation for all MFP parameters is between -0.4% and 1.4%. The error for efficiencies is slightly higher and 0.5% - 4.7%. The error for most of the mechanical performance parameters ($1^{st}f$, $2^{nd}f$, MOI and $Stress$) is between -4.9% and 3.7%. The largest error is observed for $1^{st}f$ of design 126051 (-7.7%) and design 13022 (-7.5%).

Table 7.7 Comparison of predicted (Kriging) and validation values for three optimal designs

design		$1^{st}f$	$2^{nd}f$	η_{50k}	η_{60k}	η_{70k}	η_{80k}	η_{90k}	MFP_{50k}	MFP_{60k}	MFP_{70k}	MFP_{80k}	MFP_{90k}	MOI	$Stress$
7971	Kriging	9345	14296	62.0%	68.6%	68.8%	65.4%	55.6%	23.9	23.9	23.3	22.3	21.2	8.7167e-5	0.79
	CFD/FEA Validation	9766	14206	61.7%	66.9%	67.4%	64.1%	53.8%	23.8	23.7	23.2	22.3	20.9	8.4058e-5	0.80
	error	-4.3%	0.6%	0.5%	2.5%	2.1%	2.0%	3.3%	0.4%	0.8%	0.4%	0.0%	1.4%	3.7%	-0.9%
	Compared to baseline	30.6%	5.0%	3.0%	0.6%	0.0%	1.3%	-1.6%	-0.4%	-0.8%	-1.7%	-2.6%	-5.0%	-4.8%	-19.4%
12651	Kriging	8341	13549	62.6%	69.5%	70.2%	66.7%	55.7%	23.9	23.9	23.3	22.4	21.3	8.8233e-5	0.87
	CFD/FEA Validation	9033	13690	62.2%	67.4%	68.0%	64.3%	53.2%	24.0	23.8	23.4	22.5	21.1	8.6308e-5	0.92
	error	-7.7%	-1.0%	0.6%	3.1%	3.2%	3.7%	4.7%	-0.4%	0.4%	-0.4%	-0.4%	0.9%	2.2%	-4.9%
	Compared to baseline	20.8%	1.1%	3.8%	1.4%	0.9%	1.6%	-2.7%	0.4%	-0.4%	-0.8%	-1.7%	-4.1%	-2.3%	-6.8%
13022	Kriging	8366	13345	62.9%	69.4%	70.0%	65.7%	54.4%	24.1	24.0	23.3	22.4	21.3	8.8267e-5	0.99
	CFD/FEA Validation	9046	13546	62.5%	67.4%	67.9%	63.4%	53.0%	24.0	23.8	23.4	22.4	21.0	8.6492e-5	1.03
	error	-7.5%	-1.5%	0.6%	3.0%	3.1%	3.6%	2.6%	0.4%	0.8%	-0.4%	0.0%	1.4%	2.1%	-4.2%
	Compared to baseline	21.0%	0.1%	4.3%	1.4%	0.7%	0.2%	-3.1%	0.4%	-0.4%	-0.8%	-2.2%	-4.5%	-2.1%	4.6%
baseline	CFD/FEA	7479	13535	59.9%	66.5%	67.4%	63.3%	54.7%	23.9	23.9	23.6	22.9	22.0	8.8342e-5	0.99

Similar to Optimisation 1, the trade-off between the efficiency (η_{50k}) and the mechanical performance ($Stress$, $1^{st}f$, $2^{nd}f$ and MOI) of design 7971, design 12651 and design 13022 is captured through CFD/FEA validation and is shown in Figure 7.31. Design 7971 has the lowest η_{50k} but best mechanical performance and design 13022 has the highest η_{50k} but worst mechanical performance especially Stress. Design 12651 is selected for further analysis in the following subsections since design 7971 has less efficiency improvement and design 13022 has too high stress.

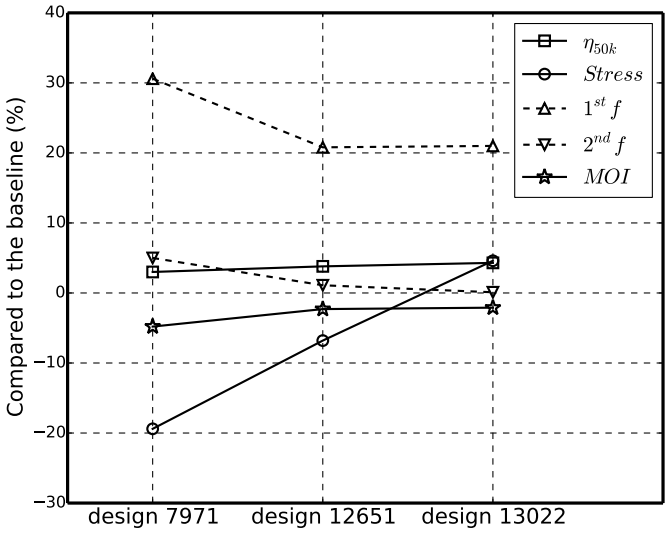

Fig. 7.31 Comparison of performance improvements for design 7971, design 12651 and design 13022

7.3.2 Comparison of Meridional Geometry, $\beta_{b,LE}$ and Performance Maps (baseline and design 12651)

The comparison of meridional geometries for the baseline and design 12651 is shown in Figure 7.32. The most obvious difference in the meridional shape of these two designs are the LE angle α_1 and the exducer width W_2.

The comparison of design parameters is shown in Table 7.8. It can be seen that the values of all the design parameters for design 12651 are not close to any boundaries specified in the DOE. It should be noted that the thickness parameter

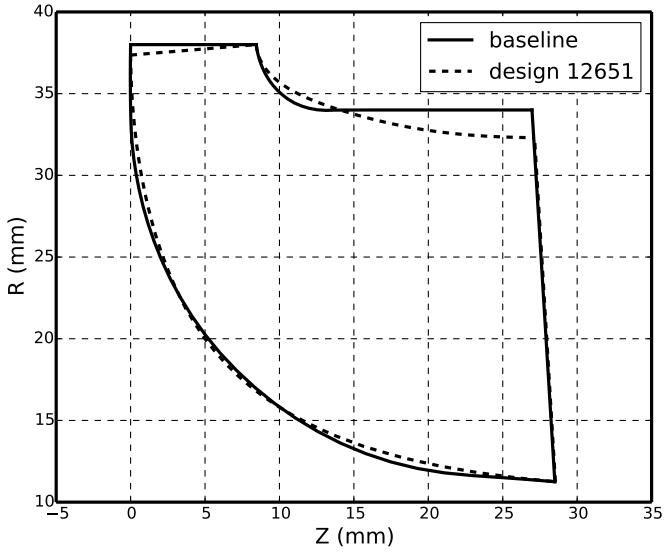

Fig. 7.32 Comparison of meridional geometries

(Th) of design 12651 is increased by 8.5% which is helpful to reduce the stress and increase the vibration frequencies.

Table 7.8 Comparison of design parameters

Design Parameters	baseline	design 12651	min	max
W_1 (mm)	8.441	8.441	7	11
W_2 (mm)	22.25	21.05	15	24
α_1 $(^\circ)$	0	4.33	0	30
Y_{hub} (mm)	—	19.371	16	21
$DRVT_{LE,h}$	—	-0.056	-0.8	0.6
NC_{hub}	—	0.087	0.05	0.156
$r\bar{V}_{\theta TE,hub}$	—	0.015	0	0.04
$SLOPE_{hub}$	—	1.77	1.0	2.5
Th	1.0	1.085	1.0	1.2

Another major difference in the blade geometry of these two designs are the LE blade angle $\beta_{b,LE}$ as shown in Figure 7.33. The baseline has a conventional zero blade angle in the LE while the design 12651's $\beta_{b,LE}$ is varying linearly from -14°

to -3° (hub to shroud). Therefore, the design 12651 is a so-called backswept LE design.

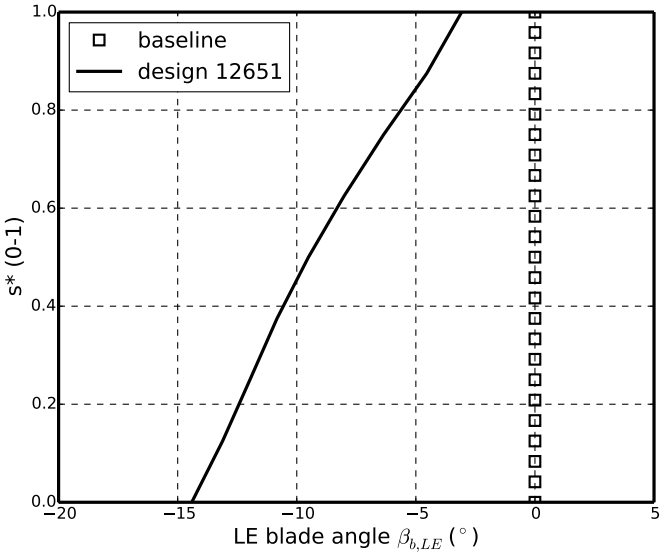

Fig. 7.33 Comparison of LE blade angles

The MFP and η_{t-s} comparison of these two designs for different speeds are shown in Figure 7.34 and Figure 7.35. The MFP of the design 12651 is slightly higher than the MFP of the baseline when $U/C_{is} < 0.5$. The MFP of design 12651 becomes lower than that of the baseline when $U/C_{is} > 0.5$ and this difference increases when U/C_{is} increases. The maximum MFP difference is 4.0% for MFP_{90k}. The η_{t-s} of design 12651 is higher than the baseline when $U/C_{is} < 0.8$ and lower when $U/C_{is} > 0.8$. The maximum efficiency improvement is around 4.0% for $\eta_{t-s,50k}$.

7.3.3 Comparison of Internal Flow Field (baseline and design 12651 @ RPM = 50k)

In this subsection, the internal flow field details of the baseline and design 12651 at RPM = 50k ($U/C_{is} = 0.5$) where the maximum efficiency difference is achieved as shown in Figure 7.35.

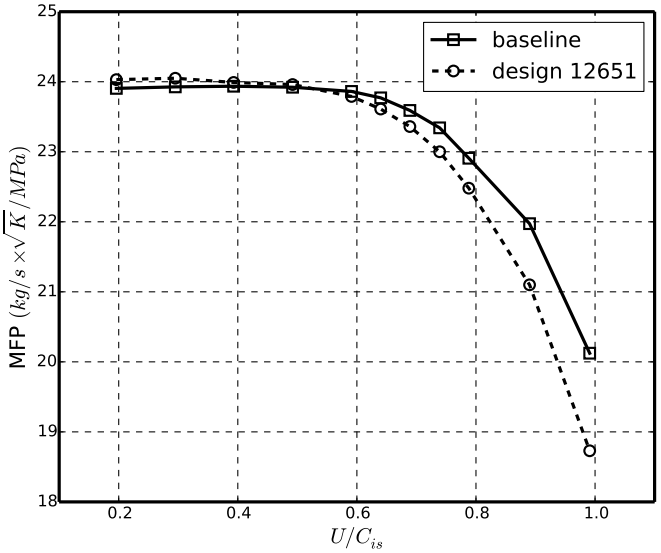

Fig. 7.34 Comparison of MFP

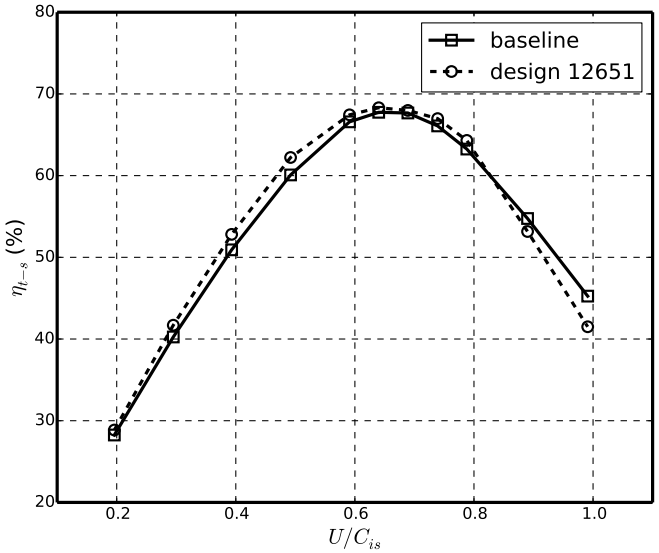

Fig. 7.35 Comparison of t-s efficiency

7.3.3.1 Relative Velocity Vector

The relative velocity vector plots of the baseline and design 12651 at different spanwise locations are shown in Figure 7.36, Figure 7.37 and Figure 7.38. As it can be seen from these three figures, the LE of both designs are experiencing very high positive incidence with the flow separation on the suction side being caused by this incidence. It can also be clearly seen that the separation is reduced for design 12651 since it has a backswept LE (negative $\beta_{b,LE}$). The flow field near the shroud is very complicated due to the existence of the tip leakage flow.

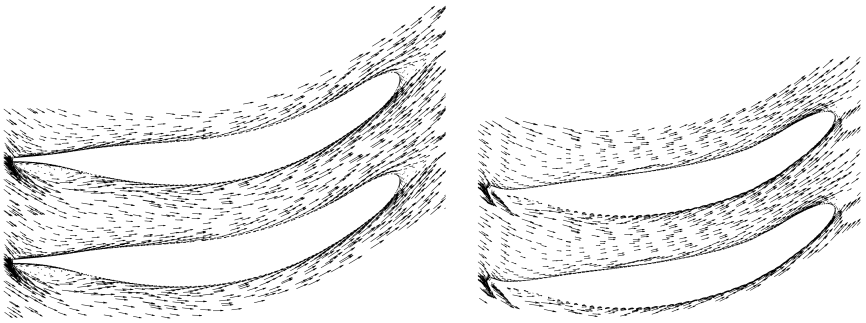

Fig. 7.36 Comparison of relative velocity vectors near the hub ($s^* = 0.1$) @ RPM = 50k (left - baseline, right - design 12651)

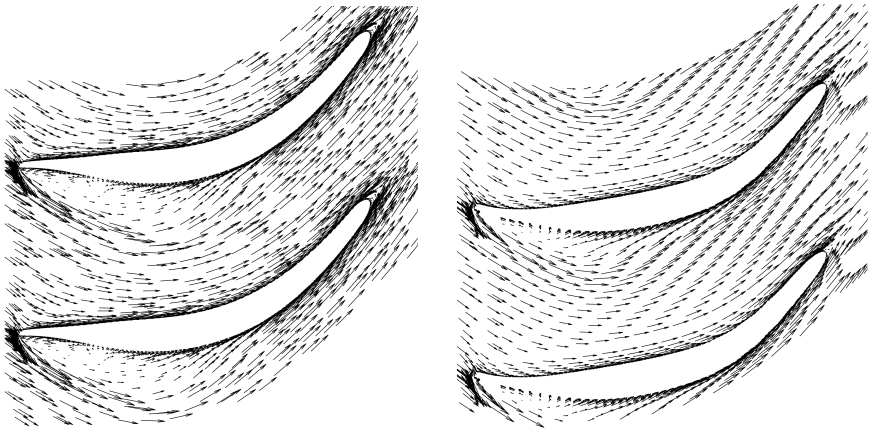

Fig. 7.37 Comparison of relative velocity vectors in the mid-span ($s^* = 0.5$) @ RPM = 50k (left - baseline, right - design 12651)

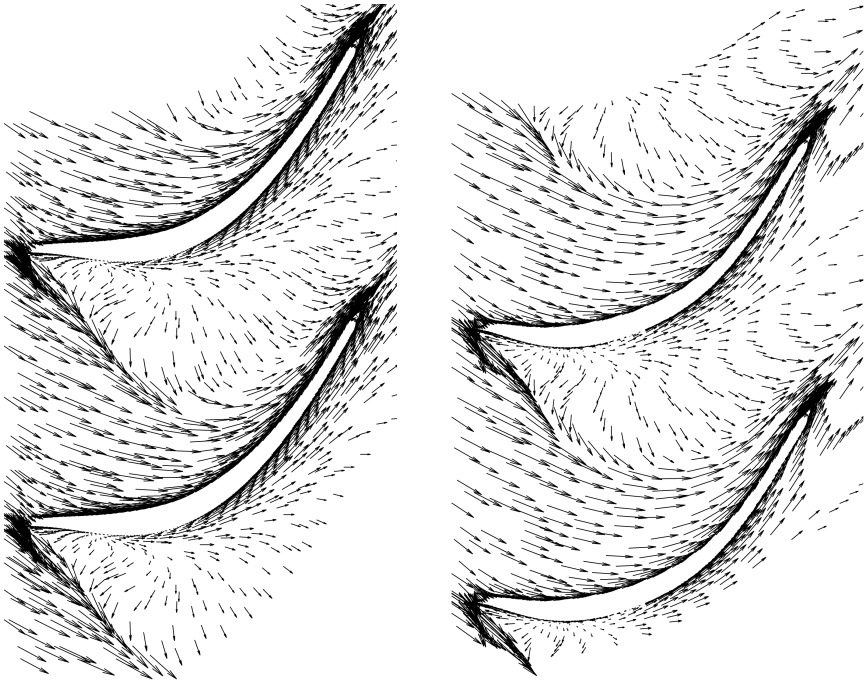

Fig. 7.38 Comparison of relative velocity vectors near the shroud ($s^* = 0.9$) @ RPM = 50k (left - baseline, right - design 12651)

7.3.3.2 Relative Mach Number

The relative Mach number contours of the baseline and design 12651 at different spanwise locations are shown in Figure 7.39, Figure 7.40 and Figure 7.41. The Mach number distribution of these two designs are very similar. The flow is accelerated to Mach number close to 0.9 near the LE. A separation can be observed near the LE suction side. The area of the low momentum region near the LE of design 12651 is smaller than that of the baseline which indicates less loss. A large area of low momentum region can be observed near the shroud which is caused by the LE incidence and the tip leakage flow.

The relative Mach number contours of the baseline and design 12651 in the blade LE and TE are shown in Figure 7.42 and Figure 7.43. The flow is accelerated near the suction side and decelerated near the pressure side due to the large positive incidence in the LE. In the TE plane of the rotor, the flow of design 12651 is more uniform than the baseline. The low momentum region near the shroud of design 12651 is obviously smaller than that of the baseline.

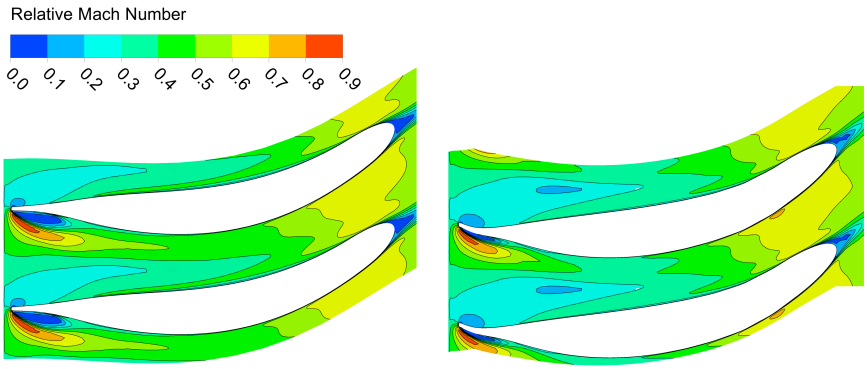

Fig. 7.39 Comparison of relative Mach number contours near the hub ($s^* = 0.1$) @ RPM = 50k (left - baseline, right - design 12651)

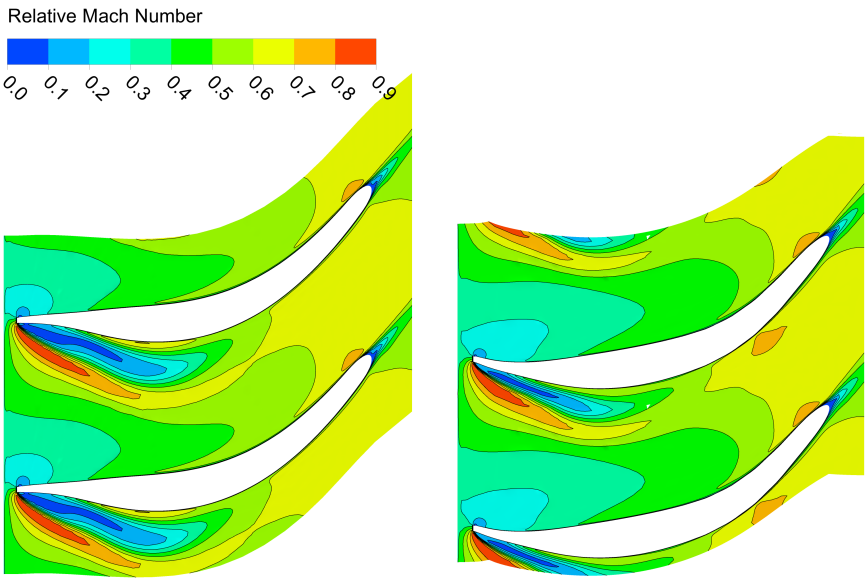

Fig. 7.40 Comparison of relative Mach number contours in the mid-span ($s^* = 0.5$) @ RPM = 50k (left - baseline, right - design 12651)

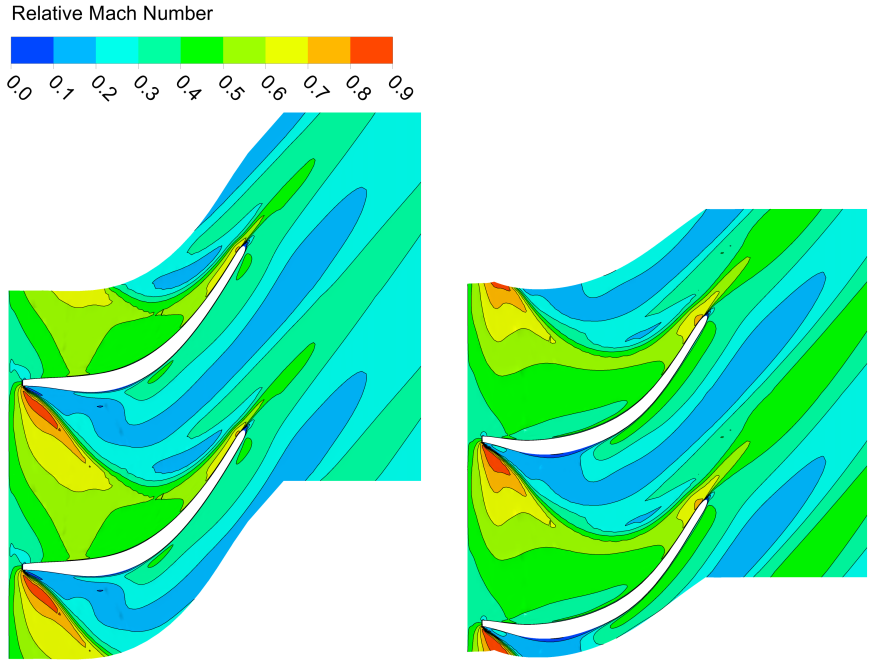

Fig. 7.41 Comparison of relative Mach number contours near the shroud ($s^* = 0.9$) @ RPM = 50k (left - baseline, right - design 12651)

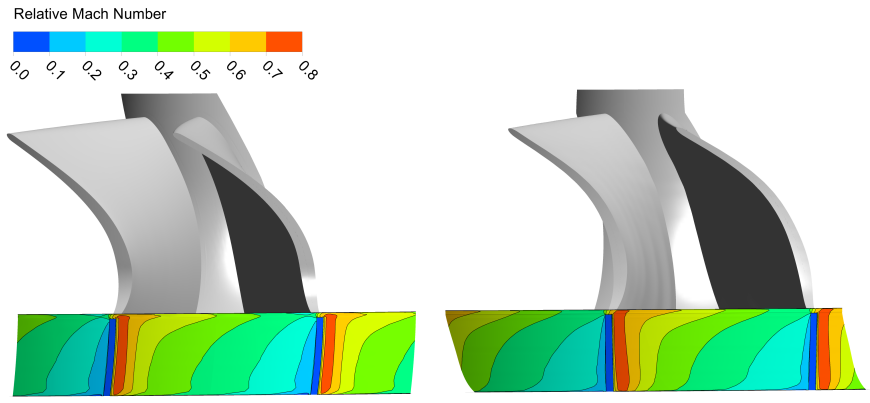

Fig. 7.42 Comparison of relative Mach number contours in the LE @ RPM = 50k (left - baseline, right - design 12651)

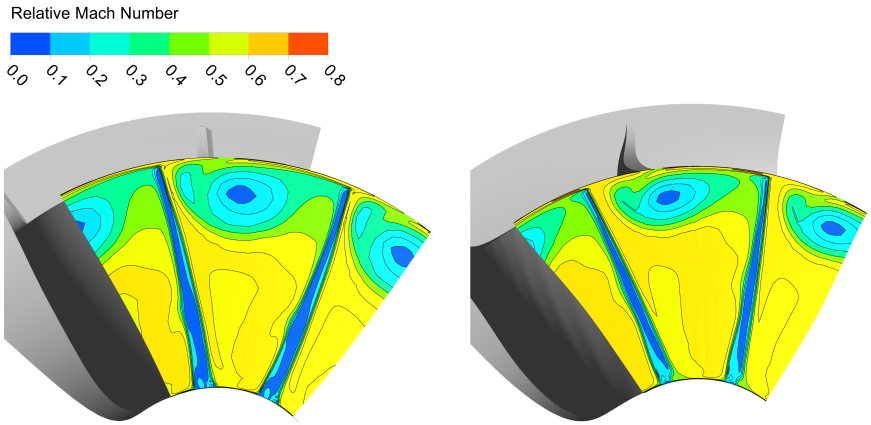

Fig. 7.43 Comparison of relative Mach number contours in the TE @ RPM = 50k (left - baseline, right - design 12651)

7.3.3.3 Blade Surface Pressure

The blade surface pressure comparison for the two designs at different spanwise locations are shown in Figure 7.44, Figure 7.45 and Figure 7.46. The large positive incidence can be observed near the hub, mid-span and shroud for these two designs. The pressure distribution in the hub and shroud are very similar. The most obvious difference is the improved pressure gradient on the pressure side of design 12651 near the shroud compared to the baseline.

7.3.3.4 Aerodynamic Blockage Factor

The B_{aero} of the baseline and design 12651 at different constant streamwise cross-sections are compared in Figure 7.47. Design 12651 shows much better flow uniformity across the rotor passage.

7.3.3.5 Blade Surface Streamline

The blade surface (suction side) streamlines comparison for the two designs is shown in Figure 7.48. Apparently, the flow starts separate later near the hub for design 12651 compared to the baseline.

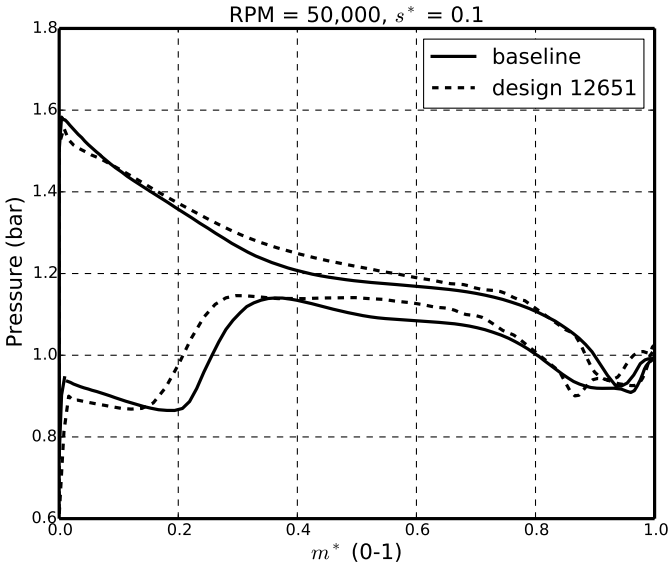

Fig. 7.44 Comparison of blade surface pressure near the hub ($s^* = 0.1$) @ RPM = 50k

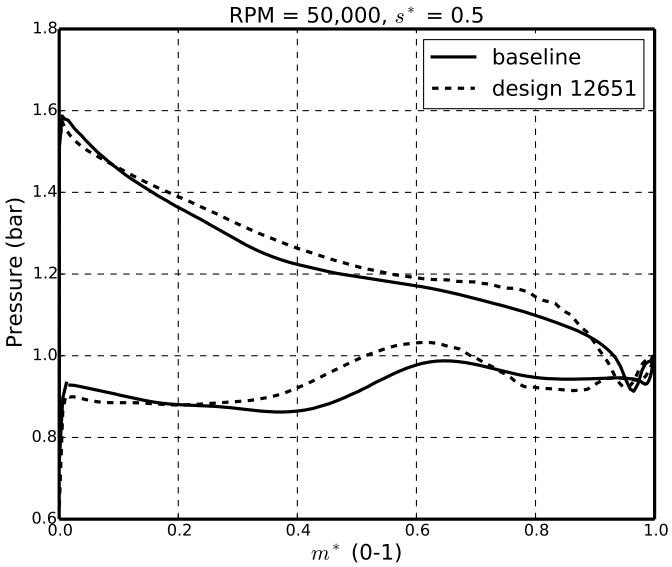

Fig. 7.45 Comparison of blade surface pressure in the mid-span ($s^* = 0.5$) @ RPM = 50k

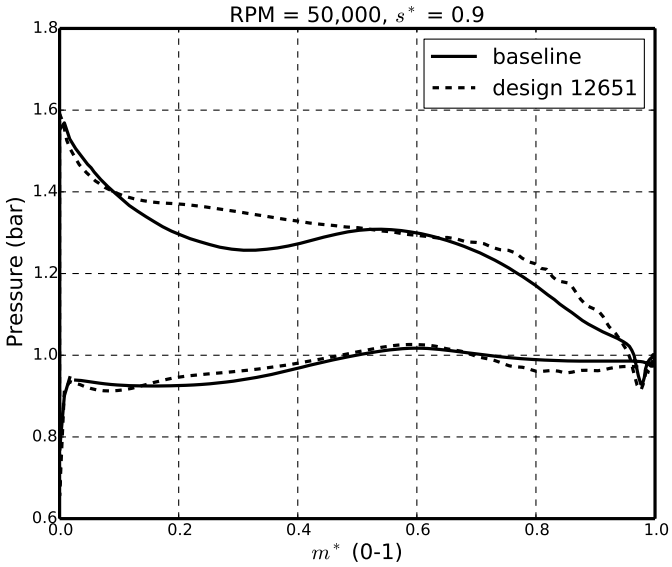

Fig. 7.46 Comparison of blade surface pressure near the shroud ($s^* = 0.9$) @ RPM = 50k

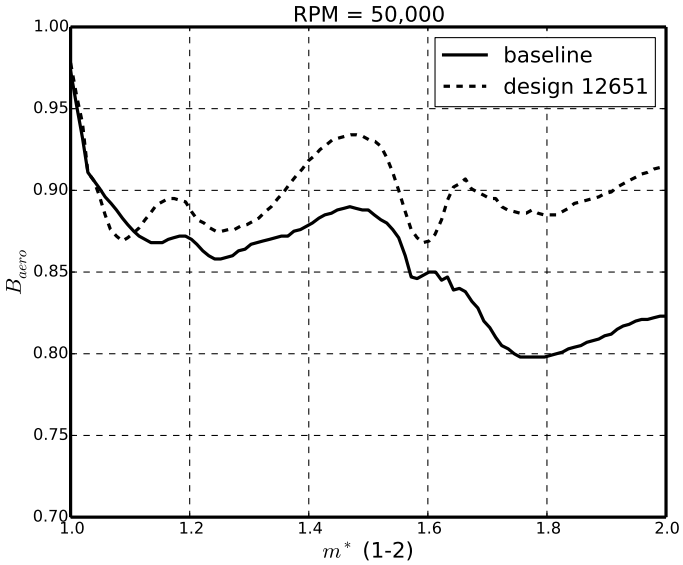

Fig. 7.47 Comparison of B_{aero} from the rotor inlet to the rotor outlet @ RPM = 50k

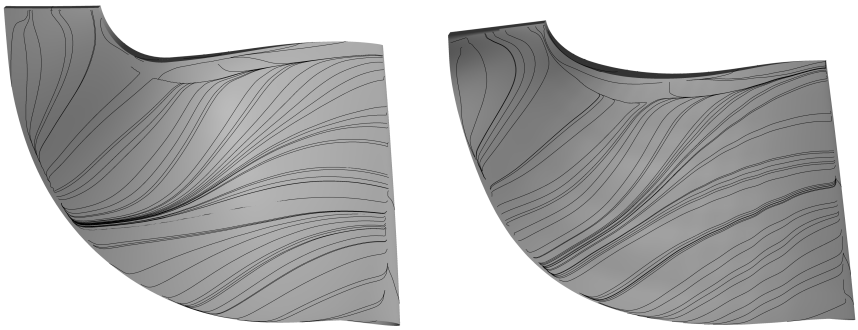

Fig. 7.48 Comparison of blade surface streamlines on the suction side @ RPM = 50k (left - baseline, right - design 12651)

7.3.3.6 Tip Leakage Flow

The streamlines of the tip leakage flow for the two designs are compared in Figure 7.49. It can seen that most of the tip leaking flow is from the flow near the LE shroud and few is from the secondary flow from the hub to the tip. It is difficult to tell which design has a better leakage flow structure from Figure 7.49 since they are very similar to each other. The calculated mass flow across the tip gap is 7.4% and 7.6% of the total turbine mass flow for the baseline and design 12651.

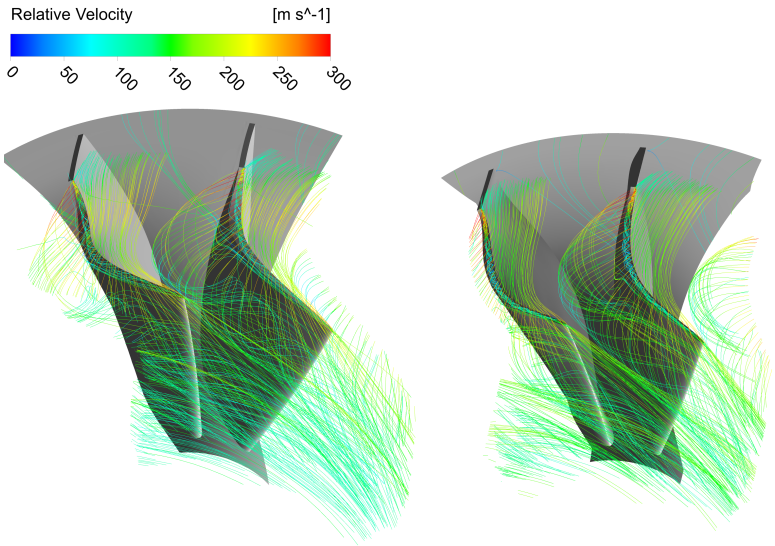

Fig. 7.49 Comparison of streamlines across the tip leakage @ RPM = 50k (left - baseline, right - design 12651)

7.3.3.7 Entropy Generation

The comparison of MCA static entropy from the nozzle inlet ($m^* = 0$) to the rotor outlet ($m^* = 2$) of the baseline and design 12651 is shown in Figure 7.50. Design 12651 shows lower entropy generation which indicates less losses from the rotor inlet to the rotor outlet compared to the baseline. This can be more clearly seen in Figure 7.51 and Figure 7.52.

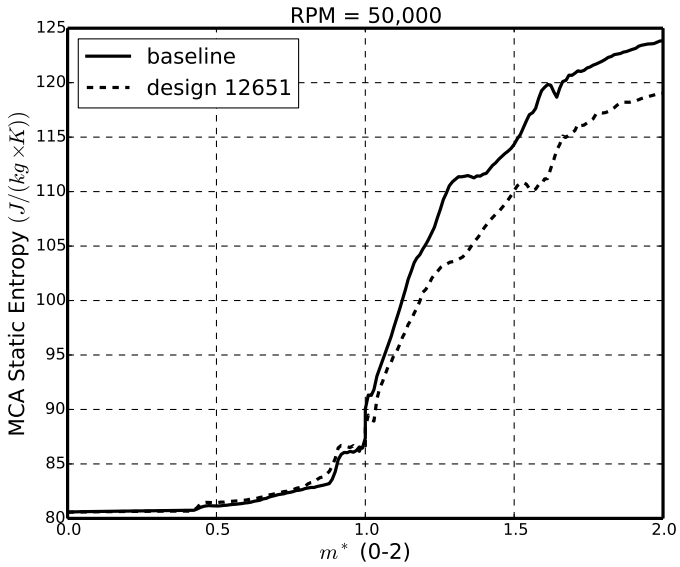

Fig. 7.50 Comparison of MCA static entropy from the nozzle inlet to the rotor outlet @ RPM = 50k

The comparison of static entropy contours for the two designs at three different streamwise locations is shown in Figure 7.51. The entropy starts to generate and accumulate in the blade suction side near the LE tip. The entropy is convected and the area with high entropy values increases when the flow develops in the streamwise direction in the rotor passage. Until the rotor TE, most of the static entropy accumulates near the tip and on the blade suction surface. The static entropy for design 12651 is always less than that of the baseline at the same streamwise location as shown in Figure 7.51.

The streamlines associated with the high entropy region are shown in Figure 7.52. It can be seen that most of the entropy generation is from the flow separation in the LE suction side. The secondary flow from the hub to the tip and the tip

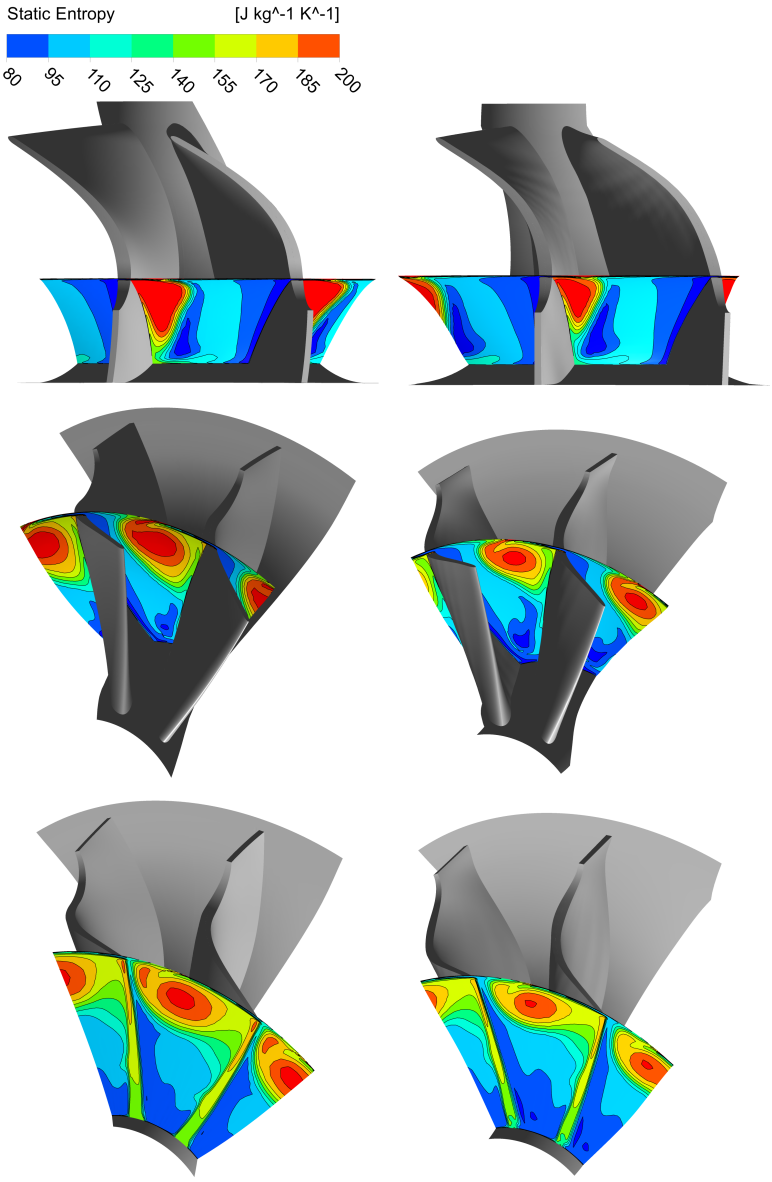

Fig. 7.51 Comparison of static entropy contours at different streamwise locations @ RPM = 50k (left - baseline, right - design 12651)

leakage flow are other less important sources for the entropy generation. The strength of the entropy vortex for design 12651 is much smaller than that of the baseline. This can be explained as design 12651 has a backswept LE which reduces the incidence loss and the separation near the LE compared to the baseline design.

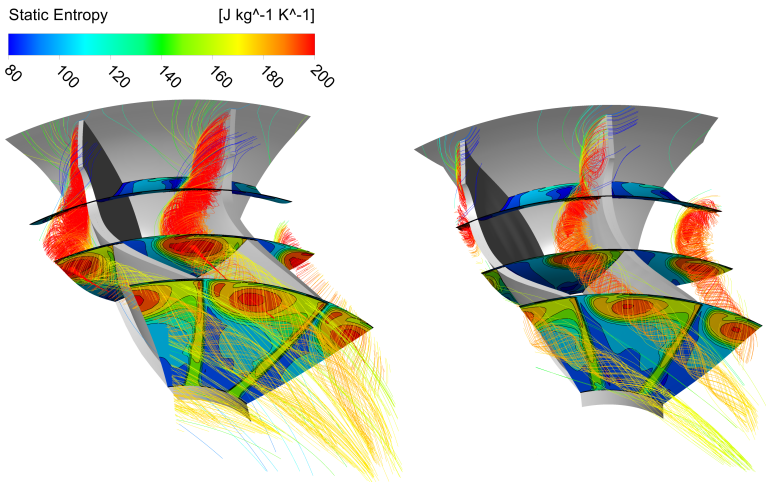

Fig. 7.52 Comparison of streamlines associated with static entropy contours at different streamwise locations @ RPM = 50k (left - baseline, right - design 12651)

7.3.3.8 Exit Kinetic Energy Loss

The meridional velocity, absolute circumferential velocity and absolute velocity contours at the rotor outlet for the two designs are compared in Figure 7.53, Figure 7.54 and Figure 7.55. The meridional velocity V_m near the shroud is increased and near the hub is decreased for design 12651 compared to the baseline. The absolute tangential velocity near the shroud of design 12651 is much lower than the baseline. The resulting absolute velocity contours of these two designs are very similar but the velocity near the hub for design 12651 is slightly lower. The exit kinetic energy loss for the baseline is 9.5% and 9.2% for design 12651.

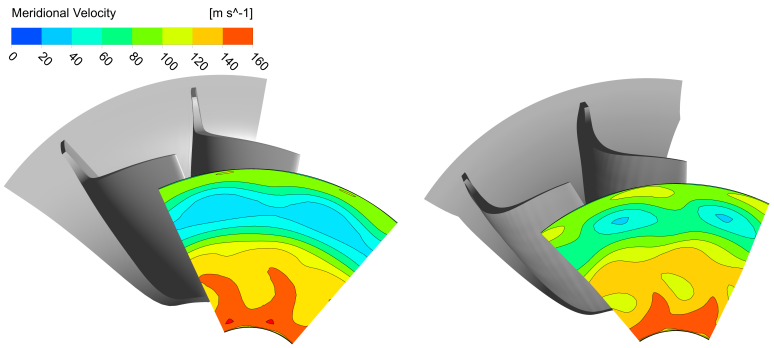

Fig. 7.53 Comparison of meridional velocity contours at the turbine outlet @ RPM = 50k (left - baseline, right - design 12651)

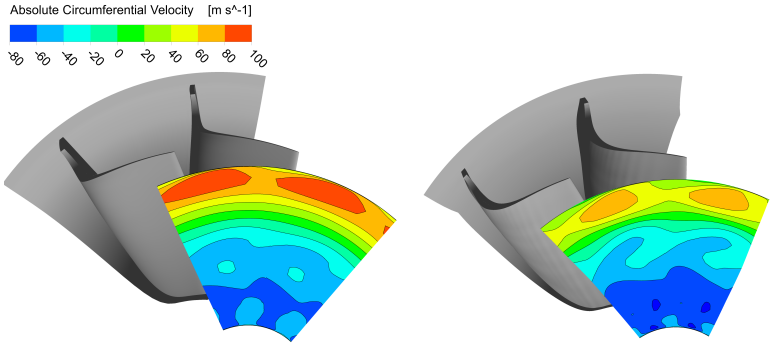

Fig. 7.54 Comparison of absolute circumferential velocity contours at the turbine outlet @ RPM = 50k (left - baseline, right - design 12651)

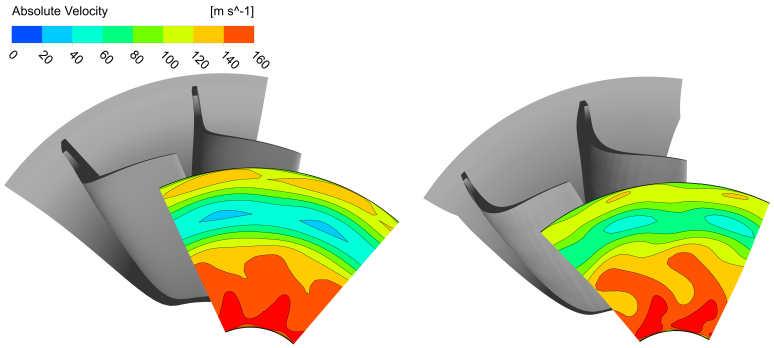

Fig. 7.55 Comparison of absolute velocity contours at the turbine outlet @ RPM = 50k (left - baseline, right - design 12651)

7.3.4 Comparison of Static Structural and Modal Analysis results (baseline and design 12651)

It is worth pointing out that the FEA analysis of all the redesigned blades shown in the previous subsections are performed for the blade without 0.5 mm trimmed in the tip, while the mechanical performance of the baseline is performed for the blade after 0.5 mm tip trimming. Trimming the tip material. The trimming of the rotor tip is helpful to reduce the MOI, the stress near the blade root and increase the blade stiffness.

To make a reasonable comparison, the results of the static structural and modal analysis of the baseline and design 12651 after tip trimming are compared in this subsection.

7.3.4.1 Stress

The comparison of stress contours for the two designs are shown in Figure 7.56, Figure 7.57 and Figure 7.58. The stress level for design 12651 is significantly reduced compared to the baseline, especially the stress near the root fillet region. The stress for design 12651 near the LE inducer part is increased which is caused by the backswept LE compared to the baseline. However, the maximum stress is still less than the stress concentration value near the TE and well below the material yield strength. The stress distribution for the two designs are very similar and the values are quite low. To sum up, the maximum stress of design 12651 is reduced by 12.5% compared to the baseline.

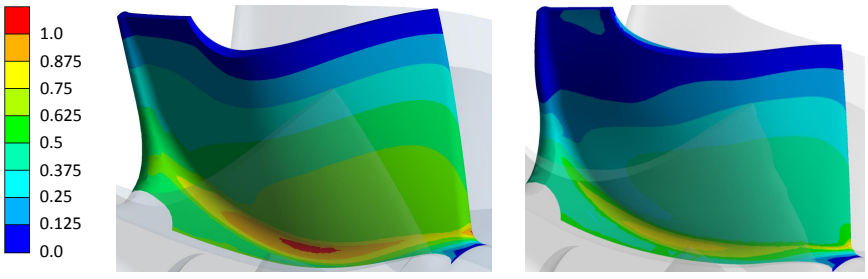

Fig. 7.56 Comparison of maximum principle stress (scaled) contours on the suction surface (left - baseline, right - design 12651)

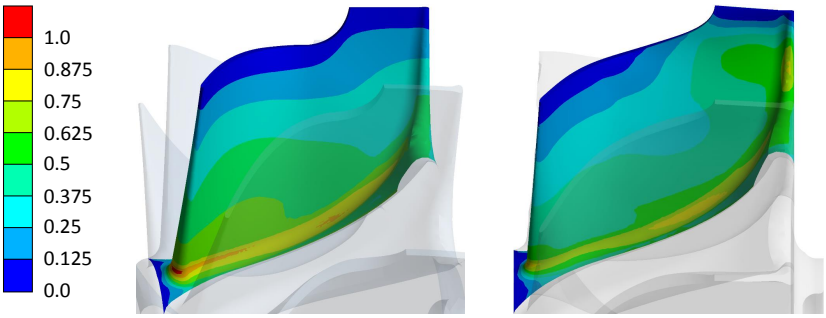

Fig. 7.57 Comparison of maximum principle stress (scaled) contours on the pressure surface (left - baseline, right - design 12651)

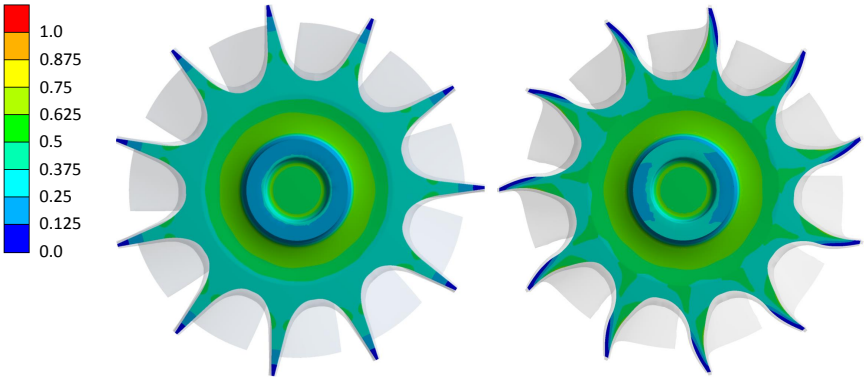

Fig. 7.58 Comparison of maximum principle stress (scaled) contours on the back face (left - baseline, right - design 12651)

7.3.4.2 Modal Frequencies

The comparison of 1^{st} and 2^{nd} vibration mode shapes for the two designs are shown in Figure 7.59 and Figure 7.60. The frequency for the 1^{st} vibration mode of design 12651 is 25.0% higher than the baseline and the frequency for the 2^{nd} vibration of design 12651 is 4.5% higher.

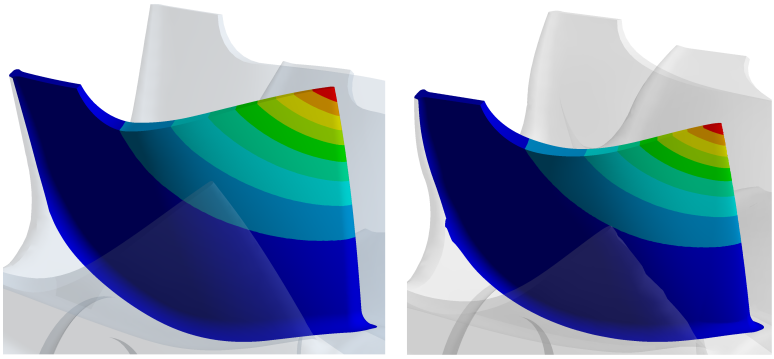

Fig. 7.59 Comparison of 1^{st} vibration mode shapes (left - baseline, right - design 12651)

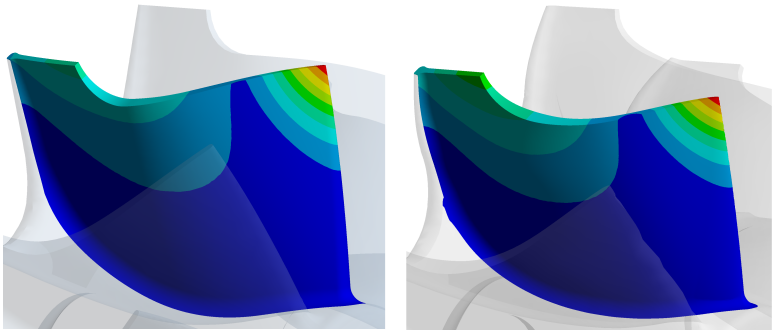

Fig. 7.60 Comparison of 2^{nd} vibration mode shapes (left - baseline, right - design 12651)

7.4 Summary

A similar optimisation methodology to that was illustrated in Chapter 5 is used in this chapter to find an optimal design which has improved efficiency in the low U/C_{is} compared to the baseline design. The major difference between the

Optimisation 2 and Optimisation 1 are the increased ranges of design parameters and the use of RFM2 which allows for blades with a backswept LE to be included in the new design space. The final optimal design obtained, design 12651, shows significant improvement in the low U/C_{is} and excellent mechanical performance compared to the baseline blade design. The performance improvements of design 12651 are summarised in Table 7.9. The only disadvantage of the new design is its $\eta_{t-s,90k}$ is lower than that of the baseline. This is less important when the turbine is running under the unsteady condition.

Table 7.9 Performance improvements compared to the baseline

	design 10535	design 12651
$\eta_{t-s,50k}$	-0.3%	3.8%
$\eta_{t-s,60k}$	-0.8%	1.4%
$\eta_{t-s,70k}$	1.8%	0.9%
$\eta_{t-s,80k}$	7.0%	1.6%
$\eta_{t-s,90k}$	9.0%	-2.7%
MFP_{50k}	0.0%	0.4%
MFP_{60k}	-0.4%	-0.4%
MFP_{70k}	-0.8%	-0.8%
MFP_{80k}	-0.9%	-1.7%
MFP_{90k}	-2.7%	-4.1%
Stress	2.7%	-12.5%
1^{st} Frequency	10.6%	25.0%
2^{nd} Frequency	1.4%	4.5%
MOI	-11.0%	-3.5%

CHAPTER 8

CONCLUSIONS AND SUGGESTIONS FOR FUTURE WORK

In this thesis a multidisciplinary and multi-point optimisation study of radial and mixed-inflow turbines for turbochargers has been carried out. The turbine aerodynamic and mechanical performance is evaluated using CFD and FEA simulations and the CFD model is validated against the experimental results of the baseline design. The final optimal design obtained (design 12651) using the inverse design method, Radial Filament Modification, DOE, Kriging approximation and MOGA shows significant improvement in all performance parameters except for $\eta_{t-s,90k}$ which is less critical for the turbine's unsteady performance.

This chapter summaries the most important conclusions and achievements in this thesis and proposes several suggestions for the future work.

8.1 Conclusions

1) A sensitivity analysis based on the linear DOE results has been proposed and has been used to reduce the number of design parameters (from 17 to 8/9). This is helpful to reduce the total number of designs needed for a Kriging DOE and increase the accuracy of the surrogate model based on the Kriging DOE results;

2) It has been shown that Kriging is more suitable to be used to construct the response surface of the turbine performance parameters compared to the second-order polynomial and RBF;

3) Design 10535 obtained through Optimisation 1 and design 12651 obtained through Optimisation 2 show improved aerodynamic and mechanical performance which are summarised in Table 7.9. Design 10535 has better efficiency in the high U/C_{is} while design 12651 has better efficiency in the low U/C_{is} which is better for unsteady performance.

8.2 Thesis Achievements

1) A systematic multidisciplinary, multi-objective and multipoint optimisation methodology which integrates the inverse design method, DOE, RFM, RSM, Kriging, MOGA, CFD and FEA for the design of turbocharger turbines has been developed and successfully applied to the design of a turbine rotor blade;

2) Turbines with a backswept LE designed using the inverse design method have better efficiency in the low U/C_{is} which is beneficial for the turbine's unsteady performance;

3) Two Radial Filament Modification methods (RFM1 and RFM2) have been applied to the 3D blades directly from the inverse design method and have successfully reduced the maximum stress level.

8.3 Suggestions for Future Work

1) The inverse design method can also be used to design the stationary turbomachinery components, for example the nozzle blade. In this study the nozzle blade is not redesigned due to the requirements from the sponsor. To achieve better turbine stage performance, the nozzle and the rotor geometries can be optimised at the same time using the similar optimisation methodology presented in this thesis. The nozzle blade can be parametrised using the meridional parameters and the blade loading parameters. The nozzle blade can be 3D which can be easily achieved by applying different

blade loading parameter in the hub and shroud. Of course, this will increase the manufacturing cost. However, the 3D nozzle allows different flow angles at the nozzle TE and may have a better control over the rotor LE incidence;

2) The stacking value is always zero and the stacking position is always at the LE for the current inverse design method for radial turbines. It is possible to use a linear or even parabolic stacking shape in the future optimisation and investigate its effect. The disadvantage of using a complex stacking shape is that it increases the manufacturing cost. It would be also helpful to try to change the stacking location from the LE to other locations which will make the current inverse design solver very unstable. Much effort needs to be put into this to understand the effect of the stacking location on the turbine performance;

3) The most challenging problem for the radial turbine design is the stress which becomes extremely high for a non-radial filament blading. In this thesis RFM1 and RFM2 are proposed to tackle this problem. It will be useful to allow the inverse design method to generate radial filament or nearly radial filament blades without any post-modification. In the current inverse design method, the blade loading parameters are only specified in the hub and shroud, which control the blade shape in the hub and shroud. The blade loading between the hub and shroud is simply linear. To generate a radial filament blade, the blade loading needs to be specified at multiple spanwise locations and the loading distribution between different layers needs to be studied carefully.

REFERENCES

M. Abidat, M. Hachemi, M. K. Hamidou, and N. C. Baines. Prediction of the Steady and Non-steady Flow Performance of A Highly Loaded Mixed Flow Turbine. *Proceedings of the Institution of Mechanical Engineers. Part A: Journal of Power and Energy*, 212(3):173–184, 1998.

J. D. Anderson. *Fundamentals of Aerodynamics*. McGraw-Hill, New York, fourth edition, 2007.

C. Arcoumanis, I. Hakeem, L. Khezzar, and R. F. Martinez-Botas. Performance of A Mixed Flow Turbocharger Turbine under Pulsating Flow Conditions. *International Gas Turbines & Aeroengine Congress & Exhibition*, ASME Paper 95-GT-210, 1995.

K. Ashihara and A. Goto. Study on Pump Impeller with Splitter Blades Designed by 3D Inverse Design Method. *ASME 2000 Fluid Engineering Division Summer Meeting*, FEDSM2000-11073, 2000.

N. C. Baines, A. Hajilouy-Benisi, and J. H. Yeo. The Pulse Flow Performance and Modelling of Radial Inflow Turbines. *Proceedings of IMechE*, C484/006: 209–219, 1994.

L. Barr and T. McNally. A Numerical Study of the Performance Characteristics of A Radial Turbine with Varying Inlet Blade Angle. *IMechE* 8^{th} *International Conference on Turbochargers and Turbocharging*, pages 169–181, 2006.

L. Barr, S. Spence, and P. Eynon. Design and Analysis of A Radial Turbine with Back Swept Blading. *Fluid Machinery and Fluid Mechanics*, pages 115–121, 2009.

P. Beauchamp and A. R. Seebass. Shock-free Turbomachinery Blade Design. *AIAA Journal*, 23(2):249–253, 1985.

A. Betz and I. Flügge-Lotz. Design of Centrifugal Impeller Blades. *NACA TM 902*, 1939.

D. Bonaiuti and M. Zangeneh. On the Coupling of Inverse Design and Optimization Techniques for the Multiobjective, Multipoint Design of Turbomachinery Blades. *Journal of Turbomachinery*, 131(2):021014, 2009.

E. Bonataki, P. Chaviaropoulos, and K. D. Papailiou. An Inverse Inviscid Method for the Design of Quasi-three-dimensional Turbomachinery Cascades. *Journal of Fluids Engineering*, 115(1):121–127, 1993.

J. E. Borges. *Three-Dimensional Design of Turbomachinery*. PhD thesis, Cambridge University, Engineering Department, 1986.

J. E. Borges. A Three-dimensional Inverse Method in Turbomachinery: Part I - Theory. *Journal of Turbomachinery*, 112(3):346–354, 1990a.

J. E. Borges. A Three-dimensional Inverse Method in Turbomachinery: Part II - Experimental Verification. *Journal of Turbomachinery*, 112(3):355–361, 1990b.

M. P. Boyce. *Gas Turbine Engineering Handbook*. Gulf Professional Publishing, Houston, second edition, 2002.

R. Cai. A Summary of Developments of the Mean-streamline Method in China. *Journal of Engineering for Gas Turbines and Power*, 106(2):300–305, 1984.

H. N. Cantrell and J. E. Fowler. The Aerodynamic Design of Two Dimensional Turbine Cascades for Incompressible Flows with High Speed Computer. *Journal of Basic Engineering*, 81(3), 1959.

M. Capobianco and A. Gambarotta. Unsteady Flow Performance of Turbocharger Radial Turbines. *IMechE 4^{th} International Conference on Turbochargers and Turbocharging*, C405/017, 1990.

M. Capobianco and S. Marelli. Experimental Investigation into the Pulsating Flow Performance of A Turbocharger Turbine in the Closed and Open Waste-gate Region. *IMechE 9^{th} International Conference on Turbochargers and Turbocharging*, pages 373–385, 2010.

M. Capobianco and S. Marelli. Experimental Analysis of Unsteady Flow Performance in An Automotive Turbocharger Turbine Fitted with A Waste-gate Valve. *Proceedings of the Institution of Mechanical Engineers. Part D: Journal of Automobile Engineering*, 225(8):1087–1097, 2011.

R. D. Cedar and P. Stow. A Compatible Mixed Design and Analysis Finite Element Method for the Design of Turbomachinery Blades. *International Journal for Numerical Methods in Fluids*, 5(4):331–345, 1985.

C. Chahine, J. R. Seume, and T. Verstraete. The Influence of Metamodeling Techniques on the Multidisciplinary Design Optimization of A Radial Compressor Impeller. *ASME Turbo Expo 2012*, GT2012-68358:1951–1964, 2012.

H. Chen, I. Hakeem, and R. F. Martinez-Botas. Modelling of A Turbocharger Turbine under Pulsating Inlet Conditions. *Proceedings of the Institution of Mechanical Engineers. Part A: Journal of Power and Energy*, 201:397–408, 1996.

N. X. Chen, M. Dong, and J. L Zhang. A Numerical Method for Solving Aerodynamic Hybrid Problem of Fully 3D Flow in Turbomachinery. *Proceedings of the 1st International Symposium on Experimental and Computational Aerodynamics of Internal Flows*, pages 441–448, 1990.

N. X. Chen, F. X. Zhang, and M. Dong. Stream-funtion-coordinate Method for 2D and 3D Aerodynamic Inverse Design in Turbomachinery. *Inverse Problems in Engineering*, 1(3):207–229, 1995.

M. S. Chiong, S. Rajoo, A. Romagnoli, and R. Martinez-Botas. Unsteady Performance Prediction of A Single Entry Mixed Flow Turbine Using 1-D Gas Dynamic Code Extended with Meanline Model. *Proceedings of ASME Turbo Expo 2012*, GT2012-69176, 2012.

H-S Chung and J. J. Alonso. Multiobjective Optimization Using Approximation Model-Based Genetic Algorithms. *10th AIAA/ISSMO Symposium on Multidisciplinary Analysis and Optimization*, 2004.

C. D. Copeland, P. Newton, R. F. Martinez-Botas, and M. Seiler. A Comparison of Timescales within A Pulsed Flow Turbocharger Turbine. *10th International Conference on Turbochargers and Turbocharging*, pages 389–404, 2002.

A. Costall, S. Szymko, R. F. Martinez-Botas, D. Filsinger, and D. Ninkovic. Assessment of Unsteady Behavior in Turbocharger Turbines. *ASME Turbo Expo 2006: Power for Land, Sea, and Air*, pages 1023–1038, 2006.

A. W. Costall, R. M. McDavid, R. F. Martinez-Botas, and N. C. Baines. Pulse Performance Modeling of A Twin Entry Turbocharger Turbine under Full and Unequal Admission. *Journal of Turbomachinery*, 133(2):021004, 2011.

G. R. Costello. Method of Designing Cascade Blades with Prescribed Velocity Distributions in Compressible Potential Flows. *NACA-978*, 1950.

G. R. Costello, R. L. Cummings, and J. T. Sinnette Jr. Detailed Computational Procedure for Design of Cascade Blades with Prescribed Velocity Distributions in Compressible Potential Flows. *NACA-1060*, 1952.

A. Dale and N. Watson. Vaneless Diffuser Turbocharger Turbine Performance. *Proceedings of IMechE*, C110/86:65–76, 1986.

T. Dang and V. Isgro. Euler-based Inverse Method for Turbomachine Blades Part 1: Two-dimensional Cascades. *AIAA Journal*, 33(12):2309–2315, 1995.

T. Dang, S. Damle, and X. Qiu. Euler-based Inverse Method for Turbomachine Blades Part 2: Tthree-dimensional Flows. *AIAA Journal*, 38(11):2007–2013, 2000.

T. Q. Dang. Design of Turbomachinery Blading in Transonic Flows by the Circulation Method. *Journal of Turbomachinery*, 114(1):141–146, 1992.

T. Q. Dang. A Fully Three-dimensional Inverse Method for Turbomachinery Blading in Transonic Flows. *Journal of Turbomachinery*, 115(2):354–361, 1993.

K. Deb, S. Agrawal, A. Pratap, and T. Meyarivan. A Fast Elitist Non-dominated Sorting Genetic Algorithm for Multi-objective Optimization: NSGA-II. *Proceedings of the Parallel Problem Solving from Nature VI Conference*, pages 849–858, 2000.

J. D. Denton. An Improved Time-Marching Method for Turbomachinery Flow Calculation. *Journal of Engineering for Power*, 105(3):514–521, 1983.

J. D. Denton. The Use of A Distributed Body Force to Simulate Viscous Effects in 3D Flow Calculations. *ASME 1986 International Gas Turbine Conference and Exhibit*, 86-GT-144:V001T01A058, 1986.

J. D. Denton. The Calculation of Three-Dimensional Viscous Flow Through Multistage Turbomachines. *Journal of Turbomachinery*, 114(1):18–26, 1992.

R. Dornberger, D. Buche, and P. Stoll. Multidisciplinary Optimization in Turbomachinery Design. *European Congress on Computational Methods in Applied Sciences and Engineering*, 2000.

R. P. Dring. Blockage in Axial Compressors. *Journal of Engineering for Gas Turbines and Power*, 106(3):712–714, 1984.

S. M. Jr. Futral and D. E. Holeski. Experimental Results of Varying the Blade Shroud Clearance in A 6.02-inch Radial-inflow Turbine. *NASA TN D-5513*, 1970.

J. Galindo, P. Fajardo, R. Navarro, and L. M. García-Cuevas. Characterization of A Radial Turbocharger Turbine in Pulsating Flow by Means of CFD and its Application to Engine Modeling. *Applied Energy*, 103:116–127, 2013.

P. Garabedian and D. Korn. A Systematic Method for Computer Design of Supercritical Airfoils in Cascade. *Communications on Pure and Applied Mathematics*, 29(4):369–382, 1976.

W. S. Ghaly. *A Parametric Study of Radial Turbomachinery Blade Design in Three-Dimensional Subsonic Flow*. PhD thesis, MIT, Department of Aeronautics and Astronautics, 1986.

W. S. Ghaly. A Parametric Study of Radial Turbomachinery Blade Design in Three-dimensional Subsonic Flow. *Journal of Turbomachinery*, 112(3):338–345, 1990.

T. Goel, R. Vaidyanatham, R. T. Haftka, W. Shyy, N. V. Queipo, and K. Tucker. Response Surface Approximation of Pareto Optimal Front in Multi-objective Optimization. *Computer Methods in Applied Mechanics and Engineering*, 196: 879–893, 2007.

I. Hakeem, C-C Su, A. Costall, and R. F. Martinez-Botas. Effect of Volute Geometry on the Steady and Unsteady Performance of Mixed-flow. *Proceedings of the Institution of Mechanical Engineers. Part A: Journal of Power and Energy*, 221:535–550, 2007.

M. Hamel, M. Abidat, and S. A. Litim. Investigation of the Mixed Flow Turbine Performance under Inlet Pulsating Flow Conditions. *Comptes Rendus Mécanique*, 340(3):165–176, 2012.

T. Hamidreza, B. Masoud, and T. R. Mohammad. An Investigation on Turbocharger Turbine Performance Parameters under Inlet Pulsating Flow. *Journal of Fluids Engineering*, 134(8):081102, 2012.

J. T. Hamrick, A. Ginsburg, and W. M. Osborn. Methods of Analysis for Compressible Flow through Mixed-flow Centrifugal Impeller of Arbitrary Design. *NACA TN 2165*, 1950.

W. R. Hawthorne, C. Wang, C. S. Tan, and J. E. McCune. Theory of Blade Design for Large Deflections, Part I: Two-Dimensional Cascade. *Journal of Engineering for Gas Turbines and Power*, 106:346–353, 1984.

D. E. Hobson. *Shock-free Transonic Flow in Turbomachinery Cascades*. PhD thesis, Cambridge University, 1974.

L. Huang, W. Zhuge, Y. Zhang, L. Hu, D. Yang, and J. Wang. Numerical Investigation of the Effect of Rotor Blade Leading Edge Geometry on the Performance of a Variable Geometry Turbine. *Proceedings of ASME Turbo Expo 2012*, GT2012-69267, 2012.

A. Jameson, W. Schmidt, and E. Turkel. Numerical Solutions of the Euler Equations by Finite Volume Methods Using Runge-Kutta Time-stepping Schemes. *AIAA paper*, 1259(11), 1981.

W. Jansen and A. M. Kirschner. Impeller Blade Design Method for Centrifugal Compressors. *NASA SP 304*, pages 537–563, 1974.

J. Jiang and T. Dang. Design Method for Turbomachine Blades With Finite Thickness by the Circulation Method. *ASME 1994 International Gas Turbine and Aeroengine Congress and Exposition*, 94-GT-368:V001T01A128, 1994.

N. Karamanis and R. F. Martinez-Botas. Mixed-flow Turbines for Automotive Turbochargers: Steady and Unsteady Performance. *Proceedings of the Institution of Mechanical Engineers. Part D: Journal of Automobile Engineering*.

J-H Kim, J-H Choi, A. Husain, and K-Y Kim. Performance Enhancement of Axial Fan Blade through Multi-objective Optimization Techniques. *Journal of Mechanical Science and Technology*, 24(10):2059–2066, 2010.

D.G. Korn. Numerical Design of Transonic Cascades. *Journal of computational physics*, 29(1):20–34, 1978.

H. Kosuge, N. Yamanaka, I. Ariga, and I. Watanabe. Performance of Radial Flow Turbines under Pulsating Flow Conditions. *Journal of Engineering for Power*, 98(1):53–59, 1976.

J. K. W. Lam, Q. D. H. Roberts, and G. T. McDonnell. Flow Modelling of A Turbocharger Turbine under Pulsating Flow. *IMechE 7^{th} International Conference on Turbochargers and Turbocharging*, C602/025, 2002.

Y. Lian and M. Liou. Multiobjective Optimization Using Coupled Response Surface Model and Evolutionary Algorithm. *AIAA Journal*, 43(6):1316–1325, 2005.

M. J. Lighthill. *A Mathematical Method of Cascade Design*. HM Stationery Office, 1945.

M. J. Lighthill. *An Introduction to Fourier Analysis and Generalized Functions*. Cambridge University Press, London, 1959.

M. W. McBride. The Design and Analysis of Turbomachinery in An Incompressible, Steady Flow Using the Streamline Curvature Method. *PENNSYLVANIA STATE UNIV UNIVERSITY PARK APPLIED RESEARCH LAB*, ARL/PSU/TM-79-33, 1979.

G. Meauzé. An Inverse Time Marching Method for the Definition of Cascade Geometry. *Journal of Engineering for Power*, 104(3):650–656, 1982.

G. Meauzé and A. Lesain. Use of An Inverse Method for the Design of High Efficiency Compressor and Turbine Blades with Large Change in Radius. *ASME 1984 International Gas Turbine Conference and Exhibit*, 84-GT-167: V001T01A035, 1984.

F. Menter. Zonal Two Equation k-ω Turbulence Models for Aerodynamic Flows. *24^{th} Fluid Dynamics Conference*, 1993.

L. Mueller, Z. Alsalihi, and T. Verstraete. Multidisciplinary Optimization of A Turbocharger Radial Turbine. *Journal of Turbomachinery*, 135(2):021022, 2013.

R. A. Novak and G. Haymann-Haber. A Mixed-flow Cascade Passage Design Procedure Based on A Power Series Expansion. *Journal of Engineering for Power*, 105(2):231–242, 1983.

H. Okamoto, A. Goto, and M. Furukawa. Design of A Fan Using 3-D Inverse Design Method and CFD for High Efficiency and Low Aerodynamic Noise. *ASME 2009 Fluid Engineering Division Summer Meeting*, FEDSM2009-78454, 2009.

M. H. Padzillah, S. Rajoo, and R. F. Martinez-Botas. Numerical Assessment of Unsteady Flow Effects on A Nozzled Turbocharger Turbine. *Proceedings of ASME Turbo Expo 2012*, GT2012-69062, 2012.

Edward Palmer. Personal Communication, August 2012-02-17.

S. Pierret. Multi-objective Optimization of Three Dimensional Turbomachinery Blades. *European Conference for Aerospace Sciences*, 2005.

S. Pierret, R. Filomeno Coelho, and H. Kato. Multidisciplinary and Multiple Operating Points Shape Optimization of Three-dimensional Compressor Blades. *Structural and Multidisciplinary Optimization*, 33(1):61–70, 2007.

N. V. Queipo, R. T. Haftka, W. Shyy, T. Goel, R. Vaidyanathan, and P. K. Tucker. Surrogate-based Analysis and Optimization. *Progress in Aerospace Sciences*, 41 (1):1–28, 2005.

S. Rajoo and R. Martinez-Botas. Mixed Flow Turbine Research: A Review. *Journal of Turbomachinery*, 130(4):044001, 2008.

S. Rajoo and R. F. Martinez-Botas. Unsteady Effect in A Nozzled Turbocharger Turbine. *Journal of Turbomachinery*, 132(3):031001, 2010.

H. Roclawski, M. Böhle, and M. Gugau. Multidisciplinary Design Optimization of A Mixed Flow Turbine Wheel. *ASME Turbo Expo 2012*, GT2012-68233: 499–509, 2012.

J. M. Sanz. Design of Supercritical Cascades with High Solidity. *AIAA Journal*, 21(9):1289–1293, 1983.

J. M. Sanz, E. R. McFarland, N. L., Sanger, T. F. Gelder, and R. H. Cavicchi. Design and Performance of A Fixed, Nonaccelerating Guide Vane Cascade that Operates over An Inlet Flow Angle of 60 deg. *Journal of Engineering for Gas Turbines and Power*, 107(2):477–484, 1985.

F. G. Sator. Inverse Computation of Profile Shapes for Given Transonic Flow-configurations with and without Detached Bow-shocks in Two-dimensional Turbomachinery Cascades. *Journal of Engineering for Power*, 99(4):601–607, 1977.

E. Schmidt and P. Berger. Inverse Design of Supercritical Nozzles and Cascades. *International Journal for Numerical Methods in Engineering*, 22(2):417–432, 1986.

U. Siller, C. Vob, and E. Nicke. Automated Multidisciplinary Optimization of A Transonic Axial Compressor. *47th AIAA Aerospace Sciences Meeting including the New Horizons Forum and Aerospace Exposition*, 2009.

S. K. Singh. A Design Time Marching Method for the Generation of Blades in A Cascade. *ASME 1986 International Gas Turbine Conference and Exhibit*, 86-GT-167:V001T01A064, 1986.

H. Sobieczky and D. S. Dulikravich. A Computational Design Method for Transonic Turbomachinery Cascades. *ASME 1982 International Gas Turbine Conference and Exhibit*, 1982.

J. D. Stanitz. Design of Two Dimensional Channels with Prescribed Velocity Distribution along the Channel Walls. *NACA TN 2593*, 1952.

J. D. Stanitz. General Design Method for Three-dimensional, Potential Flow Fields. *NACA CR 3288*, 1980.

H. Tabatabaei, M. Boroomand, and M. Taeibi-Rahni. Experimental and Numerical Study of the Effect of Pulsating Flow on the Turbocharger Turbine Performance Parameters. *SAE Technical Paper*, No.2013-01-0938, 2013.

C. S. Tan, W. R. Hawthorne, J. E. McCune, and C. Wang. Theory of Blade Design for Large Deflections, Part II: Annular Cascades. *Journal of Engineering for Gas Turbines and Power*, 106:354–365, 1984.

W. T. Thompkins and S. S. Tong. Inverse or Design Calculations for Nonpotential Flow in Turbomachinery Blade Passages. *Journal of Engineering for Power*, 104(2):281–285, 1982.

J. F. Thompson, F. C. Thames, and C. W. Mastin. Boundary-fitted Curvilinear Coordinate Systems for Solution of Partial Differential Equations on Fields Containing and Number of Arbitrary Two-dimensional Bodies. *NASA CR-2729*, 1977.

W. T. Tiow and M. Zangeneh. A Viscous Transonic Inverse Design Method for Turbomachinery Blades: Part I — 2D Cascades. *ASME 1998 International Gas Turbine and Aeroengine Congress and Exhibition*, 98-GT-125:V001T01A037, 1998.

W. T. Tiow and M. Zangeneh. A Three-Dimensional Viscous Transonic Inverse Design Method. *ASME Turbo Expo 2000*, 2000-GT-0525:V001T03A089, 2000.

W. D. Tjokroaminata. A Design Study of Radial Inflow Turbines with Splitter Blades in Three-dimensional Flow. Master's thesis, MIT, Department of Aeronautics and Astronautics, 1992.

W. D. Tjokroaminata, C. S. Tan, and W. R. Hawthorne. A Design Study of Radial Inflow Turbines With Splitter Blades in Three-Dimensional Flow. *Journal of Turbomachinery*, 118(2):353–361, 1996.

S. S. Tong and W. T. Thompkins. A Design Calculation Procedure for Shock-Free or Strong Passage Shock Turbomachinery Cascades. *Journal of Engineering for Power*, 105(2):369–376, 1983.

A. Uenishi. A Design Method and the Performance of Two-dimensional Turbine Cascades for High Subsonic Flow. *ASME Paper*, 71-GT-34:V001T01A034, 1971.

T. Verstraete, Z. Alsalihi, and R. A. Van den Braembussche. Multidisciplinary Optimization of A Radial Compressor for Microgas Turbine Applications. *Journal of Turbomachinery*, 132(3):031004, 2007.

J. Walkingshaw, S. Spence, J. Ehrhard, and D. Thornhill. An Investigation into Improving Off-design Performance in A Turbocharger Turbine Utilizing Non-radial Blading. *ASME Turbo Expo 2011*, GT2011-45717:2023–2032, 2011.

F. J. Wallace and S. G. A. Pasha. Design, Construction and Testing of A Mixed Flow Gas Turbine. *The second international JSME Symposium on Fluid Machinery and Fluids*, pages 213–224, 1972.

Z. Wang. Inverse Design Calculations for Transonic Cascades. *ASME 1985 International Gas Turbine Conference and Exhibit*, pages V001T03A005–V001T03A005, 1985.

Z. Wang. A Method for Aerodynamic Design of Blades in Quasi-three-dimensional Calculation of Turbomachines. *Journal of Turbomachinery*, 110(2):181–186, 1988.

H. Watanabe and H. Harada. Suppression of Secondary Flows in A Turbine Nozzle with Controlled Stacking Shape and Exit Circulation by 3D Inverse Design Method. *International Gas Turbines & Aeroengine Congress & Exhibition*, 1999.

H. Watanabe, H. Okamoto, S. Guo, A. Goto, and M. Zangeneh. Optimization of Microturbine Aerodynamics Using CFD, Inverse Design and FEM Structural Analysis (2^{nd} Report: Turbine Design). *ASME Turbo Expo 2004*, GT2004-53583, 2004.

M. Watson and M. S. Janota. *Turbocharging the Internal Combustion Engine*. The Macmillan Press, London and Basingstoke, 1982.

A. Whitfield and N. C. Baines. *Design of Radial Turbomachines*. Longman Scientific & Technical, Essex, 1990.

D. E. Winterbone, B. Nikpour, and G. I. Alexander. Measurement of the Performance of A Radial Inflow Turbine in Conditional Steady and Unsteady Flow. *Proceedings of IMechE*, C405/015:153–162, 1990.

D. E. Winterbone, B. Nikpour, and H. Frost. A Contribution to the Understanding of Turbocharger Turbine Performance in Pulsating Flow. *Proc. Inst. Mech. Eng., Part C: Mech. Eng. Sci.*, Paper C433/011:19–28, 1991.

L. C. Wright and R. A. Novak. Aerodynamic Design and Development of the General Electric CJ805-23 Aft Fan Component. *ASME Paper No. 60-WA-270*, 1960.

C-H Wu and C. A. Brown. A Theory of the Direct and Inverse Problems of A Compressible Flow Past Cascades of Arbitrary Airfoils. *Journal of Aeronautical Sciences*, 19(3):183–196, 1952.

J. Z. Wu, H. Y. Ma, and M. D. Zhou. *Vorticity and Vortex Dynamics*. Springer, Berlin, 2005.

Y. L. Yang. *A Design Study of Radial Inflow Turbines in Three-dimensional Flow*. PhD thesis, MIT, Department of Aeronautics and Astronautics, 1991.

Y. L. Yang. Inverse Design of Turbomachinery Blading for Arbitrary Blade Thickness in Three-dimensional Transonic Flow. *ASME 1997 International Gas Turbine and Aeroengine Congress and Exhibition*, 1997.

Y. L. Yang, C. S. Tan, and W. R. Hawthorne. Aerodynamic Design of Turbomachinery Blading in Three-dimensional Flow: An application to Radial Inflow Turbines. *Journal of Turbomachinery*, 115(3):602–613, 1993.

M. Zangeneh. Three Dimensional Design of A High Speed Radial-inflow Turbine by a Novel Design Method. *Gas Turbine & Aeroengine Congress & Exposition*, 1990.

M. Zangeneh. A Compressible Three-dimensional Design Method for Radial and Mixed Flow Turbomachinery Blades. *International Journal for Numerical Methods for Fluids*, 13(5):599–624, 1991.

M. Zangeneh and D. V. C. Roduner. Improving A Vaned Diffuser for A Given Centrifugal Impeller by 3D Inverse Design. *ASME Turbo Expo 2002*, GT2002-30621, 2002.

M. Zangeneh, A. Goto, and T. Takemura. Suppression of Secondary Flows in A Mixed-flow Pump Impeller by Application of Three-dimensional Inverse Design Method: Part 1 —— Design and Numerical Validation. *Journal of Turbomachinery*, 118:536–543, 1996.

M. Zangeneh, B. Nikpour, and H. Watanabe. Development of A High Performance Centrifugal Compressor Using A 3D Inverse Design Technique. *IMechE 9th International Conference on Turbochargers and Turbocharging*, pages 135–145, 2010.

M. Zangeneh-Kazemi. *Three-Dimensional Design of Radial-Inflow Turbines*. PhD thesis, Cambridge University, Engineering Department, 1986.

L. Zannetti. Time-Dependent Method to Solve the Inverse Problem for Internal Flows. *AIAA Journal*, 18(7):754–758, 1980.

L. Zannetti and T. Ayele. Time Dependent Computation of the Euler Equations for Designing Fully 3D Turbomachinery Blade Rows, Including the Case of Transonic Shockfree Design. *25th AIAA Aerospace Sciences Meeting*, AIAA-87-0007, 1987.

J. Zhang and M. Zangeneh. Increasing Pulse Energy Recovery of Radial Turbocharger Turbine by 3D Inverse Design Method. *ASME Turbo Expo 2015*, GT2015-43579, 2015.

J. Zhang, M. Zangeneh, and P. Eynon. A 3D Inverse Design based Multidisciplinary Optimization on the Radial and Mixed-inflow Turbines for Turbochargers. *IMechE 11th International Conference on Turbochargers and Turbocharging*, pages 399–410, 2014.

J. Zhang, P. Gomes, M. Zangeneh, and B. Choo. Design of A Centrifugal Compressor Stage and A Radial-inflow Turbine Stage for A Supercritical CO_2 Recompression Brayton Cycle by Using 3D Inverse Design Method. *ASME Turbo Expo 2017*, GT2017-64631, 2017.

X-L Zhao, C-L Sun, and C-H Wu. A Simple Method for Solving Three Dimensional Inverse Problems of Turbomachine Flow and the Annular Constraint Condition. *Journal of Engineering for Gas Turbines and Power*, 107(2):293–300, 1985.

APPENDIX A

FORMULATIONS OF INVERSE DESIGN METHOD

In this section, a detailed description and derivation of all formulations used in the inverse design method (Circulation Method) is presented. This method was originally proposed by Hawthorne et al. [1984] for the design of 2D cascades with infinitely thin blades in the incompressible flow. It has been extended to the 3D design of axial machines with the incompressible flow by Tan et al. [1984]. Borges [1986] using the finite difference approach and Ghaly [1986] using the finite element approach extended this method to the application of turbomachines with arbitrary hub and shroud profiles, for example radial-inflow turbines and centrifugal compressors. Zangeneh-Kazemi [1986] added the flow compressibility and the blockage effect due to the blade thickness into this method.

Basic Assumptions

The following basic assumptions for this inverse design method are made first:

1) The flow is steady, invisicd and uniform at the inlet;

2) There is no heat transfer;

3) The working fluid is compressible and an ideal gas;

4) The blade has zero thickness;

5) There is no incidence at the leading edge and no trailing edge shed vorticity;

6) The flow is subsonic.

Assumption 1) with Kelvin's circulation theory implies that the only vorticity in the entire flow field including the inlet domain, the blade row and the outlet domain is bounded on the solid blade surfaces and called blade bound vorticity. Using assumption 4), each blade can be represented by single sheet of vorticity. To account for the blockage effect of the blade thickness a mean stream surface thickness parameter is used in the continuity equation of the mean flow.

The blade shape is defined by:

$$\alpha\left(\theta, r, z\right) = \theta - f\left(r, z\right) = \pm n\frac{2\pi}{B} \tag{A.1}$$

Where r, θ and z are cylindrical coordinates in a right-handed coordinate system, f is the angular coordinate (or called wrap angle) of a point on the blade camber line, B is the number of blades, $n = 0,1,2,\ldots,B-1$ and α is the blade surfaces at $\theta = f\left(r, z\right) \pm n\frac{2\pi}{B}$.

The symbol of the over bar '$-$' is defined as a circumferential mean, for example:

$$\overline{A}\left(r, z\right) = \frac{B}{2\pi}\int_0^{\frac{2\pi}{B}} A\left(r, \theta, z\right)d\theta \tag{A.2}$$

Where A can be a scalar or a vector.

A periodic Dirac delta function with the period of $\frac{2\pi}{B}$ is also defined by:

$$\sum_{n=-\infty}^{\infty}\delta\left(\alpha - n\frac{2\pi}{B}\right) = \begin{cases} +\infty & \alpha = n\frac{2\pi}{B} \\ 0 & \alpha \neq n\frac{2\pi}{B} \end{cases} \tag{A.3}$$

The absolute vorticity only bounded to the blade surfaces can be written as:

$$\begin{aligned}\vec{\Omega}(r,\theta,z) &= \sum_{n=-\infty}^{\infty} \vec{\Omega}(r,\theta,z)\,|_{\alpha=n\frac{2\pi}{B}} \\ &= \sum_{n=-\infty}^{\infty} \int_0^{\frac{2\pi}{B}} \vec{\Omega}(r,\theta,z)\,\delta\left(\alpha - n\frac{2\pi}{B}\right) d\theta \\ &= \frac{B}{2\pi}\int_0^{\frac{2\pi}{B}} \vec{\Omega}(r,\theta,z)\,d\theta \frac{2\pi}{B} \sum_{n=-\infty}^{\infty} \delta\left(\alpha - n\frac{2\pi}{B}\right) \\ &= \overline{\vec{\Omega}}(r,z)\,\delta_P(\alpha) \end{aligned} \tag{A.4}$$

Where $\delta_P(\alpha)$ (see Lighthill [1959]) is defined by Equation A.5.

$$\delta_P(\alpha) = \frac{2\pi}{B} \sum_{n=-\infty}^{\infty} \delta\left(\alpha - n\frac{2\pi}{B}\right) = \sum_{n=-\infty}^{\infty} e^{inB\alpha} \tag{A.5}$$

Monge-Clebsch Decomposition

Using Monge-Clebsch decomposition (Wu et al. [2005]) the absolute velocity vector $\vec{V}$ can be decomposed into a potential part plus a rotational part by:

$$\vec{V}(r,\theta,z) = \nabla\Phi(r,\theta,z) + \lambda(r,\theta,z)\,\nabla\mu(r,\theta,z) \tag{A.6}$$

Where Φ, λ and μ are called Monge-Clebsch scalars, $\nabla\Phi$ accounts for the potential part of the flow and $\lambda\nabla\mu$ accounts for the rotational part. The vorticity $\vec{\Omega}$ can be obtained by taking the curl of Equation A.6:

$$\begin{aligned}\vec{\Omega}(r,\theta,z) &= \nabla \times \vec{V}(r,\theta,z) \\ &= \nabla \times [\nabla\Phi(r,\theta,z) + \lambda(r,\theta,z)\,\nabla\mu(r,\theta,z)] \\ &= \nabla \times [\nabla\Phi(r,\theta,z)] + \nabla \times [\lambda(r,\theta,z)\,\nabla\mu(r,\theta,z)] \\ &= \nabla \times [\lambda(r,\theta,z)\,\nabla\mu(r,\theta,z)] \\ &= \lambda(r,\theta,z)\,\nabla \times \nabla\mu(r,\theta,z) + \nabla\lambda(r,\theta,z) \times \nabla\mu(r,\theta,z) \\ &= \nabla\lambda(r,\theta,z) \times \nabla\mu(r,\theta,z) \end{aligned} \tag{A.7}$$

One special feature of Equation A.7 is that when vorticity $\vec{\Omega}$ can be written in the form of the cross product of gradients of two scalars, the Monge-Clebsch decomposition of the velocity vector can be written down using Equation A.6

immediately. From Equation A.7 it can be seen that $\vec{\Omega}$ is perpendicular to vectors $\nabla\lambda$ and $\nabla\mu$. As it is mentioned above, the only vorticity is bounded on the blade surfaces. Therefore, vorticity vector $\vec{\Omega}$ is always lying on the blade surface and perpendicular to $\nabla\alpha$, where $\nabla\alpha$ is perpendicular to blade surfaces α. One of the Monge-Clebsch scalars can be assumed to be α and Equation A.7 can be rewritten in the following form using Equation A.1:

$$\begin{aligned}
\vec{\Omega}(r,\theta,z) &= \nabla\lambda(r,\theta,z)\times\nabla\alpha(r,\theta,z)\\
&= \left[\frac{\partial\lambda(r,\theta,z)}{\partial r},\frac{\partial\lambda(r,\theta,z)}{r\partial\theta},\frac{\partial\lambda(r,\theta,z)}{\partial z}\right]\times\left[\frac{\partial\alpha(r,\theta,z)}{\partial r},\frac{\partial\alpha(r,\theta,z)}{r\partial\theta},\frac{\partial\alpha(r,\theta,z)}{\partial z}\right]\\
&= \left[\frac{\partial\lambda(r,\theta,z)}{\partial r},\frac{\partial\lambda(r,\theta,z)}{r\partial\theta},\frac{\partial\lambda(r,\theta,z)}{\partial z}\right]\times\left[\frac{-\partial f(r,z)}{\partial r},\frac{1}{r},\frac{-\partial f(r,z)}{\partial z}\right]
\end{aligned} \tag{A.8}$$

Taking the circumferential mean of both sides of Equation A.8, the mean vorticity $\overline{\vec{\Omega}}$ can be computed:

$$\begin{aligned}
\overline{\vec{\Omega}}(r,z) &= \overline{\left[\frac{\partial\lambda(r,\theta,z)}{\partial r},\frac{\partial\lambda(r,\theta,z)}{r\partial\theta},\frac{\partial\lambda(r,\theta,z)}{\partial z}\right]\times\left[\frac{-\partial f(r,z)}{\partial r},\frac{1}{r},\frac{-\partial f(r,z)}{\partial z}\right]}\\
&= \left[\overline{\frac{\partial\lambda(r,\theta,z)}{\partial r}},\overline{\frac{\partial\lambda(r,\theta,z)}{r\partial\theta}},\overline{\frac{\partial\lambda(r,\theta,z)}{\partial z}}\right]\times\left[\frac{-\partial f(r,z)}{\partial r},\frac{1}{r},\frac{-\partial f(r,z)}{\partial z}\right]\\
&= \left[\frac{\partial\overline{\lambda}(r,z)}{\partial r},\frac{\partial\overline{\lambda}(r,z)}{r\partial\theta},\frac{\partial\overline{\lambda}(r,z)}{\partial z}\right]\times\left[\frac{-\partial f(r,z)}{\partial r},\frac{1}{r},\frac{-\partial f(r,z)}{\partial z}\right]\\
&= \left[\frac{\partial\overline{\lambda}(r,z)}{\partial r},0,\frac{\partial\overline{\lambda}(r,z)}{\partial z}\right]\times\left[\frac{-\partial f(r,z)}{\partial r},\frac{1}{r},\frac{-\partial f(r,z)}{\partial z}\right]\\
&= \left[-\frac{\partial\overline{\lambda}(r,z)}{r\partial z},\frac{\partial\overline{\lambda}(r,z)}{\partial r}\frac{\partial f(r,z)}{\partial z}-\frac{\partial\overline{\lambda}(r,z)}{\partial z}\frac{\partial f(r,z)}{\partial r},\frac{\partial\overline{\lambda}(r,z)}{r\partial r}\right]
\end{aligned} \tag{A.9}$$

To determine another Monge-Clebsch scalar $\overline{\lambda}$, the mean vorticity $\overline{\vec{\Omega}}$ is expressed by taking the circumferential mean of the curl of the velocity $\overline{\vec{V}}$:

$$\begin{aligned}
\overline{\vec{\Omega}}(r,z) &= \overline{\nabla \times \vec{V}}(r,\theta,z) \\
&= \nabla \times \overline{\vec{V}}(r,z) \\
&= \nabla \times \left[\overline{V}_r(r,z), \overline{V}_\theta(r,z), \overline{V}_z(r,z)\right] \\
&= \left[\frac{\partial \overline{V}_z(r,z)}{r\partial\theta} - \frac{\partial \overline{V}_\theta(r,z)}{\partial z}, \frac{\partial \overline{V}_r(r,z)}{\partial z} - \frac{\partial \overline{V}_z(r,z)}{\partial r}, \frac{\partial r\overline{V}_\theta(r,z)}{r\partial r} - \frac{\partial \overline{V}_r(r,z)}{r\partial\theta}\right] \\
&= \left[-\frac{\partial \overline{V}_\theta(r,z)}{\partial z}, \frac{\partial \overline{V}_r(r,z)}{\partial z} - \frac{\partial \overline{V}_z(r,z)}{\partial r}, \frac{\partial r\overline{V}_\theta(r,z)}{r\partial r}\right] \\
&= \left[-\frac{\partial r\overline{V}_\theta(r,z)}{r\partial z}, \frac{\partial \overline{V}_r(r,z)}{\partial z} - \frac{\partial \overline{V}_z(r,z)}{\partial r}, \frac{\partial r\overline{V}_\theta(r,z)}{r\partial r}\right]
\end{aligned} \tag{A.10}$$

By comparing Equation A.9 and Equation A.10, we can get:

$$\overline{\lambda}(r,z) = r\overline{V}_\theta(r,z) \tag{A.11}$$

Therefore, Equation A.4 and Equation A.9 become:

$$\vec{\Omega}(r,\theta,z) = \left[\nabla r\overline{V}_\theta(r,z) \times \nabla\alpha(r,\theta,z)\right]\delta_P(\alpha) \tag{A.12}$$

$$\bar{\vec{\Omega}}(r,z) = \nabla r\overline{V}_\theta(r,z) \times \nabla\alpha(r,\theta,z) \tag{A.13}$$

The absolute vorticity $\vec{\Omega}$ in Equation A.12 can be rewritten by Equation A.14 using a periodic sawtooth function $S(\alpha)$ (Lighthill [1959]) which is defined by

Equation A.15 and Equation A.16.

$$\begin{aligned}
\nabla \times \overrightarrow{V}(r,\theta,z) &= \vec{\Omega}(r,\theta,z) \\
&= \left[\nabla r\overline{V}_\theta(r,z) \times \nabla\alpha(r,\theta,z)\right]\delta_P(\alpha) \\
&= \nabla r\overline{V}_\theta(r,z) \times \nabla\alpha(r,\theta,z) + \nabla r\overline{V}_\theta(r,z) \times [(\delta_P(\alpha)-1)\nabla\alpha(r,\theta,z)] \\
&= \nabla r\overline{V}_\theta(r,z) \times \nabla\alpha(r,\theta,z) + \nabla r\overline{V}_\theta(r,z) \times [S'(\alpha)\nabla\alpha(r,\theta,z)] \\
&= \nabla r\overline{V}_\theta(r,z) \times \nabla\alpha(r,\theta,z) + \nabla r\overline{V}_\theta(r,z) \times \nabla S(\alpha) \\
&= \nabla r\overline{V}_\theta(r,z) \times \nabla\alpha(r,\theta,z) - \nabla S(\alpha) \times \nabla r\overline{V}_\theta(r,z) \\
&= \nabla r\overline{V}_\theta(r,z) \times \nabla\alpha(r,\theta,z) + \nabla r\overline{V}_\theta(r,z)[\nabla \times \nabla\alpha(r,\theta,z)] \\
&\quad - \nabla S(\alpha) \times \nabla r\overline{V}_\theta(r,z) - S(\alpha)\left[\nabla \times \nabla r\overline{V}_\theta(r,z)\right] \\
&= \nabla \times \left[r\overline{V}_\theta(r,z)\nabla\alpha(r,\theta,z)\right] - \nabla \times \left[S(\alpha)\nabla r\overline{V}_\theta(r,z)\right] \\
&= \nabla \times \nabla\Phi(r,\theta,z) + \nabla \times \left[r\overline{V}_\theta(r,z)\nabla\alpha(r,\theta,z)\right] - \nabla \times \left[S(\alpha)\nabla r\overline{V}_\theta(r,z)\right] \\
&= \nabla \times \left[\nabla\Phi(r,\theta,z) + r\overline{V}_\theta(r,z)\nabla\alpha(r,\theta,z) - S(\alpha)\nabla r\overline{V}_\theta(r,z)\right]
\end{aligned} \tag{A.14}$$

$$\frac{dS(\alpha)}{d\alpha} = S'(\alpha) = \delta_P(\alpha) - 1 = \sum_{n=-\infty}^{\infty} e^{inB\alpha} - 1 = 2\sum_{n=1}^{\infty} e^{inB\alpha} \tag{A.15}$$

$$S(\alpha) = 2\sum_{n=1}^{\infty} \frac{e^{inB\alpha}}{inB} + C \tag{A.16}$$

By comparing both sides of Equation A.14, the expression for velocity vector $\vec{V}$ can be obtained:

$$\overrightarrow{V}(r,\theta,z) = \nabla\Phi(r,\theta,z) + r\overline{V}_\theta(r,z)\nabla\alpha(r,\theta,z) - S(\alpha)\nabla r\overline{V}_\theta(r,z) \tag{A.17}$$

Since the flow is periodic in the circumferential direction, it is convenient to express the flow variables as the summation of a mean part ($\overline{\square}$) and a periodic part ($\widetilde{\square}$). This summation corresponds to the mathematical representation of the flow variables by a Fourier series in which the mean part is the zeroth harmonic while the periodic part constitutes the nonzeroth harmonics. Therefore, velocity $\vec{V}$ can be expressed in the form of the summation of a mean velocity $\overrightarrow{\overline{V}}$ and a

periodic velocity $\widetilde{\overrightarrow{V}}$ as shown in Equation A.18.

$$\overrightarrow{V}(r,\theta,z) = \overline{\overrightarrow{V}}(r,z) + \widetilde{\overrightarrow{V}}(r,\theta,z) \tag{A.18}$$

$\overline{\overrightarrow{V}}$ and $\widetilde{\overrightarrow{V}}$ can be written in the following form:

$$\overline{\overrightarrow{V}}(r,z) = \nabla\overline{\Phi}(r,z) + r\overline{V}_{\theta}(r,z)\nabla\alpha(r,\theta,z) \tag{A.19}$$

$$\widetilde{\overrightarrow{V}}(r,\theta,z) = \nabla\widetilde{\Phi}(r,\theta,z) - S(\alpha)\nabla r\overline{V}_{\theta}(r,z) \tag{A.20}$$

Where $\overline{\Phi}$ is the potential function for the mean flow and $\widetilde{\Phi}$ is the potential function for the periodic flow. Since the flow field is irrotational in the inlet (upstream) and outlet (downstream) domains, the last term on the RHS of Equation A.19 and Equation A.20 are equal to zero in those regions of the flow field.

Calculation of Flow Field

In this subsection the governing equations of the mean and periodic flow using two different approaches (approximate approach and exact approach) will be derived. First the continuity equation in the relative frame of reference is introduced.

Continuity Equation

The blades are assumed to be rotating with a constant speed ω. Therefore, using Equation A.18 and Equation A.22 the relative velocity $\vec{W}$ can be written as:

$$\begin{aligned}\overrightarrow{W}(r,\theta,z) &= \overrightarrow{V}(r,\theta,z) - \overrightarrow{\omega}\times\overrightarrow{r} \\ &= \overline{\overrightarrow{V}}(r,z) + \widetilde{\overrightarrow{V}}(r,\theta,z) - \overrightarrow{\omega}\times\overrightarrow{r} \\ &= \overline{\overrightarrow{W}}(r,z) + \widetilde{\overrightarrow{V}}(r,\theta,z)\end{aligned} \tag{A.21}$$

Where the mean relative velocity $\overrightarrow{\overline{W}}$ is defined by:

$$\begin{aligned}\overrightarrow{\overline{W}}(r,z) &= \overline{\overrightarrow{V}(r,z) - \overrightarrow{\omega} \times \overrightarrow{r}} \\ &= \overrightarrow{\overline{V}}(r,z) - \overline{\overrightarrow{\omega} \times \overrightarrow{r}} \\ &= \overrightarrow{\overline{V}}(r,z) - \overrightarrow{\omega} \times \overrightarrow{r}\end{aligned} \tag{A.22}$$

The continuity equation of a steady and compressible flow can be written as:

$$\begin{aligned}&\nabla \cdot \left[\rho(r,\theta,z)\overrightarrow{W}(r,\theta,z)\right] = 0 \\ &\rho(r,\theta,z)\nabla \cdot \overrightarrow{W}(r,\theta,z) + \overrightarrow{W}(r,\theta,z) \cdot \nabla\rho(r,\theta,z) = 0 \\ &\nabla \cdot \overrightarrow{W}(r,\theta,z) = -\overrightarrow{W}(r,\theta,z) \cdot \frac{\nabla\rho(r,\theta,z)}{\rho(r,\theta,z)} \\ &\nabla \cdot \overrightarrow{W}(r,\theta,z) = -\overrightarrow{W}(r,\theta,z) \cdot \nabla \ln\rho(r,\theta,z)\end{aligned} \tag{A.23}$$

Taking the circumferential mean of both sides of Equation A.23 we have:

$$\begin{aligned}\overline{\nabla \cdot \overrightarrow{W}(r,\theta,z)} &= \overline{-\overrightarrow{W}(r,\theta,z) \cdot \nabla \ln\rho(r,\theta,z)} \\ \nabla \cdot \overrightarrow{\overline{W}}(r,z) &= -\overline{\overrightarrow{W}(r,\theta,z) \cdot \nabla \ln\rho(r,\theta,z)}\end{aligned} \tag{A.24}$$

Equation A.24 is the exact expression of the continuity equation for the mean flow. The exact expression of the continuity equation for the periodic flow can be obtained using the divergence of Equation A.21, Equation A.23 and Equation A.24 as shown below:

$$\begin{aligned}\nabla \cdot \widetilde{\overrightarrow{V}}(r,\theta,z) &= \nabla \cdot \left[\overrightarrow{W}(r,\theta,z) - \overrightarrow{\overline{W}}(r,z)\right] \\ &= \nabla \cdot \overrightarrow{W}(r,\theta,z) - \nabla \cdot \overrightarrow{\overline{W}}(r,z) \\ &= -\overrightarrow{W}(r,\theta,z) \cdot \nabla \ln\rho(r,\theta,z) + \overline{\overrightarrow{W}(r,\theta,z) \cdot \nabla \ln\rho(r,\theta,z)}\end{aligned} \tag{A.25}$$

To derive the approximate expressions of the continuity equation for the mean and periodic flow, the density ρ is assumed to be split into a mean part $\overline{\rho}$ and a periodic part $\widetilde{\rho}$:

$$\rho(r,\theta,z) = \overline{\rho}(r,z) + \widetilde{\rho}(r,\theta,z) \tag{A.26}$$

Substituting Equation A.21 and Equation A.26 into Equation A.23, we can get:

$$\begin{aligned}
\nabla \cdot \left[\overline{\overrightarrow{W}}(r,z) + \widetilde{\overrightarrow{V}}(r,\theta,z)\right] &= -\left[\overline{\overrightarrow{W}}(r,z) + \widetilde{\overrightarrow{V}}(r,\theta,z)\right] \cdot \nabla \ln\left[\overline{\rho}(r,z) + \widetilde{\rho}(r,\theta,z)\right] \\
\nabla \cdot \overline{\overrightarrow{W}}(r,z) + \nabla \cdot \widetilde{\overrightarrow{V}}(r,\theta,z) &= -\left[\overline{\overrightarrow{W}}(r,z) + \widetilde{\overrightarrow{V}}(r,\theta,z)\right] \cdot \nabla \ln\left\{\overline{\rho}(r,z)\left[1 + \frac{\widetilde{\rho}(r,\theta,z)}{\overline{\rho}(r,z)}\right]\right\} \\
\nabla \cdot \overline{\overrightarrow{W}}(r,z) + \nabla \cdot \widetilde{\overrightarrow{V}}(r,\theta,z) &= -\left[\overline{\overrightarrow{W}}(r,z) + \widetilde{\overrightarrow{V}}(r,\theta,z)\right] \cdot \left\{\nabla \ln \overline{\rho}(r,z) + \nabla \ln\left[1 + \frac{\widetilde{\rho}(r,\theta,z)}{\overline{\rho}(r,z)}\right]\right\}
\end{aligned} \tag{A.27}$$

If the circumferential variation of the density $\widetilde{\rho}$ is assumed to be negligible compared to the mean density $\overline{\rho}$ ($\frac{\widetilde{\rho}}{\overline{\rho}} \approx 0$), Equation A.27 can be reduced to:

$$\nabla \cdot \overline{\overrightarrow{W}}(r,z) + \nabla \cdot \widetilde{\overrightarrow{V}}(r,\theta,z) = -\left[\overline{\overrightarrow{W}}(r,z) + \widetilde{\overrightarrow{V}}(r,\theta,z)\right] \cdot \nabla \ln \overline{\rho}(r,z) \tag{A.28}$$

Hence, the approximate mean flow continuity equation is reduced to:

$$\begin{aligned}
\nabla \cdot \overline{\overrightarrow{W}}(r,z) &= -\overline{\overrightarrow{W}}(r,z) \cdot \nabla \ln \overline{\rho}(r,z) \\
\nabla \cdot \left[\overline{\rho}(r,z)\,\overline{\overrightarrow{W}}(r,z)\right] &= 0
\end{aligned} \tag{A.29}$$

The approximate periodic flow continuity equation is reduced to:

$$\nabla \cdot \widetilde{\overrightarrow{V}}(r,\theta,z) = -\widetilde{\overrightarrow{V}}(r,\theta,z) \cdot \nabla \ln \overline{\rho}(r,z) \tag{A.30}$$

Blockage Effects

In the beginning of this section we have assumed that the blade has zero thickness. However, in some cases, for example the hub thickness of a radial-inflow turbine in the exducer part is very large and its blockage effect cannot be neglected. To account for the blockage effect caused by the blade thickness, a blockage factor B_f is introduced into the mean flow continuity equation. The approximate mean flow continuity equation (Equation A.29) including blockage factor B_f becomes:

$$\nabla \cdot \left[\overline{\rho}(r,z)\,B_f(r,z)\,\overline{\overrightarrow{W}}(r,z)\right] = 0 \tag{A.31}$$

Where B_f is defined as:

$$B_f(r,z) = \frac{2\pi r - t_\theta(r,z)\,B}{2\pi r} = 1 - \frac{t_\theta(r,z)\,B}{2\pi r} \tag{A.32}$$

Where r is the radius, t_θ is the blade tangential thickness and B is the number of blades. In the case that the blade normal thickness t_N is defined, the tangential thickness can be obtained based on the normal thickness t_N and the estimated blade camber line f:

$$\begin{aligned} t_\theta(r,z) &= t_N(r,z)\sqrt{1 + r^2\left[\frac{\partial f(r,z)}{\partial r}\right]^2 + r^2\left[\frac{\partial f(r,z)}{\partial z}\right]^2} \\ &= t_N(r,z)\sqrt{1 + r^2\left[\frac{\partial f(r,z)}{\partial m}\right]^2} \end{aligned} \tag{A.33}$$

Solving Approximate Mean Flow Continuity Equation

To solve Equation A.31, a stream function Ψ can be defined:

$$\begin{aligned} \overline{W}_r(r,z) = \overline{V}_r(r,z) &= -\frac{\rho_i}{r\overline{\rho}(r,z)\,B_f(r,z)}\frac{\partial\Psi(r,z)}{\partial z} \\ \overline{W}_z(r,z) = \overline{V}_z(r,z) &= \frac{\rho_i}{r\overline{\rho}(r,z)\,B_f(r,z)}\frac{\partial\Psi(r,z)}{\partial r} \end{aligned} \tag{A.34}$$

Where ρ_i is a reference density and Ψ is the so-called Stokes stream function for 3D axisymmetric flow. To simplify Equation A.34 an artificial density ρ_a is defined:

$$\rho_a(r,z) = \frac{\rho_i}{\overline{\rho}(r,z)} \tag{A.35}$$

Using Equation A.35 to simplify Equation A.34 we can get:

$$\begin{aligned} \overline{W}_r(r,z) = \overline{V}_r(r,z) &= -\frac{\rho_a(r,z)}{rB_f(r,z)}\frac{\partial\Psi(r,z)}{\partial z} \\ \overline{W}_z(r,z) = \overline{V}_z(r,z) &= \frac{\rho_a(r,z)}{rB_f(r,z)}\frac{\partial\Psi(r,z)}{\partial r} \end{aligned} \tag{A.36}$$

The stream function Ψ defined by Equation A.36 automatically satisfies Equation A.31. To get another equation for the unknown stream function Ψ, comparing the tangential component of the mean vorticity $\overline{\Omega}_\theta$ in Equation A.9 and Equa-

tion A.10, we can get:

$$\begin{aligned}\overline{\Omega}_\theta(r,z) &= \frac{\partial r\overline{V}_\theta(r,z)}{\partial r}\frac{\partial f(r,z)}{\partial z} - \frac{\partial r\overline{V}_\theta(r,z)}{\partial z}\frac{\partial f(r,z)}{\partial r} \\ &= \frac{\partial \overline{V}_r(r,z)}{\partial z} - \frac{\partial \overline{V}_z(r,z)}{\partial r}\end{aligned} \tag{A.37}$$

Substituting Equation A.36 into Equation A.37, the following equation for the unknown stream function Ψ can be obtained:

$$\begin{aligned}&\frac{\partial \overline{V}_r(r,z)}{\partial z} - \frac{\partial \overline{V}_z(r,z)}{\partial r} = \frac{\partial\left[-\frac{\rho_a(r,z)}{rB_f(r,z)}\frac{\partial\Psi(r,z)}{\partial z}\right]}{\partial z} - \frac{\partial\left[\frac{\rho_a(r,z)}{rB_f(r,z)}\frac{\partial\Psi(r,z)}{\partial r}\right]}{\partial r} \\ &= -\frac{1}{rB_f(r,z)}\frac{\partial\rho_a(r,z)}{\partial z}\frac{\partial\Psi(r,z)}{\partial z} + \frac{\rho_a(r,z)}{rB_f^2(r,z)}\frac{\partial B_f(r,z)}{\partial z}\frac{\partial\Psi(r,z)}{\partial z} - \frac{\rho_a(r,z)}{rB_f(r,z)}\frac{\partial\Psi^2(r,z)}{\partial z^2} \\ &\quad - \frac{1}{rB_f(r,z)}\frac{\partial\rho_a(r,z)}{\partial r}\frac{\partial\Psi(r,z)}{\partial r} + \frac{\rho_a(r,z)}{r^2B_f(r,z)}\frac{\partial\Psi(r,z)}{\partial r} + \frac{\rho_a(r,z)}{rB_f^2(r,z)}\frac{\partial B_f(r,z)}{\partial r}\frac{\partial\Psi(r,z)}{\partial r} \\ &\quad - \frac{\rho_a(r,z)}{rB_f(r,z)}\frac{\partial\Psi^2(r,z)}{\partial r^2} \\ &= \frac{\partial r\overline{V}_\theta(r,z)}{\partial r}\frac{\partial f(r,z)}{\partial z} - \frac{\partial r\overline{V}_\theta(r,z)}{\partial z}\frac{\partial f(r,z)}{\partial r}\end{aligned} \tag{A.38}$$

Rearranging Equation A.38 we can get:

$$\begin{aligned}&\frac{\partial\Psi^2(r,z)}{\partial r^2} - \frac{\partial\Psi(r,z)}{r\partial r} + \frac{\partial\Psi^2(r,z)}{\partial z^2} + \frac{\partial\Psi(r,z)}{\partial r}\left[\frac{\partial\ln\rho_a(r,z)}{\partial r} - \frac{\partial\ln B_f(r,z)}{\partial r}\right] \\ &\quad + \frac{\partial\Psi(r,z)}{\partial z}\left[\frac{\partial\ln\rho_a(r,z)}{\partial z} - \frac{\partial\ln B_f(r,z)}{\partial z}\right] \\ &= \frac{rB_f(r,z)}{\rho_a(r,z)}\left[\frac{\partial r\overline{V}_\theta(r,z)}{\partial z}\frac{\partial f(r,z)}{\partial r} - \frac{\partial r\overline{V}_\theta(r,z)}{\partial r}\frac{\partial f(r,z)}{\partial z}\right]\end{aligned} \tag{A.39}$$

Where the RHS of Equation A.39 is zero outside the blade row since the flow is assumed to be irrotational in the inlet and outlet domains. This elliptic partial differential equation can be solved subject to boundary conditions at the hub, shroud, upstream and downstream boundaries.

1) The boundary conditions at the hub and shroud are that no flow passes through these solid walls which implies that the hub and shroud lines are streamlines of the flow. Therefore, the following boundary conditions apply at the hub and shroud:

$$\Psi(r,z) = const \tag{A.40}$$

2) The far upstream boundary condition is obtained from the known mean velocity at the far upstream $\overrightarrow{\overline{V}}_{-\infty}$ which is a design specification by using:

$$-\frac{\rho_a(r,z)}{r}\frac{\partial\Psi(r,z)}{\partial s(r,z)} = \overrightarrow{\overline{V}}_{-\infty}\cdot\vec{n} \tag{A.41}$$

Where s is the distance along the far upstream boundary and $\vec{n}$ is the unit vector perpendicular to it.

3) In the absence of the shed vorticity, the velocity at the far downstream $\overrightarrow{\overline{V}}_{\infty}$ will be uniform and hence the boundary condition is given by:

$$-\frac{\rho_a(r,z)}{r}\frac{\partial\Psi(r,z)}{\partial s(r,z)} = \overrightarrow{\overline{V}}_{\infty}\cdot\vec{n} \tag{A.42}$$

Solving Approximate Periodic Flow Continuity Equation

To solve Equation A.30, take the divergence of Equation A.20 and use Equation A.30 to get:

$$\begin{aligned}
&\nabla^2\widetilde{\Phi}(r,\theta,z) - \nabla\cdot\overrightarrow{\widetilde{V}}(r,\theta,z) = \nabla\cdot\left[S(\alpha)\nabla r\overline{V}_\theta(r,z)\right]\\
&\nabla^2\widetilde{\Phi}(r,\theta,z) + \overrightarrow{\widetilde{V}}(r,\theta,z)\cdot\nabla\ln\overline{\rho}(r,z) = S(\alpha)\nabla^2 r\overline{V}_\theta(r,z) + S'(\alpha)\nabla\alpha\cdot\nabla r\overline{V}_\theta(r,z)\\
&\nabla^2\widetilde{\Phi}(r,\theta,z) + \left[\nabla\widetilde{\Phi}(r,\theta,z) - S(\alpha)\nabla r\overline{V}_\theta(r,z)\right]\cdot\nabla\ln\overline{\rho}(r,z) = S(\alpha)\nabla^2 r\overline{V}_\theta(r,z)\\
&\qquad\qquad + S'(\alpha)\nabla\alpha\cdot\nabla r\overline{V}_\theta(r,z)\\
&\nabla^2\widetilde{\Phi}(r,\theta,z) + \nabla\widetilde{\Phi}(r,\theta,z)\cdot\nabla\ln\overline{\rho}(r,z) = S(\alpha)\nabla^2 r\overline{V}_\theta(r,z) + S'(\alpha)\nabla\alpha\cdot\nabla r\overline{V}_\theta(r,z)\\
&\qquad\qquad + S(\alpha)\nabla r\overline{V}_\theta(r,z)\cdot\nabla\ln\overline{\rho}(r,z)
\end{aligned} \tag{A.43}$$

Where the three terms on the RHS will be zero outside the blade row. Since the flow is periodic in the tangential direction, the periodic potential function $\widetilde{\Phi}$ can be expressed in terms of a complex Fourier series of the form:

$$\widetilde{\Phi}(r,\theta,z) = \sum_{n=-\infty,n\neq0}^{\infty}\widetilde{\Phi}_n(r,z)e^{inB\theta} \tag{A.44}$$

Where $\widetilde{\Phi}_n$ is the Fourier coefficients of the potential function of the periodic flow $\widetilde{\Phi}$.

Substituting Equation A.44 into the LHS of Equation A.43, we can get:

$$\begin{aligned}
&\nabla^2\widetilde{\Phi}\left(r,\theta,z\right)+\nabla\widetilde{\Phi}\left(r,\theta,z\right)\cdot\nabla\ln\overline{\rho}\left(r,z\right)\\
&=\sum_{n=-\infty,n\neq0}^{\infty}e^{inB\theta}\left[\frac{\partial^2\widetilde{\Phi}_n\left(r,z\right)}{\partial r^2}+\frac{\partial\widetilde{\Phi}_n\left(r,z\right)}{r\partial r}+\frac{\partial^2\widetilde{\Phi}_n\left(r,z\right)}{\partial z^2}\right.\\
&\qquad\left.+\frac{\partial\widetilde{\Phi}_n\left(r,z\right)}{\partial r}\frac{\partial\ln\overline{\rho}\left(r,z\right)}{\partial r}+\frac{\partial\widetilde{\Phi}_n\left(r,z\right)}{\partial z}\frac{\partial\ln\overline{\rho}\left(r,z\right)}{\partial z}-\frac{n^2B^2}{r^2}\widetilde{\Phi}_n\left(r,z\right)\right]
\end{aligned}\tag{A.45}$$

Substituting Equation A.1, Equation A.15 and Equation A.16 into the RHS of Equation A.43, we can get:

$$\begin{aligned}
&S\left(\alpha\right)\nabla^2r\overline{V}_\theta\left(r,z\right)+S^{'}\left(\alpha\right)\nabla\alpha\cdot\nabla r\overline{V}_\theta\left(r,z\right)+S\left(\alpha\right)\nabla r\overline{V}_\theta\left(r,z\right)\cdot\nabla\ln\overline{\rho}\left(r,z\right)\\
&=\sum_{n=-\infty,n\neq0}^{\infty}e^{inB[\theta-f(r,z)]}\left\{\frac{1}{inB}\left[\nabla^2r\overline{V}_\theta\left(r,z\right)+\frac{\partial r\overline{V}_\theta\left(r,z\right)}{\partial r}\frac{\partial\ln\overline{\rho}\left(r,z\right)}{\partial r}+\frac{\partial r\overline{V}_\theta\left(r,z\right)}{\partial z}\frac{\partial\ln\overline{\rho}\left(r,z\right)}{\partial z}\right]\right.\\
&\qquad\left.-\frac{\partial f\left(r,z\right)}{\partial r}\frac{\partial r\overline{V}_\theta\left(r,z\right)}{\partial r}-\frac{\partial f\left(r,z\right)}{\partial z}\frac{\partial r\overline{V}_\theta\left(r,z\right)}{\partial z}\right\}
\end{aligned}\tag{A.46}$$

Comparing Equation A.45 and Equation A.46, the following second order partial differential equation for $\widetilde{\Phi}_n$ can be written down:

$$\begin{aligned}
&\frac{\partial^2\widetilde{\Phi}_n\left(r,z\right)}{\partial r^2}+\frac{\partial\widetilde{\Phi}_n\left(r,z\right)}{r\partial r}+\frac{\partial^2\widetilde{\Phi}_n\left(r,z\right)}{\partial z^2}+\frac{\partial\widetilde{\Phi}_n\left(r,z\right)}{\partial r}\frac{\partial\ln\overline{\rho}\left(r,z\right)}{\partial r}\\
&\quad+\frac{\partial\widetilde{\Phi}_n\left(r,z\right)}{\partial z}\frac{\partial\ln\overline{\rho}\left(r,z\right)}{\partial z}-\frac{n^2B^2}{r^2}\widetilde{\Phi}_n\left(r,z\right)\\
&=\frac{e^{-inBf(r,z)}}{inB}\left[\nabla^2r\overline{V}_\theta\left(r,z\right)+\frac{\partial r\overline{V}_\theta\left(r,z\right)}{\partial r}\frac{\partial\ln\overline{\rho}\left(r,z\right)}{\partial r}+\frac{\partial r\overline{V}_\theta\left(r,z\right)}{\partial z}\frac{\partial\ln\overline{\rho}\left(r,z\right)}{\partial z}\right]\\
&\quad-e^{-inBf(r,z)}\left[\frac{\partial f\left(r,z\right)}{\partial r}\frac{\partial r\overline{V}_\theta\left(r,z\right)}{\partial r}+\frac{\partial f\left(r,z\right)}{\partial z}\frac{\partial r\overline{V}_\theta\left(r,z\right)}{\partial z}\right]\qquad(n\neq0)
\end{aligned}\tag{A.47}$$

When $n=0$, Equation A.47 corresponds to the Monge-Clebsch formulation of the mean flow continuity equation and therefore has to be neglected in the solution of the periodic flow field. In order to solve Equation A.47 for $\widetilde{\Phi}_n$, boundary conditions need to be applied on the four boundaries of the physical domain including the hub wall, the shroud wall, the upstream (inlet) and the downstream (outlet) boundaries.

1) The periodic velocity $\widetilde{\overrightarrow{V}}$ normal to the hub and the shroud must be zero. This condition can be expressed by:

$$\widetilde{\overrightarrow{V}}(r,\theta,z)\cdot\overrightarrow{n}=0 \tag{A.48}$$

Where $\overrightarrow{n}$ is the unit vector normal to the hub or shroud walls.

2) Substituting Equation A.20 into Equation A.48 along with Equation A.16 and Equation A.44, the following equation for the hub and shroud boundary conditions can be obtained:

$$\begin{aligned}
\left[\nabla\widetilde{\Phi}(r,\theta,z)-S(\alpha)\nabla r\overline{V}_{\theta}(r,z)\right]\cdot\overrightarrow{n}&=0\\
\nabla\widetilde{\Phi}(r,\theta,z)\cdot\overrightarrow{n}&=S(\alpha)\nabla r\overline{V}_{\theta}(r,z)\cdot\overrightarrow{n}\\
\nabla\sum_{n=-\infty,n\neq0}^{\infty}\widetilde{\Phi}_n(r,z)\,e^{inB\theta}\cdot\overrightarrow{n}&=\sum_{n=-\infty,n\neq0}^{\infty}\frac{e^{inB[\theta-f(r,z)]}}{inB}\nabla r\overline{V}_{\theta}(r,z)\cdot\overrightarrow{n}\\
\nabla\widetilde{\Phi}_n(r,z)\cdot\overrightarrow{n}&=\frac{e^{-inBf(r,z)}}{inB}\nabla r\overline{V}_{\theta}(r,z)\cdot\overrightarrow{n}\\
\frac{\partial\widetilde{\Phi}_n(r,z)}{\partial\overrightarrow{n}}&=\frac{e^{-inBf(r,z)}}{inB}\frac{\partial r\overline{V}_{\theta}(r,z)}{\partial\overrightarrow{n}}
\end{aligned} \tag{A.49}$$

3) At the far upstream and downstream the flow is uniform. This is the result of the fact that the periodic velocity $\widetilde{\overrightarrow{V}}$ vanishes as the upstream boundary is approached. In the absence of the shed vorticity the same phenomenon occurs as the far downstream boundary is approached. This condition can be expressed by:

$$\widetilde{\Phi}_n(r,z)=0 \tag{A.50}$$

Equation A.47 then can be solved subject to the Neumann boundary condition (Equation A.49) and the Dirichlet boundary condition (Equation A.50).

Solving Exact Mean Flow Continuity Equation

To solve Equation A.24, a stream function cannot be defined directly. Therefore, a special artificial density ρ_m needs to be defined first which satisfies:

$$\nabla\cdot\left[\rho_m(r,z)\,\overline{\overrightarrow{W}}(r,z)\right]=0 \tag{A.51}$$

Where ρ_m can be obtained through Equation A.24 and Equation A.51:

$$\begin{aligned}\nabla \cdot \left[\rho_m(r,z)\overrightarrow{\overrightarrow{W}}(r,z)\right] &= \overrightarrow{\overrightarrow{W}}(r,z)\cdot\nabla\rho_m(r,z) + \rho_m(r,z)\nabla\cdot\overrightarrow{\overrightarrow{W}}(r,z) = 0 \\ \overrightarrow{\overrightarrow{W}}(r,z)\cdot\nabla\rho_m(r,z) - \rho_m(r,z)&\overline{\overrightarrow{\overrightarrow{W}}(r,\theta,z)\cdot\nabla\ln\rho(r,\theta,z)} = 0 \\ \overrightarrow{\overrightarrow{W}}(r,z)\cdot\nabla\ln\rho_m(r,z) &= \overline{\overrightarrow{\overrightarrow{W}}(r,\theta,z)\cdot\nabla\ln\rho(r,\theta,z)} \end{aligned} \quad \text{(A.52)}$$

Then an exactly same equation for the stream function of the exact mean flow as Equation A.39 is obtained. The only difference is that ρ_a is defined by:

$$\rho_a(r,z) = \frac{\rho_i}{\rho_m(r,z)} \quad \text{(A.53)}$$

Solving Exact Periodic Flow Continuity Equation

To solve Equation A.25, take the divergence of Equation A.20 and use Equation A.25 to get:

$$\begin{aligned}\nabla^2\widetilde{\Phi}(r,\theta,z) = S(\alpha)\nabla^2 r\overline{V}_\theta(r,z) + &S'(\alpha)\nabla\alpha\cdot\nabla r\overline{V}_\theta(r,z) \\ -\overrightarrow{W}(r,\theta,z)\cdot\nabla\ln\rho(r,\theta,z) + &\overline{\overrightarrow{W}(r,\theta,z)\cdot\nabla\ln\rho(r,\theta,z)}\end{aligned} \quad \text{(A.54)}$$

Equation A.54 is very similar to Equation A.43 apart from the last two terms on the RHS, whose determination need the computation of the velocity and the density throughout the flow field. The similar method can be used to solve Equation A.54 by expanding both sides of Equation A.54 in the form of Fourier series in the tangential direction. This method needs the Fourier coefficients of the last two terms on the RHS of Equation A.54 to be computed. Since the flow quantities are only known at discrete points inside the computational domain, the Fourier coefficients of the last two terms on the RHS of Equation A.54 can be computed by using Discrete Fourier Transform (DFT).

The periodic potential function $\widetilde{\Phi}$ can be approximately expressed in the form of a truncated IDFT:

$$\begin{aligned}\widetilde{\Phi}(r,\theta,z) &\approx \sum_{n=-\frac{N}{2}}^{\frac{N}{2}-1} \widetilde{\Phi}_n(r,z)\, e^{inB\theta} \\ \widetilde{\Phi}(r,\theta_j,z) &\approx \sum_{n=-\frac{N}{2}}^{\frac{N}{2}-1} \widetilde{\Phi}_n(r,z)\, e^{ik_n\theta_j}\end{aligned} \tag{A.55}$$

Where θ_j defined by Equation A.56 gives the values of θ, the tangential coordinate of points on a uniformly spaced grid in the tangential direction with spacing $\Delta\theta$ and total number of grids N.

$$\theta_j = j\Delta\theta \qquad (j = 0, 1, 2, \ldots, N) \tag{A.56}$$

The set k_n should be chosen to make the function $e^{ik_n\theta_j}$ periodic and equally spaced and it should also reduce the aliasing effects which can be found when a continuous function is sampled at discrete intervals.

$$k_n = nB = \frac{2\pi n}{N\Delta\theta} \qquad \left(n = -\frac{N}{2}, \ldots, -1, 0, 1, \ldots, \frac{N}{2}-1\right) \tag{A.57}$$

Using Equation A.55, Equation A.56 and Equation A.57 the following equation for the exact periodic flow potential function can be obtained:

$$\begin{aligned}&\frac{\partial^2\widetilde{\Phi}_n(r,z)}{\partial r^2} + \frac{\partial\widetilde{\Phi}_n(r,z)}{r\partial r} + \frac{\partial^2\widetilde{\Phi}_n(r,z)}{\partial z^2} - \frac{n^2B^2}{r^2}\widetilde{\Phi}_n(r,z) \\ &= \frac{e^{-inBf(r,z)}}{inB}\nabla^2 r\overline{V}_\theta(r,z) - e^{-inBf(r,z)}\left[\frac{\partial f(r,z)}{\partial r}\frac{\partial r\overline{V}_\theta(r,z)}{\partial r} + \frac{\partial f(r,z)}{\partial z}\frac{\partial r\overline{V}_\theta(r,z)}{\partial z}\right] + F_n(r,z) \\ &\qquad\qquad \left(n = -\frac{N}{2}, \ldots, -1, 0, 1, \ldots, \frac{N}{2}-1\right)\end{aligned} \tag{A.58}$$

Where F_n is the Fourier coefficients of $-\overrightarrow{W}\cdot\nabla\ln\rho + \overline{\overrightarrow{W}\cdot\nabla\ln\rho}$. When $n = 0$, Equation A.58 corresponds to the Monge-Clebsch formulation of the mean flow continuity equation and therefore has to be neglected in the solution of the periodic

flow field. Equation A.58 then can be rewritten as:

$$\frac{\partial^2\widetilde{\Phi}_n(r,z)}{\partial r^2}+\frac{\partial\widetilde{\Phi}_n(r,z)}{r\partial r}+\frac{\partial^2\widetilde{\Phi}_n(r,z)}{\partial z^2}-\frac{n^2B^2}{r^2}\widetilde{\Phi}_n(r,z)$$
$$=\frac{e^{-inBf(r,z)}}{inB}\nabla^2 r\overline{V}_\theta(r,z)-e^{-inBf(r,z)}\left[\frac{\partial f(r,z)}{\partial r}\frac{\partial r\overline{V}_\theta(r,z)}{\partial r}+\frac{\partial f(r,z)}{\partial z}\frac{\partial r\overline{V}_\theta(r,z)}{\partial z}\right]$$
$$-R_n(r,z)\qquad\left(n=-\frac{N}{2},\ldots,-1,1,\ldots,\frac{N}{2}-1\right)\tag{A.59}$$

Where R_n is the Fourier coefficients of $\overrightarrow{W}\cdot\nabla\ln\rho$ and defined as:

$$R_n(r,z)=\frac{1}{N}\sum_{j=1}^{N}\left[\overrightarrow{W}(r,\theta_j,z)\cdot\nabla\ln\rho(r,\theta_j,z)\right]e^{-\frac{i2\pi nj}{N}}\tag{A.60}$$

Since the potential function of the periodic flow $\widetilde{\Phi}$ is a real function, its Fourier transform has the following property:

$$\widetilde{\Phi}_{-n}(r,z)=\widetilde{\Phi}_n^*(r,z)\qquad\left(n=1,2,\ldots,\frac{N}{2}\right)\tag{A.61}$$

Where * denotes complex conjugation. Therefore, Equation A.59 and Equation A.60 only need to be solved for half of the frequency spectrum k_n given in Equation A.57 and subjected to boundary conditions (Equation A.49 and Equation A.50).

Calculation of Density

The first law of thermodynamics for a steady, inviscid and no body force flow can be written as:

$$\overrightarrow{W}(r,\theta,z)\cdot\nabla H^{rot}(r,\theta,z)=0\tag{A.62}$$

Where $\overrightarrow{W}$ is the relative velocity vector and H^{rot} is the rothalpy. Since the inlet flow is uniform H^{rot} remains constant:

$$H^{rot}(r,\theta,z)=h(r,\theta,z)+\frac{1}{2}\overrightarrow{W}(r,\theta,z)\cdot\overrightarrow{W}(r,\theta,z)-\frac{1}{2}\omega^2r^2=const\tag{A.63}$$

Where h is the static enthalpy and ω is the rotational speed. Using the perfect gas equation and the isentropic relation, we have:

$$\begin{aligned}\frac{\rho\left(r,\theta,z\right)}{\rho^{rot}} &= \left[\frac{h\left(r,\theta,z\right)}{H^{rot}}\right]^{\frac{1}{\gamma-1}} \\ &= \left[\frac{H^{rot}-\frac{1}{2}\overrightarrow{W}\left(r,\theta,z\right)\cdot\overrightarrow{W}\left(r,\theta,z\right)+\frac{1}{2}\omega^2r^2}{H^{rot}}\right]^{\frac{1}{\gamma-1}} \\ &= \left[\frac{2c_PT^{rot}-\overrightarrow{W}\left(r,\theta,z\right)\cdot\overrightarrow{W}\left(r,\theta,z\right)+\omega^2r^2}{2c_PT^{rot}}\right]^{\frac{1}{\gamma-1}}\end{aligned} \tag{A.64}$$

In the case of the approximation approach the latest values of the mean velocity $\overrightarrow{\overline{W}}\left(r,z\right)$, calculated from Equation A.36, are used in Equation A.64 to obtain a new estimation for the mean density $\overline{\rho}\left(r,z\right)$.

$$\frac{\overline{\rho}\left(r,z\right)}{\rho^{rot}} = \left[\frac{2c_PT^{rot}-\overrightarrow{\overline{W}}\left(r,z\right)\cdot\overrightarrow{\overline{W}}\left(r,z\right)+\omega^2r^2}{2c_PT^{rot}}\right]^{\frac{1}{\gamma-1}} \tag{A.65}$$

In the case of the exact approach the full 3D velocity field $\overrightarrow{W}\left(r,\theta,z\right)$ is used in Equation A.64 to obtain the density $\rho\left(r,\theta,z\right)$ throughout the 3D flow field. The mean velocity values are obtained similarly by using Equation A.36, while the periodic velocities $\overrightarrow{\widetilde{V}}\left(r,\theta,z\right)$ are computed by using IDFT of Equation A.20 as shown below:

$$\begin{aligned}\widetilde{V}_r\left(r,\theta,z\right) &= IDFT\left[\frac{\partial\widetilde{\Phi}_n\left(r,z\right)}{\partial r}-\frac{\partial r\overline{V}_\theta\left(r,z\right)}{\partial r}\frac{e^{-ik_nf(r,z)}}{ik_n}\right] \\ \widetilde{V}_\theta\left(r,\theta,z\right) &= IDFT\left[\frac{ik_n}{r}\widetilde{\Phi}_n\left(r,z\right)\right] \\ \widetilde{V}_z\left(r,\theta,z\right) &= IDFT\left[\frac{\partial\widetilde{\Phi}_n\left(r,z\right)}{\partial z}-\frac{\partial r\overline{V}_\theta\left(r,z\right)}{\partial z}\frac{e^{-ik_nf(r,z)}}{ik_n}\right]\end{aligned} \tag{A.66}$$

Once the density filed $\rho(r,\theta,z)$ is available, the Fourier transform of the natural logarithm of the density is computed by:

$$\rho_n(r,z) = \frac{1}{N}\sum_{j=1}^{N}[\ln\rho_n(r,\theta_j,z)]e^{\frac{i2\pi jn}{N}} \qquad \theta_j = j\Delta\theta \tag{A.67}$$

The derivative of $ln\rho_n(r,\theta_j,z)$ in the tangential direction is computed by taking the IDFT of $\frac{ik_n\rho_n(r,z)}{r}$, while the axial and radial derivatives of $ln\rho_n(r,\theta_j,z)$ are computed by calculating the IDFT of the corresponding derivatives of $\rho_n(r,z)$.

Using velocity filed $\overrightarrow{W}(r,\theta,z)$ and the derivatives of $ln\rho_n(r,\theta_j,z)$, the term $\overrightarrow{W}(r,\theta,z)\cdot\nabla\ln\rho(r,\theta,z)$ can be determined.

The Fourier transform of $\overrightarrow{W}(r,\theta,z)\cdot\nabla\ln\rho(r,\theta,z)$ is computed as in Equation A.60 to get $R_n(r,z)$ which is required for Equation A.59.

The 0^{th} component of Equation A.60 which corresponds to $\overline{\overrightarrow{W}(r,\theta,z)\cdot\nabla\ln\rho(r,\theta,z)}$ can be used in Equation A.52 to calculate the special artificial density ρ_m.

Calculation of Blade Shape

Once the flow field is calculated, the blade shape then can be computed by using the blade boundary condition that the relative velocity vector on the blade must be aligned with the blade surface. The blade boundary condition can be defined as:

$$\overrightarrow{W}_{bl}(r,\theta,z)\cdot\nabla\alpha(r,\theta,z) = 0 \tag{A.68}$$

Where $\overrightarrow{W}_{bl}(r,\theta,z)$ is the relative velocity on the blade camber surface and defined by Equation A.69, $\overrightarrow{W}_{bl}(r,\theta^+,z)$ and $\overrightarrow{W}_{bl}(r,\theta^-,z)$ are the relative velocities on the blade pressure and suction surfaces and $\nabla\alpha(r,\theta,z)$ is the vector normal to the blade surface $\alpha(r,\theta,z)$ which is defined by Equation A.1.

$$\begin{aligned}\overrightarrow{W}_{bl}(r,\theta,z) &= \frac{\overrightarrow{W}^{+}_{bl}(r,\theta,z)+\overrightarrow{W}^{-}_{bl}(r,\theta,z)}{2}\\ &= \frac{\overrightarrow{W}_{bl}(r,\theta^+,z)+\overrightarrow{W}_{bl}(r,\theta^-,z)}{2}\end{aligned} \tag{A.69}$$

Using Equation A.1 and Equation A.21 to expand Equation A.68 in the vector format, we get:

$$\begin{aligned}
\left[\overline{W}_r + \widetilde{V}_{r,bl}, \overline{W}_\theta + \widetilde{V}_{\theta,bl}, \overline{W}_z + \widetilde{V}_{z,bl}\right] \cdot \left[\frac{\partial\alpha\left(r,\theta,z\right)}{\partial r}, \frac{\partial\alpha\left(r,\theta,z\right)}{r\partial\theta}, \frac{\partial\alpha\left(r,\theta,z\right)}{\partial z}\right] &= 0 \\
\left[\overline{V}_r + \widetilde{V}_{r,bl}, \overline{V}_\theta - \omega r + \widetilde{V}_{\theta,bl}, \overline{V}_z + \widetilde{V}_{z,bl}\right] \cdot \left[\frac{-\partial f\left(r,z\right)}{\partial r}, \frac{1}{r}, \frac{-\partial f\left(r,z\right)}{\partial z}\right] &= 0 \\
\left(\overline{V}_r + \widetilde{V}_{r,bl}\right)\frac{\partial f\left(r,z\right)}{\partial r} + \left(\overline{V}_z + \widetilde{V}_{z,bl}\right)\frac{\partial f\left(r,z\right)}{\partial z} &= \frac{\overline{V}_\theta}{r} + \frac{\widetilde{V}_{\theta,bl}}{r} - \omega \\
\left(\overline{V}_r + \widetilde{V}_{r,bl}\right)\frac{\partial f\left(r,z\right)}{\partial r} + \left(\overline{V}_z + \widetilde{V}_{z,bl}\right)\frac{\partial f\left(r,z\right)}{\partial z} &= \frac{r\overline{V}_\theta}{r^2} + \frac{\widetilde{V}_{\theta,bl}}{r} - \omega
\end{aligned} \tag{A.70}$$

Where $\overline{V}_r$, $\overline{V}_\theta$ and $\overline{V}_z$ are the radial, tangential and axial components of the mean absolute velocity, $\widetilde{V}_{r,bl}$, $\widetilde{V}_{\theta,bl}$ and $\widetilde{V}_{z,bl}$ are the radial, tangential and axial components of the periodic velocity on the blade camber surface and $f\left(r,z\right)$ is the blade camber. Equation A.70 is a first-order hyperbolic partial differential equation which needs to be integrated along the meridional projection of streamlines on the blade surface in order to find the blade camber $f\left(r,z\right)$. This integration requires the input of some initial conditions of $f\left(r,z\right)$ to get a unique solution. This initial value of $f\left(r,z\right)$ is called the stacking condition of the blade which can be implemented by predefining the values of $f\left(r,z\right)$ along a quasi-orthogonal, for example at the blade LE or TE.

Description of Flow Charts

In this subsection, a step by step description of the flow charts of this inverse design method is given.

Approximate Approach

The following steps are taken to calculate the blade geometry when the approximate continuity equations (Equation A.29 and Equation A.30) are used to compute the flow field.

1) The design specifications, including the meridional geometry, the inlet velocity, the inlet total temperature, the flow properties, the blade stacking condition, the blade rotational speed, the blade normal thickness distribution and the number of blades, are given. The meridional geometry is defined by points along the hub and shroud curves where the quasi-orthogonals connect hub and shroud through these points. The blade LE and TE must be aligned with these quasi-orthogonals.

2) A curvilinear-body-fitted coordinate system (ξ, η) plane (Thompson et al. [1977]) is generated by the transformation from the physical (r, z) plane. All partial differential equations are solved in the (ξ, η) plane.

3) Initial values for the blade camber $f(r, z)$ and the mean density $\overline{\rho}(r, z)$ are obtained by assuming zero periodic velocities $\widetilde{\vec{V}}(r, \theta, z)$ and uniform mean velocities $\overline{\vec{V}}(r, z)$ along quasi-orthogonals (Equation A.36).

4) The blade blockage factor $B_f(r, z)$ is computed using Equation A.32 while the blade tangential thickness $t_\theta(r, z)$ is updated using Equation A.33. The blade camber $f(r, z) = f^{n-1}(r, z)$ is from the previous iteration and the blade normal thickness $t_N(r, z)$ is an input. Therefore, the stream function $\Psi(r, z)$ for the mean flow field can be solved using Equation A.39. The mean flow velocities $\overline{V}_r(r, z)$ and $\overline{V}_z(r, z)$ can be obtained from Equation A.36.

5) The mean density $\overline{\rho}(r, z)$ is computed using Equation A.65 with the mean flow velocities obtained in the previous step.

6) The potential function of the periodic flow $\widetilde{\Phi}(r, \theta, z)$ is solved using Equation A.44 and Equation A.47 subject to boundary conditions specified in Equation A.49 and Equation A.50.

7) The periodic velocity on the blade $\widetilde{V}_{bl}(r, \theta_j, z)$ is computed using the gradient of Equation A.55 with $\theta_j = f(r, z)$.

8) The blade camber $f(r, z)$ is updated using Equation A.70 with the mean and periodic velocities obtained from step 4) and 7).

9) If the maximum difference between the updated blade camber $f^n(r, z)$ and the blade camber obtained from the previous iteration $f^{n-1}(r, z)$ is greater than the specified tolerance, the programme will go back to step 4) and continue the calculation. The code will stop when the blade camber difference

is less than the tolerance or the prescribed maximum number of iterations is reached.

Exact Approach

When the exact mean flow continuity equation is used, step 1), 2) and 3) in the previous subsection are followed. Then the following steps are taken:

4) The mean flow stream function $\Psi(r,z)$ is solved using an equation similar to Equation A.39 while $\rho_a(r,z)$ is defined by Equation A.53. For the first iteration, when the periodic velocity is unknown, the mean density $\overline{\rho}(r,z)$ computed in step 3) is used for the calculation of the mean flow stream function $\Psi(r,z)$.

5) The potential function of the periodic flow $\widetilde{\Phi}(r,\theta,z)$ is computed using Equation A.59 subject to boundary conditions specified in Equation A.49 and Equation A.50.

6) The flow mean velocity $\overline{V}_r(r,z)$ or $\overline{W}_r(r,z)$ is calculated using Equation A.36 and the periodic velocity at the blade $\widetilde{V}_{bl}(r,\theta_j,z)$ is computed using the gradient of Equation A.55 with $\theta_j = f(r,z)$.

7) The blade camber $f(r,z)$ is updated using Equation A.70 with the mean and periodic velocities obtained from step 6).

8) If the maximum difference between the updated blade camber $f^n(r,z)$ and the blade camber obtained from the previous iteration $f^{n-1}(r,z)$ is less than the specified tolerance, the code is regarded as converged. Otherwise, the following steps are taken.

9) The periodic velocity $\widetilde{\overrightarrow{V}}(r,\theta,z)$ through the flow field is computed using Equation A.66.

10) The density $\rho(r,\theta,z)$ through the flow field is computed using Equation A.64.

11) The Fourier transform of the natural logarithm of the density is computed using Equation A.67.

12) The derivative of $ln\rho_n(r,\theta_j,z)$ in the tangential direction is computed by taking the IFT of $\frac{ik_n\rho_n(r,z)}{r}$, while the axial and radial derivatives of $ln\rho_n(r,\theta_j,z)$ are computed by calculating the IFT of the corresponding derivatives of $\rho_n(r,z)$.

13) The relative velocity $\overrightarrow{W}(r,\theta,z)$ can be obtained using Equation A.21 and Equation A.22 with the mean velocity $\overline{V}_r(r,z)$ from step 6) and the periodic velocity $\widetilde{\overrightarrow{V}}(r,\theta,z)$ from step 9). Using velocity filed $\overrightarrow{W}(r,\theta,z)$ and the derivatives of $ln\rho_n(r,\theta_j,z)$, the term $\overrightarrow{W}(r,\theta,z)\cdot\nabla\ln\rho(r,\theta,z)$ can be determined.

14) The Fourier transform of $\overrightarrow{W}(r,\theta,z)\cdot\nabla\ln\rho(r,\theta,z)$ is computed using Equation A.60. The 0th component of Equation A.60 $R_0(r,z)$ is equal to $\overline{\overrightarrow{W}(r,\theta,z)\cdot\nabla\ln\rho(r,\theta,z)}$ (the mean of $\overrightarrow{W}(r,\theta,z)\cdot\nabla\ln\rho(r,\theta,z)$) which is used together with $\overline{\overrightarrow{W}}(r,z)$ in Equation A.52 to compute the special artificial density $\rho_m(r,z)$.

15) Equation A.53 is used with $\rho_m(r,z)$ to update $\rho_a(r,z)$. Then step 4) to 8) are followed until the difference between $f^n(r,z)$ and $f^{n-1}(r,z)$ is less than the tolerance or the maximum number of iterations is reached.

APPENDIX B

LIST OF PUBLICATIONS

J. Zhang, M. Zangeneh, and P. Eynon. A 3D Inverse Design based Multidisciplinary Optimization on the Radial and Mixed-inflow Turbines for Turbochargers. *IMechE 11th International Conference on Turbochargers and Turbocharging*, pages 399–410, 2014.

J. Zhang and M. Zangeneh. Increasing Pulse Energy Recovery of Radial Turbocharger Turbine by 3D Inverse Design Method. *ASME Turbo Expo 2015*, GT2015-43579, 2015.

J. Zhang, P. Gomes, M. Zangeneh, and B. Choo. Design of A Centrifugal Compressor Stage and A Radial-inflow Turbine Stage for A Supercritical CO_2 Recompression Brayton Cycle by Using 3D Inverse Design Method. *ASME Turbo Expo 2017*, GT2017-64631, 2017.